



AFRL-RQ-WP-TR-2013-0174

**MIDWEST STRUCTURAL SCIENCES CENTER
2006 – 2013 Final Report**

John Lambros, Daniel J. Bodony, and C. Armando Duarte

University of Illinois at Urbana-Champaign

**SEPTEMBER 2013
Final Report**

Approved for public release; distribution unlimited.

See additional restrictions described on inside pages

STINFO COPY

**AIR FORCE RESEARCH LABORATORY
AEROSPACE SYSTEMS DIRECTORATE
WRIGHT-PATTERSON AIR FORCE BASE, OH 45433-7542
AIR FORCE MATERIEL COMMAND
UNITED STATES AIR FORCE**

NOTICE AND SIGNATURE PAGE

Using Government drawings, specifications, or other data included in this document for any purpose other than Government procurement does not in any way obligate the U.S. Government. The fact that the Government formulated or supplied the drawings, specifications, or other data does not license the holder or any other person or corporation; or convey any rights or permission to manufacture, use, or sell any patented invention that may relate to them.

This report was cleared for public release by the USAF 88th Air Base Wing (88 ABW) Public Affairs Office (PAO) and is available to the general public, including foreign nationals.

Copies may be obtained from the Defense Technical Information Center (DTIC)
(<http://www.dtic.mil>).

AFRL-RQ-WP-TR-2013-0174 HAS BEEN REVIEWED AND IS APPROVED FOR
PUBLICATION IN ACCORDANCE WITH ASSIGNED DISTRIBUTION STATEMENT.

*//Signature//

STEPHEN MICHAEL SPOTTSWOOD
Senior Aerospace Engineer
Hypersonic Sciences Branch
Air Force Research Laboratory

//Signature//

MARK A. AMENDT, Chief
Hypersonic Sciences Branch
Aerospace Systems Directorate
Air Force Research Laboratory

*//Signature//

ROBERT A. MERCIER
Deputy for Technology
High Speed Systems Division
Air Force Research Laboratory

This report is published in the interest of scientific and technical information exchange, and its publication does not constitute the Government's approval or disapproval of its ideas or findings.

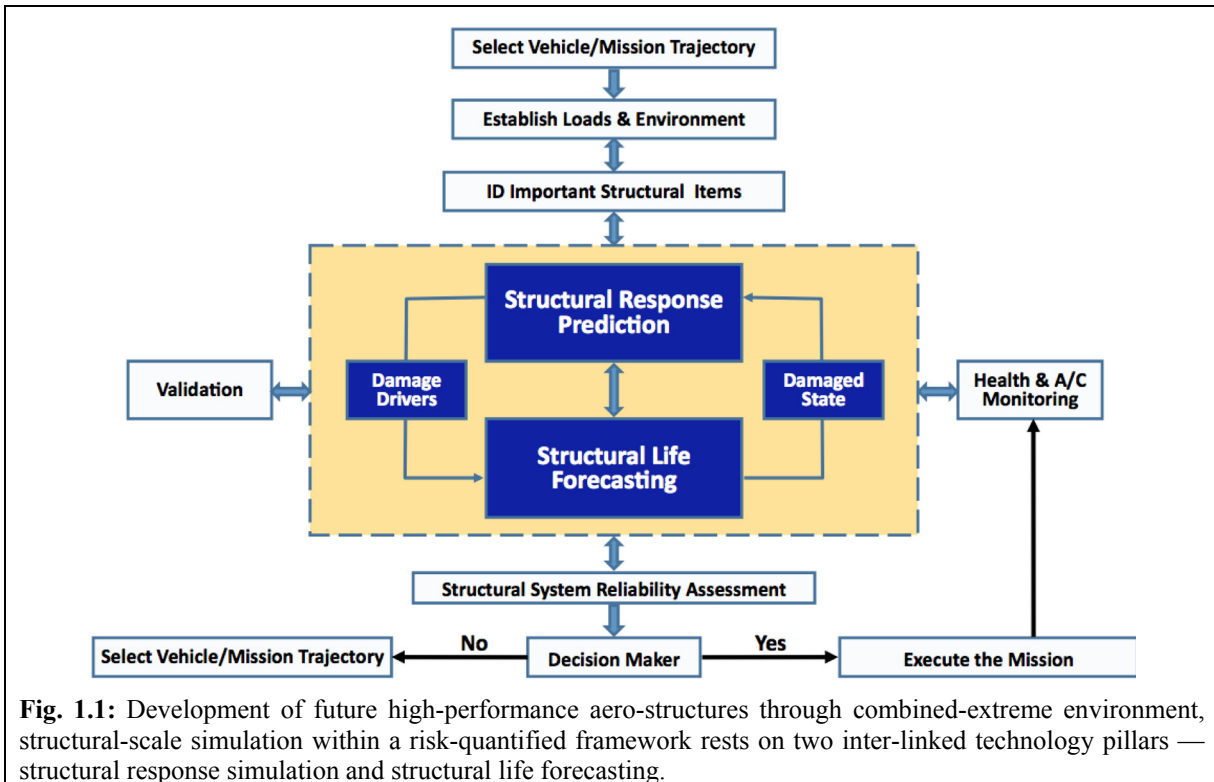
*Disseminated copies will show “//Signature//” stamped or typed above the signature blocks.

REPORT DOCUMENTATION PAGE				Form Approved OMB No. 0704-0188	
<p>The public reporting burden for this collection of information is estimated to average 1 hour per response, including the time for reviewing instructions, searching existing data sources, gathering and maintaining the data needed, and completing and reviewing the collection of information. Send comments regarding this burden estimate or any other aspect of this collection of information, including suggestions for reducing this burden, to Department of Defense, Washington Headquarters Services, Directorate for Information Operations and Reports (0704-0188), 1215 Jefferson Davis Highway, Suite 1204, Arlington, VA 22202-4302. Respondents should be aware that notwithstanding any other provision of law, no person shall be subject to any penalty for failing to comply with a collection of information if it does not display a currently valid OMB control number. PLEASE DO NOT RETURN YOUR FORM TO THE ABOVE ADDRESS.</p>					
1. REPORT DATE (DD-MM-YY) September 2013		2. REPORT TYPE Final		3. DATES COVERED (From - To) 01 June 2006 – 01 September 2013	
4. TITLE AND SUBTITLE MIDWEST STRUCTURAL SCIENCES CENTER 2006 – 2013 Final Report				5a. CONTRACT NUMBER FA8650-06-2-3620	
				5b. GRANT NUMBER	
				5c. PROGRAM ELEMENT NUMBER 62201F	
6. AUTHOR(S) John Lambros, Daniel J. Bodony, and C. Armando Duarte				5d. PROJECT NUMBER 2401	
				5e. TASK NUMBER	
				5f. WORK UNIT NUMBER Q03Z	
7. PERFORMING ORGANIZATION NAME(S) AND ADDRESS(ES) University of Illinois at Urbana-Champaign Midwest Structural Sciences Center 2276 Digital Computing Lab Urbana, IL 61801				8. PERFORMING ORGANIZATION REPORT NUMBER	
9. SPONSORING/MONITORING AGENCY NAME(S) AND ADDRESS(ES) Air Force Research Laboratory Aerospace Systems Directorate Wright-Patterson Air Force Base, OH 45433-7542 Air Force Materiel Command United States Air Force				10. SPONSORING/MONITORING AGENCY ACRONYM(S) AFRL/RQHF	
				11. SPONSORING/MONITORING AGENCY REPORT NUMBER(S) AFRL-RQ-WP-TR-2013-0174	
12. DISTRIBUTION/AVAILABILITY STATEMENT Approved for public release; distribution unlimited.					
13. SUPPLEMENTARY NOTES PAO Case Number: 88ABW-2013-2516; Clearance Date: 29 May 2013. Report contains color.					
14. ABSTRACT The Midwest Structural Sciences Center is a collaboration between the Structural Sciences Center, Aerospace Systems Directorate of the Air Force Research Laboratory (AFRL/RQHF SSC), and a team of faculty, graduate students, and professional staff researchers of the University of Illinois at Urbana-Champaign (UI), Wright State University, University of Cincinnati, and the University of Texas at San Antonio. The team works closely to simulate, model and test structures and materials for use in future air-and space-vehicles in a risk quantified design process.					
15. SUBJECT TERMS					
16. SECURITY CLASSIFICATION OF:			17. LIMITATION OF ABSTRACT: SAR	18. NUMBER OF PAGES 192	19a. NAME OF RESPONSIBLE PERSON (Monitor) L. Michael Spottswood 19b. TELEPHONE NUMBER (Include Area Code) N/A
a. REPORT Unclassified	b. ABSTRACT Unclassified	c. THIS PAGE Unclassified			

1. MOTIVATION AND BACKGROUND

Long standing interests of the United States Air Force (USAF) that can provide “game-changing” operational capabilities include prompt global strike, operationally responsive space access and sustained hypersonic flight. Although large amounts of effort have been expended in achieving these capabilities, they have so far proven somewhat elusive, in part because of structural and material limitations placed upon current designs. A common theme among all these applications is the use of the aircraft/spacecraft structure in an extreme, and highly coupled, aero-thermo-acoustic loading environment. During typical operating conditions in such environments, the crafts are subjected to random loading arising from engine noise, shock impingement on the surface (most often transient in nature), turbulence, and other aeroacoustic vibrations. These random aeroacoustic pressure loads spanning 10’s to 1000’s of Hz frequency, combined with other extreme conditions such as elevated temperatures, plasma formation, *etc.*, often lead to failure of the aircraft structure in modes not predicted by conventional design methods. Therefore novel design tools are needed in order to develop new structures that are capable of operating in such extreme and coupled environments.

In addition to the design itself of novel aircraft structures that are capable of operating in such environments, the operational principles of sustained hypersonic flight and reusable space flight themselves also require evolution. A recent focus of the Air Force Research Laboratories’ research efforts is the realization of the “Digital Twin” concept. In this concept scientifically based design tools are taken beyond the design stage itself and are applied throughout the continued operational life of the vehicle. The goal of the Digital Twin is to have a digital platform of the aircraft, with its current state of damage updated after every mission, combined with appropriate multi-physics models of its operation, that will be able to predict the future limit states of the aircraft when subjected to some future mission parameters. In this way scientifically based *robust predictivity* becomes an operational tool. Figure 1.1 shows a schematic of this process. The highlighted area in the dashed box is a feedback loop illustrating how structural response will be coupled with life prediction to periodically update the state of damage existing in the Digital Twin to follow what has been happening to the actual aircraft/spacecraft. (Periodically the existing state of the Digital Twin as predicted by this algorithm could be adjusted by on board Structural Health Monitoring systems.) The same algorithm can then also be used for making predictions of future flights.



There are significant scientific challenges in predicting the response of structures in extreme environments including a detailed understanding of aero-thermo-elastic coupling; the computational cost and complexity of large-scale models; material and process nonlinearity, temperature dependence and degradation; spatial variation of material and structural properties; and uncertainty in loads, material properties, geometry, and boundary conditions. Therefore there is a need to bridge these scientific gaps. The Midwest Structural Sciences Center (MSSC) and its interactions with the SSC was borne out of this need for expanding our scientific understanding of such complex coupled phenomena.

The MSSC is a collaborative effort between the Structural Sciences Center, Aerospace Systems Directorate of the Air Force Research Laboratory (AFRL/RQHF), and a team of faculty, graduate students, and professional staff researchers of the University of Illinois at Urbana-Champaign (UIUC), University of Cincinnati (UC), Wright State University (WSU), University of Texas at San Antonio (UTSA) and the Air Force Institute of Technology (AFIT). The team works closely to simulate, model, test, and assess structures and materials for use in future air- and spaceframes. The MSSC team was viewed as a “living organization” whose members change over time to meet the needs of the collaborative partnership. Throughout MSSC graduate research assistants, and on occasion undergraduate students and postdoctoral scholars, worked with faculty at the universities and their colleagues at AFRL/RQHF to evaluate and extend our understanding of materials and structures in aerospace structural components that experience extreme combined environments. Although varying among projects to a large degree, collaboration among the partners was frequent (co-advised research projects and graduate theses, teamed simulation and experiments, co-authored journal articles and project proposal submissions, etc.). Computational resources, graduate assistantships, experimental facilities and AFRL/RQ visitor office spaces were earmarked to directly support the MSSC, as have graduate student tuition waivers from the various institutions involved.

This final report gives an overview of the activities of MSSC during its almost seven year existence from October 2006 to February 2013. The immediate next section, Section 2, provides summaries of all the projects that occurred under the umbrella of the MSSC, both at UIUC and elsewhere. The short summaries are meant to give the reader that is not familiar with the MSSC a quick overview of what actually took place during the 7 years of the MSSC. For the reader interested in more details on specific topics, Section 4 provides additional information. Section 3 deals with a brief overview of the history of the center and the reasoning behind how the research efforts evolved during these 7 years. The appendix and attachments provide copies of all publications that have originated from MSSC, and those provide even more detail than is presented in Section 4.

2. MSSC PROJECT SUMMARIES: 2006-2013

In the 7-year course of the MSSC the center's efforts evolved over time both because of a periodic reconsideration of activities residing on the critical path of research necessary to achieve the center's goals and because of natural attrition from certain projects ending or from personnel relocating. Overall, throughout the center's existence, however, a consistent naming and numbering scheme was employed to categorize ongoing projects. This section of the final report is meant to give a brief overview of **all** center activities from its inception to its completion. Significantly more detail on each of these projects, as well as the evolution of the overall center directions, are given in the next two sections.

Four categories of projects were executed through the course of MSSC. These are outlined in Table 2.1 and are denoted by the initials, A, B, C and D. **Projects A (Response Prediction)** dealt with the development of numerical and theoretical methodologies for the understanding and simulation of coupled aero-thermo-acoustic loading situations.

Table 2.1: MSSC research themes.	
A— Response Prediction:	Coupled Aero-Thermo-Mechanical-Acoustic Analysis and Simulation
B— Life Prediction:	Identification and Definition of Structural Limit States
C— Uncertainty:	Framework and Methodologies for Risk-quantified Structural Assessment
D— Experimental Assessment:	Discovery and Limit State Characterization

Most efforts in this category were restricted to simple material behavior (*e.g.*, linear elastic) but allowed for very complex loading and boundary conditions and a coupled model response. The efforts consisted of both highly sophisticated full-field, multiscale, multiphysics simulations and reduced order modeling efforts. **Projects B (Life Prediction)** were focused on developing simulation tools that would account for material nonlinearity and eventual failure, manifested first as plasticity and, eventually, as fatigue failure. The approach of these projects was primarily computational in nature and had as a goal the prediction of structural limit states under coupled loading environments and investigating how these limit states would differ from simpler model predications (*e.g.*, for solely an elastic material as was employed in the A projects). A longer term goal of this research is the combination of the methodologies developed in both A and B projects into a unified framework. **Projects C (Uncertainty)** dealt with another important aspect of limit state prediction in realistic situations – uncertainty quantification and risk assessment. Although well established in other industries (*e.g.*, nuclear) uncertainty quantification is relatively new in aerospace studies. However, it is a necessary part of achieving the Digital Twin concept of *predictive* failure estimation since deterministic aircraft/spacecraft response calculation in complex aero-thermo-acoustic loading environments will not be possible. **Projects D (Experimental Assessment)** concentrated on the experimental characterization of coupled thermomechanical loading problems. New experimental methods were developed to provide validation quality data for coupled high temperature and acoustic loading environments, and to quantitatively study mechanisms of fatigue crack initiation. As such, projects in this category are most closely related to the theoretical studies in projects B and were meant to provide a basis for the analysis performed there as well as a validation of the results of B projects. The existence of such a distinct category involving experimentation does not imply that all experimental efforts in the center were concentrated here and no other experiments were performed. In fact other experimental efforts both within MSSC and SSC took place separately from D and where specifically targeted for certain aspects of projects in categories A and C. However, although the bulk of MSSC activities are computational in nature, the existence of a separate category for

Table 2.2: Senior personnel involved in MSSC.

University of Illinois

Aerospace Engineering

Bodony — Acoustic response prediction
Geubelle — Multiscale analysis, FEA
Lambros — Experiments, optical methods

Civil Engineering

Duarte — GFEA, structural analysis, multiscale analysis
Paulino — Topology optimization, fracture
Song — Risk, reliability, stochastic events, FEA

Computational Science and Engineering

Brandyberry — Uncertainty quantification and risk analysis

Mechanical Engineering

Huang — Multiscale fracture mechanics
Sहितoglu — Thermomechanical response, experiments
Tortorelli — Sensitivity, optimization

University of Texas, San Antonio

Millwater — System reliability

University of Cincinnati

Qian — Multiscale methods

Wright State University

Huang, Penmetsa — Risk, failure probability assessment

AFIT

Palazotto — Fracture and failure

Experimental Assessment is done in recognition of the fact that as knowledge evolves in this area, new techniques will be needed both in terms of diagnostics and in terms of analysis.

Since the numbering scheme described above was maintained throughout the life of the center, this section will present short summaries of each of the projects undertaken in these areas. Thus a reader previously unfamiliar with the center can obtain a quick overview of the center's activities over its entire 7 year history. Each project has start and completion years quoted as well as the names of personnel associated with it. Table 2.2 shows a listing of all senior personnel that have taken part in the MSSC through its lifetime, their primary area of interest/expertise and their affiliation at the time of involvement in MSSC.

A. Response Prediction: Coupled Aero-Thermo-Mechanical-Acoustic Analysis and Simulation

A1 Design of STATS using Topology Optimization

Personnel: Paulino, Stump (Graduate student, UIUC), Byrd, Haney (AFRL)

Start: 2006; End: 2008

Summary: The acronym STATS refers to Spatially Tailored AeroThermal Structures in the recognition of the fact that future structures will not consist of separate components (such as sub-structure and TPS), but will rather form a unified but functionally tailored structure. Consequently, some way of optimizing the topology of both the materials used in STATS and their spatial placement is necessary. Here, continuum (as opposed to traditional) topology optimization was used as a rational means of obtaining innovative structural designs, which can improve performance and lower costs. This project dealt with a multiscale 2D and 3D continuum topology optimization that accounts for material gradient effects. By multiscale we mean that the framework separated both the material and component scales. For example, if we consider a functionally graded STATS material, this system would optimize not only topological arrangement at the component scale, but also material property distribution within a candidate arrangement.

A2 Generalized FEM Analysis for Transient Simulations

Personnel: Duarte, O'Hara (Graduate student, UIUC), Eason (AFRL)

Start: 2006; End: 2010

Summary: Often in coupled aero-thermo-acoustic problems it is possible for small variations in localized response (e.g., the localized heating at the location of shock impingement in a hypersonic inlet) to affect global structural response and eventually dictate failure at the structural level. It is therefore desirable to obtain very accurate and robust solutions both at the global and local scales for such problems. However traditional schemes (such as finite elements) would necessitate extremely large problems of very fine meshing to achieve this goal. In order to provide an efficient and robust solution method, especially in a transient setting, a new approach was used here. This approach blends the global-local FEM with the Generalized FEM, to form the so-called Generalized FEM with Global-Local Enrichments (GFEM^{gl}). With this strategy, small local domains containing regions of interest, *i.e.*, localized spikes in the temperature field, are used to solve boundary value problems (BVPs) in order to capture the behavior at the local level. The solutions from these BVPs are used to enrich the global FE mesh, in effect creating FE shape functions capable of representing well the physics of the problem. In essence, these shape functions capture the physics of the localized spikes at very small length scales, and transfer this information to the global mesh at very large length scales. This approach is very attractive in that it enables the capturing of very localized effects with relatively coarse meshes.

A3 Integrated Fluid/Structure Interaction Simulation

Personnel: Geubelle, Bodony, Joumaa (Graduate student, UIUC) Sucheendran (Graduate student, UIUC), Kuester (Undergraduate student, UIUC), Halvorson (Undergraduate student, UIUC), Hollkamp (AFRL), Gordon (AFRL)

Start 2006; End: 2010

Summary: This project was dedicated to the development, implementation and verification of a boundary element solver able to simulate a wide range of 2D and 3D acoustic problems involving static and moving boundaries. This particular numerical method was adopted for its ability to capture very efficiently the response of an infinite linear acoustic medium, as the infinite nature of the domain is naturally included in the Green's function that defines the boundary integral formulation. With the acoustic solver fully verified and its stability and accuracy characteristics assessed, it was coupled with the linear and nonlinear structural finite element solver also developed and verified over the past few years. The coupled structural/acoustic solver relied on matching spatial and temporal discretizations. Recent advances in the modeling of multiphysics problems were also introduced, allowing for non-matching spatial and temporal discretizations between the acoustic and structural domains. The ultimate goal is to use the coupled solver to investigate the dynamics of thin-walled structures in the presence of high acoustic loads.

- A4 Analytical Prediction of Dynamic Response of Functionally Graded Material (FGM)**
Personnel: Palazotto, Larson (AFIT student)
Start 2007; End: 2008

Summary: AFIT Professor Anthony Palazotto completed Project A4, “Analytical Prediction of Dynamic Response of FGM”. Thermal deformation of cylindrical composite shells was investigated in A4, in which a thermal distribution represents a varying heat environment over an aircraft surface. This project compared FGM to conventional metals for aircraft applications.

- A5 Multiphysics, Coupled Analysis of Extreme-Environment Structures**
Personnel: Bodony, Geubelle, Ostoich (Graduate student UIUC), Spottswood (AFRL)
Start: 2008, End: 2013

Summary: This project developed and utilized a set of computational tools suitable for predicting the interaction of high speed boundary layers with mechanically- and thermally-compliant panels. Motivated by the need to understand better the fluid-structure interaction of large acreage panels proposed for use in sustained-flight, reusable hypersonic vehicles, the project targeted the required level of numerical fidelity, algorithms, and computational parallel performance to yield so-called “truth model” simulations that could be used to evaluate reduced order models and quantify the level of coupling between the fluid and the solid. The project ultimately targeted a Mach 2.25 turbulent boundary layer, characteristic of that found in the inlet duct of an air-breathing hypersonic vehicle, flowing adjacent to a thin metallic alloy panel. A simple geometry was used---a nominally flat panel fully clamped to two rigid sections---to permit focused investigation on the physics. The simulations utilized a direct numerical simulation approach in the fluid and a fully nonlinear, finite strain model for the solid and showed that significant fluid-structural coupling was present that could not be modeled effectively in a one-way approach. Two panel thicknesses were considered: one that would flutter and a thicker one that would not. For the fluttering case, the panel vibrations modified the fluid to affect the turbulence production and surface pressure loading at low frequencies, while the fluid imposed large-amplitude standing waves on the panel with a definite timescale. For the thicker panel, the turbulent boundary layer loads excited several panel modes, including higher modes relative to the fluttering panel. Initial calculations showed that one-way vs. two-way coupled simulations yielded different response histories of the panel but with similar response amplitudes. However, larger calculations are needed to establish the reliability of one-way coupling for predicting panel response.

A6 Non-Intrusive Implementation of Multiscale Capabilities in a General Purpose FEA Platform

Personnel: Duarte, Pereira (Graduate student, UIUC), Plews (Graduate student, UIUC), Eason (AFRL)

Start: 2008, End: 2010

Summary: This project was funded by a separate project through UTC (Contract Number: F33601-03-F-0060, Task Order Number: USAF-0060-50-SC-0001). However for completeness a brief summary is included here. Additional details can be found in the final report compiled specifically for this project. This project provided a feasibility study of adding predictive multiscale capabilities to existing Finite Element Analysis (FEA) platforms in a non-intrusive manner. The approach is based on the Generalized Finite Element Method (GFEM) enriched with global-local functions (GFEM^{gl}). Detailed mathematical formulation of the proposed methodology is in the report submitted to General Dynamics Information Technology. Two representative cases of relevance to the US Air Force were considered in this study. The first dealt with static problems while the second addressed the case of transient simulations. The formulations involve exchange of (pseudo) loads and solutions between GFEM and FEA codes. Thus, it is applicable to most available FEA platforms. There is one important additional benefit of using the algorithm for time-dependent problems. The global problem does not have to be solved from scratch at each time integration step since the large global scale matrix does not change with time. This is in contrast with the adaptive FEM. Adaptivity must be used in order to resolve fine scale features of the solution. This, however, requires the reconstruction and factorization of global matrices after each adaptivity step. Since the location of fine scale features is time dependent, mesh adaptivity is usually required after each time step. This study demonstrated the feasibility of a non-intrusive implementation of multiscale capabilities in a general-purpose FEM platform using the GFEM. The formulations are also attractive from the computational point of view especially when applied to time-dependent multiscale problems.

A7 Multiscale Thermo/Strain Field Coupling

Personnel: Duarte, Plews (Graduate student, UIUC), Eason (AFRL)

Start: 2009; End: 2010

Summary: As discussed earlier, the availability of computationally efficient techniques to solve multiphysics, multiscale thermal strain problems is of great importance in the structural design and response prediction of hypersonic flight vehicles. Generalized finite element methods (GFEMs) provide an especially useful means for simulations of this nature, enabling the generation of specialized enrichment functions tailored to the problem at hand. In this case, multiscale effects can be characterized by special global-scale enrichments derived from small-scale boundary value problems, leading to the so-called GFEM with global-local enrichments (GFEM^{gl}) – see project A2. Building upon a framework for temperature gradients resulting from transient, sharp thermal loads, here steps were taken to develop a GFEM platform to resolve localized thermomechanical stresses and strains while maintaining a coarse, structural-scale mesh. The primary focus

of Project A7 has been the development of an interface between the GFEM^{gl} for thermal analysis implemented in the scope of Project A2 with a well-known, commercial finite element analysis software package, ABAQUS, without any intrusive code modifications, in order to facilitate the transitioning of this technology to the Air Force. In the nonintrusive interface developed here, only loads (or right-hand-sides) and solutions are exchanged between ABAQUS and a separate GFEM analysis code, while still enabling the use of the full feature set of the standard GFEM^{gl}.

B. Life Prediction: Identification and Definition of Structural Limit States

B1(x) Failure Analysis of Functionally Graded Aircraft Components in Combined Environments

Personnel: Huang, Xiao (Graduate student, UIUC), Tuegel (AFRL)
Start: 2006; End: 2007

Summary: The aim of this project was to develop a scalable cohesive failure model for functionally graded materials and structures based on the experimentally identified mechanisms. Such a model could be used to predict the crack nucleation, initiation and progressive growth in various material systems. Cohesive law for fiber/matrix interfaces in composites that are characterized by the van der Waals force were established. The tensile cohesive strength and cohesive energy were given in terms of the densities of reinforcements and matrix, as well as the parameters in the van der Waals force. Simple, analytical expressions of the cohesive law were obtained, which are useful to study the effect of interfaces on the macroscopic behavior of the composites. The effect of matrix surface roughness on the cohesive law is also studied. The project was terminated after less than one year because of the departure of the PI from the University of Illinois.

B1 Mechanism-Based Cohesive Failure Model for Functionally Graded Aircraft Components and Structures

Personnel: Paulino, Park (Postdoc UIUC), Gain (Graduate student, UIUC), Tuegel (AFRL)
Start: 2008; End: 2010

Summary: This project continued the main theme of project B1(x), but employing a different team of researchers and a different approach. The goal of the project was to develop a macroscale cohesive failure model capable of modeling fatigue crack growth in brittle and ductile materials at high temperatures. In addition, the project aimed at developing a robust methodology of extracting such a law from comparison to appropriate experimental results. The Park-Paulino-Roesler (PPR) potential was employed for the cohesive model and was modified for inclusion in fatigue problems. A direct and an inverse problem approach was also used to extract cohesive zone models from full-field experimental data. The methodology was illustrated in successfully predicting the cohesive law governing quasi-static monotonic loading fracture of a brittle polymeric material. Future plans involved the inclusion of thermal effects and material ductility, but these were not realized as the project was terminated in 2010.

B2 Imperfections and Defect Tolerance of Aircraft Shells and Structures

Personnel: Tortorelli, Watts (Graduate student, UIUC), Eason (AFRL)
Start 2009; End: 2011

Summary: The goal of this project was to develop a methodology to optimize functionally graded materials (FGMs) for applications in Spatially Tailored Aero-thermal Structures (STATs). The approach was to quantitatively characterize the microstructure of two-phase FGMs, *e.g.*, a metal-ceramic FGM, with the goal of developing a mapping of the microstructure's phase morphology to the composite's material properties. In conjunction with other projects, this will enable the ability to predict the properties of novel FGM materials, as well as to optimize FGMs in design applications.

B3 3D Cyclic Plasticity Model for Thermomechanical Loading in Large-scale Analyses

Personnel: Dodds, Sobotka (Postdoc, UIUC), Gockel (AFRL)
Start: 2010, End: 2012

Summary: A prerequisite for the successful understanding of coupled thermoacoustic fatigue and the development of predictive fatigue models is the establishment of robust plasticity models that are capable of accurately handling *cyclic plasticity* under simultaneous thermal and mechanical loads. Existing plasticity models such as the Fredrick-Armstrong (2007) model or the Johnson-Cook (1983) model are generally phenomenological and provide accurate results only for a small subset of thermomechanical loading conditions. The present effort has two goals: (i) the development of a new plasticity model capable of modeling complex thermal and mechanical cyclic in metals, and (ii) the implementation of this model into a structural level solver that will predict macroscale stress/strain states in structural panel-like objects subjected to thermoacoustic loading. The structural solver should be integrated with both a thermal transport and a fluid-solid interaction framework so that the loading experienced by these panel-like structures is representative of hypersonic flight mission conditions. The structural solver will also be coupled with a finer length scale model that will be able to predict fatigue life (project B4) given a set of macroscopic stresses and strains evaluated by the plastic model developed here. The new model is called the Generalized Plasticity (GP) Model and in this work has been modified to include thermal loading capability. The GP theory retains important features of conventional plasticity models: stability and normality principles, elastic and plastic ranges, and unique solutions, while at the same time satisfying thermodynamic considerations of the Clausius-Duhem inequality.

B4 Towards a Fatigue Initiation Theory for Multiaxial Thermomechanical Fatigue

Personnel: Sehitoglu, Oral (Postdoc, UIUC), Penmetsa (AFRL)

Start: 2011, End: 2012

Summary: The goal of this project was to formulate a novel criterion for fatigue damage initiation that would be capable of handling multiaxial loading conditions at elevated temperatures, though initially only isothermal. Certain such models had been proposed in the past, but were limited to room temperature conditions. This project studied two length scales: the continuum, macroscale, where the material was modeled as a homogeneous plastically deforming material, and the microscale, where grain structure came into play. For the macroscale model, existing multiaxial fatigue damage prediction models based on the Findley parameter were modified for use at high temperatures, while the material was modeled with the Generalized Plasticity material model that was developed by project B3. For the microscale model, a fatigue damage initiation criterion based on critical energy of persistent slip band pile ups at grain boundaries was investigated. Both models were applied to the material of interest in the MSSC, the nickel superalloy Hastelloy X, with very good results. Although this effort did not directly link the microscale with the macroscale models, it did explore avenues of how this would be possible in the future.

C. Life Prediction: Framework and Methodologies for Risk-quantified Structural Assessment

C1 Uncertainty/Risk Quantification Methods for STATS

Personnel: Song, Lee (Graduate student, UIUC), Tuegel (AFRL)

Start: 2006; End: 2010

Summary: The goal of this project was to develop novel stochastic methods that quantify the uncertainty and risk of spatially tailored aero-thermal structures (STATS) using advanced computational simulations. The primary focus was on methods that identify important input uncertainties, which enable us to set the priority of limited resources on the dominant uncertainties during condition based maintenance as well as risk informed design of aircraft structures.

C2 Validation of Simulations Having Uncertainties in Both Simulation and Experiments

Personnel: Brandyberry, Tudor (Undergraduate student UIUC), Gruenwald (Graduate student UIUC), Haney (AFRL)

Start 2006; End: 2009

Summary: This project involves uncertainty quantification and validation of computer simulations of thin, curved beams under random vibration loads, including nonlinear effects. These beams serve as simple surrogates for thin aircraft panel skins under vibration loads. A validation process was sought for the simulations that incorporates both the system uncertainties in the simulations, as well as experimental uncertainties in the measured data.

C3 Risk-Based Design Plots for Aircraft Damage Tolerant Design

Personnel: Penmetsa
Start: 2007; End: 2008

C4 System Reliability with Correlated Failure Mode

Personnel: Millwater, Smith (Graduate student, Texas San Antonio), Domyancic (Graduate student, Texas San Antonio), Sparkman, Wieland, Tuegel (AFRL)
Start: 2008; End: 2011

C5 Probabilistic Cohesive Zone Model for Fiber Bridging

Personnel: Penmetsa, Kable, Shanmugam, Tuegel (AFRL)
Start: 2008; End: 2010

Summary: The main focus of this research was to validate the probabilistic cohesive zone model calibration process using known material test data. Probabilistic cohesive zone models were developed using experimental results from an unknown aluminum material. AFRL collaborators performed testing of a unidirectional composite material (IM7/977-3) using double cantilever beam (DCB) specimens with and without Z-pins. Z-pins are inserted in Z-direction of the laminate to increase the strength of the composite. In both a cases probabilistic cohesive zone models were extracted that account for variability using a probability density function.

C6 Enriched Space-time Finite Element Method

Personnel: Qian, Yang, Chirptukar, Alpert, Eason (AFRL), Spottswood (AFRL)
Start: 2010; End: 2011

D. Experimental Discovery and Limit State Characterization

D1 Experimental Investigation of Thermomechanical Fatigue Failure Modes

Personnel: Sehitoglu, Efstathiou (Graduate student, UIUC), Hauber (AFRL)
Start: 2006; End: 2009

Summary: This project was tasked with the thermomechanical study of fatigue response of functionally graded materials (FGMs) and metals. A multiscale experimental approach using the optical technique of digital image correlation (DIC) was used. Extensive experimentation on commercially purchased FGMs proved that they had significant drawbacks when used at high temperatures. Shifting our focus to metallic materials, a study of how microstructural inhomogeneities affect fatigue damage accumulation in Ti was initiated. Here we characterized the spatial distribution of residual deformation at the mesoscale (a few grains) and at the macroscale (hundreds of grains) in titanium subjected to cyclic tensile loading. The two results were related to each other through the concept of a plastic Representative Volume Element (RVE) of material. RVE sizes in plastically deforming metals were for the first time extracted experimentally.

D2 Development of Experimental Techniques for Validating a Coupled Thermomechanical Fatigue Simulation Framework

Personnel: Lambros, Carroll (Graduate student, UIUC), Chona (AFRL)

Start: 2006; End: 2010

Summary: The objective of this project was to develop experimental techniques for extreme environments such as thermomechanical fatigue. As a sample material system, metallic materials were used in this work to develop the relevant experimental methods. The materials consisted either of Ti or Ni based alloys, both commonly used in the aerospace industry currently. Initial stages of this effort involved developing macroscale techniques for high temperature fracture experimentation. Subsequently the effort concentrated on fatigue crack growth, but at room temperature. Since fatigue damage initiates and accumulates at the grain level, our experimentation focused on microscale techniques with sub-grain level resolution. Building on the work of D1, we developed an ultra-high resolution *ex situ* DIC measurement methodology. This coupled, with high magnification *in situ* fatigue measurements, produced an unprecedented amount of experimental data at both the macroscale and the microscale during fatigue crack growth in Ti and Ni based alloys.

D3 Thermomechanical Fatigue of Hastelloy X: Role of Combined Loading on Material Response

Personnel: Sehitoglu, Abuzaid (Graduate student, UIUC), Penmetsa (AFRL)

Start: 2008; End: 2012

Summary: This project, as a continuation of project D1, was primarily concerned with an experimental assessment of cyclic plasticity and fatigue of the nickel super-alloy Hastelloy X. With close ties to projects D1 and D2, this effort used the optical technique of Digital Image Correlation to study the development of plastic strain during cyclic loading and fatigue loading. Using ultra-high resolution DIC, the observed evolution of plastic deformation elucidated the role of grain and twin boundaries in slip accumulation at the microscale. This plastic strain was *quantified* over the entire microstructure, and related to the grain orientation and type of grain boundaries. When extending these measurements to fatigue, it was observed that strain concentration sites that developed early on would always transition into fatigue damage at the (much) later stage. After understanding the role of boundaries in either transmitting or blocking plastic deformation, these results were combined with the fatigue damage prediction models developed in project B4 to predict the observed scatter in fatigue life of Hastelloy X.

D4 Thermomechanical Fatigue of Hastelloy X: Role of Defects

Personnel: Lambros, Casperson (graduate student, UIUC), Chona (AFRL)

Start: 2010; End: 2012

Summary: This project formed a continuation of project D2 and built upon the results of that work. The first part of project D2 had studied crack face closure during fatigue at room temperature. Project D4 concentrated on extending those results to high temperature situations. Using induction heating, the same material that was used in D2

and D3 (Hastelloy X) was subjected to thermomechanical fatigue crack growth at temperatures up to 650°C. Closure at those temperatures was measured and was found to be similar to that at room temperature for isothermal conditions. However, an interesting phenomenon was observed in relation to *thermal overloads or thermal jumps*. Depending on the amount of overload, crack closure was reduced, and was even eliminated in some cases, directly after the overload. This phenomenon was investigated and was found to be the counterpart of mechanical overloads which, as is known, significantly affect fatigue crack growth.

3. MSSC Timeline — 2006-2013

The MSSC began in October 2006 under the technical direction of Prof. Daniel Tortorelli of the Mechanical Science and Engineering Department at UIUC, with the participation of 9 faculty and 9 graduate students from UIUC and a number of personnel from AFRL. An early emphasis of the center was placed on graduate student training, and therefore a conscious decision was made for each project to couple one faculty member with one graduate student and at least one collaborator from AFRL. Initial project planning of center activities stressed the need for moving away from current design practices that employ a sub-structure with a distinct thermal protection system (TPS), the latter of which is essentially parasitic. Rather, the intent was to concentrate on the concept of a “hot structure”, *i.e.* one in which an integrated, perhaps multifunctional, structure will serve both as the load carrying structure and as the thermal protection element. Initial discussions among the combined MSSC/SSC team centered around the general needs of the Air Force along these directions, and based on these discussions individual MSSC faculty proposed a series of projects to be performed. The project proposals, including plans for student recruitment, were evaluated by the MSSC steering committee which generally consisted of 3 members from AFRL and 3 members from UIUC, including the technical director (initially Prof. Tortorelli) and the executive director (William Dick) of the center. The initial project selection was based on three general themes: Structural Response Modeling, Failure Modeling, and Experimental Discovery and Validation. A little while later, a fourth theme was added, that of Uncertainty Quantification and Risk Assessment, to eventually make the four groupings, A, B, C, and D presented earlier.

The earliest incarnation of the MSSC had efforts approximately evenly balanced between the Structural Response Modeling, Failure Modeling, and Experimental Validation areas, with perhaps a little more effort in A, the Structural Response area. The Experimental Discovery and Validation, drove the need for “standardizing” on a particular material. Although the analytical/computational aspects of the center could be done with an understanding that in the timeframe of the center’s activities novel material would have been developed, the experimental efforts necessitated procuring actual material systems that could be used for experimental validation. Therefore the initial efforts of the center revolved around the class of materials known as Functionally Graded Materials (FGMs). These are metal-ceramic composites that have been developed over the past several decades primarily for wear, thermal, and impact protection applications. Several simulation and modeling projects were started investigating the response of metal-ceramic FGMs and their promise as future thermally protected materials. FGMs are highly inhomogeneous metal-ceramic mixtures, essentially composites, which exhibit a (near) continuous variation of constituent concentration, thus eliminating the stress concentration that exists when bonding disparate materials, such as a TPS onto a sub-structure. Both simulation and experimental projects were designed initially around the concept of FGMs (*e.g.*, A1, B1 B1x, D1, D2). The MSSC, through supplemental AFRL funding, was able to procure a number of different FGMs from various sources (Ti/TiB from BAE Systems and Ti-6Al-4V/ZrO₂ from SPS Syntex, a subsidiary of Sumitomo Inc., Japan). Unfortunately, although mostly adequate at room temperature, both these materials had significant problems when used even at moderately high temperatures (a few hundred degrees over ambient) either because of residual stress issues, or because of degradation and crumbling when heated. This fact inhibited the progress of the experimental validation efforts of the center. At the same time, because of the departure from the

center of a number of personnel that were working on the numerical study of FGMs, a decision was made to move away from the FGM concept and allow studies on more general materials.

At about the same timeframe, the technical direction of the center moved to Prof. Glaucio Paulino of the Civil and Environmental Engineering Department. The continued efforts of the center were then refocused to include a more general category of structures called Spatially Tailored AeroThermal Structures (STATS). The idea behind STATS was somewhat broader than an FGM in that it was envisioned that material tailorability in the future would be such as to allow the formation of highly inhomogeneous material systems of very disparate phases so that the integral results could perform a multitude of tasks simultaneously. A similar set of problems to those encountered with the FGMs, particularly lack of actual material, were also encountered during the study of STATS. At this time in the progression of the center a significant, and at the time novel, emphasis was placed on the issue of Uncertainty Quantification (UQ), and correspondingly a large number of the group C projects were initiated. Since at that time there was only limited faculty expertise on the topic of UQ at UIUC (Prof. Song of the Civil and Environmental Engineering Department had just been hired in this area), a number of other collaborations were initiated to deal with uncertainty quantification at various levels from the material level involving individual cracks (*e.g.*, project C5) to the entire aircraft structure (*e.g.*, projects C1, C2, C4). Internal collaborations were formed with research scientists from the Computational Science and Engineering Program at UIUC, and external collaborations with Wright State University and the University of Texas San Antonio.

Through various discussions within and outside the MSSC steering committee, and motivated by the renewal at the time of the Aerosciences Collaborative Center, a decision was taken to investigate in more detail the fluid-structure interaction aspects of how loads would be generated during hypersonic flight, and how exactly aeroacoustic loading would transition onto the aircraft structure. In the process, this also led to a desire for a much better understanding of the AFRL Sub-Element (SEF) facility. As a result, although one such effort was present from the beginning of the center (A3), a new project (A5) and a new faculty researcher, Prof. Bodony from Aerospace Engineering, were added to the center's efforts, considerably strengthening that aspect of the work.

The confluence of the realization that STATS had similar issues to the FGM problems, along with an increasing focus on integrating the center's efforts with the Air Force future concept of a Digital Twin, precipitated a third directional evolution of the research efforts of the center. In parallel, since a lot of our efforts had matured over the first few years and both their outcomes and their impact had become more clear, a set of further goals for the center were developed during an "extended steering committee" meeting that took place on March 29, 2010 at UIUC. At that meeting an in-depth discussion took place to lay out the remaining 2.5 years of the center and how to integrate those efforts into the Digital Twin concept. The aim of the Digital Twin is that each aircraft (which in the future will number far fewer than the hundreds of units manufactured now) will be accompanied by a "personalized" digital model which includes its current (potentially damaged) state that will be evolved in parallel to the real aircraft as missions accumulate. Therefore at any given time in the life of the aircraft the Digital Twin will be a faithful "reproduction" of the actual unit. Thus, with appropriate predictive models the Digital Twin can be used for forecasting future aircraft states and therefore can possibly be applied as a decision making tool for mission acceptability. Based upon this concept, which involves a continuous feedback between external agents (aerodynamics loads), evolving state (damage drivers) and future predictivity (reliable predictive models) as shown in Fig. 1.1, it was decided to

focus the center's efforts, rather than the four earlier topics, onto two key aspects, namely: (i) Structural Response Prediction, and (ii) Life Forecasting, bringing the center more inline with the feedback loop shown in the center of Fig. 1.1. So as to avoid confusion, it was decided, however, to keep the existing project numbering and slowly phase out projects that would end but did not lay on the critical path for the focus of the center any longer. Therefore at this stage only a certain number of the A and B projects were maintained, and these were in fact grouped together into the two categories by combining the experimental efforts, which dealt primarily with fatigue initiation and growth, with the modeling efforts of the Limit State estimation (projects B) into a unified entity. Thus more significant and direct connections between experiments and modeling would be made during the remaining part of the center. In addition, there was also a realization that it would be difficult to directly transition a lot of the sophisticated numerical framework developed in MSSC to industrial applications. Therefore additional efforts in projects A were made for facilitating technology transfer to applications. Finally, also at about the same timeframe the technical direction of the center passed from Prof. Paulino to Prof. John Lambros of the Aerospace Engineering department.

During the March 29, 2010 meeting, where the decision to focus onto the two aspects of Structural Response Prediction and Life Forecasting was made, it was also realized that the center already had several active projects in the area of Structural Response Prediction, but had very few efforts on the Life Forecasting side. Therefore it was decided to (a) divert significant center resources to the Life Forecasting efforts (namely two new postdoctoral research fellows), (b) add senior personnel as needed (at this stage Prof. Dodds joined the MSSC effort), and (c) provide a fairly detailed research plan that would closely combine the new elements of fatigue life prediction (projects B3 and B4) with the existing experimental efforts of fatigue crack growth (projects D). The discussion concluded that two aspects would be necessary in order to predictively model fatigue failure: an understanding of cyclic plasticity through appropriate bulk plastic thermomechanical constitutive laws, and a thermally-dependent multiaxial failure prediction model. These two aspects would initially be investigated separately, but down the line could be combined into one unified model, which eventually would also be combined with the structural response prediction models. To start out with, however, structural prediction would merely provide an external loading dataset to the forecasting algorithms.

At this meeting it was also decided to "standardize" Center activities around a common material that would be available for experimental evaluation. Following the material procurement problems of the FGM and STATS initial efforts, the MSSC experimental projects, which were already ongoing from the inception of the Center, continued their work with metallic materials that were commercially available. Initially these materials consisted of Al alloys, Ti and Ti-based alloys. However, the temperature attainable by such materials was limited to a few hundred °C. Consequently, at the suggestion of personnel from AFRL, the experimental efforts of the center then focused on Ni-based superalloys. Such materials are commonly available and have been studied extensively in the past. They are also widely used in high temperature aerospace applications, albeit primarily related to aircraft engines rather than primary structural components because of their increased density over material such as Ti and Al. However, early conceptual studies of hypersonic aircraft had considered Ni-based superalloys as possible components for leading edges and other areas of intense heating (Zuchowski, 2010). Based on this, early in the life of the Center, the experimental projects started working with Hastelloy X, a Ni-based superalloy from Haynes Co. Since the experimental projects had shown considerable success using this material, which was able to maintain relatively large stiffness and strength for

temperatures up to 1,000°C, at the March 29, 2010 meeting it was decided that the life prediction efforts, and the extent possible the structural response efforts, would all concentrate on analyzing the Hastelloy X material.

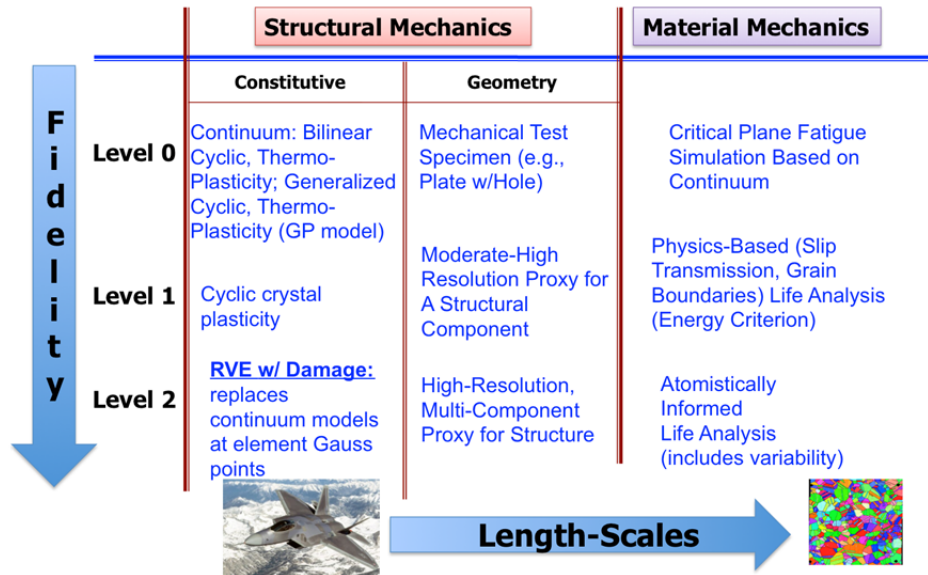
Since the remaining time of MSSC was then about 3 years, and realistically any new personnel would have some time lag in starting, only about 2.5 years worth of research effort was deemed possible. Therefore the discussion was focused on breaking down the life prediction efforts into tasks that would be feasible during the 2.5 years remaining in MSSC, and additional tasks that would be undertaken in any future efforts. The task breakdown was defined in “Levels” which were of increasing difficulty in implementation, and are summarized in Tables 3.1 and 3.2. The first level, which was labeled “Level 0” and encompassed what was deemed feasible for the remaining time of the MSSC, concentrated on developing a novel plasticity model that could accurately account for repeated cyclic plasticity but under variable temperature as well. That was realized by project B3. The second element was the development of a multiaxial temperature dependent failure model, and was realized by project B4. The efforts of these two projects were coupled together on a tested benchmark application – the analysis of a ramp panel from the NASP concept design. This example, which is described in detail in the discussion of B3, brings together the efforts of thermomechanical plastic modeling, fatigue damage prediction and external aerothermal loading, the latter supplied by Dr. Adam Culler who had developed a coupled simulation framework for predicting such loading, but did not include as sophisticated a material model. At present these three schemes are integrated serially, *i.e.*, the output from one serves as the input to the next. However, as mentioned above, in the future they could be integrated into one unified framework.

The subsequent levels were planned out for later years, although some inroads were started on Level 1 in the present effort. Specifically, some aspects of the life prediction efforts of project B4 started developing a microstructurally based model with higher fidelity than the continuum model, and with more features, such as the ability to predict fatigue life variability results at the macroscale from deterministic simulations at the meso/microscale.

Table 3.1: Table for research progression of coupled thermomechanical fatigue life prediction models.

Level	Time	Scientific Effort	Outcome
0	11/2012	<ul style="list-style-type: none"> Thermal cyclic plasticity continuum model for Hastelloy X 3D solid model in WARP3D for transient nonlinear dynamic response of aeroacoustic loads Multiaxial TMF life prediction model 	<ul style="list-style-type: none"> B3: GPS continuum model; Ramp panel study; Hastelloy X application B4: Critical plane model with Findley parameter and thermal effects
1	3-5 yrs	<ul style="list-style-type: none"> Cyclic crystal plasticity model with temperature effects Two way coupling on thermomechanical effects Failure model that allows for failure evolution More sophisticated life prediction model: crack initiation/nucleation of slip at a boundary, impingement at boundary, micro-structure as a parameter (e.g. add texture). 	<ul style="list-style-type: none"> B4 and D3: Grain boundary based fatigue crack initiation model for Hastelloy X BN: Crystal plasticity in WARP3D
2	5-8 yrs	<ul style="list-style-type: none"> Multi-scale single physics integrated model for plasticity and fatigue; Single Physics (i.e., no fluids, chemistry) but multi-scale 	
3	8+ yrs	<ul style="list-style-type: none"> Coupled everything – multi-physics multi-scale 	

Table 3.2: Interrelation among fidelity level and length scale in planned fatigue modeling.



4. PROJECT DETAILS — 2006-2013

A1 Design of STATS using Topology Optimization

Personnel: Paulino, Stump (Graduate student, UIUC), Byrd, Haney (AFRL)

Start: 2006; End: 2008

Topology optimization is a useful tool to properly capture non-intuitive designs of multifunctional materials. It is relevant for STATS (Spatially Tailored AeroThermal Structures) as it helps to understand the conceptual design of structures, including complex loading cases and complex physics interactions, e.g. thermo-mechanical-acoustic loadings and coupled nonlinear behavior. The present work concentrated on the development of the three-dimensional computer code considering the features proposed and identified in earlier studies. The computational platform is based on the C/C++ libraries LibMesh (finite element framework), PETSc (Portable, Extensible Toolkit for Scientific computation) and the in-house solver RMINRES (Recycling MINimum RESidual method), which utilizes the Krylov subspace recycling. The code developed in this framework is robust enough to solve large problems, and flexible enough to incorporate new features for optimal design.

The specific computational efforts focused on the design of thermal structures by topology optimization. To illustrate the features of the code, the simulation of a leading edge problem, as shown in Fig. A1.1, is performed. The solution of this problem highlights the importance of considering the correct physics. If steady-state heat transfer is considered with no convection, then a non-physical density distribution, as illustrated by Fig. A1.2, is obtained. However, if a convection-dominated solution is considered, then the solution of Fig. A1.3 is obtained, which is more physical than the previous one. In the latter solution, a special FEM was developed with lumped convection, rather than consistent convection because numerical problems may arise when the latter case is employed (e.g., nonphysical oscillations of the temperature profile). The poor modeling of convection can adversely influence the design space search of the optimization algorithm, however, a lumped convection scheme solves this problem.

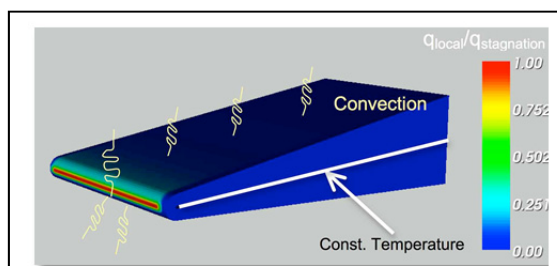


Fig. A1.1: Heat flux distribution and convection for leading edge problem.

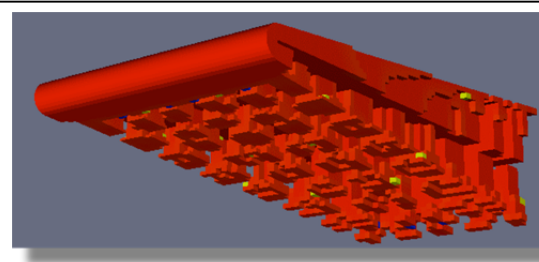


Fig. A1.2: Non-physical (incorrect) density distribution obtained if convection is not accounted for. Topology optimization solution considers penalization with $p=3$ and no continuation. FEM discretization consists of 852,768 elements and 156,240 DOFs.

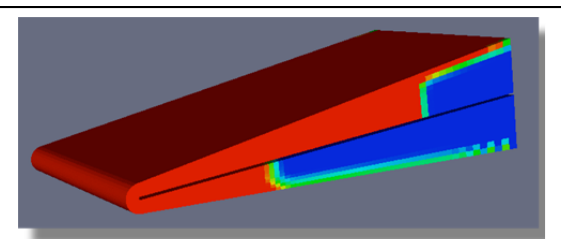


Fig. A1.3: Physical density distribution obtained when convection is accounted for.

elung of convection can adversely influence the design space search of the optimization algorithm, however, a lumped convection scheme solves this problem.

Further extension of this work consists of exploring the CAMD approach as it is important for functionally graded STATS. For realistic simulations, non-linear effects must be considered

such as radiation boundary conditions, and temperature dependent material properties. Moreover, the internal radiation problem needs to be addressed (e.g. using a parametric level set or homogenization). This project was terminated in 2006 as the graduate student involved in it moved into a different research area.

A2 Generalized FEM Analysis for Transient Simulations

Personnel: Duarte, O'Hara (Graduate student, UIUC), Eason (AFRL)

Start: 2006; End: 2010

This section presents details of the Generalized Finite Element Method (GFEM) framework developed within the scope of Project A2 for resolving intense, localized thermal gradients in the structural analysis of hypersonic air vehicles.

A.2.1 Steady-State Heat Conduction

Consider a domain $\Omega \subset \mathbb{R}^3$ with boundary $\partial\Omega$ decomposed as $\partial\Omega = \Gamma_u \cup \Gamma_f$ with $\Gamma_u \cap \Gamma_f = \emptyset$. The strong form of the governing equation is given by Poisson's equation

$$-\nabla(\kappa \nabla u) = Q(\mathbf{x}) \quad \text{in } \Omega$$

where $u(\mathbf{x})$ is the temperature field, κ is the thermal conductivity tensor and $Q(\mathbf{x})$ is the internal heat source. Boundary conditions on $\partial\Omega$ are

$$\begin{aligned} u &= \bar{u} \quad \text{on } \Gamma_u \\ -\kappa \nabla u \cdot \mathbf{n} &= \bar{f} \quad \text{on } \Gamma_f \end{aligned}$$

where \mathbf{n} is the outward unit normal vector to Γ_f and \bar{f} and \bar{u} are prescribed normal heat flux and temperature, respectively. Weak and Galerkin forms of the problem follow as usual; details can be found in O'Hara (2010) dissertation.

Model Problem

A model problem representative of thermal loads experienced by a hypersonic vehicle subjected to a Type IV interaction is defined in this section. This problem is used to assess the performance of the FEM and the GFEM when solving problems with solutions exhibiting highly localized sharp thermal gradients. The solution of the model problem is given by

$$u(x) = \exp^{-\gamma(x-x_0)^2} + \sin\left(\frac{\pi x}{L}\right) \quad (\text{A.2-1})$$

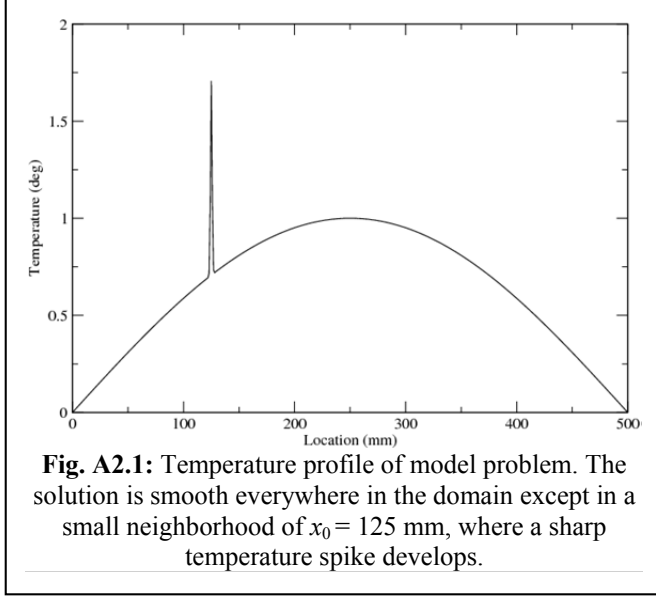
where $x_0 = 125 \text{ mm}$, $L = 500 \text{ mm}$ and γ is a parameter controlling the roughness of the solution (usually taken as 1.0). The temperature profile (A.2-1) is shown in Fig. A2.1. The temperature distribution on a plate Ω has a sharp localized spike in a small neighborhood of x_0 . This model problem was originally proposed by Merle and Dolbow (2002) and was also analyzed by O'Hara (2010). The domain is taken as $\Omega = \{\mathbf{x} \in \mathbb{R}^3 : 0 < x < 500, 0 < y < 250, 0 < z < 30\}$ where all dimensions are in mm . Homogeneous Dirichlet boundary conditions are applied on faces $x=0$ and $x=500$ and homogeneous Neumann boundary conditions are prescribed on all other faces. A heat source given by

$$Q(\mathbf{x}) = -\nabla^2 u(\mathbf{x}),$$

with $u(\mathbf{x})$ defined in (A.2-1), is prescribed in Ω . The energy norm associated with the problem is given by

$$\|u\|_E = \sqrt{B(u,u)} = \sqrt{\int_{\Omega} (\nabla u) \kappa (\nabla u) d\Omega}$$

where $B(u,u)$ is the bilinear form associated with the Laplace operator.



In the numerical experiments presented below, the accuracy of a numerical approximation u_h of u is measured using the relative error in the energy norm, i.e.,

$$e_E^r = \frac{\|u - u_h\|_E}{\|u\|_E} = \sqrt{\frac{B(u,u) - B(u_h, u_h)}{B(u,u)}}$$

With the temperature field varying only in the x direction, the exact energy of the solution can be obtained from (A.2-2), where A is the cross-section area (in 3-D) in the yz plane. MATLAB was used for the symbolic integration of (A.2-2). The reference value for the energy corresponding to (A.2-1) is

$$B(u,u) = 9474.62$$

$$B(u,u) = \left| \int_0^l -\kappa \left(\frac{du}{dx} \right)^2 dx \cdot A \right| \quad (\text{A.2-2})$$

GFEM discretizations

A shape function, ϕ_{ai} , in the GFEM is computed from the product of a linear finite element shape function, φ_{α} , and an enrichment function, L_{ai} ,

$$\phi_{ai}(\mathbf{x}) = \varphi_{\alpha}(\mathbf{x}) L_{ai}(\mathbf{x}) \quad (\text{no summation on } \alpha),$$

where α is a node in the finite element mesh. The linear finite element shape functions $\varphi_{\alpha}, \alpha = 1, \dots, N$, in a finite element mesh with N nodes constitute a partition of unity, i.e., $\sum_{\alpha=1}^N \varphi_{\alpha}(\mathbf{x}) = 1$ for all \mathbf{x} in a domain Ω covered by the finite element mesh. This is a key property used in partition of unity methods.

Analysis of the Model Problem Using GFEM

Figure A2.2 shows the *hp*-adapted FEM/GFEM mesh used in a 3D discretization of the model steady-state heat transfer problem, as well as the temperature field as computed from the discretization. Please refer to O'Hara's (2010) dissertation for many more details on convergence of the methodology applied to the model problem.

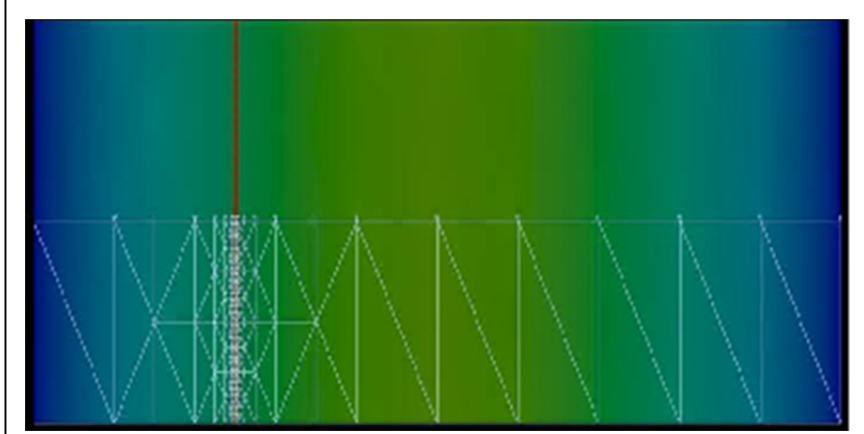


Fig. A2.2: Example of a highly graded mesh and the associated well-resolved spike in the temperature field.

GFEM with global—local enrichment functions (GFEM^{gl})

The GFEM with global-local enrichment functions (GFEM^{gl}) allows for on-the-fly, numerical creation of

custom enrichments via the solution of smaller, *hp*-adapted local problems which enclose features of interest in the structural-scale (global) domain. The basic GFEM^{gl} solution procedure is comprised of a coarse-scale initial solution, extraction and solution of local problems, and enrichment and reanalysis of the global problem.

Initial Global (IG) Problem: An initial coarse-scale analysis is first performed on the global problem on $\bar{\Omega}_G = \Omega_G \cup \partial\Omega_G$, yielding initial solution u^0 . The initial global problem is formulated as, for all $v^0 \in X_G(\Omega_G)$, find $u^0 \in X_G(\Omega_G)$ such that

$$\begin{aligned} & \int_{\Omega_G} \nabla u^0 \kappa \nabla v^0 d\Omega + \eta \int_{\Gamma_G^u} u^0 v^0 d\Gamma + \int_{\Gamma_G^c} \alpha u^0 v^0 d\Gamma \\ &= \int_{\Omega_G} q v^0 d\Omega + \int_{\Gamma_G^f} \bar{f} v^0 d\Gamma + \eta \int_{\Gamma_G^u} \bar{u} v^0 d\Gamma + \int_{\Gamma_G^c} \alpha u_\infty v^0 d\Gamma, \end{aligned} \quad (\text{A.2-3})$$

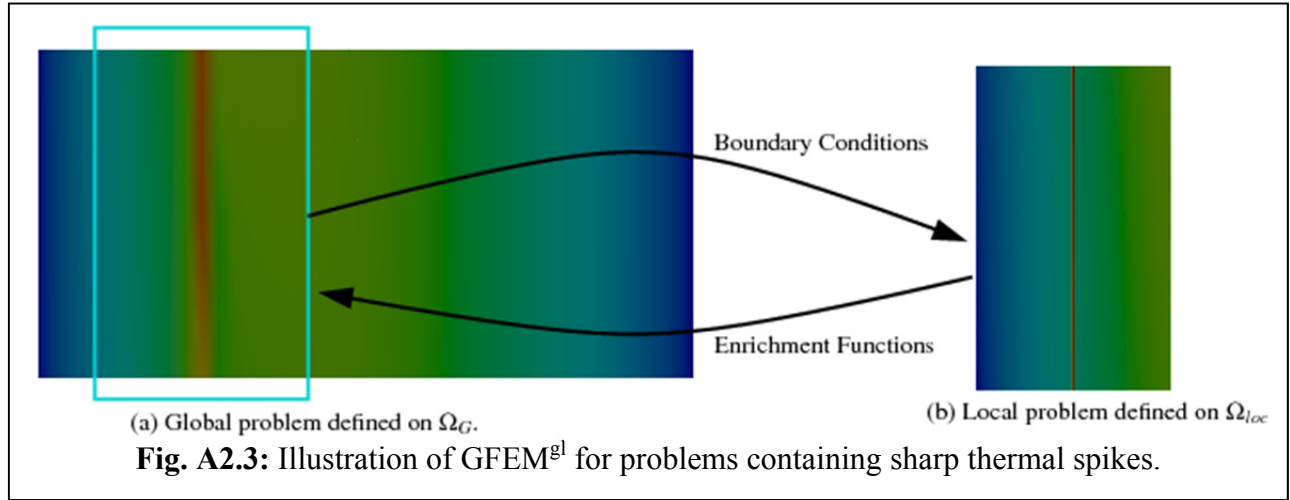
where η is a predetermined penalty parameter for enforcement of Dirichlet boundary conditions, and $X_G(\Omega_G)$ is a GFEM discretization of $H^1(\Omega_G)$.

Local Problem(s): The initial global solution resulting from the linear system of equations implied by (A.2-3) is then used directly as a Dirichlet boundary condition in a local problem. The local domain is comprised of $\bar{\Omega}_L = \Omega_L \cup \partial\Omega_L$, a subdomain of Ω_G , which in practice is taken to be a user-specified, small subset of *hp*-adapted finite elements copied from the global problem. The local problem is formulated as follows:

For all $v_L \in X_L(\Omega_L)$, find $u_L \in X_L(\Omega_L)$ such that

$$\begin{aligned} & \int_{\Omega_L} \nabla u_L \kappa \nabla v_L d\Omega + \eta \int_{\partial\Omega_L \setminus (\partial\Omega_L \cap \Gamma_G^f)} u_L v_L d\Gamma + \int_{\partial\Omega_L \cap \Gamma_G^c} \alpha u_L v_L d\Gamma \\ &= \eta \int_{\partial\Omega_L \setminus (\partial\Omega_L \cap \partial\Omega_G)} u^0 v_L d\Gamma + \eta \int_{\partial\Omega_L \cap \Gamma_G^u} \bar{u} v_L d\Gamma + \int_{\Omega_L} q v_L d\Omega + \int_{\partial\Omega_L \cap \Gamma_G^f} \bar{f} v_L d\Gamma \\ &+ \int_{\partial\Omega_L \cap \Gamma_G^c} \alpha u_\infty v_L d\Gamma, \end{aligned}$$

where $X_L(\Omega_L)$ is again a GFEM discretization of $H^1(\Omega_L)$. The initial global and local problem steps comprise a procedure akin to the familiar global-local FEM.



Enriched Global (EG) Problem: In general, the local problem may not provide a satisfactory estimate of the actual global solution. Taking the global-local analysis one step further, the solution u_L yielded by the local problem is used in the GFEM^{gl} to build so-called global-local shape functions

$$\phi_\alpha^{\text{gl}}(\mathbf{x}) = \varphi_\alpha(\mathbf{x})u_L(\mathbf{x})$$

numerically, which are in turn added to the global approximation space and utilized to enrich and re-solve the global problem as defined in (A.2-3). This step is termed the enriched global (EG) problem, the solution of which is denoted u^E . The procedure is shown pictorially in Fig. A2.3.

Analysis of Model Problem Using the $GFEM^{gl}$

The generalized FEM with global-local enrichment functions ($GFEM^{gl}$) described above is to solve the model problem. The global, Ω_G , and local, Ω_L , domains are discretized with four node tetrahedral GFEM elements. Quadratic and quartic ($p=4$) elements are used in global and local domains, respectively. Uniform meshes are used in the global domain, which are generated by dicing hexahedral cells into 6 tetrahedra. Mesh refinement is increased in the x -direction because the solution only exhibits a gradient in the x -direction.

Creation of Local Problems: Local domains and their corresponding initial discretizations are defined by copying elements from the global mesh around the thermal spike. This is done with the aid of global seed nodes which are selected via a bounding box containing the temperature spike. Let \mathcal{I}_{seed}

denote the indices of all global seed nodes in the bounding box. A local domain corresponding to a mesh with one layer of elements around the seed nodes is given by

$$\Omega_L^{n_{lay}=1} := \bigcup_{\beta \in \mathcal{I}_{seed}} \omega_\beta$$

where ω_β is the union of (copy of) global elements sharing node \mathbf{x}_β , $\beta \in \mathcal{I}_{seed}$, while additional layers are generated recursively in the same manner. A local mesh is shown in Fig. A2.4 corresponding to an initial global mesh with 9 levels of local refinement. The seed nodes used to create the local domains are the same nodes which are then enriched with the local solution (global-local enrichments).

The convergence of the enriched global problem when h -extensions are performed in the local problem is outlined in O'Hara's (2010) dissertation, so please refer for detailed results. For instance, the computational cost is examined for each global mesh case. Additionally, strategies are discussed for improving local problem boundary condition error by performing multiple global—local iterations and/or increasing the physical size of the local problem.

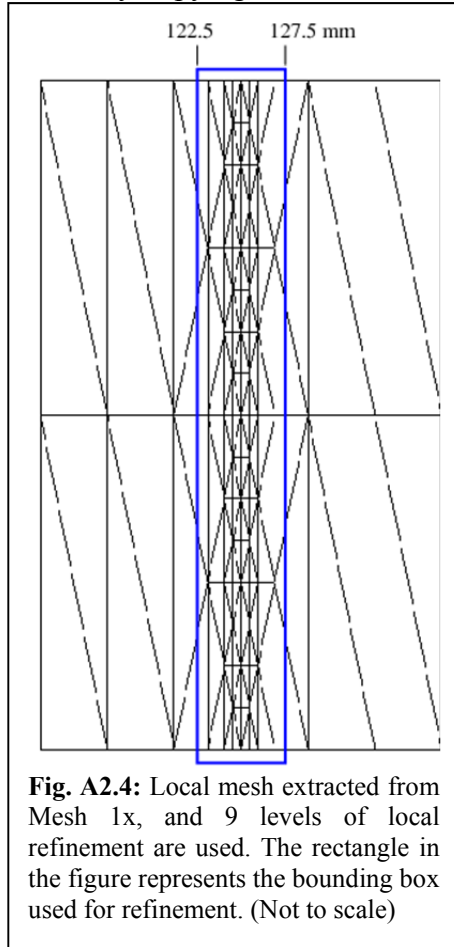


Fig. A2.4: Local mesh extracted from Mesh 1x, and 9 levels of local refinement are used. The rectangle in the figure represents the bounding box used for refinement. (Not to scale)

The following figures, Fig. A2.5, show temperature distributions computed in each phase of the $GFEM^{gl}$ —initial global, local, and enriched global problems—corresponding to 13 levels of

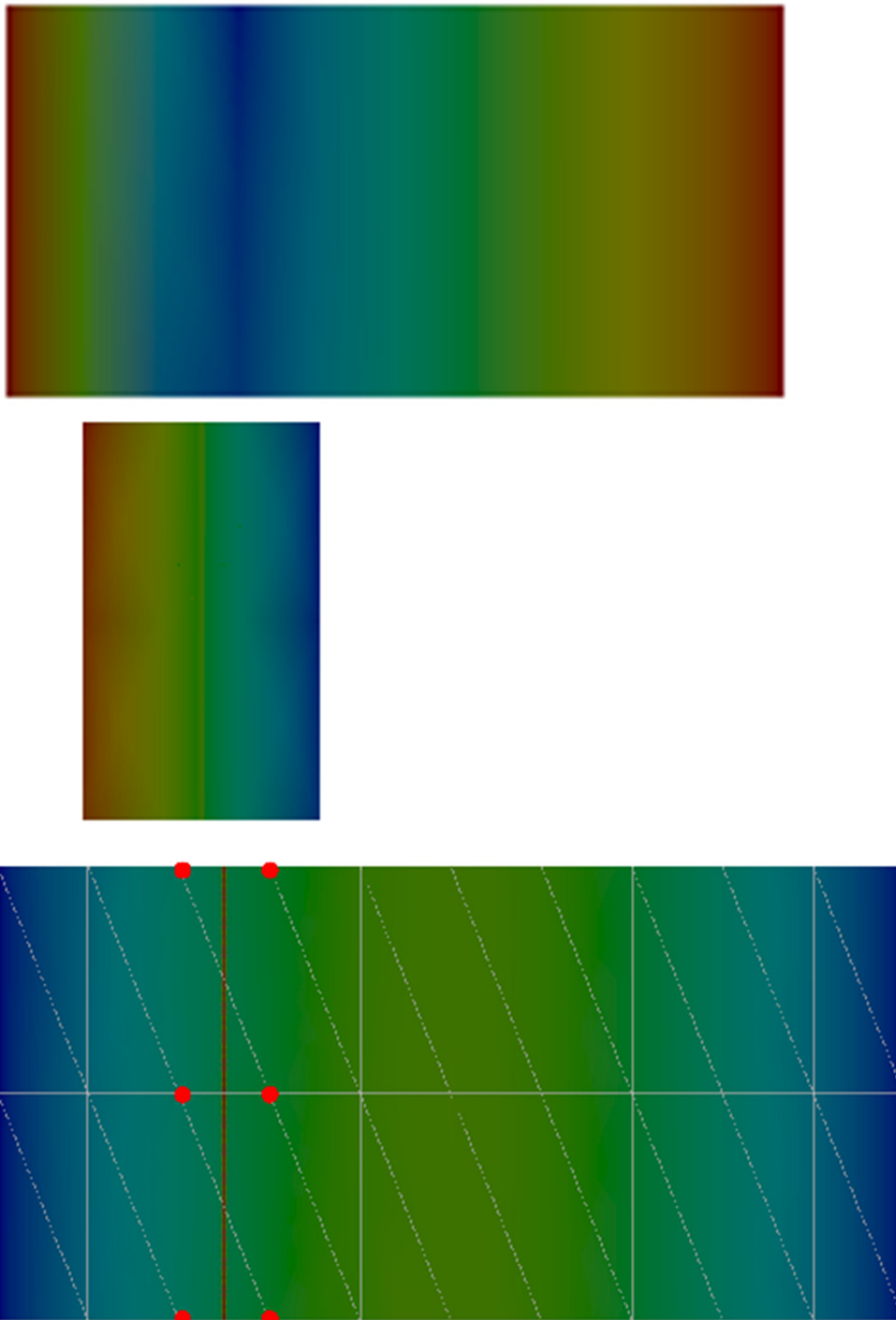


Fig. A2.5: Temperature distributions computed in the initial global (top left), local (top right), and enriched global (bottom) problems corresponding to a coarse initial mesh with 13 levels of refinement in the local problem. Red glyphs denote enriched nodes in the global problem.

refinement in the local problem. One point of interest is the resolution of the spike in the

enriched global problem, where a well-resolved spike can be seen in the temperature field even with the use of very large elements. In fact, the spike in the temperature field falls within elements, and not along a line of nodes, reflecting the shape of the specially-tailored enrichment functions from the local problem.

A.2.2 Transient Heat Conduction

Consider a domain $\Omega \subset \mathbb{R}^3$ with boundary $\partial\Omega$ decomposed as $\partial\Omega = \Gamma_c \cup \Gamma_f$ with $\Gamma_c \cap \Gamma_f = \emptyset$. The strong form of the governing equation is given by the 3D heat equation

$$\rho c \frac{\partial u}{\partial t} = \nabla(\kappa \nabla u) + Q(\mathbf{x}, t) \quad \text{in } \Omega$$

where $u(\mathbf{x}, t)$ is the temperature field, ρc is the volumetric heat capacity, and $Q(\mathbf{x}, t)$ is the internal heat source. In the general case, κ is the thermal conductivity tensor, but in this instance, only isotropic materials are considered, therefore the thermal conductivity is merely a scalar, $\kappa = \kappa(\mathbf{x})$, and the material need not be homogeneous.

Both convective and Neumann boundary conditions prescribed on Γ_c and Γ_f , respectively are considered. The boundary $\partial\Omega = \Gamma_c \cup \Gamma_f$ and $\Gamma_c \cap \Gamma_f = \emptyset$. At any time t , the normal flux is prescribed as

$$\begin{aligned} -\kappa \frac{\partial u}{\partial n} &= \eta(\bar{u} - u) \quad \text{on } \Gamma_c \\ -\kappa \frac{\partial u}{\partial n} &= \bar{f} \quad \text{on } \Gamma_f \end{aligned}$$

where \bar{u} and η are the prescribed fluid temperature and convective coefficient, respectively. Dirichlet boundary conditions can be treated as a limiting case of convective boundary conditions by selecting a large value for the convective coefficient η (penalty method). The initial conditions must also be satisfied

$$u(\mathbf{x}, 0) = u^0(\mathbf{x}) \quad \text{at } t^0$$

where $u^0(\mathbf{x})$ is the prescribed temperature field at time $t = t^0$.

Two formulations for time integration of the 3D heat equation are given. In the first formulation it is discretized first in space, and then in time. With this formulation strategy, the algorithm is appropriate for analyses which *do not* include time-dependencies in the shape functions. For the case with time-dependent shape-functions it is important to discretize the equations first in time, and then in space, as is discussed by Fries and Zilian (2009). The formulation for time-dependent shape functions is subsequently presented in (2) below. Two different, widely used time-stepping algorithms for the transient heat equation are presented. Both methods are equivalent, with slightly different formulations, but both amount to the generalized trapezoidal rule, or the α -method.

Spatial—Temporal Discretization

(1) Formulation for α -method

The formulation given by Reddy starts with a system of spatially discretized equations as in (A.2-4), and utilizes the finite difference assumption in (A.2-5).

$$M\dot{\mathbf{u}}^{n+1} + K\mathbf{u}^{n+1} = \mathbf{f}^{n+1} \quad (4.2-4)$$

$$\mathbf{u}^{n+1} = \mathbf{u}^n + \Delta t \left[\alpha \dot{\mathbf{u}}^{n+1} + (1-\alpha) \dot{\mathbf{u}}^n \right] \quad (A.2-5)$$

Equation (A.2-5) is used to eliminate $\dot{\mathbf{u}}^{n+1}$ from (A.2-4), yielding the discrete system of equations used for time-integration:

$$\left[M + \alpha \Delta t K \right] \mathbf{u}^{n+1} = \left[M - (1-\alpha) \Delta t K \right] \mathbf{u}^n + \Delta t \left[\alpha \mathbf{f}^{n+1} + (1-\alpha) \mathbf{f}^n \right] \quad (A.2-6)$$

The potential draw-back of this particular formulation is that it starts from a fully, spatially-discretized system, in which the quantities have previously been defined as

$$M_{ij}^{el} = \int_{\Omega^{el}} \rho c \phi_i \phi_j d\Omega^{el}$$

$$K_{ij}^{el} = \int_{\Omega^{el}} \kappa_{pq} \frac{\partial \phi_i}{\partial x_p} \frac{\partial \phi_j}{\partial x_q} d\Omega^{el} \quad (\text{summation on } p, q=1,2,3),$$

$$F_i^{el} = \int_{\Omega^{el}} Q(\mathbf{x}, t) \phi_i d\Omega^{el} + \int_{\Gamma_f^{el}} \bar{f}(\mathbf{x}, t) \phi_i d\Gamma_f^{el}$$

where ϕ is the vector of finite element shape functions, Ω^{el} is the domain, Γ_f^{el} is the boundary of the domain with prescribed, normal fluxes, $Q(\mathbf{x}, t)$ is the internal source, ρc is the volumetric heat capacity, $\bar{f}(\mathbf{x}, t)$ is the prescribed heat flux, and κ_{pq} is the thermal conductivity of the material. Again, we are assuming an isotropic material, therefore, $\kappa_{pq} = \kappa \quad \forall p, q$. $\{\mathbf{u}^{n+1}\}$ is the solution vector at t^{n+1} and $\{\dot{\mathbf{u}}^{n+1}\}$ is the derivative with respect to time. (A.2-6) is then computed on an element-by-element basis and assembled to form the global system of equations. The previous formulation is the widely used α -method, suitable for transient heat transfer simulations, but the formulation is in no way modified to incorporate the use of time-dependent shape functions.

(2) Formulation for α -method

The following formulation is presented by Hughes. In this case we start from a spatially discretized system of equations. The spatially-discrete governing equations of are:

$$M\mathbf{v}^{n+1} + K\mathbf{u}^{n+1} = \mathbf{f}^{n+1}$$

$$\mathbf{u}^{n+1} = \mathbf{u}^n + \Delta t \mathbf{v}^{n+\alpha}$$

$$\mathbf{v}^{n+\alpha} = (1-\alpha) \mathbf{v}^n + \alpha \mathbf{v}^{n+1}$$

where $\alpha \in [0,1]$. The following predictor (A.2-7) and corrector (A.2-8) are used to define \mathbf{u}^{n+1} . One can then solve for \mathbf{v}^{n+1} in terms of \mathbf{u}^{n+1} and other known quantities, and effectively eliminate \mathbf{v}^{n+1} from (A.2-4).

$$\hat{\mathbf{u}}^{n+1} = \mathbf{u}^n + (1-\alpha) \Delta t \mathbf{v}^n \quad (A.2-7)$$

$$\mathbf{u}^{n+1} = \hat{\mathbf{u}}^{n+1} + \alpha \Delta t \mathbf{v}^{n+1} \quad (A.2-8)$$

$$\mathbf{v}^{n+1} = \frac{\mathbf{u}^{n+1} - \hat{\mathbf{u}}^{n+1}}{\alpha \Delta t} \quad (\text{A.2-9})$$

(A.2-9) is now plugged into (A.2-4) and the following equation is posed which can be algebraically manipulated and solved for \mathbf{u}^{n+1} .

$$M \frac{\mathbf{u}^{n+1} - \hat{\mathbf{u}}^{n+1}}{\alpha \Delta t} + K \mathbf{u}^{n+1} = \mathbf{f}^{n+1}$$

Moving known quantities to the right-hand-side and quantities dependent upon \mathbf{u}^{n+1} to the left-hand-side yields

$$M \frac{\mathbf{u}^{n+1}}{\alpha \Delta t} + K \mathbf{u}^{n+1} = \mathbf{f}^{n+1} + M \frac{\hat{\mathbf{u}}^{n+1}}{\alpha \Delta t} \quad (\text{A.2-10})$$

(A.2-7) is then plugged in to (A.2-10) and simple algebra can be used to arrive at the following equations yielding \mathbf{u}^{n+1} and \mathbf{v}^{n+1} , respectively.

$$\frac{1}{\alpha \Delta t} [M + \alpha \Delta t K] \mathbf{u}^{n+1} = \mathbf{f}^{n+1} + \frac{M}{\alpha \Delta t} [\mathbf{u}^n + (1 - \alpha) \Delta t \mathbf{v}^n] \quad (\text{A.2-11})$$

$$\mathbf{v}^{n+1} = \frac{\mathbf{u}^{n+1} - \hat{\mathbf{u}}^{n+1}}{\alpha \Delta t} = \frac{\mathbf{u}^{n+1} - (\mathbf{u}^n + (1 - \alpha) \Delta t \mathbf{v}^n)}{\alpha \Delta t} \quad (\text{A.2-12})$$

At this point it is reasonable to verify that (A.2-11) and (A.2-6) are equivalent. First (A.2-6) is divided by $\alpha \Delta t$ and some terms are rearranged as follows

$$\frac{1}{\alpha \Delta t} [M + \alpha \Delta t K] \mathbf{u}^{n+1} = \frac{\alpha \Delta t \mathbf{f}^{n+1}}{\alpha \Delta t} + \frac{M}{\alpha \Delta t} \mathbf{u}^n - \frac{(1 - \alpha) \Delta t K \mathbf{u}^n}{\alpha \Delta t} + \frac{(1 - \alpha) \Delta t \mathbf{f}^n}{\alpha \Delta t} \quad (\text{A.2-13})$$

From (A.2-13) it can be deduced that the left-hand-side is equivalent for both equations, as well as the first two terms on the right-hand-side. The question is now to verify that the following is true:

$$\frac{M}{\alpha \Delta t} (1 - \alpha) \Delta t \mathbf{v}^n = - \frac{(1 - \alpha) \Delta t K \mathbf{u}^n}{\alpha \Delta t} + \frac{(1 - \alpha) \Delta t \mathbf{f}^n}{\alpha \Delta t} \quad (\text{A.2-14})$$

which can be rearranged as follows:

$$\frac{(1 - \alpha) \Delta t}{\alpha \Delta t} M \mathbf{v}^n = \frac{(1 - \alpha) \Delta t}{\alpha \Delta t} \{ \mathbf{f}^n - K \mathbf{u}^n \} \quad (\text{A.2-15})$$

Dropping the coefficient common to both sides of the equation yields the following equality, which is known to be true from (A.2-6).

$$M \mathbf{v}^n = \{ \mathbf{f}^n - K \mathbf{u}^n \} \quad (\text{A.2-16})$$

From the previous it is apparent that the two formulations are not form-equivalent, but are in fact mathematically equivalent as would be expected.

Temporal—Spatial Discretization

The formulation starts with the strong form of the governing equation:

$$\rho c \frac{\partial u}{\partial t} = \nabla \cdot \kappa \nabla u + Q \quad (\text{A.2-17})$$

The equation is multiplied by a weighting function, w , and integrated over the domain, Ω .

$$\int_{\Omega} w \rho c \frac{\partial u}{\partial t} d\Omega = \int_{\Omega} (w \nabla \cdot \kappa \nabla u + w Q) d\Omega \quad (\text{A.2-18})$$

Integration by parts is performed on the first term of the right-hand-side, and the domain integral is moved to the left-hand-side of the equation. The boundary term is left on the right-hand-side with the applied source term.

$$\int_{\Omega} \left(w \rho c \frac{\partial u}{\partial t} + \nabla w \cdot \kappa \nabla u \right) d\Omega = \int_{\partial\Omega} w \kappa \nabla u \cdot \tilde{n} d\Gamma + \int_{\Omega} w Q d\Omega \quad (\text{A.2-19})$$

The term $\nabla u \cdot \tilde{n}$ is equivalent to $\frac{\partial u}{\partial n}$, and when multiplied by the conductivity, κ , yields the applied normal flux. The weak form of the system of equations, which will subsequently be discretized first in time, then in space is posed as follows

$$\int_{\Omega} \left(w \rho c \frac{\partial u}{\partial t} + \nabla w \cdot \kappa \nabla u \right) d\Omega = \int_{\partial\Omega} w \kappa \frac{\partial u}{\partial n} d\Gamma + \int_{\Omega} w Q d\Omega \quad (\text{A.2-20})$$

The system of equations is first discretized in time. To this end the following finite difference approximations are used, yielding the generalized trapezoidal rule, or α -method, used for the time-marching scheme.

$$\frac{\partial u}{\partial t} = \frac{u^{n+1} - u^n}{\Delta t} \quad (\text{A.2-21})$$

$$u^{n+\alpha} = (1 - \alpha)u^n + \alpha u^{n+1} \quad (\text{A.2-22})$$

Plugging (A.2-21) and (A.2-22) into (A.2-20) yields the temporally discretized system of equations.

$$\begin{aligned} \int_{\Omega} \left(w \rho c \frac{u^{n+1} - u^n}{\Delta t} + \nabla w \cdot \kappa \left[(1 - \alpha) \nabla u^n + \alpha \nabla u^{n+1} \right] \right) d\Omega = \\ \int_{\Omega} w \left[\alpha Q^{n+1} + (1 - \alpha) Q^n \right] d\Omega + \int_{\partial\Omega} w \kappa \left[\alpha \frac{\partial u^{n+1}}{\partial n} + (1 - \alpha) \frac{\partial u^n}{\partial n} \right] d\Gamma \end{aligned} \quad (\text{A.2-23})$$

The boundary terms on $\partial\Omega = \Gamma_c \cup \Gamma_f$ are considered first in detail, as follows:

$$\begin{aligned} \int_{\partial\Omega} w \kappa \left[\alpha \frac{\partial u^{n+1}}{\partial n} + (1 - \alpha) \frac{\partial u^n}{\partial n} \right] d\Gamma = \alpha \int_{\Gamma_f} w \bar{f}^{n+1} d\Gamma + (1 - \alpha) \int_{\Gamma_f} w \bar{f}^n d\Gamma + \\ \alpha \int_{\Gamma_c} w \gamma \bar{u}^{n+1} d\Gamma - \alpha \int_{\Gamma_c} w \gamma u^{n+1} d\Gamma + (1 - \alpha) \int_{\Gamma_c} w \gamma \bar{u}^n d\Gamma - (1 - \alpha) \int_{\Gamma_c} w \gamma u^n d\Gamma \end{aligned} \quad (\text{A.2-24})$$

(A.2-23) is rearranged, with the proper boundary terms (A.2-24), such that terms involving u^{n+1} are moved to the left-hand-side, and all known terms (those not dependent upon u^{n+1}) are moved to the right-hand-side.

$$\begin{aligned} \frac{1}{\Delta t} \int_{\Omega} w \rho c u^{n+1} d\Omega + \alpha \int_{\Omega} \nabla w \cdot \kappa \nabla u^{n+1} d\Omega + \alpha \int_{\Gamma_c} w \gamma u^{n+1} d\Gamma = \frac{1}{\Delta t} \int_{\Omega} \rho c w u^n d\Omega \\ - (1 - \alpha) \int_{\Omega} \nabla w \cdot \kappa \nabla u^n d\Omega + \alpha \int_{\Omega} w Q^{n+1} d\Omega + (1 - \alpha) \int_{\Omega} w Q^n d\Omega + \alpha \int_{\Gamma_f} w \bar{f}^{n+1} d\Gamma \\ + (1 - \alpha) \int_{\Gamma_f} w \bar{f}^n d\Gamma + \alpha \int_{\Gamma_c} w \gamma \bar{u}^{n+1} d\Gamma + (1 - \alpha) \int_{\Gamma_c} w \gamma \bar{u}^n d\Gamma - (1 - \alpha) \int_{\Gamma_c} w \gamma u^n d\Gamma \end{aligned} \quad (\text{A.2-25})$$

In the previous equation, the loading terms are defined as $Q^n = Q(\mathbf{x}, t^n)$ and $\bar{f}^n = \bar{f}(\mathbf{x}, t^n)$.

At this point, the system of equations is fully discretized in time. For the spatial discretization, generalized finite element shape functions are used, which may have time-dependencies. At any given time, t^n , one defines $u^n(\mathbf{x}, t^n) = \phi^n(\mathbf{x}, t^n) \cdot \mathbf{u}^n(t^n)$, where $\mathbf{u}^n(t^n)$ is the vector of degrees of freedom, and $\phi^n(\mathbf{x}, t^n)$ is the vector of finite element shape functions at t^n . Due to the potential time-dependent nature of the shape functions, it is very important to properly select the discretization for the weight function, w . In the current implementation, w is required to be consistent across each term of (A.2-25). To this end, the weighting function, w , is discretized using finite element shape functions at time t^{n+1} . In the aforementioned equations, $w = w^{n+1}(\mathbf{x}, t^{n+1}) = \phi^{n+1}(\mathbf{x}, t^{n+1}) \cdot \mathbf{w}^{n+1}(t^{n+1})$. (A.2-25) is now discretized on a term-by-term basis using the previously defined discretizations:

$$\int_{\Omega} \rho c w^{n+1} u^{n+1} d\Omega = (\mathbf{w}^{n+1})^T \int_{\Omega} \phi^{n+1} \rho c (\phi^{n+1})^T d\Omega \mathbf{u}^{n+1} = (\mathbf{w}^{n+1})^T M^{n+1} \mathbf{u}^{n+1} \quad (\text{A.2-26})$$

$$\int_{\Omega} \rho c w^{n+1} u^n d\Omega = (\mathbf{w}^{n+1})^T \int_{\Omega} \phi^{n+1} \rho c (\phi^n)^T d\Omega \mathbf{u}^n = (\mathbf{w}^{n+1})^T M^{n+1,n} \mathbf{u}^n \quad (\text{A.2-27})$$

$$\int_{\Omega} \nabla w^{n+1} \cdot \kappa \nabla u^{n+1} d\Omega = (\mathbf{w}^{n+1})^T \int_{\Omega} \nabla \phi^{n+1} \kappa (\nabla \phi^{n+1})^T d\Omega \mathbf{u}^{n+1} = (\mathbf{w}^{n+1})^T K^{n+1} \mathbf{u}^{n+1} \quad (\text{A.2-28})$$

$$\int_{\Omega} \nabla w^{n+1} \cdot \kappa \nabla u^n d\Omega = (\mathbf{w}^{n+1})^T \int_{\Omega} \nabla \phi^{n+1} \kappa (\nabla \phi^n)^T d\Omega \mathbf{u}^n = (\mathbf{w}^{n+1})^T K^{n+1,n} \mathbf{u}^n \quad (\text{A.2-29})$$

$$\int_{\Omega} w^{n+1} Q^{n+1} d\Omega = (\mathbf{w}^{n+1})^T \int_{\Omega} \phi^{n+1} Q^{n+1} d\Omega = (\mathbf{w}^{n+1})^T \mathbf{f}_Q^{n+1} \quad (\text{A.2-30})$$

$$\int_{\Omega} w^{n+1} Q^n d\Omega = (\mathbf{w}^{n+1})^T \int_{\Omega} \phi^{n+1} Q^n d\Omega = (\mathbf{w}^{n+1})^T \mathbf{f}_Q^{n+1,n} \quad (\text{A.2-31})$$

$$\int_{\Gamma_f} w^{n+1} \bar{f}^{n+1} d\Gamma = (\mathbf{w}^{n+1})^T \int_{\Gamma_f} \phi^{n+1} \bar{f}^{n+1} d\Gamma = (\mathbf{w}^{n+1})^T \mathbf{f}_N^{n+1} \quad (\text{A.2-32})$$

$$\int_{\Gamma_f} w^{n+1} \bar{f}^n d\Gamma = (\mathbf{w}^{n+1})^T \int_{\Gamma_f} \phi^{n+1} \bar{f}^n d\Gamma = (\mathbf{w}^{n+1})^T \mathbf{f}_N^{n+1,n} \quad (\text{A.2-33})$$

$$\int_{\Gamma_c} \gamma w^{n+1} u^{n+1} d\Gamma = (\mathbf{w}^{n+1})^T \int_{\Gamma_c} \phi^{n+1} \gamma (\phi^{n+1})^T d\Gamma \mathbf{u}^{n+1} = (\mathbf{w}^{n+1})^T M_c^{n+1} \mathbf{u}^{n+1} \quad (\text{A.2-34})$$

$$\int_{\Gamma_c} \gamma w^{n+1} u^n d\Gamma = (\mathbf{w}^{n+1})^T \int_{\Gamma_c} \phi^{n+1} \gamma (\phi^n)^T d\Gamma \mathbf{u}^n = (\mathbf{w}^{n+1})^T M_c^{n+1,n} \mathbf{u}^n \quad (\text{A.2-35})$$

$$\int_{\Gamma_c} \gamma w^{n+1} \bar{u}^{n+1} d\Gamma = (\mathbf{w}^{n+1})^T \int_{\Gamma_c} \phi^{n+1} \gamma \bar{u}^{n+1} d\Gamma = (\mathbf{w}^{n+1})^T \mathbf{f}_c^{n+1} \quad (\text{A.2-36})$$

$$\int_{\Gamma_c} \gamma w^{n+1} \bar{u}^n d\Gamma = (\mathbf{w}^{n+1})^T \int_{\Gamma_c} \phi^{n+1} \gamma \bar{u}^n d\Gamma = (\mathbf{w}^{n+1})^T \mathbf{f}_c^{n+1,n} \quad (\text{A.2-37})$$

Since equation (A.2-25) must hold for any admissible weight function w , it must hold also for any \mathbf{w}^{n+1} . As such, one can pose the fully discretized system of equations as

$$\begin{aligned} \left[\frac{1}{\Delta t} M^{n+1} + \alpha K^{n+1} + \alpha M_c^{n+1} \right] \mathbf{u}^{n+1} = & \left[\frac{1}{\Delta t} M^{n+1,n} - (1-\alpha)K^{n+1,n} - (1-\alpha)M_c^{n+1,n} \right] \mathbf{u}^n \\ & + \alpha \mathbf{f}_Q^{n+1} + (1-\alpha)\mathbf{f}_Q^{n+1,n} + \alpha \mathbf{f}_N^{n+1} + (1-\alpha)\mathbf{f}_N^{n+1,n} + \alpha \mathbf{f}_c^{n+1} + (1-\alpha)\mathbf{f}_c^{n+1,n} \end{aligned} \quad (\text{A.2-38})$$

More concisely, the above equation is re-written as:

$$\left[\frac{1}{\Delta t} M^{n+1} + \alpha K^{n+1} \right] \mathbf{u}^{n+1} = \left[\frac{1}{\Delta t} M^{n+1,n} - (1-\alpha)K^{n+1,n} \right] \mathbf{u}^n + \alpha \hat{\mathbf{f}}^{n+1} + (1-\alpha)\hat{\mathbf{f}}^{n+1,n} \quad (\text{A.2-39})$$

where

$$K^{n+1} = K^{n+1} + M_c^{n+1} \quad (\text{A.2-40})$$

$$K^{n+1,n} = K^{n+1,n} + M_c^{n+1,n} \quad (\text{A.2-41})$$

$$\hat{\mathbf{f}}^{n+1} = \mathbf{f}_Q^{n+1} + \mathbf{f}_N^{n+1} + \mathbf{f}_c^{n+1} \quad (\text{A.2-42})$$

$$\hat{\mathbf{f}}^{n+1,n} = \mathbf{f}_Q^{n+1,n} + \mathbf{f}_N^{n+1,n} + \mathbf{f}_c^{n+1,n} \quad (\text{A.2-43})$$

In all of the above equations, \mathbf{u}^n are known values obtained from the solution at t^n . It is noted that if the shape functions are not time-dependent, $M^{n+1} = M^{n+1,n} = M$, $K^{n+1} = K^{n+1,n} = K$, $\mathbf{f}_Q^{n+1,n} = \mathbf{f}_Q^n$, $\mathbf{f}_N^{n+1,n} = \mathbf{f}_N^n$ and $\mathbf{f}_c^{n+1,n} = \mathbf{f}_c^n$. It is further noted that if the convective boundary terms are neglected, (A.2-39) is equivalent to (A.2-6).

For the analyses presented in the subsequent sections, the value of α is taken as $\alpha = 1$, yielding the unconditionally stable, Backward Euler algorithm. As such, only the non-symmetric capacity matrix, $M^{n+1,n}$ is required, and it need not be assembled directly. The vector term $M^{n+1,n}\mathbf{u}^n$ can be computed as

$$M^{n+1,n}\mathbf{u}^n = \int_{\Omega} \phi^{n+1} \rho c (\phi^n)^T \mathbf{u}^n d\Omega = \int_{\Omega} \rho c \phi^{n+1} u^n d\Omega \quad (\text{A.2-44})$$

where $u^n = (\phi^n)^T \mathbf{u}^n$, is the GFEM solution from time step t^n . A detailed study of the critical time step size for GFEM discretizations using the above formulations can be found in O'Hara's (2010) dissertation.

Model Problem

The problem selected for verification involves a sharp spatial gradient in the temperature field (A.2-45), as well as in the resulting source term (A.2-46). There is also a temporal gradient, but it is smooth in nature.

$$u(\mathbf{x}, t) = \left(\exp^{-\gamma(x-x_0)^2} + \sin\left(\frac{\pi x}{L}\right) \right) * \exp^{(-t)} \quad (\text{A.2-45})$$

$$Q(\mathbf{x}, t) = \rho c \frac{\partial u}{\partial t}(\mathbf{x}, t) - \kappa \frac{\partial^2 u}{\partial x^2}(\mathbf{x}, t), \quad (\text{A.2-46})$$

The initial and boundary conditions are given in (A.2-47) and (A.2-48), respectively. Refer to O'Hara's dissertation for additional details.

$$u(\mathbf{x}, 0) = \exp^{-\gamma(x-x_0)^2} + \sin\left(\frac{\pi x}{L}\right), \quad (\text{A.2-47})$$

$$u(0,t) = u(L,t) = 0, \quad (\text{A.2-48})$$

In the above equations, $x_0 = 125 \text{ mm}$, $L = 500 \text{ mm}$ and γ is a parameter controlling the roughness of the solution. Unless otherwise indicated, the value of γ is taken as 1.0. The material properties are taken as thermal conductivity, $\kappa = 1$ and volumetric heat capacity, $\rho c = \left(\frac{\pi}{L}\right)^2$. The

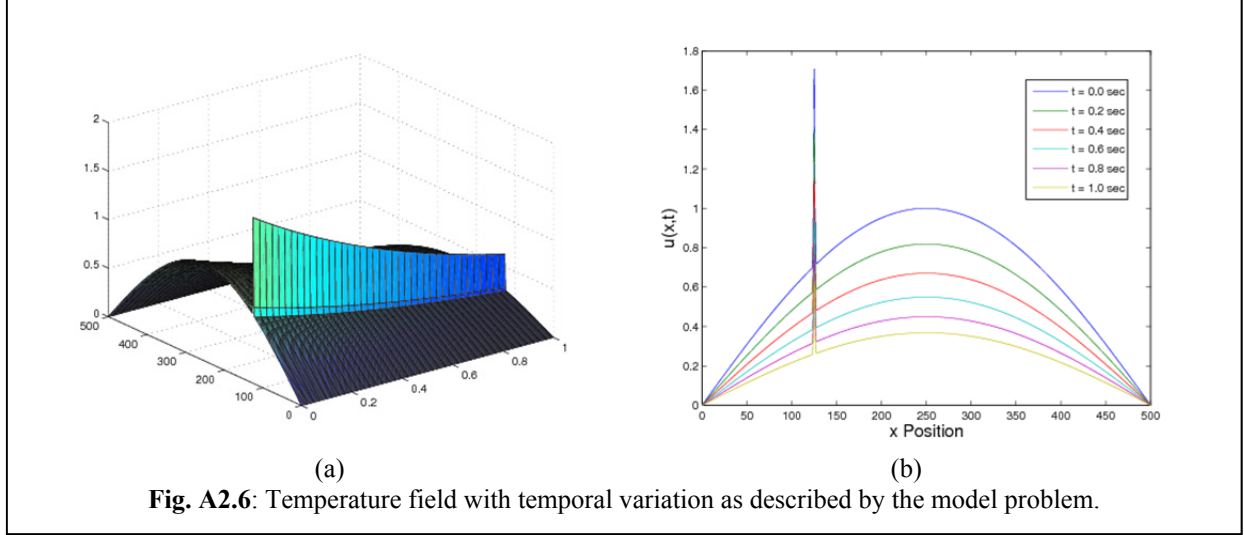


Fig. A2.6: Temperature field with temporal variation as described by the model problem.

reference solution (A.2-45) is plotted in Fig. A2.6a and the initial condition (A.2-47) is plotted in Fig. A2.6b. The value of x_0 indicates the location of the thermal spike. From the temporal standpoint, the solution undergoes a smooth, exponential decay in time.

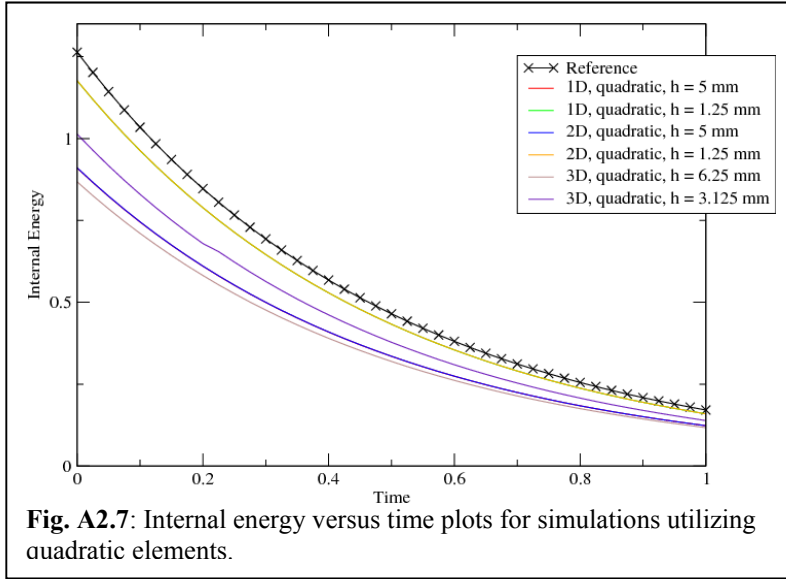


Fig. A2.7: Internal energy versus time plots for simulations utilizing quadratic elements.

Below, the heat equation with Q given by (A.2-46), initial and boundary conditions given in (A.2-47) and (A.2-48), respectively, is solved using 1-, 2- and 3-D *GFEM* discretizations.

The exact internal energy, $U(t)$, in the solution domain Ω is

given by

$$U(t) = \int_{\Omega} (\kappa \nabla u) \cdot (\nabla u) d\Omega, \quad (\text{A.2-49})$$

while the internal energy of the *GFEM* solution at time t^n is given by

$$U_{hp}(t^n) = \int_{\Omega} (\kappa \nabla u^n) \cdot (\nabla u^n) d\Omega \quad (\text{A.2-50})$$

Internal energy results from select simulations are shown in Fig. A2.7, while more detailed results can be found in O'Hara's dissertation.

A.2.3 ReAnalysis for GFEM^{gl} Discretizations

Algorithmic Formulation for Steady-State ReAnalysis

GFEM^{gl} simulations result in stiffness matrices with hierarchical structures, consisting of global degrees of freedom, global—local or fine scale enrichment degrees of freedom, and coupling terms. We similarly assume that we can partition the vector of degrees of freedom (load vector) into fine-scale and coarse-scale degrees of freedom (loads). That is,

$$K_G^{partitioned} \bar{\mathbf{u}}_G^{partitioned} = \mathbf{f}_G^{partitioned} \quad (\text{A.2-51})$$

in which we define

$$K_G^{partitioned} = \begin{bmatrix} K_G^0 & K_G^{0,gl} \\ K_G^{gl,0} & K_G^{gl} \end{bmatrix} \quad (\text{A.2-52})$$

$$\bar{\mathbf{u}}_G^{partitioned} = \left\{ \bar{\mathbf{u}}_G^0, \bar{\mathbf{u}}_G^{gl} \right\}^T \quad (\text{A.2-53})$$

$$\mathbf{f}_G^{partitioned} = \left\{ \mathbf{f}_G^0, \mathbf{f}_G^{gl} \right\}^T \quad (\text{A.2-54})$$

where $(\cdot)^0$ indicates a quantity associated with the coarse scale, and $(\cdot)^{gl}$ indicates a quantity associated with the fine scale.

Static Condensation The first equation obtained from (A.2-51) yields

$$\bar{\mathbf{u}}_G^0 = (K_G^0)^{-1} \left[\mathbf{f}_G^0 - K_G^{0,gl} \bar{\mathbf{u}}_G^{gl} \right] \quad (\text{A.2-55})$$

Substituting this back into the second equation from (A.2-51), and rearranging so that the known quantities are in the right-hand-side, yields

$$\left[K_G^{gl} - K_G^{gl,0} (K_G^0)^{-1} K_G^{0,gl} \right] \bar{\mathbf{u}}_G^{gl} = \mathbf{f}_G^{gl} - K_G^{gl,0} (K_G^0)^{-1} \mathbf{f}_G^0, \quad (\text{A.2-56})$$

For convenience (A.2-56) can be written as

$$K_G^{gl} \bar{\mathbf{u}}_G^{gl} = \hat{\mathbf{f}}_G^{gl} \quad (\text{A.2-57})$$

where

$$K_G^{gl} = \left[K_G^{gl} - K_G^{gl,0} (K_G^0)^{-1} K_G^{0,gl} \right] \quad (\text{A.2-58})$$

$$\hat{\mathbf{f}}_G^{gl} = \left\{ \mathbf{f}_G^{gl} - K_G^{gl,0} (K_G^0)^{-1} \mathbf{f}_G^0 \right\} \quad (\text{A.2-59})$$

The solution to (A.2-57) is computationally inexpensive, since the dimension of the additional fine-scale dofs is very small compared to the dimension of the fixed, coarse-scale system. The calculation of both K_G^{gl} and $\hat{\mathbf{f}}_G^{gl}$ require only the forward/backward substitution of the factorization of K_G^0 , which is only computed once, and then re-used for each loading condition. Once $\bar{\mathbf{u}}_G^{gl}$ is calculated, the computation of $\bar{\mathbf{u}}_G^0$ also requires only the forward/backward substitution of the factorization of K_G^0 , as shown in (A.2-55). A detailed study of the increase in computational efficiency due to the ReAnalysis algorithm for the steady-state case is given in O'Hara's (2010) dissertation.

Algorithmic Formulation for Transient ReAnalysis

In the $GFEM^{gl}$ as applied to transient simulations, there is once again a significant amount of reusable information, that if utilized, can achieve much better efficiency. The speed-up in terms of CPU time will be significantly amplified as the number of time-steps is increased, as noted in the previous section. We start the formulation for the transient analysis by first assuming that we can partition the global matrices and vectors into portions representing the fixed coarse-scale dofs and the evolving fine-scale dofs.

$$K_G^{partitioned} \bar{\mathbf{u}}_G^{partitioned} = \mathbf{f}_G^{partitioned} \quad (\text{A.2-60})$$

in which we again define the following

$$K_G^{partitioned} = \begin{bmatrix} K_G^0 & K_G^{0,gl} \\ K_G^{gl,0} & K_G^{gl} \end{bmatrix} \quad (\text{A.2-61})$$

For transient simulations, taking into account inertial effects as discussed in detail in Chapter 3 of O'Hara (2010), we define the following at time t^{n+1} :

$$K_G^0 = [M_{CS}^0 + \alpha \Delta t K_{CS}^0] \quad (\text{A.2-62})$$

$$K_G^{gl(n+1)} = [M_{FS}^{gl(n+1)} + \alpha \Delta t K_{FS}^{gl(n+1)}] \quad (\text{A.2-63})$$

$$K_G^{gl,0(n+1)} = [M_{FS-CS}^{gl,0(n+1)} + \alpha \Delta t K_{FS-CS}^{gl,0(n+1)}] \quad (\text{A.2-64})$$

$$K_G^{0,gl(n+1)} = [M_{CS-FS}^{0,gl(n+1)} + \alpha \Delta t K_{CS-FS}^{0,gl(n+1)}] \quad (\text{A.2-65})$$

In the previous equations, K_G^0 is the effective stiffness matrix associated with the fixed, coarse-scale mesh. It is computed as a combination of the fixed, coarse-scale stiffness matrix, K_{CS}^0 , and the fixed, coarse-scale capacity matrix, M_{CS}^0 . This effective stiffness matrix may be assembled and factorized once, and this information can then be saved for use at each subsequent time-step. $K_G^{gl(n+1)}$ is the effective stiffness matrix for the fine-scale dofs, which must be assembled and factorized at each time step. It is, however; much smaller in dimension than K_G^0 , and thus less expensive to assemble and factorize. $K_G^{gl,0(n+1)}$ and $K_G^{0,gl(n+1)}$ represent the coupling between the coarse and fine-scales and will also need to be assembled and factorized at each time-step. These two matrices are related as $K_G^{gl,0(n+1)} = (K_G^{0,gl(n+1)})^T$.

Next, we define

$$\bar{\mathbf{u}}_G^{partitioned} = \left\{ \bar{\mathbf{u}}_G^{0(n+1)}, \bar{\mathbf{u}}_G^{gl(n+1)} \right\}^T \quad (\text{A.2-66})$$

where $\bar{\mathbf{u}}_G^{0(n+1)}$ and $\bar{\mathbf{u}}_G^{gl(n+1)}$ are again, degrees of freedom associated with the coarse- and fine-scales, respectively.

The right-hand-side of (A.2-60) is defined as

$$\mathbf{f}_G^{partitioned} = \left\{ \mathbf{f}_G^{0(n+1)}, \mathbf{f}_G^{gl(n+1)} \right\}^T \quad (\text{A.2-67})$$

where $\mathbf{f}_G^{0(n+1)}$ and $\mathbf{f}_G^{gl(n+1)}$ are the effective load vectors associated with the coarse- and fine-scales, respectively. To define the effective load vectors, further analysis is required to properly account for the inertial effects. The right-hand-side of (A.2-60) is written as

$$\begin{aligned}
\begin{bmatrix} \mathbf{f}_G^{0(n+1)} \\ \mathbf{f}_G^{gl(n+1)} \end{bmatrix} &= \Delta t \begin{bmatrix} \alpha \mathbf{f}_{CS}^{0(n+1)} + (1-\alpha) \mathbf{f}_{CS}^{0(n)} \\ \alpha \mathbf{f}_{FS}^{gl(n+1)} + (1-\alpha) \tilde{\mathbf{f}}_{FS}^{gl(n+1,n)} \end{bmatrix} + \\
&\begin{bmatrix} M_{CS}^0 & M_{CS-FS}^{0,gl(n+1,n)} \\ M_{FS-CS}^{gl,0(n+1,n)} & M_{FS}^{gl(n+1,n)} \end{bmatrix} * \begin{bmatrix} \bar{\mathbf{u}}_G^{0(n)} \\ \bar{\mathbf{u}}_G^{gl(n)} \end{bmatrix} - \\
(1-\alpha) \Delta t &\begin{bmatrix} K_{CS}^0 & K_{CS-FS}^{0,gl(n+1,n)} \\ K_{FS-CS}^{gl,0(n+1,n)} & K_{FS}^{gl(n+1,n)} \end{bmatrix} * \begin{bmatrix} \bar{\mathbf{u}}_G^{0(n)} \\ \bar{\mathbf{u}}_G^{gl(n)} \end{bmatrix}
\end{aligned} \tag{A.2-68}$$

For simplicity we define

$$\Psi_{CS}^0 = M_{CS}^0 - (1-\alpha) \Delta t K_{CS}^0 \tag{A.2-69}$$

$$\bar{\Psi}_{CS-FS}^{0,gl(n+1,n)} = M_{CS-FS}^{0,gl(n+1,n)} - (1-\alpha) \Delta t K_{CS-FS}^{0,gl(n+1,n)} \tag{A.2-70}$$

$$\bar{\Psi}_{FS-CS}^{gl,0(n+1,n)} = M_{FS-CS}^{gl,0(n+1,n)} - (1-\alpha) \Delta t K_{FS-CS}^{gl,0(n+1,n)} \tag{A.2-71}$$

$$\bar{\Psi}_{FS}^{gl(n+1,n)} = M_{FS}^{gl(n+1,n)} - (1-\alpha) \Delta t K_{FS}^{gl(n+1,n)} \tag{A.2-72}$$

It should be noted, in the previous equations, (\approx) indicates a quantity which takes into account the time-dependent nature of the shape functions, and requires finite element shape functions from time steps t^n and t^{n+1} . With the simplifications provided by (A.2-69)-(A.2-72), the components of the effective, partitioned load vector are written as

$$\mathbf{f}_G^{0(n+1)} = \alpha \Delta t \mathbf{f}_{CS}^{0(n+1)} + (1-\alpha) \Delta t \mathbf{f}_{CS}^{0(n)} + \Psi_{CS}^0 \bar{\mathbf{u}}_G^{0(n)} + \bar{\Psi}_{CS-FS}^{0,gl(n+1,n)} \bar{\mathbf{u}}_G^{gl(n)} \tag{A.2-73}$$

$$\mathbf{f}_G^{gl(n+1)} = \alpha \Delta t \mathbf{f}_{FS}^{gl(n+1)} + (1-\alpha) \Delta t \tilde{\mathbf{f}}_{FS}^{gl(n+1,n)} + \bar{\Psi}_{FS-CS}^{gl,0(n+1,n)} \bar{\mathbf{u}}_G^{0(n)} + \bar{\Psi}_{FS}^{gl(n+1,n)} \bar{\mathbf{u}}_G^{gl(n)} \tag{A.2-74}$$

With each of the effective matrices and vectors defined, we can follow the static condensation scheme presented in Section 1 to efficiently solve the partitioned system of equations at any time t^{n+1} . Verification examples are given for the transient implementation in O'Hara (2010).

A.2.4 Computational Cost Analysis

Most problems of engineering relevance are solved using multi-step algorithms. Examples include: fatigue crack growth simulations; time-dependent problems; material or geometrically non-linear problems; *etc.* Furthermore, failure of structural components involves highly localized phenomena. The GFEM described in Section A2 takes advantage of these features and is able to solve this class of problems in a much more computationally efficient

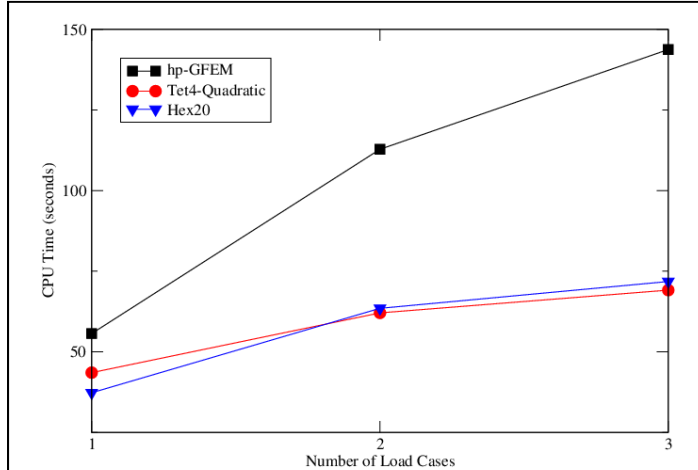


Fig. A2.8: Amount of CPU time required versus the number of loading cases considered (O'Hara *et al.*, 2012).

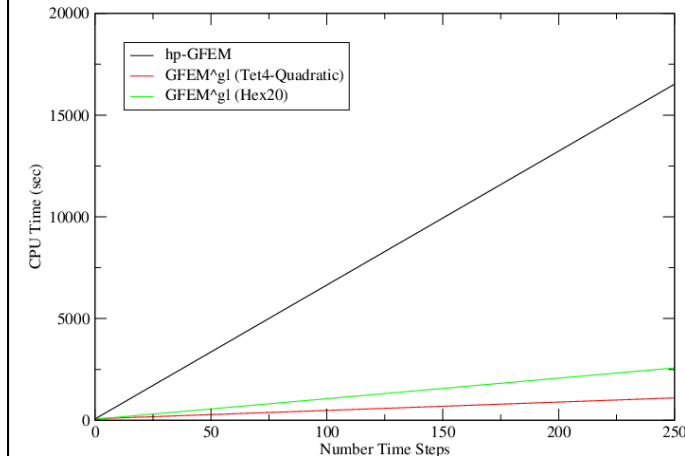


Fig. A2.9: CPU time requirements versus number of time-steps considered for *hp*-GFEM simulations as well as GFEM^{gl} simulations using both Tet4-Quadratic and Hex20 elements in the coarse, global domain (O'Hara *et al.*, 2012).

manner than available FEM. This has been demonstrated in detail for the cases of (i) Steady-state problems with multiple, localized, thermal loads (*e.g.*, Section 6.2 of (O'Hara *et al.*, 2012); (ii) Time-dependent problems with localized thermal gradients (*e.g.*, Section 7.2 of (O'Hara *et al.*, 2012); (iii) Three-dimensional simulations of fatigue crack growth (Pereira *et al.*, 2012).

The GFEM^{gl} explores the hierarchical structure of the global matrices, such as in (A.2-52) and (A.2-68). In problems involving localized phenomena, most entries of matrices (A.2-52) and (A.2-68) remain unchanged and need not be recomputed. These sub-matrices can be factorized once and re-used in the entire simulation.

Figures A2.8 and A2.9 compare the computational performance of the GFEM^{gl} and *hp*-GFEM. The later is akin to state-of-the-art FEM. Figure A2.8 considers the case of a steady-state heat transfer problem subjected to up to three load cases. Figure A2.9 considers the case of a time-dependent heat transfer problem subjected to highly localized thermal gradients.

The GFEM^{gl} is also effective when applied to some classes of problems that do not involve localized phenomena. This can be achieved by exploring the natural parallelism of the computations in the GFEM^{gl}. The computation of enrichment functions can be performed in parallel using a single pair of scatter-gather communications in a parallel machine. Kim *et al.* (2011) demonstrate that this algorithm scales well even on shared memory machines as no communication among processors is involved.

A3 Integrated Fluid/Structure Interaction Simulation

Personnel: Geubelle, Bodony, Joumaa (Graduate student, UIUC) Sucheendran (Graduate student, UIUC), Kuester (AFRL), Halvorson (AFRL), Hollkamp (AFRL), Gordon (AFRL)

Start 2006; End: 2010

The primary goal of this project was to develop a coupled acoustic-structural solver. In order to achieve this the compressible, non-linear fluid solver, *RocfloCM*, was integrated into the *Rocstar* suite of numerical codes that was previously developed at UIUC under auspices of the DOE-funded Center for Simulation of Advanced Rockets (CSAR). The structural solver, *Rocfrac*, which was already integrated into *Rocstar*, has been optimized and has been verified using a 3D dynamical cantilever problem. Mass-proportional damping was also implemented in *Rocfrac* to simulate problems with structural damping. Communication between *RocfloCM* and *Rocfrac* is facilitated by the tools in *Rocstar*. New fluid boundary conditions using the simultaneous approximation term boundary condition were implemented in the fluid domain that makes the coupling numerically stable.

Various approaches were used to verify the code. Initially simpler 1D and 2D solutions were used to verify the code results. Results shown in Fig. A3.1 (left) for a 500 Hz, low amplitude acoustic wave impinging on a flat plate show a multi-frequency beating type of phenomenon in the center displacement of the plate. The solver was verified using the analytic solution for coupled response of a spring-mass system with a 1D fluid domain. Fig. A3.1 (right) shows the comparison of the variation of displacement of mass with time calculated using the Method of Characteristic (MOC) solution and using the 1D solver. Results have shown that the coupling algorithm in place is first-order accurate in time.

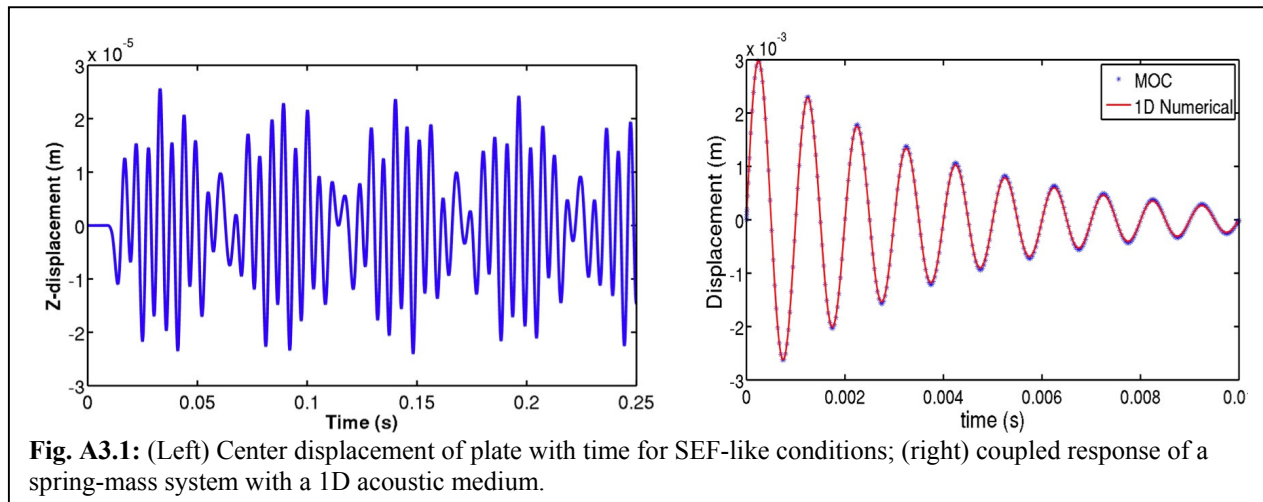
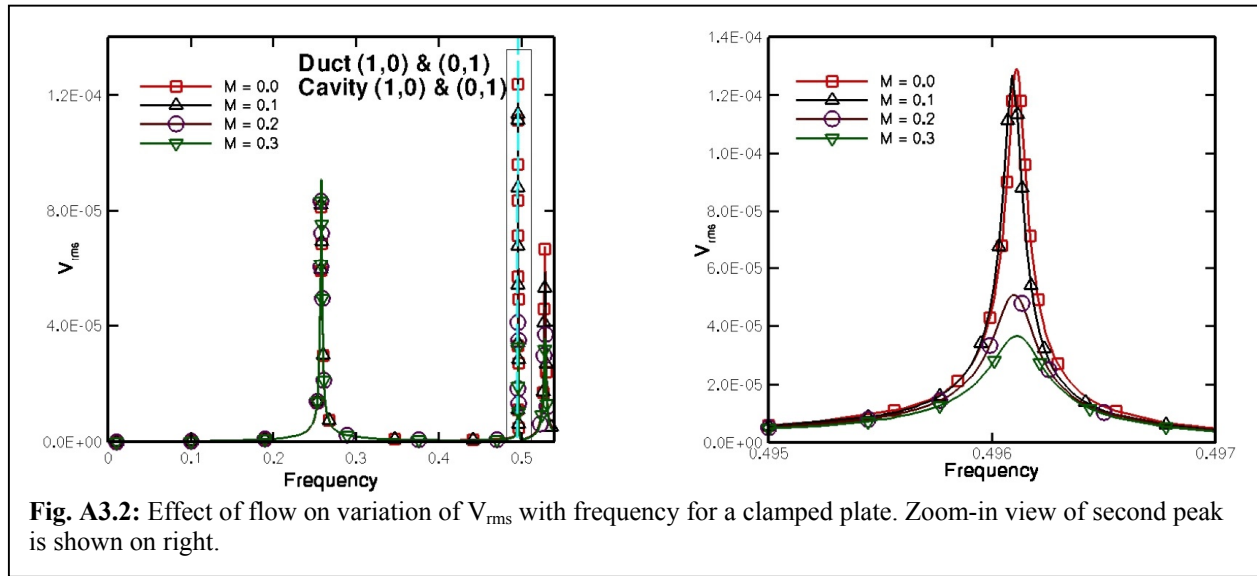


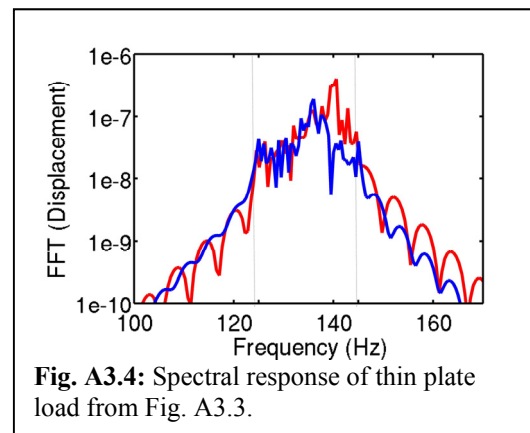
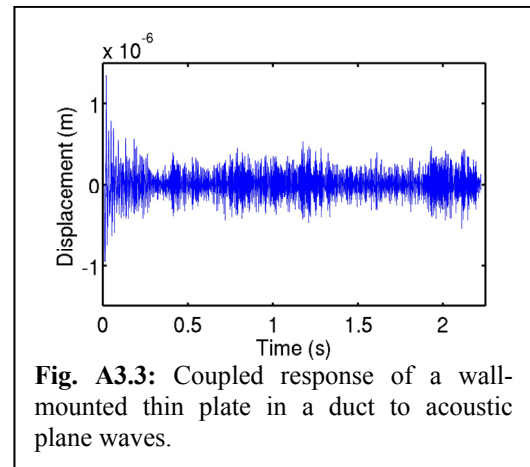
Fig. A3.1: (Left) Center displacement of plate with time for SEF-like conditions; (right) coupled response of a spring-mass system with a 1D acoustic medium.

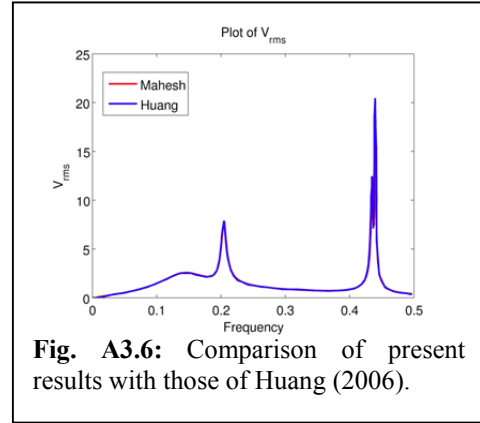
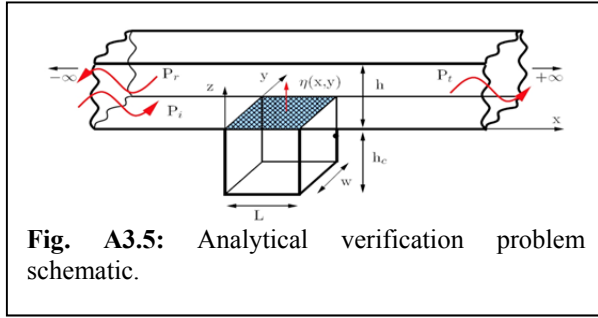
The analytical theory for the response of a simply-supported plate in a duct was extended to that for a clamped plate. The theory was also extended to account for the presence of uniform mean flow in the duct. Fig. A3.2 shows the effect of uniform mean flow on variation of integral average of plate velocity with the forcing frequency of the harmonic acoustic load in the duct. It was found that the presence of uniform mean flow in duct acts like a damper to the plate response.



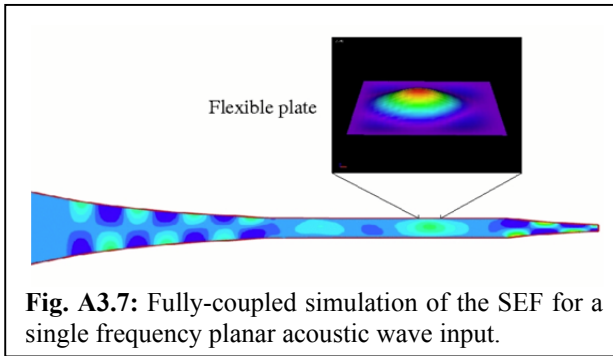
The individual fluid and solid solvers were verified with problems for which analytical results were available. The fully coupled, 3D, parallel numerical solver was verified using the coupled acoustic-structure response of a thin plate mounted in a duct predicted by the analytical theory using a broadband plane wave input spectrum centered around plate modes. For a thin, clamped Al plate mounted in a duct with SEF-like conditions, the plate response predicted using the numerical solver is shown in Fig. A3.3 for an input frequency range of 125-145 Hz at 100 dB amplitude. The spectral response of the plate is then compared with that predicted by the analytical theory, which is shown in Fig. A3.4. The two results match reasonably well. To capture the spectral response more accurately, the coupled code was made more efficient to capture longer time records. During this verification case the numerical coupled code was ported to a new parallel machine with significant performance improvement.

In addition, an analytical solution for a closely-related structural-acoustic interaction in an infinite uniform duct with a cavity-backed flexible rectangular plate was developed. Fig. A3.5 shows the geometry and other details of the problem. Fig. A3.6 shows the comparison of the plate velocity root-mean-square, V_{rms} , computed from the analytical solution and compared with existing results.



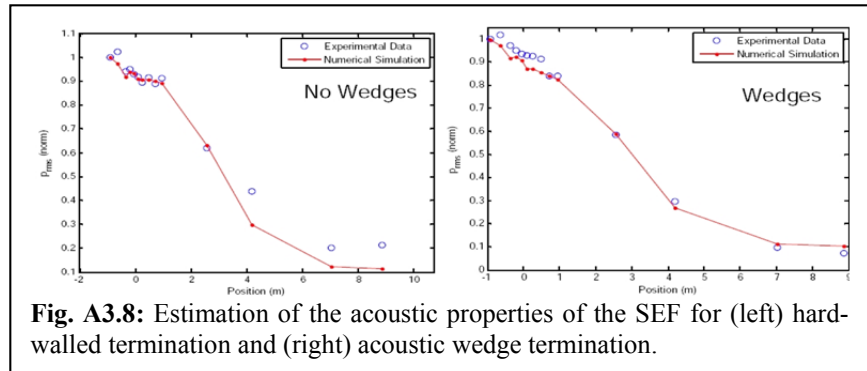


Using *RocfloCM* for solving the governing equations in the acoustic domain and using *Rocfrac* for the solution in the structural domain, a coupled structural-acoustic interaction simulation of the SEF was carried out. Fig. A3.7 shows the contour plot of the normal component of momentum in the fluid domain and vertical displacement of an aluminum plate. Due to the



disparate computational requirements in the fluid and solid domain, the capability of having separate processors for the fluid and solid domain was introduced. Since the computational requirements for solution in the fluid domain was much larger compared to the solid domain, the simulation used 64 processors in the fluid domain and 2 processors in the structural domain.

The acoustic characteristics of the facility were also investigated to provide boundary condition information of the numerical predictions of the SEF. By approximating the facility as a quasi-one-dimensional duct, a Matlab code was written that solves the 1D linearized Euler equations in the fluid domain inside the SEF with the area variation of the duct taken into account. Impedance boundary conditions and modeling the losses in the facility were implemented to replicate the experimental results. Fig. A3.8 shows the comparison of experimental data from the SEF with the Matlab code. Another quasi-one dimensional code was written to estimate the transfer function of the SEF in the spectral domain. The code takes into account the area-variation of SEF in discrete steps.



In the future, we plan to use the analytical theory to do more parametric study of the coupled acoustic-structure response of thin plates. Also we plan to use the numerical solver to study the effect of uniform mean flow in the duct on the coupled response of thin plates. The numerical solver can be used to study the nonlinear effects on the plate response. As the amplitude of acoustic loads is

increased, the nonlinearity in the fluid equations and the in-plane stresses in the plate become significant. These effects can be studied using the numerical solver.

A5 Multiphysics, Coupled Analysis of Extreme-Environment Structures

Personel: Bodony, Geubelle, Ostoich (Graduate student UIUC), Spottswood (AFRL)

Start: 2008, End: 2010

A.5.1 Introduction

High speed flight is accompanied by increasingly severe thermal and acoustic loads. A hypersonic vehicle will be partially wetted by a turbulent boundary layer that produces extreme pressure and thermal fluctuations over the majority of the outer skin. Furthermore, these vehicles require powerful propulsion systems that increase the severity of the loading in the engine inlet and exhaust regions. In order for such vehicles to be economically feasible, they must be lightweight, flexible, and reusable, shrinking the design margin envelope. The intersection of the extreme environment and stringent design requirements leads to situations where structural compliance and fluid-structure interaction become significant. Large thermoacoustic loads and unknown, interaction induced, loading scenarios significantly increase the danger of fatigue. Common assumptions (*e.g.*, structural rigidity, inviscid flow) used in design today are no longer valid in this regime. A new approach relying on few assumptions needs to be taken to understand the loading scenarios and design for flight in high speed environments.

Current state-of-the-art approaches in fluid-structure interaction exist both in numerical analysis and experiment. However, experimental approaches are limited in that there are few on-ground facilities equipped to simulate fluid-structure interaction at sufficiently extreme environmental conditions (National Research Council, 1998). Furthermore, flight testing is prohibitively expensive and, due to the probability of failure, a risky investment (DARPA, 2010, 2011). Numerical approaches are limited in their ability to predict realistic situations due to the associated computational requirements. Reduced-order models rely on possibly invalid assumptions but can generate data for large geometries over long time records. Full-order models are limited in both geometrical size and temporal length of the computation, but can provide detailed information about flow and structural response features which may be assumed negligible in the formulation of reduced-order approaches.

Few on-ground experiments focused on high speed fluid-structure interaction have been conducted. In the 1980's Glass and Hunt (1986, 1988) conducted a number of experiments in the NASA Langley 8-Foot High Temperature Tunnel (8' HTT) to study the effect of thermally bowed National Aerospace Plane (NASP) thermal protection system (TPS) panels. The studies investigated the thermal response of the structure and also the modification to the flow and associated loads due to the bowed geometry. While the structure was nominally rigid, it illuminated the effects of fluid-structural coupling in that the geometry was motivated by the phenomenon of thin TPS panels bowing due to temperature gradients introduced by aerothermal heating. Recently at the Air Force Research Laboratory (AFRL) Air Vehicles Directorate, flexible panels have been inserted in the Propulsion Directorate RC-19 supersonic wind tunnel. Innovative analysis techniques have been developed by Bebernis *et al.* (2011) to study the response of compliant panels under extreme loading conditions using high speed digital image correlation (DIC) and high speed pressure sensitive paint (PSP). Currently, the response of a flexible panel to Mach 2 oblique shock impingement is being investigated (Spottswood *et al.* 2012). Initial results have indicated the usefulness of the newly developed techniques and encourage their application to additional high-speed fluid-structural interaction experiments.

As compared to experiment, a larger variety of numerical studies of coupled problems in extreme environments have been conducted, highlighting the fact that simulating expected high speed flight conditions is much more feasible in computations than in experiments. While validating their high-fidelity fluid-thermal computational tool, Ostoich *et al.* (2012) studied numerically the 1986 experiment conducted by Glass and Hunt (1986). They found good agreement of heat flux between their direct numerical simulation and experimental results and also found additional significant features in the thermal response of the structure which would not be predicted by reduced-order models based on inviscid aerodynamics. Culler (2012) and Culler and McNamara (2011) developed a coupled framework which uses third-order piston theory (Lighthill, 1953) coupled with Eckert's Reference Enthalpy method Eckert (1956) to predict fluid aerodynamic pressure and thermal loads, and methods of varying fidelity for the thermal and structural solutions for thin panels. For their flight profile, they found the mutual interaction between structural deformation and aerodynamic heating to be significant, especially over increased time records (Culler and McNamara, 2011). While the assumptions inherent in the reduced-order formulation resulted in a loss of accuracy, it allowed the study of full flight trajectories. A high-order inviscid approach was taken by Visbal in a 2D study of the interaction of a Mach 2 oblique shock with a nonlinear von Karman plate (Visbal, 2012). He discovered that for sufficiently strong shocks self-excited oscillations arose in the coupled system. Crowell *et al.* (2011) studied the 2D fluid-thermal interaction of an oblique shock impinging on a flexible panel with prescribed surface motion under a turbulent boundary layer. The fluid solution used a finite-volume Reynolds Averaged Navier-Stokes (RANS) solver employing the Menter $k - \omega$ SST turbulence model. It was found that the panel motion significantly altered the thermal solution in the solid due to the oscillation of the heat flux spike under the shock turbulent boundary layer interaction (STBLI). However, it was noted that, due to the limitations of the RANS formulation, local shock unsteadiness associated with the STBLI could not be taken into account.

The approach taken in the current work is to use high-fidelity, high-accuracy methods to numerically investigate the aeroelastic response of a flexible panel under high speed turbulent boundary layers. To accomplish this we solve the 3D fully compressible Navier-Stokes equations, without turbulence model, and compute directly the traction loading on a compliant panel whose structural state is governed by the unsteady conservation of momentum equation. Results shed light on the consequences of fluid-structural interaction in high speed turbulent flows.

A.5.2 Computational Approach

Fluid Domain

Our fluid model describes the motion of a fully non-linear, compressible, viscous, calorically or thermally perfect gas. The Navier-Stokes equations describe conservation of mass, momentum, and total energy and are given as

$$\begin{aligned} \frac{\partial \rho}{\partial t} + \frac{\partial}{\partial x_i}(\rho u_i) &= 0, \\ \frac{\partial \rho u_i}{\partial t} + \frac{\partial}{\partial x_j}(\rho u_i u_j + p \delta_{ij} - \tau_{ij}) &= 0, \\ \frac{\partial \rho E}{\partial t} + \frac{\partial}{\partial x_j}[(\rho E + p) u_j + q_j - u_i \tau_{ij}] &= 0, \end{aligned} \tag{A.5-1}$$

where repeated indices are summed. We solve Eq. (A.5-1) on a non-uniform, non-orthogonal mesh defined by the smooth mappings

$$\mathbf{x} = \mathbf{X}(\boldsymbol{\xi}), \text{ with inverse } \boldsymbol{\xi} = \boldsymbol{\Xi}(\mathbf{x}),$$

where $\mathbf{X}^{-1} = \boldsymbol{\Xi}$ and Jacobian $J = |\partial \mathbf{X} / \partial \boldsymbol{\Xi}|$. It can be shown that Eq. (A.5-1) maps into an equivalent conservative form in the computational variables $\boldsymbol{\xi}$ (Vinokur, 1974).

Finite differences are used to approximate the spatial derivatives in the computational coordinates. We use the summation-by-parts operators (Strand, 1994; Mattsson *et al.*, 2004) which, when coupled to the simultaneous-approximation-term (SAT) boundary conditions (Carpenter *et al.*, 1994; Svård *et al.*, 2007; Svård and Nordström, 2008; Nordström *et al.*, 2009), yield a provably stable and accurate method (Bodony, 2010). The spatial approximation to $\partial / \partial \boldsymbol{\xi}$ is $\mathbf{P}^{-1} \mathbf{Q}$, where \mathbf{Q} has the property that $\mathbf{Q} + \mathbf{Q}^T = \text{diag}(-1, 0, \dots, 0, 1)$. For the SAT formulation, which is a penalization approach, a penalty term is added to the right-hand-side of the governing equations. Following the notation in Svård and Nordström (2008), the penalized equation is

$$\frac{\partial \mathbf{q}}{\partial t} = \mathcal{F}(\mathbf{q}) + \sigma^{I1} \mathbf{P}^{-1} \mathbf{E}_1 \mathbf{A}^+ (\mathbf{q} - \mathbf{g}^{I1}) + \frac{\sigma^{I2}}{Re} \mathbf{P}^{-1} \mathbf{E}_1 \mathbf{I} (\mathbf{q} - \mathbf{g}^{I2}), \quad (\text{A.5-2})$$

where σ^{I1} and σ^{I2} are the penalty parameters for the inviscid and viscous boundary conditions, respectively, and $\mathbf{E}_1 = (1, 0, \dots, 0)^T$. Here $\mathcal{F}(\mathbf{q})$ represents the divergence of the fluxes in the governing equations, \mathbf{A}^+ is a Roe matrix to be defined later, and \mathbf{I} is the identity matrix. It is known that $\sigma^{I1} \leq -2$ and

$$\sigma^{I2} \leq -\frac{1}{4P(1,1)} \max \left(\frac{\gamma \mu}{Pr \rho}, \frac{5\mu}{3\rho} \right), \quad (\text{A.5-3})$$

are required for numerical stability. In the current work, both σ^{I1} and σ^{I2} are set to -2 . The boundary data are contained in the vectors \mathbf{g}^{I1} and \mathbf{g}^{I2} . For inviscid flows one omits the second penalty term and defines the target vector by

$$\mathbf{g}^{I1} = \begin{bmatrix} \rho \\ \rho(\mathbf{u} - [(\mathbf{u} \cdot \mathbf{n}) - (\mathbf{u}_w \cdot \mathbf{n})]\mathbf{n}) \\ \rho e + \frac{1}{2}\rho|\mathbf{u} - [(\mathbf{u} \cdot \mathbf{n}) - (\mathbf{u}_w \cdot \mathbf{n})]\mathbf{n}|^2 \end{bmatrix}. \quad (\text{A.5-4})$$

The matrix $\mathbf{A}^+ = \chi \mathbf{\Lambda}^+ \chi^{-1}$ selects only the incoming characteristic variables $\mathbf{R} = \chi \mathbf{q}$, where χ transforms the conserved variables \mathbf{q} to characteristic variables \mathbf{R} . For a calorically perfect gas χ is given by Pulliam and Chaussee (1981), however, for a thermally perfect gas χ is found numerically. In both cases, χ is evaluated using the Roe average of \mathbf{q} and \mathbf{g}^{I1} . $\mathbf{\Lambda}^+ = \mathbf{\Lambda} - |\mathbf{\Lambda}|$ is a diagonal matrix containing the elements $\mathbf{\Lambda} = \text{diag}\{\hat{U}, \hat{U}, \hat{U} + c, \hat{U} - c\} |\nabla \mathbf{x} \boldsymbol{\xi}|$ where \hat{U} is the component of the velocity in the wall normal direction $\mathbf{n} = \nabla \mathbf{x} \boldsymbol{\xi} / |\nabla \mathbf{x} \boldsymbol{\xi}|$. For the viscous penalty term, the target data are

$$\mathbf{g}^{I2} = [\rho, \rho \mathbf{u}_w, \rho e(T_w) + \frac{1}{2}\rho|\mathbf{u}_w|^2]^T, \quad (\text{A.5-5})$$

which applies a no-slip, isothermal condition for a moving wall with velocity $u_w(\mathbf{x}, t)$ and with temperature $T_w(\mathbf{x}, t)$.

The temporal advancement of Eq. (A.5-1) is accomplished using an explicit 4-stage Runge Kutta method which is $O(\Delta t^4)$ accurate. The fluids code has been used in a variety of fluid-only problems involving both laminar and turbulent flows (Bodony, 2009; Sucheendran *et al.*, 2009; Zagaris *et al.*, 2010; Kim *et al.*, 2010; Bodony *et al.*, 2010; Crisfield, 1997), and a coupled fluid-thermal problem for which experimental data was available for comparison (Glass and Hunt, 1986; Ostoich *et al.*, 2012).

Solid domain

In the solid domain, the structural state is found at each point in time using a geometrically non-linear finite strain finite element solver. Conservation of linear momentum gives the strong form in the current configuration, B,

$$\nabla \cdot \boldsymbol{\sigma} + \rho \mathbf{b} = \rho \ddot{\mathbf{u}}, \quad (\text{A.5-6})$$

where $\boldsymbol{\sigma}$ is the Cauchy stress tensor, \mathbf{b} is a field of body forces, ρ is the density, and $\ddot{\mathbf{u}}$ is the acceleration. If a virtual displacement $\delta \mathbf{u}$ is applied, and Eq. (A.5-6) is integrated over the body in the current configuration, the weak form of the principal of virtual work is given. Application of the divergence theorem,

$$\int_v \nabla \cdot (\cdot) dv = \int_{\partial v} (\cdot) \cdot \hat{\mathbf{n}} da$$

gives,

$$\delta W = \int_B \boldsymbol{\sigma} : \nabla \delta \mathbf{u} dv + \int_B \rho \ddot{\mathbf{u}} \cdot \delta \mathbf{u} dv - \int_{\partial B} \mathbf{t} \cdot \delta \mathbf{u} da - \int_B \rho \mathbf{b} \cdot \delta \mathbf{u} dv = 0 \quad (\text{A.5-7})$$

where $\mathbf{t} = \boldsymbol{\sigma} \cdot \hat{\mathbf{n}}$. In this work, the problem is solved in the reference configuration, B_0 . The resulting equation after being pulled back into the reference configuration, B_0 , is

$$\delta W = \int_{B_0} \bar{\beta}^2(\Theta) \hat{\mathbf{P}} : \delta \mathbf{F} dV + \int_{B_0} \rho_0 \ddot{\mathbf{u}} \cdot \delta \mathbf{u} dV - \int_{\partial B_0} \mathbf{t}_0 \cdot \delta \mathbf{u} dA - \int_{B_0} \mathbf{b}_0 \cdot \delta \mathbf{u} dV = 0, \quad (\text{A.5-8})$$

where the subscript ()₀ denotes a quantity in the reference configuration corresponding to the unsubscripted quantity in the current configuration, and $\hat{\mathbf{P}}$ is the first Piola-Kirchhoff stress tensor. The code is coupled with a thermal solver, and the thermoelastic first Piola-Kirchhoff stress tensor is the product $\bar{\beta}^2(\Theta) \hat{\mathbf{P}}$, where $\bar{\beta}^2(\Theta)$ is the linear stretch ratio due to thermal expansion/contraction. In the current work, we do not consider the thermal state of the solid, so $\bar{\beta}^2(\Theta) = 1$. In a non-linear problem, if a body with current configuration \mathbf{x} does not satisfy $\delta W(\mathbf{x}) = 0$, then a linear correction is made, *i.e.*, δW is linearized at \mathbf{x} and multiplied by a correction \mathbf{u} to achieve $\delta W(\mathbf{x} + \mathbf{u}) = 0$

$$\delta W(\mathbf{x} + \mathbf{u}) = 0 \approx L[\delta W] = \delta W(\mathbf{x}) + D\delta W(\mathbf{x})[\mathbf{u}] = 0 \quad (\text{A.5-9})$$

where $D\delta W(\mathbf{x})[\mathbf{u}]$ is the directional derivative of $W(\mathbf{x})$ along \mathbf{u} . The terms involved in the linearization are the internal stress and traction terms

$$L[\delta W] = \delta W(\mathbf{x}) + D\delta W_{int}(\mathbf{x})[\mathbf{u}] - D\delta W_{ext}(\mathbf{x})[\mathbf{u}] = 0.$$

The linearized equation is given as

$$\begin{aligned} L[\delta W(\mathbf{x})] = & \int_{B_0} \bar{\beta}^2(\Theta) \hat{\mathbf{P}} : \delta \mathbf{F} dV + \int_{B_0} \rho_0 \ddot{\mathbf{u}} \cdot \delta \mathbf{u} dV \\ & - \int_{\partial B_0} \mathbf{t}_0 \cdot \delta \mathbf{u} dA - \int_{B_0} \mathbf{b}_0 \cdot \delta \mathbf{u} dV \\ & - \int_{\partial B_0} \delta \mathbf{u} \cdot \mathcal{B} : \nabla_{\mathbf{x}} \mathbf{u} dA + \int_{B_0} \bar{\beta}^2(\Theta) \delta \mathbf{F} : \mathcal{A} : \nabla_{\mathbf{x}} \mathbf{u} dV = 0, \end{aligned} \quad (\text{A.5-10})$$

where the elasticity tensor, $\mathcal{A} = \partial \hat{\mathbf{P}} / \partial \mathbf{F}$, and external load Jacobian, $\mathcal{B} = \partial \hat{\mathbf{t}} / \partial \mathbf{F}$. The corrected configuration $\mathbf{x}_{old} + \mathbf{u}$ is found by solving for \mathbf{u} and iterating until $\delta W(\mathbf{x}) = 0$. In order to use the finite element method to find the solution to Eq. (A.5-10) to obtain \mathbf{x} , the linearized equation must be discretized. Displacement, velocity, and acceleration are stored at 20 nodal locations per element. Values are interpolated using quadratic shape functions. After discretizing Eq. (A.5-10), multiplying through by $\delta \mathbf{u}^{-T}$ results in

$$\mathbf{M} \ddot{\mathbf{u}} + \mathbf{K} \Delta \mathbf{u} = \mathbf{R}^{ext} - \mathbf{R}^{int}, \quad (\text{A.5-11})$$

where \mathbf{R}_{int} and \mathbf{R}_{ext} are the internal and external load vectors, \mathbf{K} and \mathbf{M} are the tangent stiffness and consistent mass matrices, \mathbf{u} and $\ddot{\mathbf{u}}$ are the nodal displacement and acceleration vectors, and $\Delta \mathbf{u}$ is the linear correction to \mathbf{u} at each iteration.

Temporal advancement of Eq. (A.5-6) is accomplished using the Newmark method, a predictor-corrector scheme, used as outlined in Crisfield (1997), where the coefficients are chosen to use trapezoidal rule approximations which give an unconditionally stable scheme with $O(\Delta t^2)$ accuracy.

Fluid-solid interface treatment

The individual solvers are weakly coupled at the interface where the fluid-structural interaction takes place. The fluid and structural solutions are found independently in their respective domains at a given time step $t_n = n\Delta t$. The spatial coupling is achieved through matching nodes at the interface. At each node, the fluid solution passes the fluid stress tensor, $\boldsymbol{\tau}$, to the solid, and the solid passes updated surface coordinates, \mathbf{x} , and velocity, $\dot{\mathbf{x}}$. The full fluid stress tensor, $\boldsymbol{\tau}$, is passed rather than the traction vector, \mathbf{t} , so that the updated fluid load on the structure during the Newton-Raphson iterations can be calculated without further communication between the fluid-solid interface. In the current problem, we are simulating the interaction of a fluid over a flexible panel. The pressure difference across the panel is set to zero by subtracting the mean thermodynamic pressure from the fluid stress tensor, $\boldsymbol{\tau}$, before it is communicated to the solid. To efficiently advance the coupled system while minding the stability and accuracy

requirements of the solvers, different time step sizes are taken in the fluid and structural solution stages.

A.5.3 Temporal Direct Numerical Simulation of a Turbulent Boundary Layer

Turbulent boundary layer generation

For the simulation of a turbulent boundary layer over a compliant panel, an initial condition (IC) must be chosen such that turbulence will be achieved. To accomplish this, several methods have been used in the past such as using a periodic blowing/suction strip to create instabilities (Pirozzoli *et al.*, 2004; Pirozzoli and Grasso, 2006) and using a synthetic boundary layer prescribed at the inflow (Sandham *et al.*, 2003). The approach chosen in this work is to find the unstable eigenmodes to the linear stability equations for a compressible boundary layer (Malik, 1990). The unstable disturbances will amplify until some saturation point, and then begin to break down into smaller scales, distributing the energy across a spectrum of scales and evolving into a turbulent state.

The boundary layer growth in the streamwise direction is small, and is neglected in the current work. With this assumption, the solution is homogeneous in the streamwise and spanwise directions and those directions are treated as periodic resulting in a temporal direct numerical simulation (TDNS). The advantage of this is that a reduced length domain can be used, therefore reducing the computational cost. In linear stability theory (LST) the flow is decomposed into a mean base flow plus fluctuations about that mean,

$$\phi(x, y, z, t) = \bar{\phi}(x, y, z) + \hat{\phi}(x, y, z, t),$$

where $\phi = [u, v, p, T, w]^T$. Note that due to the parallel flow assumption the base flow is $\bar{\phi}(x, y, z) = \bar{\phi}(y) = [\bar{u}, 0, \bar{p}, \bar{T}, 0]$. Solutions to the linear stability equations are perturbations of the form

$$\hat{\phi}(x, y, z, t) = \phi'(y) \exp[i(\alpha x + \beta z - \omega t)].$$

In a TDNS, we are interested in the temporal stability of the boundary layer, and solve for complex eigenvalues, $\omega = \omega_r + i\omega_i$, and eigenfunctions, $\phi'(y)$, given real streamwise and

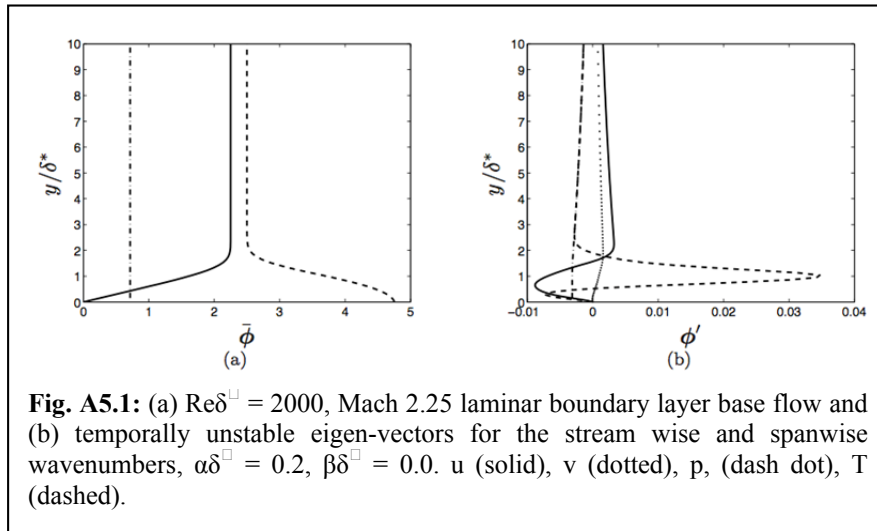


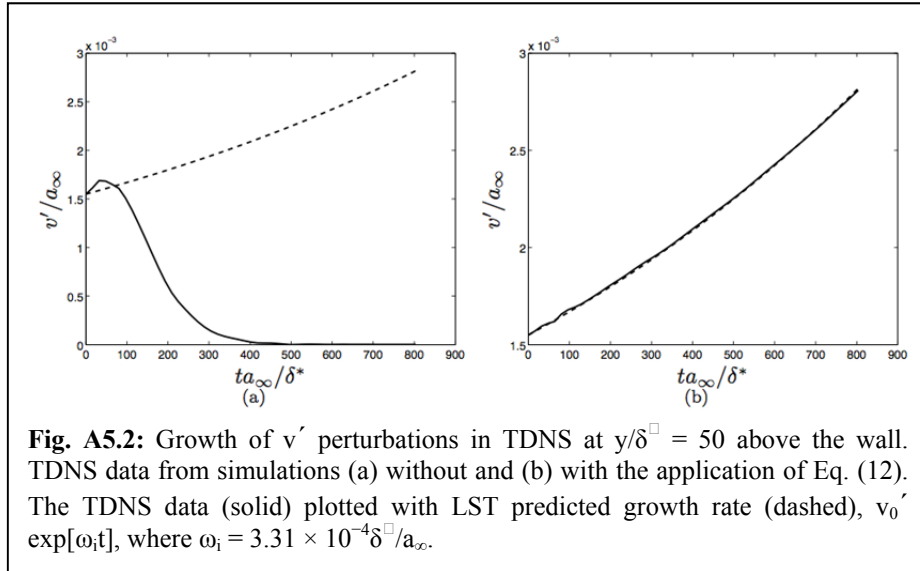
Fig. A5.1: (a) $\text{Re}\delta^* = 2000$, Mach 2.25 laminar boundary layer base flow and (b) temporally unstable eigen-vectors for the stream wise and spanwise wavenumbers, $\alpha\delta^* = 0.2$, $\beta\delta^* = 0.0$. u (solid), v (dotted), p , (dash dot), T (dashed).

spanwise wavenumbers, α and β . The unstable eigenvectors, when superposed onto the laminar boundary layer base flow, grow in time at the predicted rate, ω_i . An example $\text{Re}\delta^* = 2000$, Mach 2.25 mean profile and corresponding 2D unstable perturbations are shown in Fig. A5.1. One additional difficulty that exists with this approach is that, as noted above,

the base flow is assumed to be parallel. This base flow, however, does not satisfy the Navier-Stokes equations. When an initial condition containing a parallel base flow is introduced to a TDNS, there is an adjustment, the severity of which increases with Mach number. A consequence of the adjustment is a change in the boundary layer profile, which thickens in time. The eigenfunctions found using LST, based on the initial base flow, can no longer be expected to grow at the predicted rate. Furthermore, they oftentimes become stable with respect to the new mean profile and fail to produce the desired transition to turbulence. In this work, we suppress the growth of the boundary layer by suppressing the vertical diffusion of streamwise momentum and internal energy (Adams and Kleiser, 1996). This is accomplished by adding the forcing terms,

$$\mathbf{S} = \begin{pmatrix} 0 \\ -\frac{\partial}{\partial y} \bar{\mu} \frac{\partial \bar{u}}{\partial y} \\ 0 \\ 0 \\ -\frac{\partial}{\partial y} \bar{u} \bar{\mu} \frac{\partial \bar{u}}{\partial y} - \frac{\partial}{\partial y} \bar{k} \frac{\partial \bar{T}}{\partial y} \end{pmatrix}, \quad (\text{A.5-12})$$

to the right hand side of Eq. (A.5-1). In Eq. (A.5-12), the mean flow values are taken from the initial mean flow. Fig. A5.2 shows the amplification of the 2D perturbations to a $\text{Re}\delta^+ = 2000$ with and without the forcing terms (Eq. (A.5-12)). In the case where Eq. (A.5-12) is not applied to Eq. (A.5-1), the adjustment results in a mean flow on which the perturbations are stable and

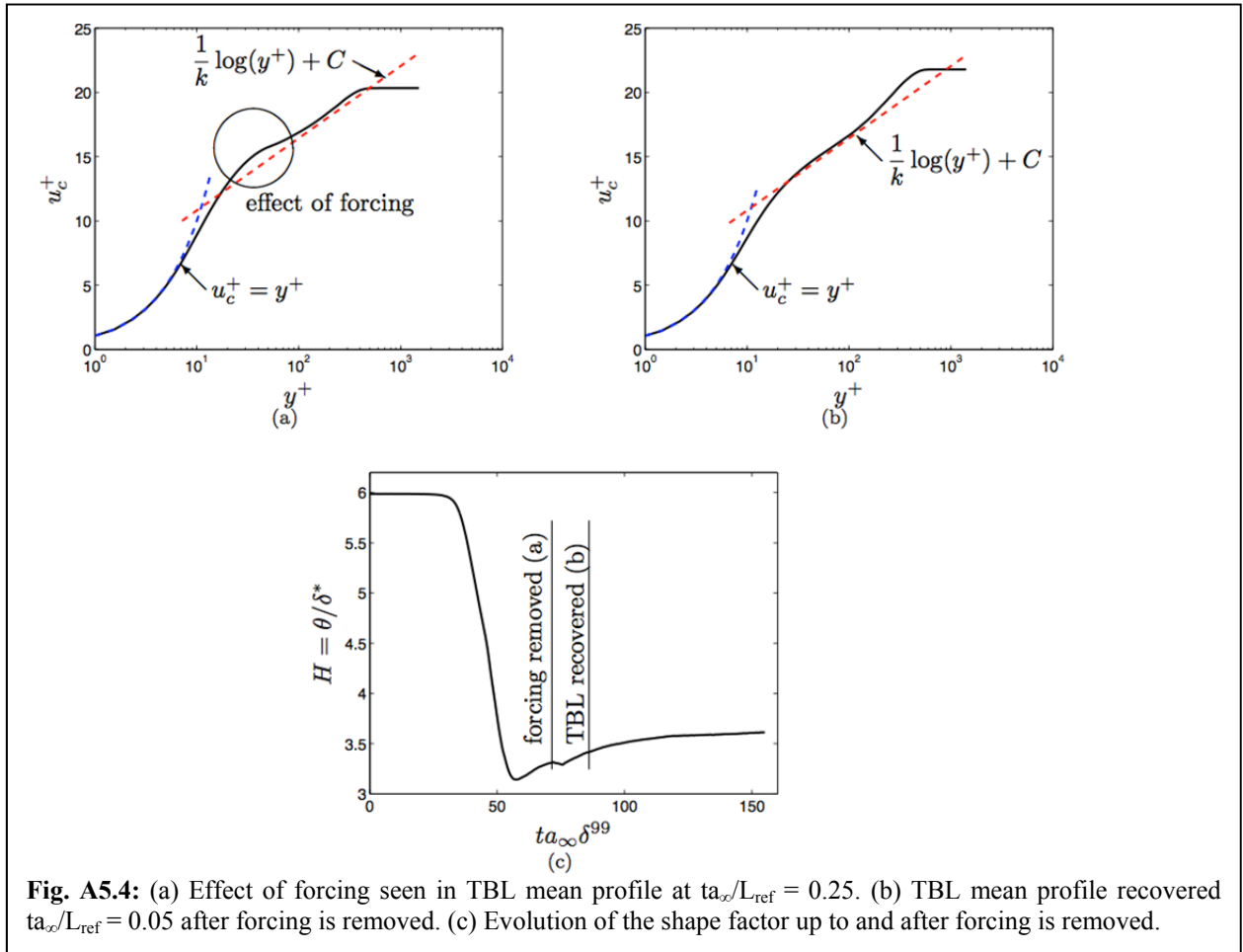
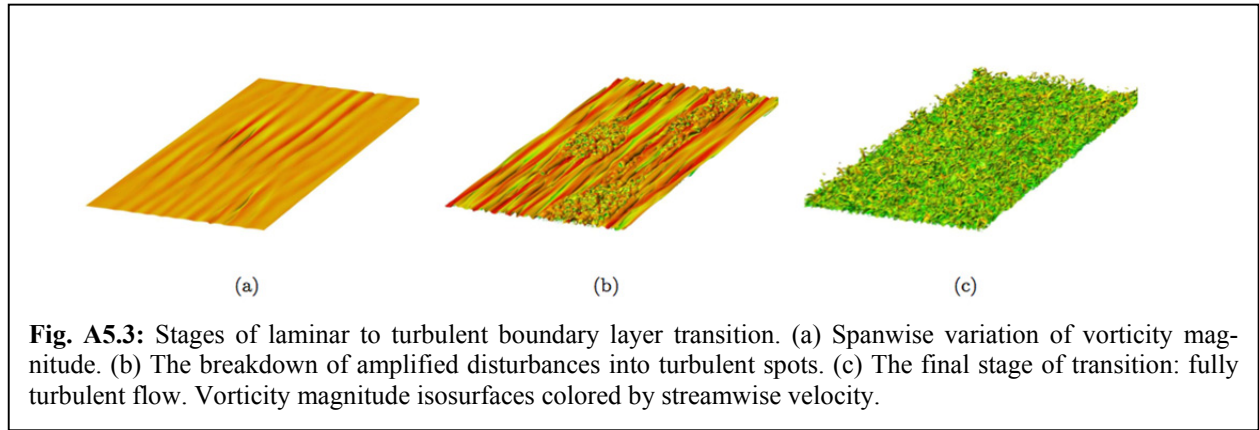


are seen to decay to zero within 500 non-dimensional time units. When forcing terms are applied, the perturbations grow at the predicted rate.

The transition to turbulence from the seeded laminar flow is composed of several stages. The 3D boundary layer, initially very similar to a 2D flow, begins to develop noticeable

spanwise variations, as can be seen in Fig. A5.3(a). After a period of amplification, the disturbances waves break down into smaller spatial and temporal scales, forming turbulent spots (Fig. A5.3(b)). The initially sporadic spots of turbulence continue to spread and eventually coalesce, finally resulting in a fully turbulent boundary layer flow (Fig. A5.3(c)). The forcing terms (Eq. (A.5-12)), while preserving the boundary layer mean flow prior to transition, leave a noticeable effect on the turbulent boundary layer after transition. In order to obtain the expected turbulent boundary layer statistics, the forcing is removed after transition is complete. The

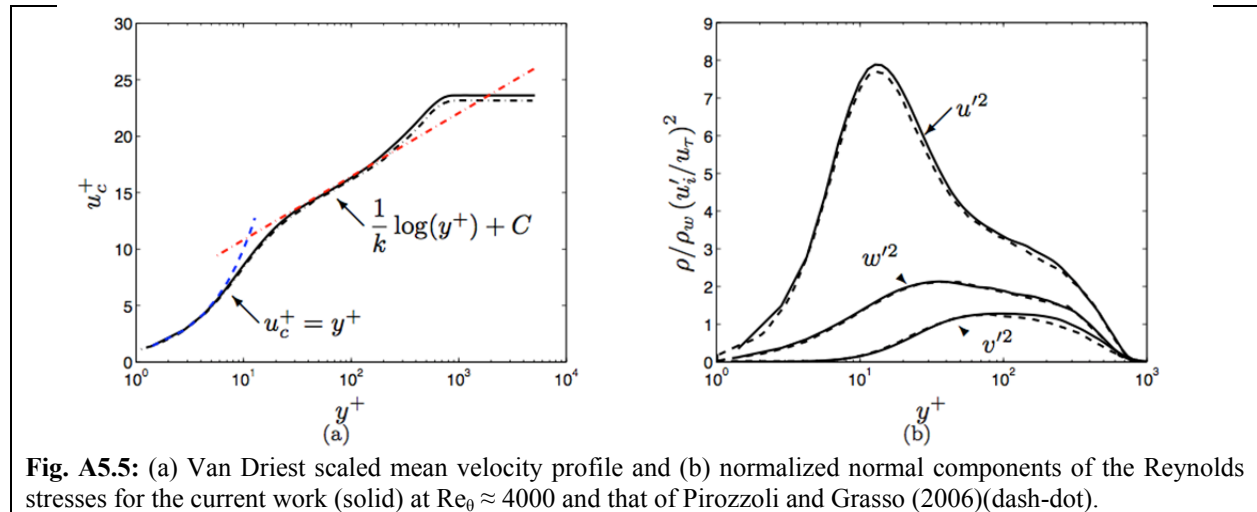
plateau of the shape factor, $H = \theta/\delta^+$, is taken to indicate the end of the transition period (Fig. A5.4(c)). The forcing is then removed and the boundary layer relaxes to its expected profile, as shown in Fig. A5.4(a) and (b), which occurs over $ta_\infty/\delta^{99} = 12$.

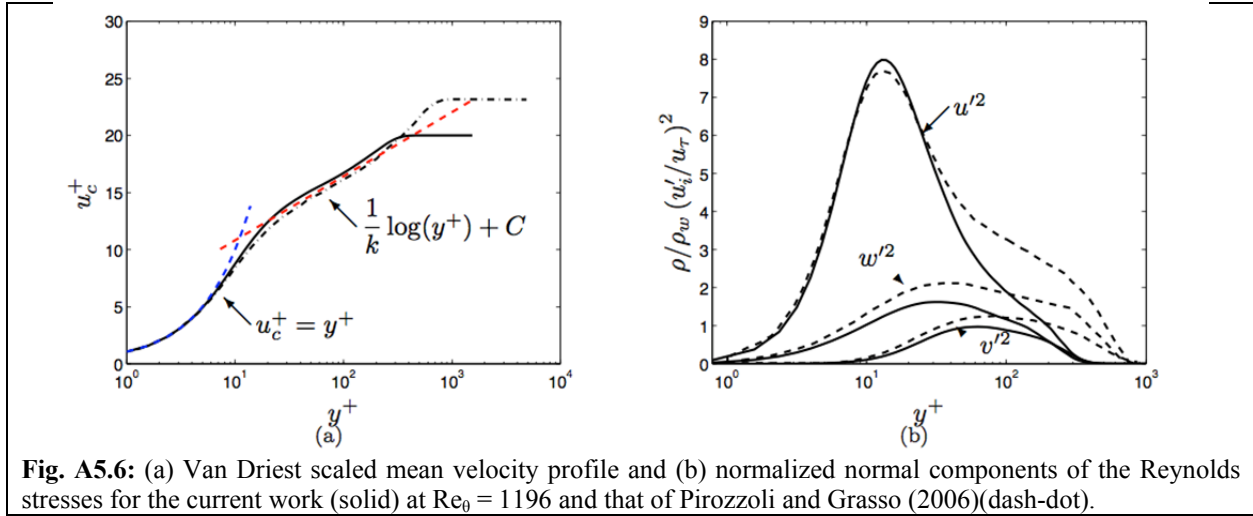


Simulation Conditions

As the computational cost associated with the DNS of a turbulent boundary layer can be staggering (proportional to Re (DARPA, 2011; Pope, 2000)), the Re of the flow in the coupled simulation is chosen to be relatively low in order to balance the costs between the three solve stages involved in the multiphysics simulation. The boundary layer has a Reynolds number based on momentum thickness of $Re_\theta = 1196$. A second turbulent boundary layer simulation at a higher Reynolds number, $Re_\theta \approx 4000$ was also run for the purpose of verification by comparison with previous work. Simulation conditions were chosen to be similar to a reference solution from Pirozzoli and Grasso (2006). One main difference exists between the current work and that of Pirozzoli and Grasso (2006): their work featured a spatially developing turbulent boundary layer, which requires a domain with a large streamwise extent, and is therefore generally more costly. As mentioned above, the current work uses a TDNS approach to model the fluid solution. This assumes periodicity in the streamwise direction, and results in a boundary layer thickness that increases in time and not space.

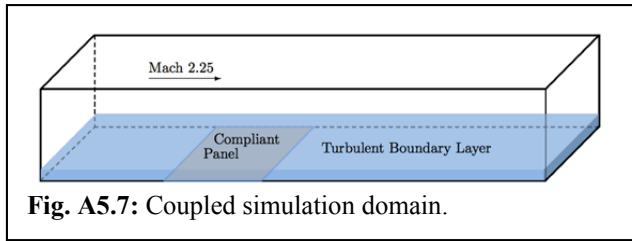
The quantities compared were mean profile and normal Reynolds stresses. As can be seen in Fig. A5.5(a), the Van Driest transformed mean velocity profile satisfies $u_c^+ = y^+$ in the viscous sublayer, and obeys the log-law, $1/k \log(y^+) + C$, in the log-law region, where $k = 0.41$ and $C = 5.20$. The comparison with the reference solution is also in agreement. Shown in Fig. A5.5(b) are the normalized, normal components of the Reynolds stresses, which are also in agreement with the reference solution. Also shown are comparisons between the reference solution and the lower Reynolds number solution planned for the coupled simulation. Figure A5.6(a) shows that the Van Driest scaled mean velocity profile still follows the same trends, obeying $u_c^+ = y^+$ and the log-law in the viscous subregion and log-law region, respectively. The effect of the lower Reynolds number produces a log-law region with shorter extent and a less pronounced wake at the boundary layer edge. The comparison between the normalized, normal components of the Reynolds stresses (Fig. A5.6(b)) shows that the peaks of the respective quantities occur in the same wall normal locations and that the profiles are similar from the wall into the buffer layer ($y^+ < 30$). Differences exist in the outer layer.





A.5.4 Coupled Simulation Results

The $0.14 \text{ m} \times 0.0127 \text{ m} \times 0.0254 \text{ m}$ fluid domain was set to the initial condition for the lower Reynolds number turbulent boundary layer. The $y = 0 \text{ m}$ boundary of the fluid domain was set to an isothermal, 322 K, no-slip boundary condition, except where a structurally compliant panel existed. The $15 \text{ }\mu\text{m}$ thick, steel compliant panel extended from $x = 0.0147 \text{ m}$ to $x = 0.0657 \text{ m}$ and across the entire span of the fluid domain. The panel was clamped on all sides, and was given a fixed temperature of 322 K. The orientation of the fluid domain and panel are shown in Fig. A5.7.



Panel deformations are shown at three different instances in time in Figs. A5.8(a)-(c). Shown in Fig. A5.8(a) is the panel state at a time early in the simulation, $t = 0.79 \text{ ms}$. The panel deflections are made up of higher mode bending waves which travel down the panel in the streamwise direction. The maximum panel deflections into and out of the boundary layer at this time are $w_{\text{up}} = 0.136 \text{ mm}$ and $w_{\text{down}} = 0.102 \text{ mm}$, respectively. An x - t diagram of the panel deformations is shown in Fig. A5.9(a). The slopes of the deformation contours, which are further from zero at earlier times, correspond to the phase velocities of the panel bending waves. The peak which exists at the downstream extent of the panel in Fig. A5.8(a) is seen in Fig. A5.9(a) to grow and accelerate as it progresses down the panel. This acceleration is the result of the non-linear stiffening of the panel as the deformation grows. At later times, Fig. A5.8(b) and Fig. A5.8(c) show that the panel deformations are characterized by larger amplitude, low spatial mode standing waves. At $t = 1.60 \text{ ms}$ the maximum panel deflections into and out of the boundary layer are $w_{\text{up}} = 0.080 \text{ mm}$ and $w_{\text{down}} = 0.239 \text{ mm}$, respectively. At $t = 1.90 \text{ ms}$ the maximum panel deflections into and out of the boundary layer are $w_{\text{up}} = 0.240 \text{ mm}$ and $w_{\text{down}} = 0.048 \text{ mm}$, respectively. The stationary nature of these waves is evidenced by the almost zero slope of the associated deflection contours shown in Fig. A5.9(a) at $t = 1.60 \text{ ms}$ and $t = 1.90 \text{ ms}$. The temporal evolution of the modal content of the panel solution is shown in Fig. A5.9(b). At

earlier times, such as $t = 0.79$ ms, there exist a variety of low and high modes with similar amplitudes. However, it is seen that at later times the lower modes (mostly (2,1)) dominate.

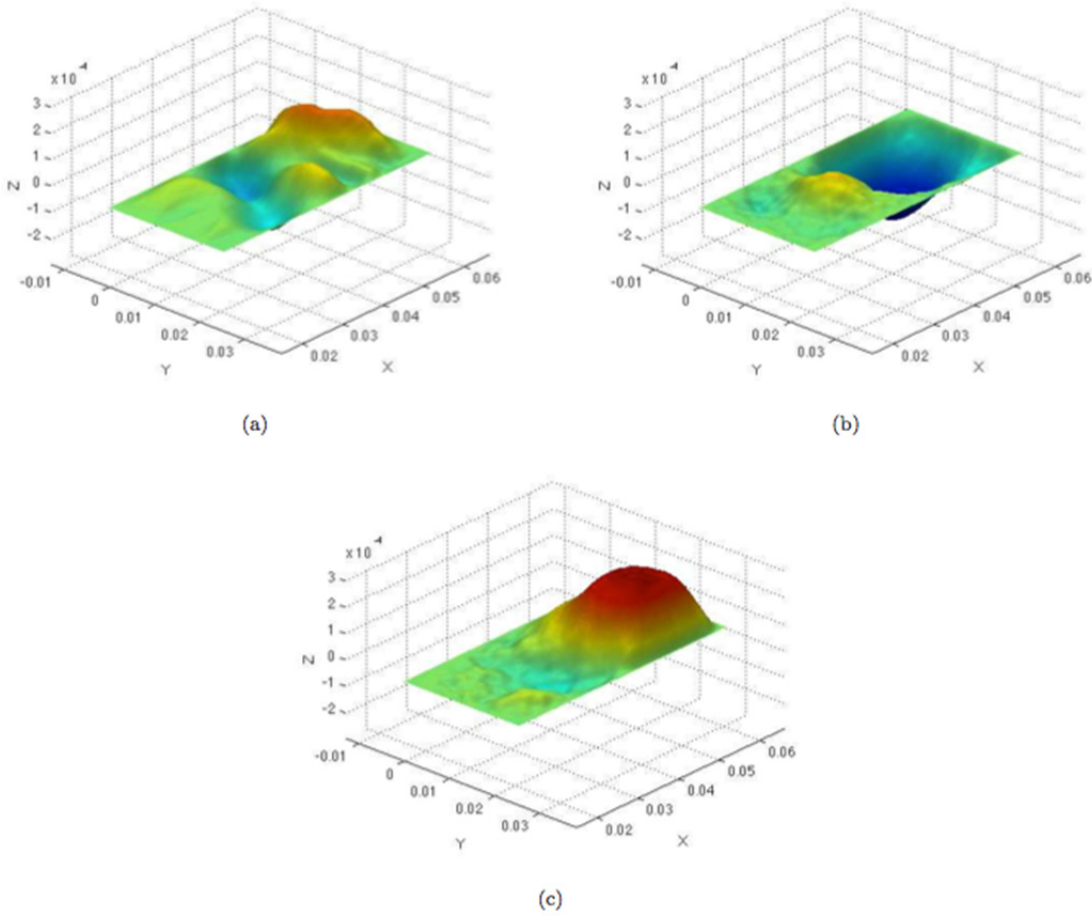


Fig. A5.8: Panel deformation at (a) $t = 0.79$ ms , (b) $t = 1.60$ ms , and (c) , $t = 1.90$ ms. Red and blue indicate deflection into and out of the boundary layer, respectively. Units are in meters.

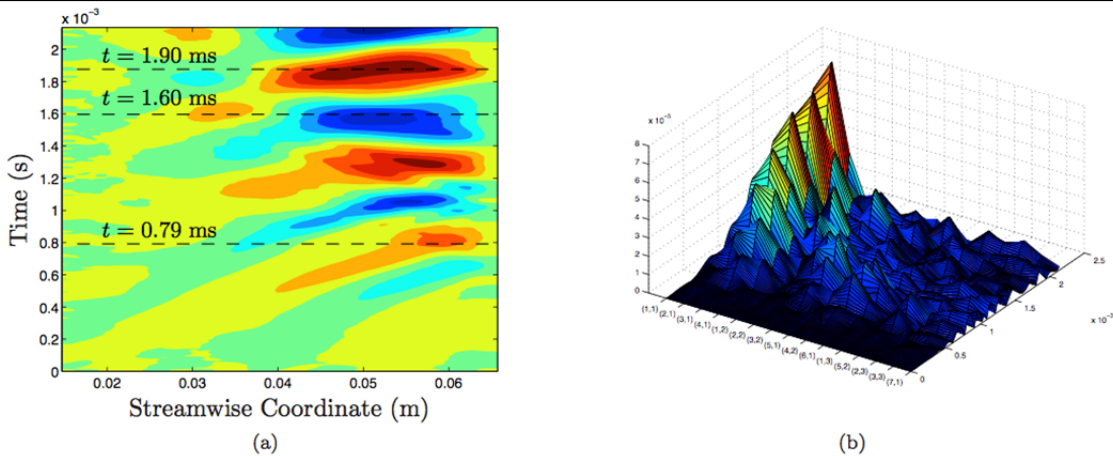


Fig. A5.9: (a) x-t diagram of panel deflections along the centerline of the panel ($z = .0127$ m). The times $t = 0.79$ ms, $t = 1.60$ ms , and $t = 1.90$ ms corresponding to Figs. A5.7(a)-(c) are marked with dashed lines. (b) Evolution of the first 15 spatial modes of the bending waves in the panel solution.

The maximum deformations over time both into and out of the flow are plotted in Fig. A5.10(a) and Fig. A5.10(b), respectively. Panel deformations approach 20 times the panel thickness, putting them well into the non-linear regime. The panel deforms 3% though the thickness of the boundary layer. At $t = 1.60$ ms and $t = 1.90$ ms the panel deflection out of and into the boundary layer are around $k^+ = 25$, where $k^+ = w/\delta v$ and δv is the viscous length. Deflections into the boundary layer extend through the viscous subregion and into the buffer region.

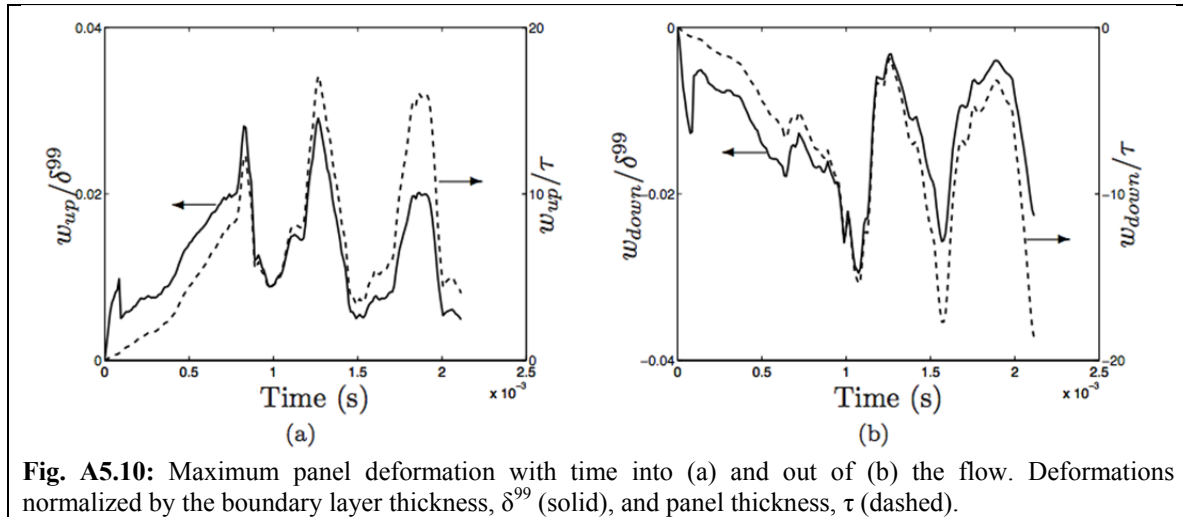
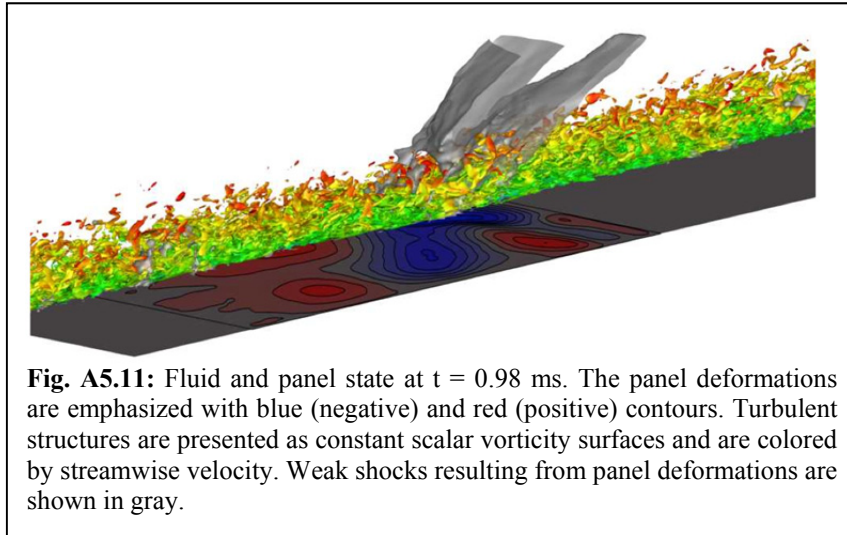
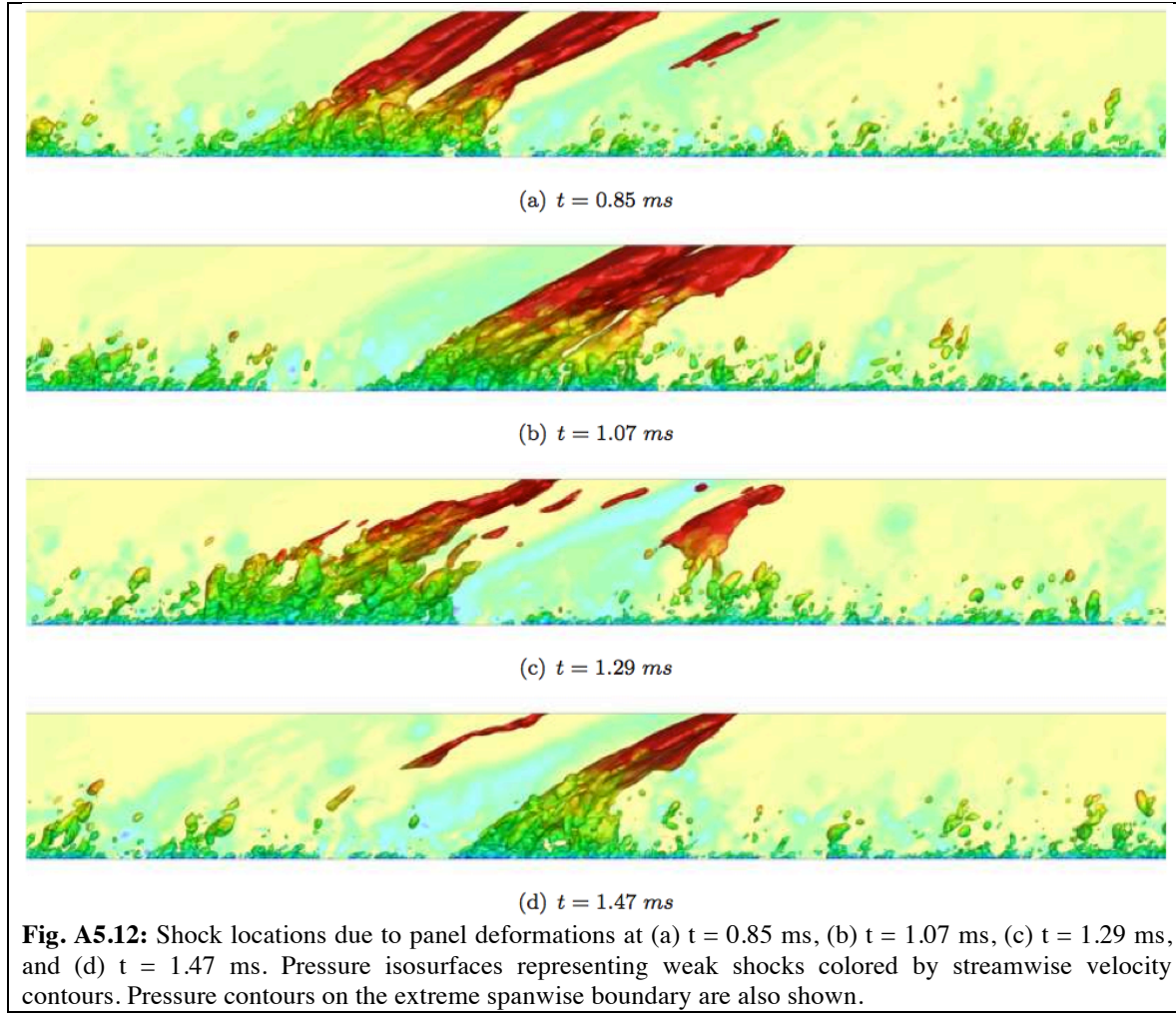


Figure A5.11 shows the coupled solution at $t = 0.98$ ms. Constant vorticity magnitude surfaces exhibit the turbulent structures present in the boundary layer and constant pressure surfaces representing weak oblique shocks are shown in gray. The panel is outlined and deformations are shown. The deformations are shallow and are emphasized with blue and red contours to indicate negative and positive deflections, respectively. The effect of the turbulent boundary layer on the panel is obvious, as shown in Figs. A5.7-A5.9, above. Figure A5.11 shows the relationship between the fluid and panel states, and is evidence that the panel



has a significant effect on the flow solution. As shown in Fig. A5.12, the bending waves propagating through the panel cause shocks to oscillate back and forth, a potential cause for concern in internal flow applications where the shocks could cause unsteady loading on an opposite wall.



Temporal averages of the wall normal flow were taken over 0.1 ms centered around $t = 1.56 \text{ ms}$ (panel down position in Fig. A5.10(b)) and $t = 1.86 \text{ ms}$ (panel up position in Fig. A5.10(a)) to investigate the effect of the panel deformations on relevant turbulence statistics. In order to ensure the independence of the samples, the sample frequency was chosen so that they were spaced by the integral timescale, δt , given by

$$\delta t = \int_0^{0.1\text{ms}} \frac{\langle u(t)u(t+s) \rangle}{\langle u(t)u(t) \rangle} ds.$$

The Reynolds shear stresses, $\langle u'v' \rangle$, were compared over the same time intervals between the compliant and rigid panel (fluid only) simulations to determine the effect that the compliant panel state had on the shear stress. The Reynolds shear stress profiles above the panel from the time interval surrounding $t = 1.56 \text{ ms}$ (panel down position) are compared in Fig. A5.13. When compared to the rigid panel case, $-\langle u'v' \rangle$ is reduced in the log-law region. The Reynolds shear stress profiles above the panel from the time interval surrounding $t = 1.86 \text{ ms}$ (panel up position) are compared in Fig. A5.14. As compared to the rigid panel case, there appears to be a deficiency

in $-\langle u'v' \rangle$ towards the boundary layer edge surrounded by large spikes. Values taken by $-\langle u'v' \rangle$ in all cases differ from previous work (De Graaff and Eaton, 2000), which may be due to the non-trivial task of taking flow statistics of over a moving surface.

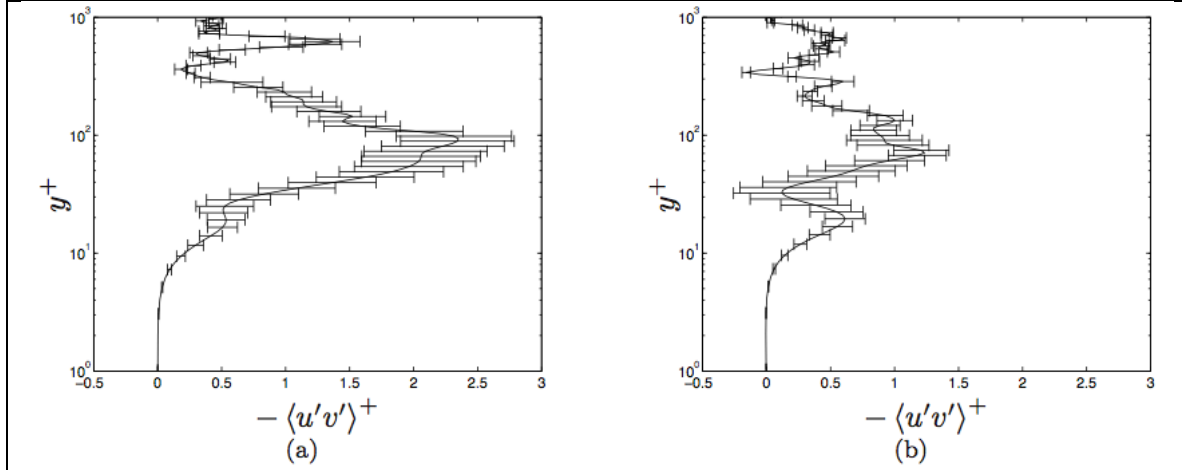


Fig. A5.13: Reynolds shear stress profile above (a) rigid and (b) compliant panel for $t = 1.56 \pm 0.05$ ms corresponding to the time when the panel is deflected out of the boundary layer. Error bars represent 95% confidence intervals.

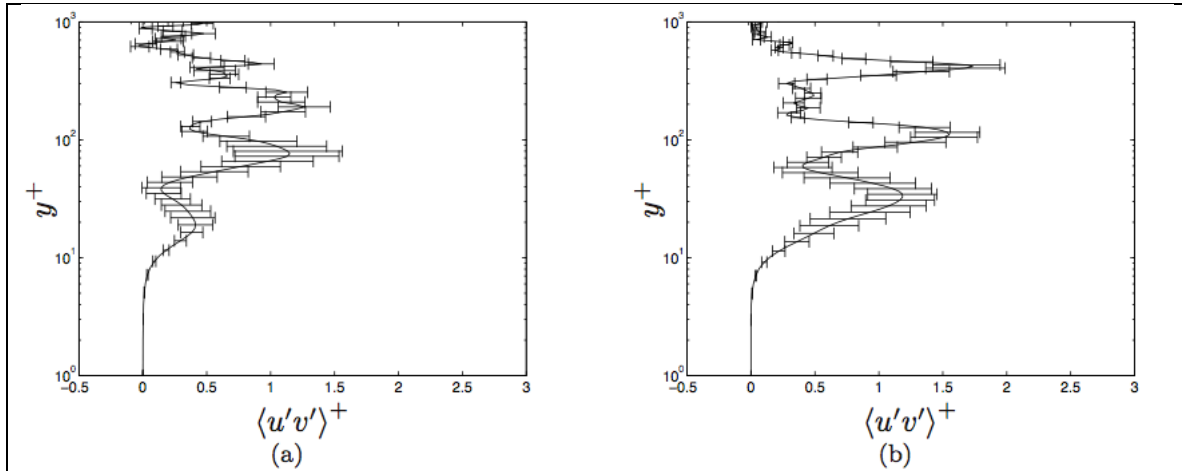


Fig. A5.14: Reynolds shear stress profile above (a) rigid and (b) compliant panel for $t = 1.86 \pm 0.05$ ms corresponding to the time when the panel is deflected out of the boundary layer. Error bars represent 95% confidence intervals.

The effect on the turbulence downstream of the panel is examined by averaging over the post-panel domain and comparing the turbulent kinetic energy (TKE, $k = 1/2 \overline{u'^2 + v'^2}$) budget computed in that region. The compressible TKE equation is given by

$$\bar{\rho} \frac{\partial k}{\partial t} + \bar{\rho} \tilde{u}_j \frac{\partial k}{\partial x_j} = P + D + T_{u'} + T_{p'} + \Pi - \rho \epsilon - ST_1 - ST_2, \quad (\text{A.5.13})$$

where

$$\begin{aligned}
P &= -\overline{\rho u''_i u''_j} \frac{\partial \tilde{u}}{\partial x_j}, & (\text{Production}) \\
D &= \frac{\partial}{\partial x_j} \overline{\tau'_{ij} u''_i}, & (\text{Viscous Diffusion}) \\
T_{u'} &= -\frac{1}{2} \frac{\partial}{\partial x_j} \overline{\rho u''_j u''_i u''_i}, & (\text{Turbulent Transport}) \\
T_{p'} &= -\frac{\partial}{\partial x_j} \overline{p' u''_j}, & (\text{Pressure Diffusion}) \\
\Pi &= \overline{p' \frac{\partial u''_j}{\partial x_j}}, & (\text{Pressure Dilatation}) \\
\rho \epsilon &= -\overline{\tau'_{ij} \frac{\partial u''_j}{\partial x_j}}, & (\text{Viscous Dissipation}) \\
ST_1 &= -\overline{u''_j} \frac{\partial \bar{p}}{\partial x_j}, & (\text{Pressure Work}) \\
ST_2 &= \overline{u''_j} \frac{\partial \bar{\tau}_{ij}}{\partial x_j} / & (\text{Additional Compressibility Term})
\end{aligned}$$

where the tilde denotes a Favre average and the double prime represents fluctuations about that average. The TKE budget (at the same time as the mean and Reynolds stress in Fig. A5.6(a) and Fig. A5.6(b)) is shown in Fig. A5.15(a). For the comparison, TKE budget terms were averaged over one panel cycle over a period shown in Fig. A5.15(b). Differences in all terms between the rigid and compliant panel cases are small. A detailed look at the comparison is shown in Fig. A5.16 between the production term temporal means, P , and the viscous dissipation term temporal means, $\rho \epsilon$, with error bars representing \pm one standard deviation. The results indicate that there is no statistical difference in either P or $\rho \epsilon$ between the rigid and compliant panel cases in the post-panel region. A similar conclusion for the other terms (not shown) is made. This result suggests that there may be local effects on the turbulence statistics (Fig. A5.13 and Fig. A5.14), however, the effects are short lived and are not seen downstream of the panel.

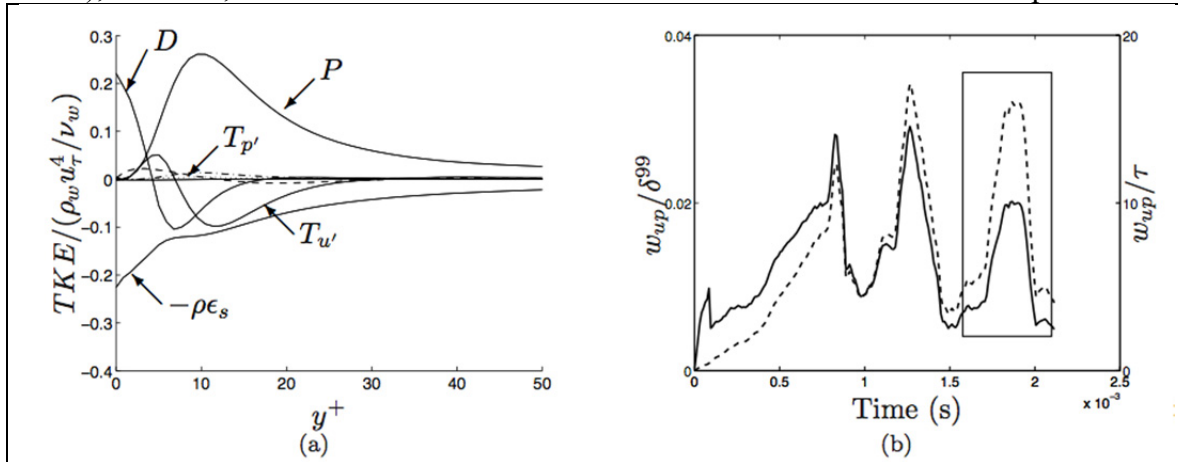
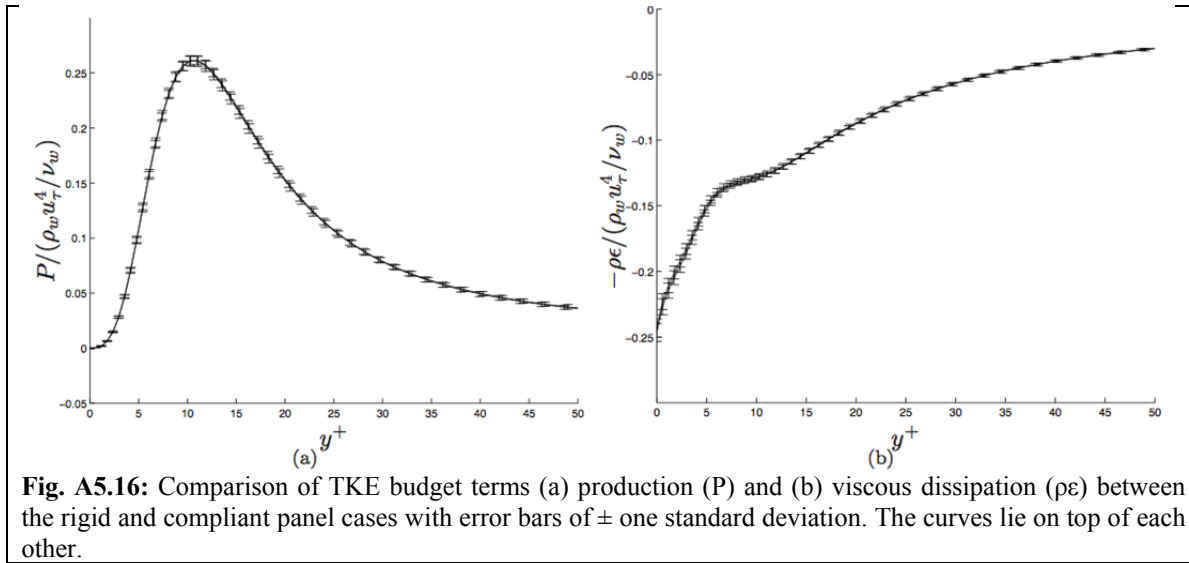
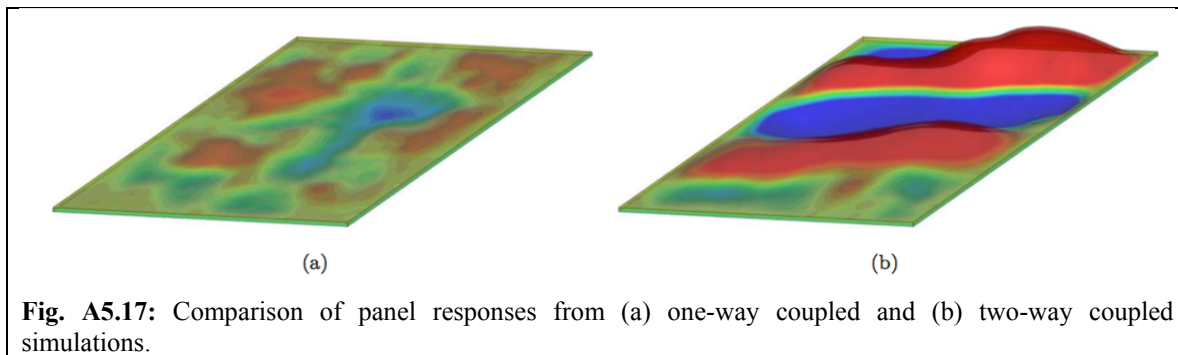


Fig. A5.15: (a) TKE budget terms of the $Re_0 = 1196$ TBL. (b) Time period over which the TKE budget is averaged for comparison of post-panel statistics between the rigid and compliant panel cases.



The level of fluid-structural coupling is varied in order to study the significance of full coupling in the panel response. Two coupled simulations with similar parameters as the one above were run from the same initial condition. The simulations differ in that one of them uses the same two-way coupling as used in the above simulations while the other only employs one-way coupling. One way coupling is defined here as passing fluid loads to the structure while not communicating the structural solution to the fluid. Figure A5.17(a) and (b) show the one-way and two-way coupled panel solutions, respectively, at the same point in time. There is a striking qualitative difference in the panel response between the two solutions which suggests that the fluid response to the panel geometry has a significant effect on the panel response. Quantitatively, the panel states are also very different. The one-way coupled panel has max. in/out deflections of $18.8\mu\text{m}/-23.1\mu\text{m}$ while the two-way panel deflections are almost an order of magnitude greater with max. in/out deflections of $150.2\mu\text{m}/-97.5\mu\text{m}$. It is hypothesized that while the turbulent fluctuations cause moderate panel deformations, the aerodynamic pressure on the deformed geometry significantly alters and amplifies the panel response.



A.5.5 Computational Cost

The fluid-thermal interaction simulations utilizing the Glass and Hunt geometry contained two solvers, one for the fluid and one for the thermal solution within solid, and two corresponding domains. The fluid grid used between 20 and 60 million grid points, with five unknowns per point. The solid grid contained approximately 667,000 nodes, with one unknown per node. Each solver was parallel. The computational cost to run the 5 s validation run used 384 processors over a period of roughly one week, yielding 64,500 core hours. The 50 s run took only 100,000 core hours as the needed resources-per-timestep dropped as the panel heated up at progressively slower rates.

The fluid-structural dynamic interaction simulations of the Mach 2 turbulent boundary layer over a thin steel panel required significantly more resources because the simulation time-step was controlled by the fluid turbulence and, since this was a direct numerical simulation where no reduced order modeling was done, all timescales must be resolved. Again two solvers were used, the same fluid solver as in the Glass and Hunt case and a new finite deformation thermomechanical solver, both fully parallel. The fluid grid contained 24 million grid points (five degrees of freedom per point) and the solid grid with 30,000 quadratic (20 node brick) finite elements (three degrees of freedom per point). Seven different runs were conducted to varying lengths of simulated time; for the longest run, 512 cores were used for roughly three continuous weeks for 258,000 core hours. In aggregate we used approximately 2 million core hours for the production runs plus all of the development and debugging.

A.5.6 Summary

A high-accuracy, high-fidelity methodology for the simulation of coupled fluid-structural problems has been developed for the purpose of predicting the structural response of a panel on an aerospace vehicle in extreme conditions. Few assumptions are made about the physical properties or solution geometry in order to achieve accurate predictions in situations where simplified approaches may be invalid and experiment may be extremely difficult. The formulation of the coupled solver was presented. Details about the method for generation of the turbulent boundary layer in a temporal direct numerical simulation were discussed and it was shown that, in high speed flows, the growth of the mean flow needs to be suppressed in order for linear stability theory to hold. Results have shown that panel deformations, in the form of traveling bending waves, amplify when they interact with the clamped panel boundaries. At later times, the deformations exhibit a standing wave behavior which is dominated by the (2,1) panel mode. The deformation approached 20 panel thicknesses, and extended into the boundary layer a distance of 25 wall units. Changes in surface topology led to the generation of oscillating shocks, which may cause localized unsteady loads on an opposing wall in internal flow applications. Turbulence statistics show that the Reynolds shear stress profiles were modified due to panel compliance. The effect on the turbulence of the interaction with the panel cannot be seen in the downstream turbulent kinetic energy budget, suggesting that panel deformations only locally alter TBL statistics. A large difference is seen in panel responses between one-way and two-way coupling showing that the aerodynamic pressures on the deformed panel significantly alter the panel response.

A6 Non-Intrusive Implementation of Multiscale Capabilities in a General Purpose FEA Platform

Personnel: Duarte, Pereira (Graduate student, UIUC), Plews (Graduate student, UIUC), Eason (AFRL)

Start: 2008, End: 2010

Details provided in relevant report already submitted.

A7 Multiscale Thermo/Strain Field Coupling

Personel: Duarte, Plews (Graduate student, UIUC), Eason (AFRL)

Start: 2009; End: 2010

A.7.1 Non-Intrusive Implementation of GFEM^{gl} ReAnalysis Algorithm for Heat Transfer in ABAQUS

The same so-called ReAnalysis algorithm discussed in Section A.2.3 of Project A2 was extended to a non-intrusive implementation in a commercial FEA code, ABAQUS. An analogous implementation was carried out simultaneously for elasticity problems. The formulation follows: the GFEM solution of the enriched global problem, u^E , can be partitioned as

$$u^E = \tilde{u}^0 + u^{gl} = \begin{bmatrix} \mathbf{N}^0 & \mathbf{N}^{gl} \end{bmatrix} \begin{bmatrix} \tilde{\mathbf{u}}^0 \\ \mathbf{u}^{gl} \end{bmatrix}, \quad (\text{A.7-1})$$

where \mathbf{N}^0 has standard FEM shape functions and \mathbf{N}^{gl} has the global-local shape functions defined previously. $\tilde{\mathbf{u}}^0$ and \mathbf{u}^{gl} have global and global-local enrichment degrees of freedom, respectively. Then, the gradient of the temperature field is defined as

$$\nabla u^E = \begin{bmatrix} \mathbf{B}^0 & \mathbf{B}^{gl} \end{bmatrix} \begin{bmatrix} \tilde{\mathbf{u}}^0 \\ \mathbf{u}^{gl} \end{bmatrix}. \quad (\text{A.7-2})$$

The resulting finite element system of equations in the enriched global problem, $\mathbf{K}\mathbf{u}^E = \mathbf{f}$ may then also be partitioned as

$$\begin{bmatrix} \mathbf{K}^0 & \mathbf{K}^{0,gl} \\ \mathbf{K}^{gl,0} & \mathbf{K}^{gl} \end{bmatrix} \begin{bmatrix} \tilde{\mathbf{u}}^0 \\ \mathbf{u}^{gl} \end{bmatrix} = \begin{bmatrix} \mathbf{f}^0 \\ \mathbf{f}^{gl} \end{bmatrix}, \quad (\text{A.7-3})$$

where

$$\mathbf{K}^0 := \int_{\Omega_G} (\mathbf{B}^0)^T \kappa \mathbf{B}^0 d\Omega$$

is computed by ABAQUS, and

$$\mathbf{K}^{0,gl} := \int_{\Omega_L} (\mathbf{B}^0)^T \kappa \mathbf{B}^{gl} d\Omega$$

$$\mathbf{K}^{gl} := \int_{\Omega_L} (\mathbf{B}^{gl})^T \kappa \mathbf{B}^{gl} d\Omega$$

are computed in a capable GFEM code. The solution to System (A.7-3) can then be found by static condensation on \mathbf{u}^{gl} , since, in general, $\dim(\tilde{\mathbf{u}}^0) \gg \dim(\mathbf{u}^{gl})$. From the first equation in System (A.7-3),

$$\begin{aligned} \tilde{\mathbf{u}}^0 &= (\mathbf{K}^0)^{-1} \mathbf{f}^0 - (\mathbf{K}^0)^{-1} \mathbf{K}^{0,gl} \mathbf{u}^{gl} \\ &= \mathbf{u}^0 - \mathbf{S}^{0,gl} \mathbf{u}^{gl}, \end{aligned} \quad (\text{A.7-4})$$

where $\mathbf{K}^{0,gl}$ are known as “pseudo-loads,”

$$\mathbf{S}^{0,gl} := (\mathbf{K}^0)^{-1} \mathbf{K}^{0,gl}$$

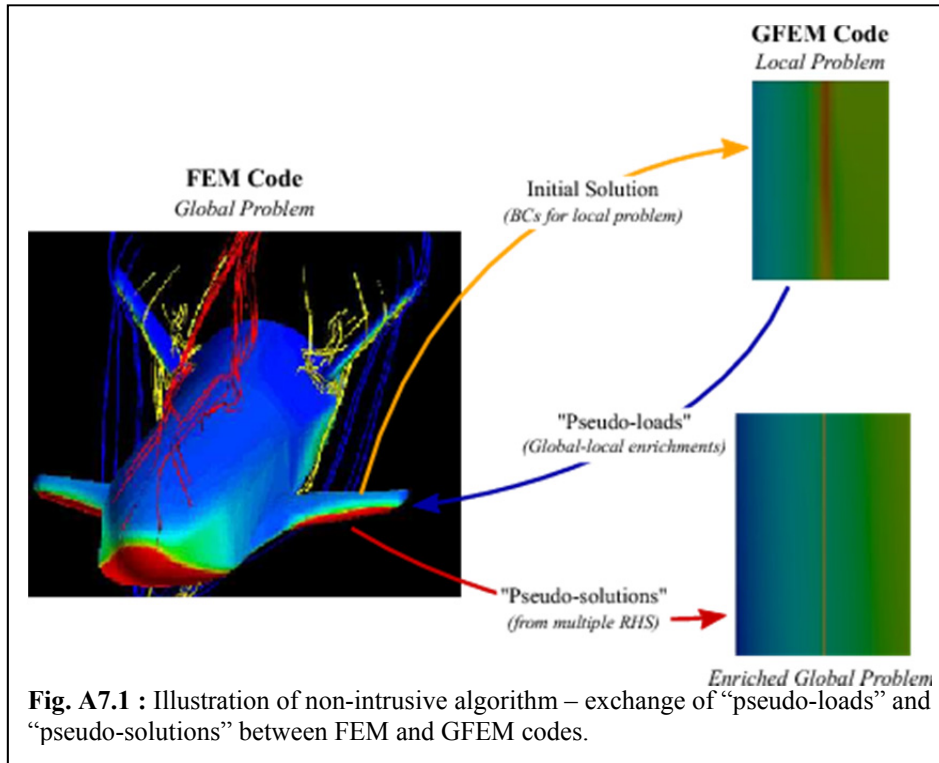
are known as “pseudo-solutions” corresponding to the pseudo-loads, and

$$\mathbf{u}^0 = (\mathbf{K}^0)^{-1} \mathbf{f}^0$$

is the initial, coarse-scale solution. Both $\mathbf{S}^{0,gl}$ and $\underline{\mathbf{u}}^0$ may be computed by ABAQUS using forward and backward substitution on a factorization of the coarse-scale global stiffness matrix, \mathbf{K}^0 . Because \mathbf{K}^0 does not change between initial global and enriched global problems, the factorization of \mathbf{K}^0 may also, if possible, be stored in ABAQUS after the initial global problem step and reused in the enriched global problem in order to reduce computational cost as well as solution time*. Substituting Equation (A.7-4) in the second equation in System (A.7-3) and rearranging,

$$\underbrace{(\mathbf{K}^{gl} - \mathbf{K}^{gl,0} \mathbf{S}^{0,gl})}_{\hat{\mathbf{K}}^{gl}} \underline{\mathbf{u}}^{gl} = \underbrace{\mathbf{f}^{gl} - \mathbf{K}^{gl,0} \underline{\mathbf{u}}^0}_{\hat{\mathbf{f}}^{gl}}, \quad (\text{A.7-5})$$

so the solution corresponding to global-local degrees of freedom comes directly from the



solution of

$$\hat{\mathbf{K}}^{gl} \underline{\mathbf{u}}^{gl} = \hat{\mathbf{f}}^{gl},$$

where $\hat{\mathbf{K}}^{gl}$ can be interpreted as the Schur complement of \mathbf{K}^0 .

Thus, the static condensation algorithm requires only the exchange of pseudo-loads and pseudo-solutions between ABAQUS and a GFEM code, making this approach extensible to almost any FEA software package. The algorithm described here is also illustrated

graphically in Fig. A7.1.

Special Treatment of Rough Loads

Standard FEM solvers cannot typically handle sharp heat fluxes applied on meshes designed to capture only the coarse-scale component of the solution, such as those of interest to the Air Force. Furthermore, application of such sharp loadings on coarse meshes may cause error in the finite element solution to propagate even far from the localized feature (so-called “error pollution,” as discussed in O’Hara (2010)). Thus, an improved strategy for handling sharp loadings within the non-intrusive framework is given.

The global load vector, \mathbf{f}^0 above, is decomposed as

$$\mathbf{f}^0 = \mathbf{f}_R^0 + \mathbf{f}_S^0,$$

* ABAQUS has limitations on reuse of the factorized global matrix. Thus, the factorization must be computed multiple times per analysis. This limitation has also been addressed in the literature.

where \mathbf{f}_R^0 is the “rough,” sharp, localized portion of the load, and \mathbf{f}_S^0 is the remaining “smooth” portion. Although ABAQUS is able to compute \mathbf{f}_S^0 without difficulty, the additional sharp load \mathbf{f}_R^0 must be numerically integrated in a GFEM code, using the local problem elements for accurate integration. In typical FEA software, a framework for applying the load of interest on a coarse mesh may not even exist. Applying *only* the smooth loading, \mathbf{f}_S^0 , in the initial global problem not only gives a satisfactory estimate of the solution to develop local problem boundary conditions but also eliminates aforesaid error pollution effects.

The recomputed full global load vector is passed during the enriched global step to ABAQUS alongside the pseudo-loads. This “improved” global analysis supersedes the solution obtained from the coarse-scale, initial global step and is used as the global solution in the static condensation algorithm for the enriched global solution. Rebuilding the global load vector serves to provide a more accurate estimate of $\underline{\mathbf{u}}^0$, which is critical to obtaining optimal convergence in the enriched global solution.

Adoption of a Quadratic Tetrahedron Partition of Unity

In the GFEM, it is common practice to choose a linear partition of unity and enrich it with higher-order polynomials to improve solution fidelity. Similarly, in the state-of-the-art *hp*-version of the finite element method, arbitrarily high-order shape functions may be hierarchically added to elements in a FE mesh.

However, in many 3D commercial FEA codes, only quadratic finite elements with Lagrangian shape functions are available*. Thus, the partition of unity used in the GFEM^{gl} global problem must accommodate the ten-noded quadratic tetrahedral element. In GFEM^{gl} *local* problems, however, ten-noded quadratic elements may be directly converted to equivalent linear tetrahedral elements for *hp*-adaptivity. Some examples of the improvement in enriched global solutions and convergence results thanks to the use of a quadratic global approximation in a standard FE solver will be shown later.

Verification of the Method

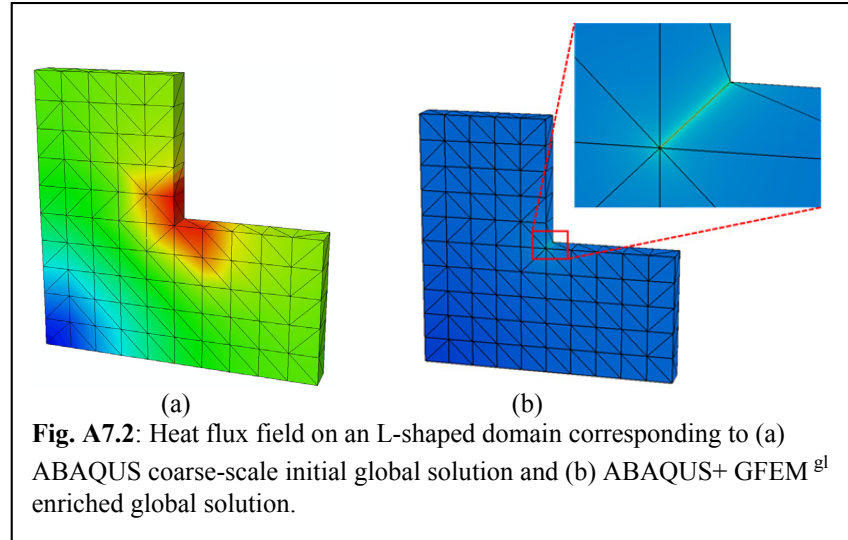
The non-intrusive GFEM^{gl} algorithm, here implemented using the commercial code ABAQUS as the FE solver (henceforth ABAQUS+ GFEM^{gl}), was verified by solving a small, three-dimensional L-shaped domain of overall dimensions $100 \times 100 \times 10$ mm. The global domain was meshed with linear (TET4) and quadratic (TET10) tetrahedral elements 10 mm in size. Inhomogeneous temperature boundary conditions of 150°C and -150°C were applied to the top and right faces of the domain, respectively. Thus, the problem exhibits a sharp heat flux singularity at the reentrant corner without the need to compute a sharp load vector, making it an ideal verification problem.

Using the GFEM^{gl} methodology, the local problem was chosen as a neighborhood around the interior corner, $\Omega_L = \{\mathbf{x} | 20 < x < 80; 20 < y < 80; 0 < z < 10\}$, while the corresponding global-local enrichment zone on the global domain was chosen to be slightly smaller, enclosing only the first layer of nodes α around the corner, $\{\alpha | 40 \leq x_\alpha \leq 60; 40 \leq y_\alpha \leq 60; 0 \leq z_\alpha \leq 10\}$. The

* In the commercial code ABAQUS, only linear “TET4” or quadratic “TET10” tetrahedral elements are implemented for heat transfer simulations.

difference in size between the local domain and corresponding global-local enrichment region in this case serves to ameliorate the effect of inaccurate boundary conditions on the local domain.

A reference solution u_{ref} was also generated using hp -GFEM (the GFEM analog of hp -FEM) with 7 levels of global mesh refinement, overall polynomial order $p = 3$, and 25 levels of geometric mesh refinement about the reentrant corner in the domain. Solutions from ABAQUS + GFEM^{gl} were compared against the hp -GFEM reference solution. For qualitative comparison, Fig. A7.2 shows the heat flux fields corresponding to initial global and enriched global solutions, respectively, on the TET10 mesh.



More detailed results, including convergence data for more representative and larger-scale problems, are given in Plews (2011).

Details of ABAQUS Implementation

The exchange of the initial global solution, pseudo-loads, and pseudo-solutions between ABAQUS and the GFEM code is facilitated by a converter code written in a combination of Python (the scripting language of ABAQUS/CAE) and C++. Because the two codes are otherwise isolated from each other, identical global models, or job files, must be present for both ABAQUS and the GFEM code. Two model files must be written for ABAQUS: one for the initial global analysis (henceforth `abaqus.inp`), and another for the enriched global problem, which will contain pseudo-loads (`abaqus_nRHS.inp`). ABAQUS/CAE output can be read and converted directly by an ABAQUS Python script (referred to here as the Python converter code).

Initial Global Problem: The procedure for the initial global problem step is as follows:

1. Call Abaqus from the GFEM code to execute model file `abaqus.inp` via Python script.
2. When problem is done executing, execute Python converter code to write initial global results \underline{u}^0 from the `.odb` file to output file readable by the GFEM code.
3. Read initial solution in the GFEM code.

Local Problem(s): Once the initial global problem solution is read in the GFEM code, execution continues, and local problems can subsequently be extracted and solved, as specified. The procedure for a local problem is as follows:

1. Extract a local domain Ω_L (selected by the user or by *a posteriori* error estimates on u^0), and apply initial solution u^0 from ABAQUS as a Dirichlet boundary condition.
2. Perform hp -adaptivity as necessary and solve local problem.

3. Using local solution u_L , compute global-local shape functions ϕ_a^{gl} as in Equation (6), and use these to assemble \mathbf{K}^{gl} and \mathbf{f}^{gl} corresponding to global-local dofs, and $\mathbf{K}^{0,gl}$, pseudo-loads to be passed to ABAQUS.
4. Recompute total global load vector \mathbf{f}^0 using refined local elements for integration.
5. Write out pseudo-loads and recomputed global load vector (including the sharp load features) to a file.

Enriched Global Problem: The enriched global problem requires multiple communications between the GFEM code and ABAQUS. In this step, because in general multiple pseudo-loads $\mathbf{K}^{0,gl}$ will be present, ABAQUS'S built-in capability to solve multiple right hand sides as part of the same job is utilized. The enriched global procedure is done as follows:

1. Read pseudo-loads and global load vector from the GFEM code in converter code, and write each right hand side therein to a separate analysis step in an input file stub readable by ABAQUS.
2. Call ABAQUS and execute enriched global model abaqus_nRHS.inp (written prior to the analysis), including file containing multiple right hand sides (*not* known prior to the analysis) written above.
3. When problem is done executing, execute Python converter code to write resulting pseudo-solutions $\mathbf{S}^{0,gl}$ and recomputed global solution \mathbf{u}^0 from the .odb file to output file readable by the GFEM code.
4. Read output file in the GFEM code and compute the global degrees of freedom, $\tilde{\mathbf{u}}^0$ as in Equation (A.7-4), the Schur complement of the global stiffness matrix, $\hat{\mathbf{K}}^{gl}$ as in Equation (A.7-5), as well as $\hat{\mathbf{f}}^{gl}$.
5. Compute the solution for global-local degrees of freedom \mathbf{u}^{gl} as in Equation (4.7-5) and total solution u^E as in Equation (A.7-1).

After the final step, any post-processed quantities which were requested by the user in the GFEM code are computed, and ABAQUS initial global and the GFEM code local and enriched global solutions may also be visualized. Execution of the program completes, and all requested output from the enriched global solution is available to the user from the GFEM code.

A.7.2 Thermomechanical Effects in a GFEM Framework

A multiscale GFEM framework for multiphysics problems was also developed within the scope of Project A7. The current implementation handles one-way-coupled thermoelasticity. Two types of thermomechanical effects were considered in this portion of the project. First, analytical or predefined temperature fields, for verification purposes, and second, multiphysics or linear thermoelastic interactions, which include the solution of both a heat transfer and a linear elasticity problem.

Formulation of Linear Thermoelasticity

Considering domain $\Omega \equiv \Omega^\theta \equiv \Omega^u$ with boundary $\partial\Omega \equiv \partial\Omega^\theta \equiv \partial\Omega^u$, where $(\bullet)^\theta$ designates a quantity in heat transfer, and $(\bullet)^u$ designates a quantity in elasticity,

$$\nabla \cdot (\kappa \nabla \theta) = -Q(\mathbf{x}) \quad \text{in } \Omega^\theta$$

$$\nabla \cdot \sigma = -\mathbf{b}(\mathbf{x}) \quad \text{in } \Omega^u,$$

where κ is the thermal conductivity tensor, $\theta \equiv \theta(\mathbf{x})$ is the temperature field, and $Q(\mathbf{x})$ is the internal heat source in the heat transfer problem. On the other hand, σ is the stress field, and $\mathbf{b}(\mathbf{x})$ is the body force in the elasticity problem.

Boundary Conditions: Boundary conditions are defined separately for each physics, and in general up to two boundary conditions—one from each physics—may be applied on any portion of the boundary, that is,

$$\partial\Omega^\theta = \Gamma_\theta \cup \Gamma_f$$

$$\partial\Omega^u = \Gamma_u \cup \Gamma_t$$

$$\Gamma_\theta \cap \Gamma_f = \emptyset$$

$$\Gamma_u \cap \Gamma_t = \emptyset.$$

For the heat transfer part of the problem,

$$\theta = \bar{\theta} \quad \text{on } \Gamma_\theta$$

$$-\kappa \nabla \theta \cdot \mathbf{n} = \bar{f} \quad \text{on } \Gamma_f,$$

where $\bar{\theta}$ is the specified temperature, and \bar{f} is the prescribed heat flux. Similarly, for the elastic portion,

$$\mathbf{u} = \bar{\mathbf{u}} \quad \text{on } \Gamma_u$$

$$\sigma \cdot \mathbf{n} = \bar{\mathbf{t}} \quad \text{on } \Gamma_t,$$

where $\bar{\mathbf{u}}$ is the prescribed displacement, and $\bar{\mathbf{t}}$ is the prescribed surface traction.

Constitutive Relations: Now, the coupling between the temperature field $\theta(\mathbf{x})$ from the heat transfer problem and $\mathbf{u}(\mathbf{x})$, the elastic displacement solution, comes from the strain-displacement and constitutive relations. As given by Hooke's Law for linear elasticity,

$$\sigma = \mathbf{C} : \varepsilon_m$$

$$\varepsilon_m = \varepsilon - \varepsilon_\theta$$

$$\varepsilon = \frac{1}{2}(\nabla \mathbf{u} + \nabla \mathbf{u}^T)$$

$$\varepsilon_\theta = \alpha \theta(\mathbf{x}),$$

where ε is the *total* strain, ε_m is known as the *mechanical* strain, and ε_θ is the *thermal* or *transformation* strain. \mathbf{C} is the tensor of elastic moduli, and $\alpha = \alpha \mathbf{1}$ is the thermal expansion tensor, where α is the linear coefficient of thermal expansion, assumed to be isotropic. Equivalently, in terms of stress,

$$\sigma = \mathbf{C} : (\varepsilon - \varepsilon_\theta)$$

$$= \mathbf{C} : \varepsilon - \mathbf{C} : \alpha \theta(\mathbf{x})$$

$$= \sigma_e - \sigma_\theta,$$

(A.7-6)

where we define

$$\sigma_e = \mathbf{C} : \varepsilon$$

$$\sigma_\theta = \mathbf{C} : \varepsilon_\theta = 3K\alpha\theta(\mathbf{x})$$

(A.7-7)

with K the elastic bulk modulus of the material.

The weak and discretized forms of the above strong formulation follow easily.

Predefined Temperature fields

To verify material models used for future multiphysics implementations, analytical temperature fields were implemented in a GFEM framework. This implementation simply follows from the above formulation; however, in this case the heat transfer problem is *not* solved, allowing, for instance, coupling with multiple analysis codes for each problem physics.

Verification Problem: The implementation was verified using the 3D temperature-induced bending beam illustrated below. In this example, the analytical linear temperature distribution resulting from the temperature boundary conditions shown was applied to the model. The mesh was constructed with a regular tetrahedral mesh and solved using a quadratic polynomial approximation in order to recover the exact solution. As expected, due to the simply supported nature of the problem, the beam experiences no stresses, and, therefore, zero strain energy.

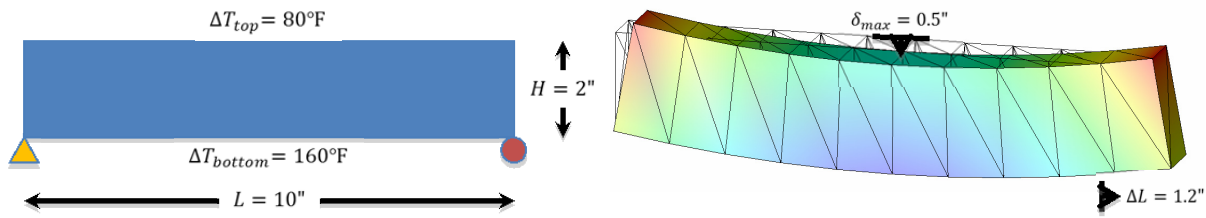


Fig. A7.3: Beam bending verification problem for analytical temperature distribution.

Implementation of Multiphysics (Linear Thermoelasticity)

Solution Scheme: Due to the existence of separate computational domains, and to allow for as much code reuse as possible, a staggered solution scheme is adopted—in this case, the staggered solution is only a one-way exchange of temperature field data. The solution procedure is as follows:

The system may be viewed as a partitioned system of equations of the form

$$\begin{bmatrix} \mathbf{K}_u & \mathbf{K}_{u\theta} \\ \mathbf{0} & \mathbf{K}_\theta \end{bmatrix} \begin{bmatrix} \mathbf{d}_u \\ \mathbf{d}_\theta \end{bmatrix} = \begin{bmatrix} \mathbf{f}_u \\ \mathbf{f}_\theta \end{bmatrix} \quad (4.7-8)$$

which may be solved exactly using the staggered form

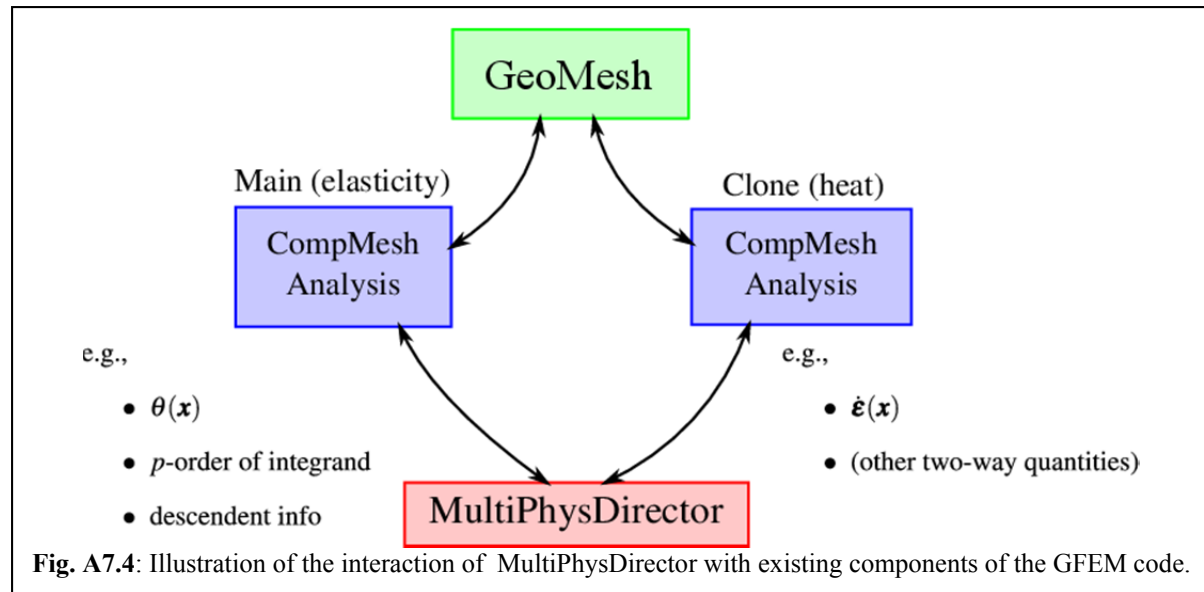
$$\mathbf{K}_\theta \mathbf{d}_\theta = \mathbf{f}_\theta \quad (4.7-9)$$

$$\begin{aligned} \mathbf{K}_u \mathbf{d}_u &= \mathbf{f}_u - \mathbf{K}_{u\theta} \mathbf{d}_\theta \\ &= \mathbf{f}_u - \mathbf{f}_{u\theta}. \end{aligned} \quad (4.7-10)$$

As noted above, due to the staggered scheme, the quantity $\mathbf{K}_{u\theta} \mathbf{d}_\theta$ exists only in theory, as the temperature field is integrated directly to form a right-hand-side $\mathbf{f}_{u\theta}$ in the thermoelasticity problem. Solving this system consists of several basic steps:

1. Divide the heat transfer and elasticity domains into separate problems.
2. Assemble the system (4.7-9) independently of the elastic solution $\mathbf{u}(\mathbf{x})$.
3. Solve (4.7-9) for heat transfer degrees of freedom \mathbf{d}_θ .
4. Assemble the system (4.7-8), obtaining $\theta(\mathbf{x})$ from the solution of system (4.7-9) in the previous step.
5. Solve (4.7-10) for thermoelastic degrees of freedom \mathbf{d}_u .

A multiphysics framework, MultiPhysDirector: To orchestrate multiphysics analyses and intervene in parts of the analysis where knowledge of multiphysics problems being solved may be necessary, a director framework was implemented in a GFEM code framework, entitled MultiPhysDirector. It is a flexible framework which circumvents the need for many invasive modifications to the current code structure and reuses many of the GFEM code's existing capabilities. The general way in which MultiPhysDirector interacts with existing code capabilities is diagrammed in the figure below. "GeoMesh" represents user input mesh data, while "CompMesh" and "Analysis" are used discretely during the analysis of each physics-subproblem.



Verification Problem: The very same verification problem which was solved in the case of predefined temperature fields was solved in order to verify the implementation of the multiphysics framework. However, in the multiphysics case, the temperature boundary conditions as illustrated in the figure from the above section were actually applied on a heat transfer domain, and the heat transfer problem was solved numerical to obtain a temperature distribution to apply to the coupled thermoelastic problem. Exact results (zero strain energy, exact maximum deflections, and zero stress through the beam) were recovered just as above in this case. Work on the MultiPhysDirector is ongoing, with more examples in line for future work.

A.7.3. Future Work

As this project is ongoing as of the end of the center, the principal investigators are currently considering:

- Nonintrusive implementation of GFEM^{gl} for multiphysics applications in a commercial FEA code such as ABAQUS.
- Implementation of thermoplasticity within the multiphysics framework as an extension to the current linear elasticity capabilities.

Extension of the GFEM^{gl} with multiphysics capabilities to support “reduced models”—for instance, coarse-scale global models of plates or shells enriched with local problem full 3D solid solutions.

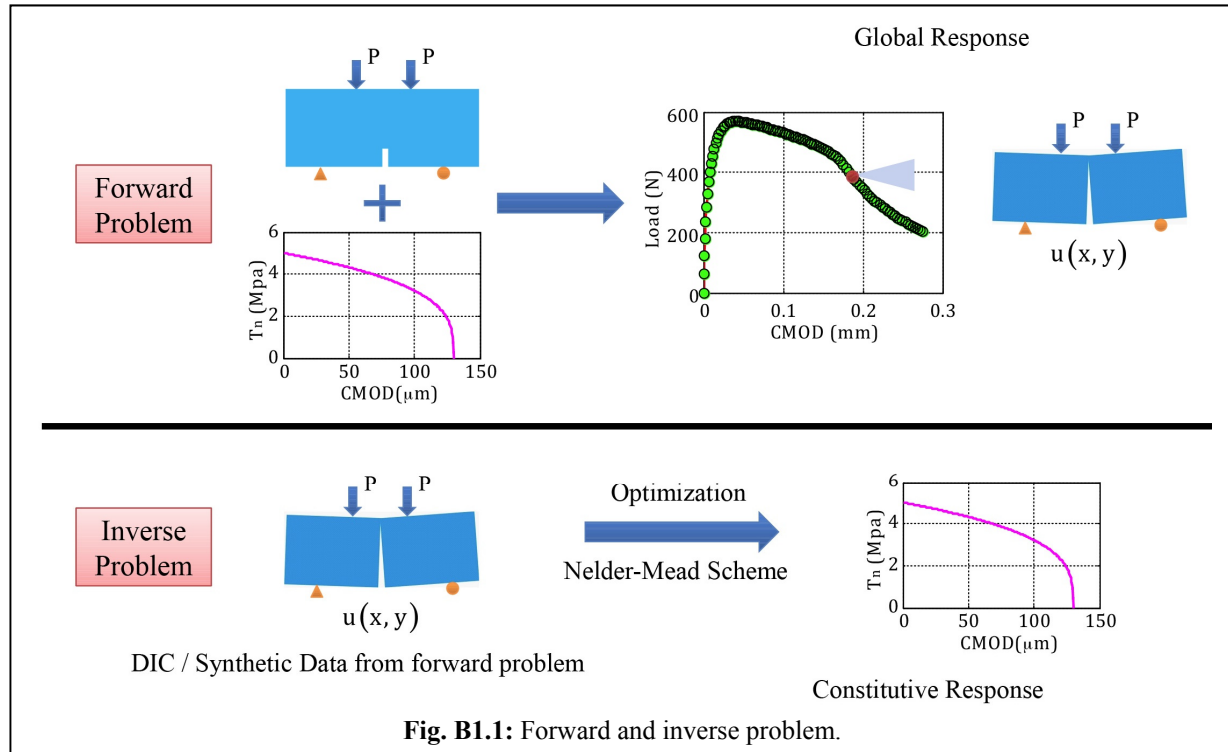
B1 Mechanism-Based Cohesive Failure Model for Functionally Graded Aircraft Components and Structures

Personnel: Paulino, Park (Postdoc UIUC), Gain (Graduate student, UIUC), Tuegel (AFRL)

Start: 2008; End: 2010

B.1.1 Forward and Inverse Problems During Quasi-static Fracture

Damage and failure of spatially tailored aero-thermal structures under extreme loading conditions can be properly assessed with a nonlinear model of cohesive fracture, which is able to



predict crack nucleation and failure sites. Both forward and inverse fracture problems are investigated in this work as illustrated by Fig. B1.1. In the forward problem, the input fracture properties are known, and the output is displacements obtained numerically using a particular material model. In the inverse problem, a hybrid technique blending computations and experiments is used to extract the cohesive properties. For instance, using an experimental technique such as digital image correlation (DIC) we can obtain a full-field experimental displacement field which can be used as input to an optimization algorithm to compute the cohesive constitutive parameters (output).

Optimization is done using the Nelder-Mead (N-M) scheme which is an unconstrained, derivative free optimization scheme, is used for the inverse analysis. Physical constraints such as positive traction along crack faces for mode-I fracture are imposed using barrier functions. Two options for the inverse analysis are adopted: namely, a shape optimization approach, and a parameter optimization for the PPR (Park-Paulino-Roesler) potential-based cohesive zone model (CZM). In the shape optimization approach, we optimize the location of points in the traction-separation domain which are later interpolated to obtain the inherent cohesive zone model. In the

parameter optimization for the PPR potential-based CZM, we optimize the PPR parameters of cohesive strength, fracture energy and shape parameter. The goal is also to validate the hybrid scheme using PMMA quasi-static crack growth experiments initially, and eventually fatigue crack growth experiments in a ductile solid. The inverse analysis takes the local displacement fields coming from the DIC procedure for PMMA as input and validates the result against the global sample response.

The underlying concept in the shape optimization technique is that the material specific CZM is obtained from interpolation of points on the traction-separation domain. The locations of points are determined using the Nelder-Mead optimization technique. In the parameter optimization scheme the Park-Paulino-Roesler model (Park *et al.* 2009) was chosen because it provides a single closed potential function which can be used to obtain traction-separation curves for both mode-I and II and can provide both intrinsic and extrinsic CZMs. For the mixed mode case, different fracture energies and cohesive strengths can be specified. Just by determining few parameters (the fracture energy, cohesive strength, and shape parameter in an extrinsic mode-I case; and additionally the initial slope for the intrinsic case) the CZM can be uniquely defined. Although we only dealt with mode-I here, the PPR provides a platform for our work to be extended to mixed mode fracture.

Typically, an inverse analysis code requires an initial guess from the user. Various initial guesses were used to test the code's robustness, as illustrated in Fig. B1.2 and B1.3. In order to resemble actual experiments, the computer code was initially tested with synthetic data added with noise before being applied to actual experiments.

Once robustness had been established, the two approaches were applied to a Polymethylmethacrylate (PMMA) quasi-static crack growth experiment. The near tip displacement field obtained experimentally by DIC was used as input to the optimization schemes. The technique successfully predicted the applied load-displacement response of a four-point bend edge cracked fracture specimen. The load versus load line displacement (LLD) plot from the experiments and the direct problem simulations are shown in Fig. B1.4(a) and (b). Both results are close to each other and give confidence in the extracted CZM.

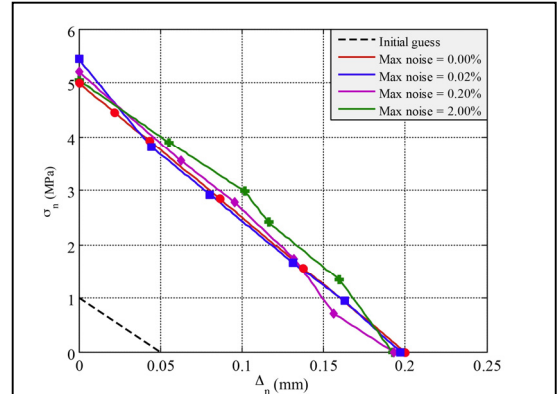


Fig. B1.2: Extracted cohesive zone model from inverse analysis (shape regularization technique) using synthetic data with different levels of noise.

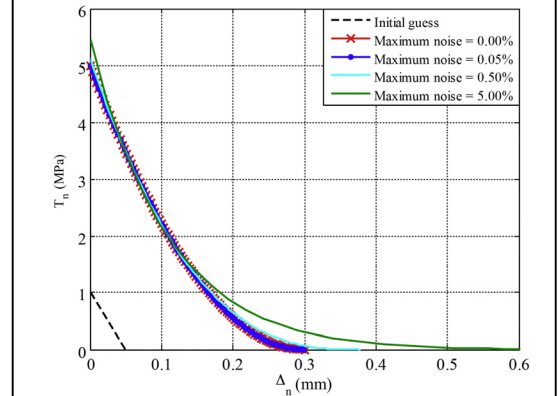
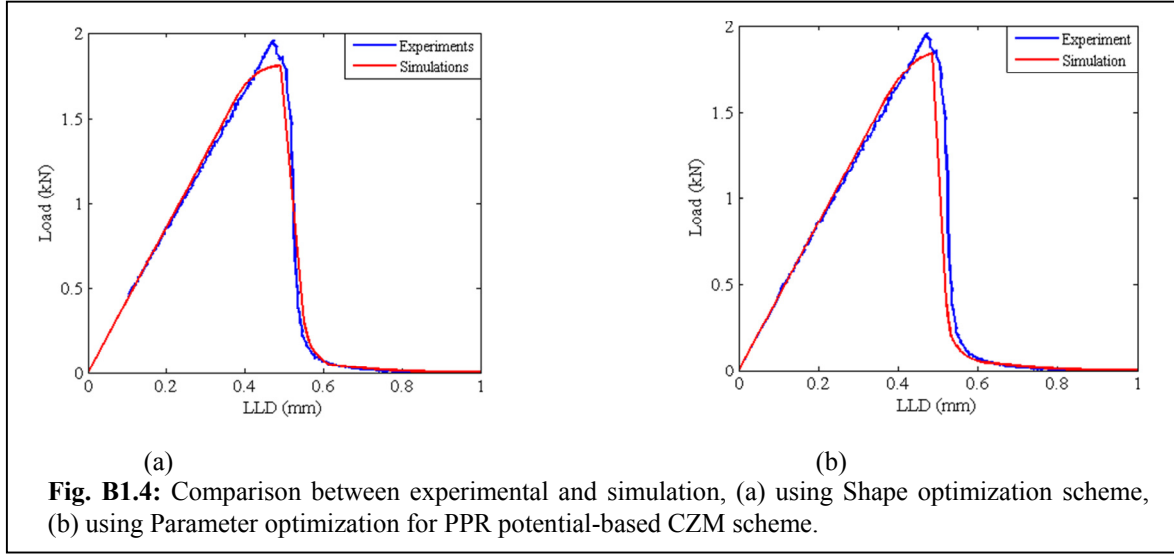


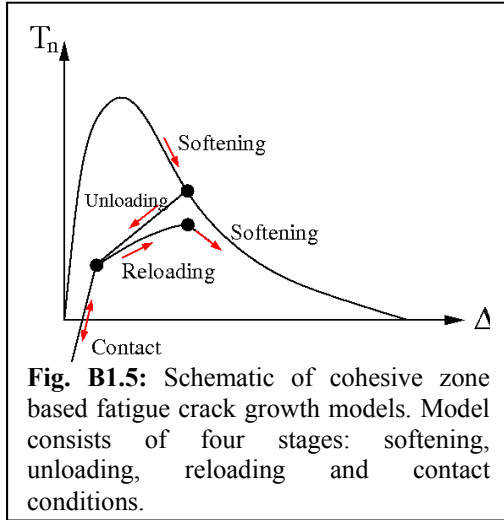
Fig. B1.3: Cohesive zone model from inverse analysis (PPR model technique) using synthetic data with different levels of noise.



B.1.2 Cohesive Model for Fatigue Crack Growth

Fatigue damage is a major failure phenomenon observed in air vehicles. Most fatigue failure investigations have been performed on the basis of linear elastic fracture mechanics based on the Paris type relations (*e.g.*, AFGROW) despite the fact that a nonlinear fracture process zone exists ahead of a fatigue crack tip. In order to capture this nonlinear crack tip behavior, cohesive zone-based fatigue crack models have been investigated in this part of the effort.

Previous cohesive zone-based fatigue crack models possess several limitations. For instance, a model parameter should be free from the number of cycles, because a real structure

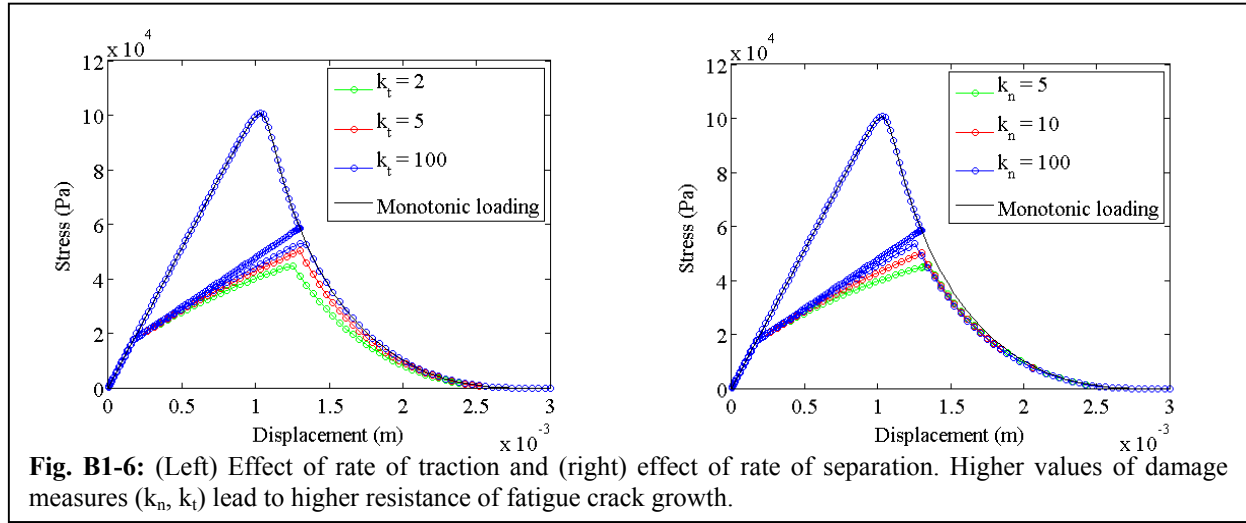


experiences arbitrary loading amplitude and frequency. Fatigue damage can occur before the cohesive traction reaches the cohesive strength. In order to overcome such limitations, and to capture the nonlinear fatigue damage processes, a novel cohesive zone based fatigue crack growth model was developed in this project. A schematic of the cohesive traction-separation relationship is shown in Fig. B1.5. The constitutive model clearly defines four stages during arbitrary fatigue loading: softening, unloading, reloading, and contact. The softening condition is based on the potential-based model (PPR), which has been investigated in conjunction with DIC techniques in this project and was discussed above. For the unloading/reloading conditions two damage measures

(k_n , k_t) and two model parameters (CC, CO) are introduced. Two damage measures are associated with the rate of separation and the rate of cohesive traction, which influence the fatigue crack growth rate. Additionally, two model parameters account for crack closure/opening effects, which can be associated with crack face roughness, oxidation of fracture surface, *etc.*

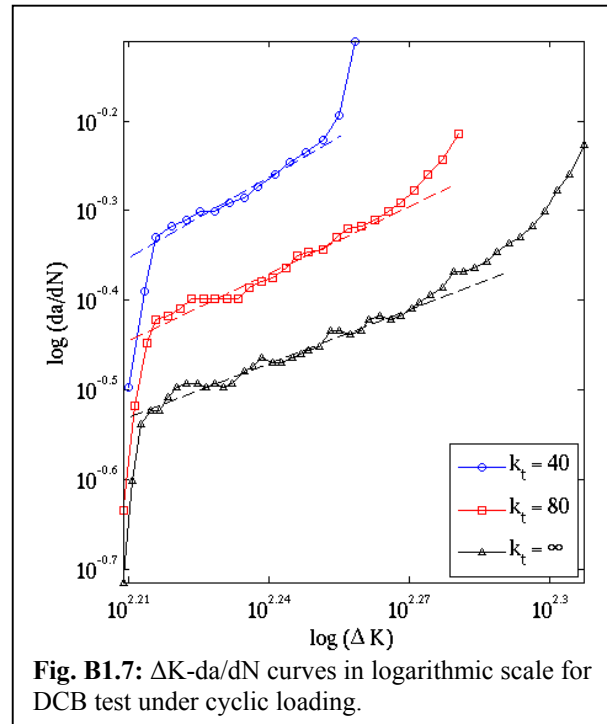
Such crack closure/opening effects lead to nonlinear load versus local crack opening relations, which are generally observed in experiments.

The proposed constitutive model is illustrated by simulating Mode-I fatigue problems.



First, a unit square domain, fixed at the bottom, is considered. At the top of the domain, the uniform displacement is first applied up to 1.3×10^{-3} . Then, the displacement is unloaded to zero, and it is reloaded up to the complete failure condition. The effect of the rate of traction is shown in Fig. B1.6 (left) – the lower value of k_t leads to further deviation from the original softening curve. The effect of the rate of separation is illustrated in Fig. B1.6 (right) – the higher value of k_n leads to the higher slope in the reloading path. Thus, the higher value of the damage measures represent the higher resistance of the fatigue damage. Next, the double cantilever beam geometry was investigated under constant loading amplitude. The $\log(\Delta K)$ versus $\log(da/dN)$ result is illustrated in Fig. B1.7. The plot clearly demonstrates that the proposed constitutive model captures the stable crack growth region that corresponds to the Paris-type relations.

An attractive feature of the proposed model is that it is completely modular, and can be implemented in commercial software. For instance, it was implemented as a user-defined element subroutine in ABAQUS, and will be included in WARP3D code (developed by the University of Illinois). Furthermore, the model will be extended to study thermomechanical fatigue of metals, which is of ultimate interest in this work.



B2 Imperfections and Defect Tolerance of Aircraft Shells and Structures

Personnel: Tortorelli, Watts (Graduate student, UIUC), Eason (AFRL)

Start 2009; End: 2011

The efforts of this project were divided into several areas: (i) generating a library of images of candidate FGMs' microstructures, (ii) developing methods to generate quantitative morphological descriptions of the microstructure, and (iii) understanding correlations between morphology and material properties.

Task (i) – Microstructure Identification: Initially, the project dealt with a Ti-ZnO₂ meant to be representative of a two phase functionally graded metal-ceramic system. A collection of micrographs of multiple scales of three compositions of this system were collected, as illustrated in the example of Fig. B2.1(a). Future work in this area will include translating these methods to a Ti-TiB FGM material system, and developing the ability to generate 3D images of the

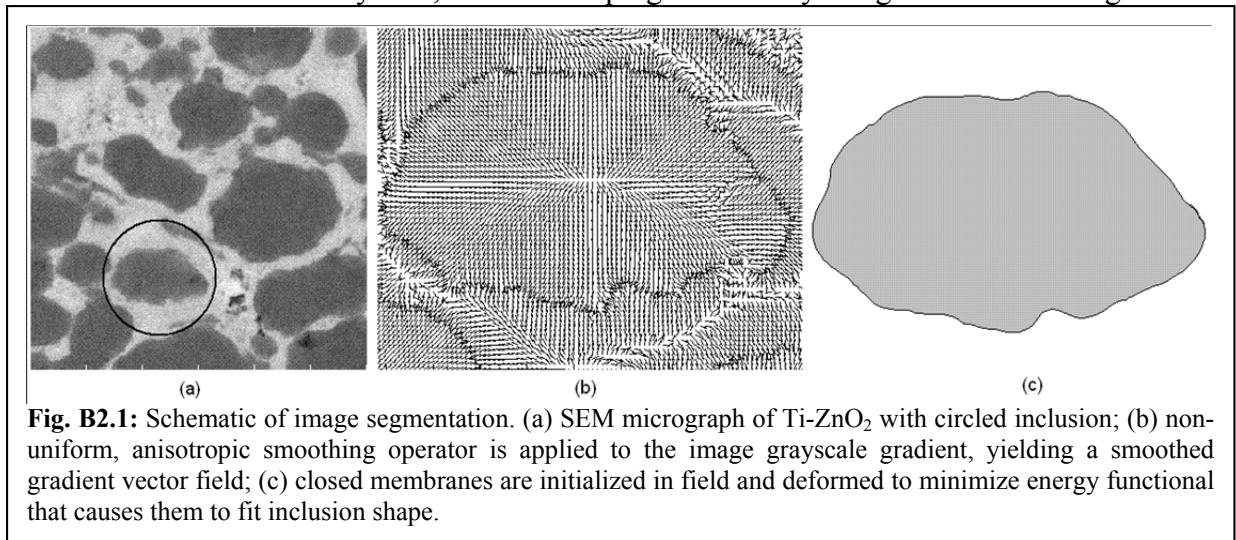


Fig. B2.1: Schematic of image segmentation. (a) SEM micrograph of Ti-ZnO₂ with circled inclusion; (b) non-uniform, anisotropic smoothing operator is applied to the image grayscale gradient, yielding a smoothed gradient vector field; (c) closed membranes are initialized in field and deformed to minimize energy functional that causes them to fit inclusion shape.

microstructure through serial sectioning or microtomography.

Task (ii) – Quantitative Microstructural Assessment: The second task was to develop numerical descriptions of the morphology of spatial patterns (*e.g.*, the material microstructure). Applying such descriptors to the micrographs generated in (i) allows us to quantitatively describe the microstructure. Such descriptions will be used in (iii) to instantiate numerical microstructure models with morphological characteristics similar to those of candidate FGM materials. We adapted methods from the literature to robustly segment images into disjoint sets — every point is unambiguously assigned to either the inclusion or the matrix phases — with well-defined boundaries. We have extended a family of recently introduced morphological descriptors, the Minkowski Valuations (MVs), which describe the complexity of microstructural patterns as a family of arbitrarily high-ordered tensors. While there are other means of describing morphology, the Minkowski functionals have the desirable properties that they are additive and motion invariant, and they have been used successfully to describe a wide array of morphologies in areas ranging from geology to astrophysics. We developed in-house software that computes the Minkowski functionals and their higher-order counterparts for 2D and 3D images.

Task (iii) – Microstructure-property relations: The third task involved the correlation of phase morphology to properties of the composite material. By meshing the segmented microstructural images (Fig. B2.2) and performing finite element analyses, we can place bounds on the homogenized properties of the composite. So far we have considered the homogenized elasticity tensor, modeling each phase with isotropic, elastic material properties. Our analysis shows that the Minkowski valuations are superior descriptors relative to the more common two-point correlation functions.

Understanding the relationship between the MVs and material properties of interest can be done either as a forward or an inverse problem. We can do this as a forward problem by generating random virtual specimens (with uncontrolled microstructure) and determine the homogenized material properties of the virtual specimens via finite element analysis. To fully understand the relationships between morphology and properties, however, we need to be able to generate specimens with a given target morphology. In this way we can observe directly what changes in the morphology have on material properties (versus coincidental changes caused by generating random images). The latter is defined as the inverse problem.

We pose this inverse problem as an optimization problem, *i.e.*, we seek the state of parameters (roughly, the microstructure itself) that optimally matches a target morphology. This inverse problem is ill-posed because the map from a microstructure to a finite morphological description is uninvertible. However, by placing a topological constraint on the morphology, we can at least define a pseudoinverse mapping, which makes the inverse problem tractable so long as the topological constraint is satisfied.

Satisfaction of the topological constraint is equivalent to ensuring that distinct pieces of the microstructure (which are controlled by our optimization parameters) do not overlap as we change the microstructure to match the target morphology. It is crucial that this constraint always be satisfied at every intermediate point in the optimization, since evaluation of the objective function is unreliable if it is not. We have written software to perform the optimization under this constraint, using techniques from contact mechanics. Fig. B2.3 shows a test of the constraint. Twenty-five small particles were initialized, and the optimizer was asked to fill the domain to 80% volume fraction, while ensuring the particles remain a finite distance apart. This simulation confirmed our constraint method works. We are now able to match target morphologies, at least for the first few orders of MVs. Fig. B2.4 illustrates satisfaction of area, perimeter, Euler characteristic, and area and perimeter centroid target values. Future work will focus on improving the conditioning of the inverse problem to speed solutions and improve matching, and

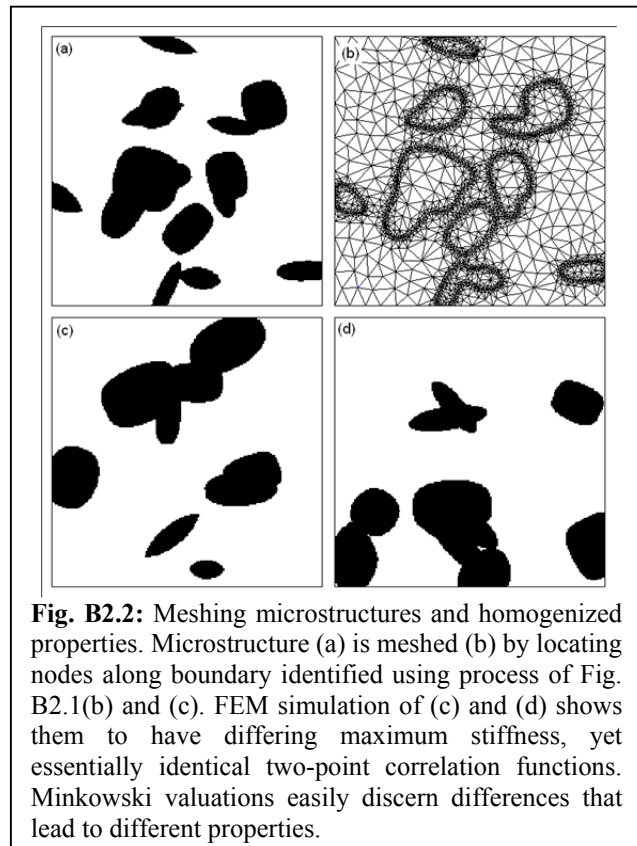


Fig. B2.2: Meshing microstructures and homogenized properties. Microstructure (a) is meshed (b) by locating nodes along boundary identified using process of Fig. B2.1(b) and (c). FEM simulation of (c) and (d) shows them to have differing maximum stiffness, yet essentially identical two-point correlation functions. Minkowski valuations easily discern differences that lead to different properties.

to remove some ad hoc approaches and replace them with methods that have provably good properties.

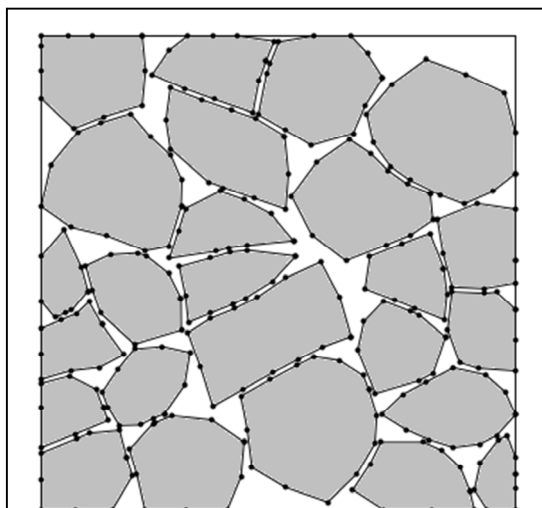


Fig. B2.3: Test of the topological non-overlap constraint. Objective is to fill domain to 80% area fraction while not allowing any particles to overlap or even touch.

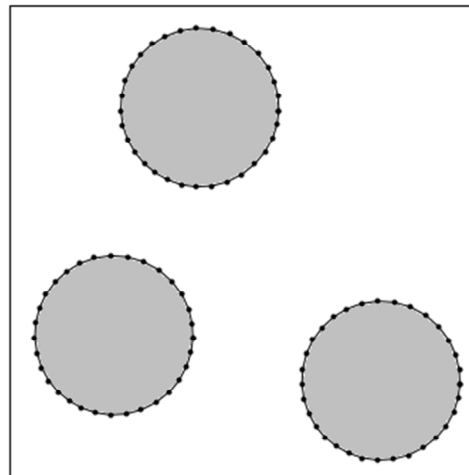


Fig. B2.4: Matching morphological descriptors. Objective is to move and distort three initially very small particles such that the final pattern has area fraction and perimeter of three discs with diameter one third the domain size, with pattern centroids at the center of the domain.

B3 3D Cyclic Plasticity Model for Thermo-mechanical Loading in Large-scale Analyses
Personnel: Dodds, Sobotka (Postdoc, UIUC), Gockel (AFRL)
Start: 2010, End: 2012

This project consists of two primary thrusts: (i) the development of a temperature-dependent plasticity model capable of accurately capturing complex thermal and mechanical cyclic loading of metallic materials, and (ii) the implementation of this model into a structural solver combined with both accurate thermo-aero-acoustic loading and fatigue failure initiation predictions. Each of these two thrusts is described below in more detail.

B.3.1 Generalized Plasticity Model

The work extends the Generalized Plasticity (GP) model for structural metals under cyclic loading proposed by Lubliner *et al.* (1993), based on the earlier work of Lubliner (1974), to incorporate temperature dependence into the elastic-plastic response. The model's flow equations satisfy the Clausius-Duhem (Lubliner, 1974) inequality through a thermodynamically consistent energy functional and retain key aspects of conventional plasticity models: Mises yield surface, normal plastic flow, and additive decomposition of strain. The GP model provides a novel approach to incorporate cyclic loading effects on the material response into 3-D finite element analyses. Auricchio and Taylor (1995) originally defined the GP model for cyclic mechanical loading of structural alloys. Material parameters within the GP model provide control over ratcheting rates and mean stress relaxation. The GP model introduces renewed plasticity (plastic flow reinitiates during reloading before reaching the previously attained flow stress) into the material rate equations.

Model summary

The modifications made for including temperature dependence in the GP can be summarized as follows:

1. Stress is given by

$$\boldsymbol{\sigma} = \mathbf{C} : [\boldsymbol{\varepsilon} - \boldsymbol{\varepsilon}^p - c_t(\theta - \theta_{ref})\mathbf{I}] , \quad (\text{B.3-1})$$

where the fourth-order tensor \mathbf{C} provides the linear elastic constitutive relationship. Here, c_t represents the coefficient of thermal expansion, and θ_{ref} signifies the reference temperature for zero thermal strains. Equation (B.3-1) represents a secant formulation for linear-elastic conditions and ensures temperature-path, history independence in the absence of plastic strains Cassenti (1983). Deviatoric strain (\mathbf{e}) and stress (\mathbf{S}) tensors reflect the main contribution of plastic flow on the material response in structural metals.

2. The yield surface is represented by

$$f = \|\mathbf{S} - \boldsymbol{\alpha}\| - (\sigma_0 + H_i \bar{e}^p) \quad (\text{B.3-2})$$

where the scalar quantity $\|\mathbf{S} - \boldsymbol{\alpha}\|$ measures the difference between the deviatoric stress and the backstress, α , σ_0 is the yield stress, and H_i an isotropic hardening parameter that are to come from experimental results.

3. The backstress itself evolves according to

$$\dot{\boldsymbol{\alpha}} = \frac{\dot{H}_k}{H_k} \boldsymbol{\alpha} + H_k \dot{\boldsymbol{\epsilon}}^p \quad (\text{B.3-3})$$

where H_k is a kinematic hardening parameter that again must be externally supplied from experiments and can be related to the isotropic hardening through

$$H_i = \tau H; \quad H_k = (1 - \tau)H; \quad 0 \leq \tau \leq 1 \quad (\text{B.3-4})$$

where τ represents the relative amounts of isotropic to kinematic hardening and ranges from 0 to 1.

4. In the GP model as originally developed the yield surface was replaced by a limit function, F , which in this work has been modified to account for thermal effects as:

$$F = h(f)[\mathbf{n} : \dot{\mathbf{S}} - \Lambda \dot{\theta}] - \dot{\lambda} \quad (\text{B.3-5})$$

where

$$h(f) = \frac{f}{\delta(\beta - f) + H\beta} \quad \text{and} \quad \Lambda = -\frac{\partial f}{\partial \theta} = \frac{\partial H_k}{\partial \theta} \frac{\boldsymbol{\alpha} : \mathbf{n}}{H_k} + \frac{\partial \sigma_0}{\partial \theta} + \frac{\partial H_i}{\partial \theta} \bar{e}^p \quad (\text{B.3-6})$$

with θ being the temperature.

5. The Kuhn-Tucker conditions below are equivalent to the MacCaulay brackets used in traditional plasticity model formulations and control whether loading, unloading or neutral loading are occurring in the material according to

$$\dot{\lambda} \geq 0; \quad F \leq 0; \quad \dot{\lambda} F = 0 \quad (\text{B.3-7})$$

The additional temperature-dependent term in Eq. (B.3.5) includes temperature-dependent effects in the limit surface function (F), and may generate additional plastic strain under conditions of constant stresses or strains. The revised form for F in Eq. (B.3.5) reverts to the isothermal GP model previously developed in Lubliner *et al.* (1993) conditions there is no change in temperature.

GP parameter estimation

Experimental stress-strain values from a single specimen loaded first in uniaxial tension and then in compression under isothermal conditions provide relevant data required to calibrate the GP model. To calibrate the GP model over a range of temperatures, several uniaxial tests at different test temperatures must be performed with linear interpolation of material parameters between temperatures based on isothermal properties.

Fig. B3.1 illustrates key material properties for the GP model. Under isothermal conditions, stress-strain data from a uniaxial test generates an experimental curve shown here by the solid line. Young's modulus, E , represents the linear curve (curve 1) starting from the unloaded configuration ($\varepsilon_u = 0$; $\sigma_u = 0$). In the GP model, the yield stress denotes the stress where experimental stress-strain results first deviate from the linear-elastic response. In many structural metals, the true (Cauchy) stress increases linearly with (log) strain following significant plastic deformation, as shown in Fig. B3.1 and is well captured by the GP model by the elastic-plastic modulus, E_T . The GP model requires specification of the plastic tangent modulus $H_u = EE_T/(E - E_T)$. Curve 3 intersects the experimental curve at the initial yield stress and has a slope equal to E_T . Curves 2 and 3 bound the nonlinear region of the GP model in monotonic uniaxial tension. The terminal stress, β_u , indicates the stress increment separating these two curves. The material parameter δ_u sets the curvature of the stress-strain response that transitions from a linear-elastic (curve 1) to the terminal linear-hardening conditions (curve 2).

For cyclic loading, τ reflects the amount of isotropic to kinematic hardening in the GP model, with $0 \leq \tau \leq 1$. The level of isotropic/kinematic hardening varies linearly with τ , i.e., if $\tau = 0.05$, then 95% of the hardening is kinematic and 5% is isotropic. The imposed loading on the uniaxial specimen must be reversed (from tension to compression) to determine the value for τ , as shown in Fig. B3.1. In these rate equations, τ is assumed not to change with temperature or accumulated plastic deformation. Consequently, τ specifies an average measure of kinematic to isotropic hardening at all relevant temperatures.

Model implementation and results

A 3D integration scheme, based on backward Euler discretization was used. This leads to a scalar quadratic expression to determine the plastic strain rate multiplier and has a symmetric

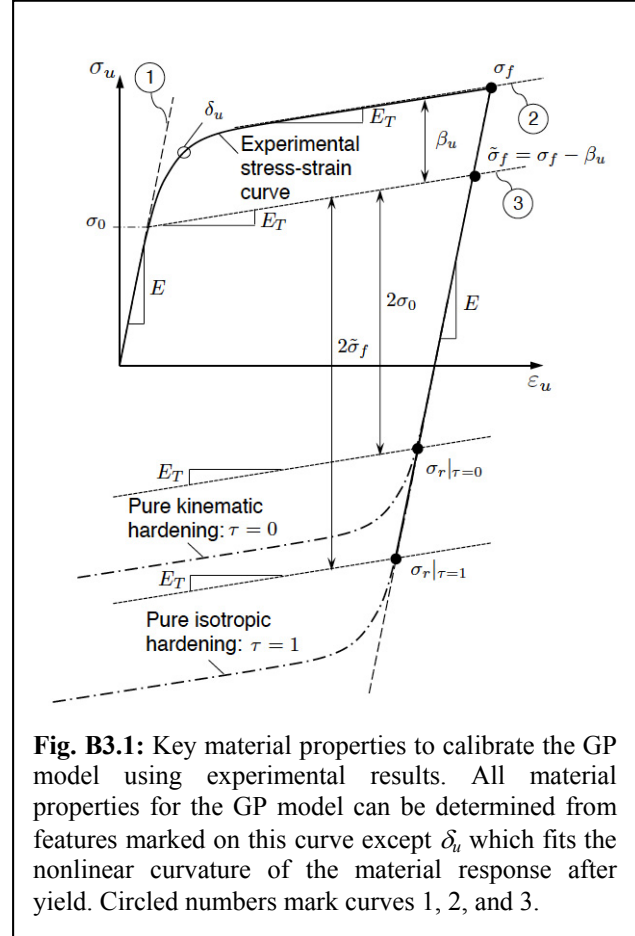


Fig. B3.1: Key material properties to calibrate the GP model using experimental results. All material properties for the GP model can be determined from features marked on this curve except δ_u which fits the nonlinear curvature of the material response after yield. Circled numbers mark curves 1, 2, and 3.

algorithmic tangent matrix. The consistent tangent minimizes the number of global iterations needed to reach an equilibrium configuration during the implicit solution. Adaptive integration of the governing GP rate equations further reduces truncation error and improves the accuracy of the material point calculations. Both properties of the integration lead to a computationally efficient implementation especially highly suited to large-scale, finite element analyses. The model was implemented and verified (through analytical, uniaxial expressions and a 3D boundary layer model) in WARP3D (<http://code.google.com/p/warp3d/>) – a highly-parallel, open-source, finite element code for nonlinear solid mechanics problems. It is applicable to both small-strain and large-strain formulations.

The modified GP model reflects key features of the elastic-plastic material response such as the premature yielding occurring in materials exhibiting a Cottrell-Stokes (1955) effect. An example is shown in Fig. B3.2 which presents experimental results of a CS type experiment on Hastelloy X – a nickel-based superalloy (Swaminathan *et al.*, 2013a). Here uniaxial tensile loading is initially performed at elevated temperature (600°C), the sample is then unloaded and cooled to room temperature upon which time it is reloaded. The reloaded material does not reach the yield stress of isothermal room temperature loading of Hastelloy X before yield begins. This

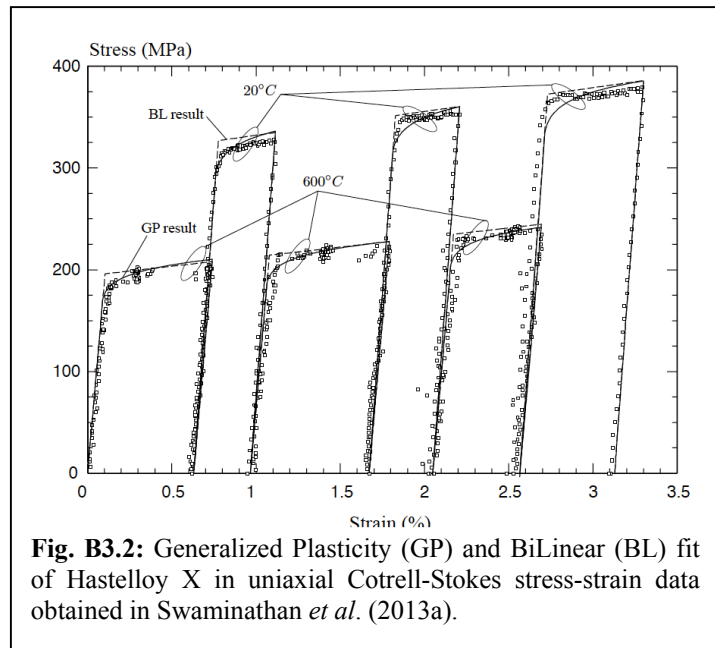


Fig. B3.2: Generalized Plasticity (GP) and BiLinear (BL) fit of Hastelloy X in uniaxial Cottrell-Stokes stress-strain data obtained in Swaminathan *et al.* (2013a).

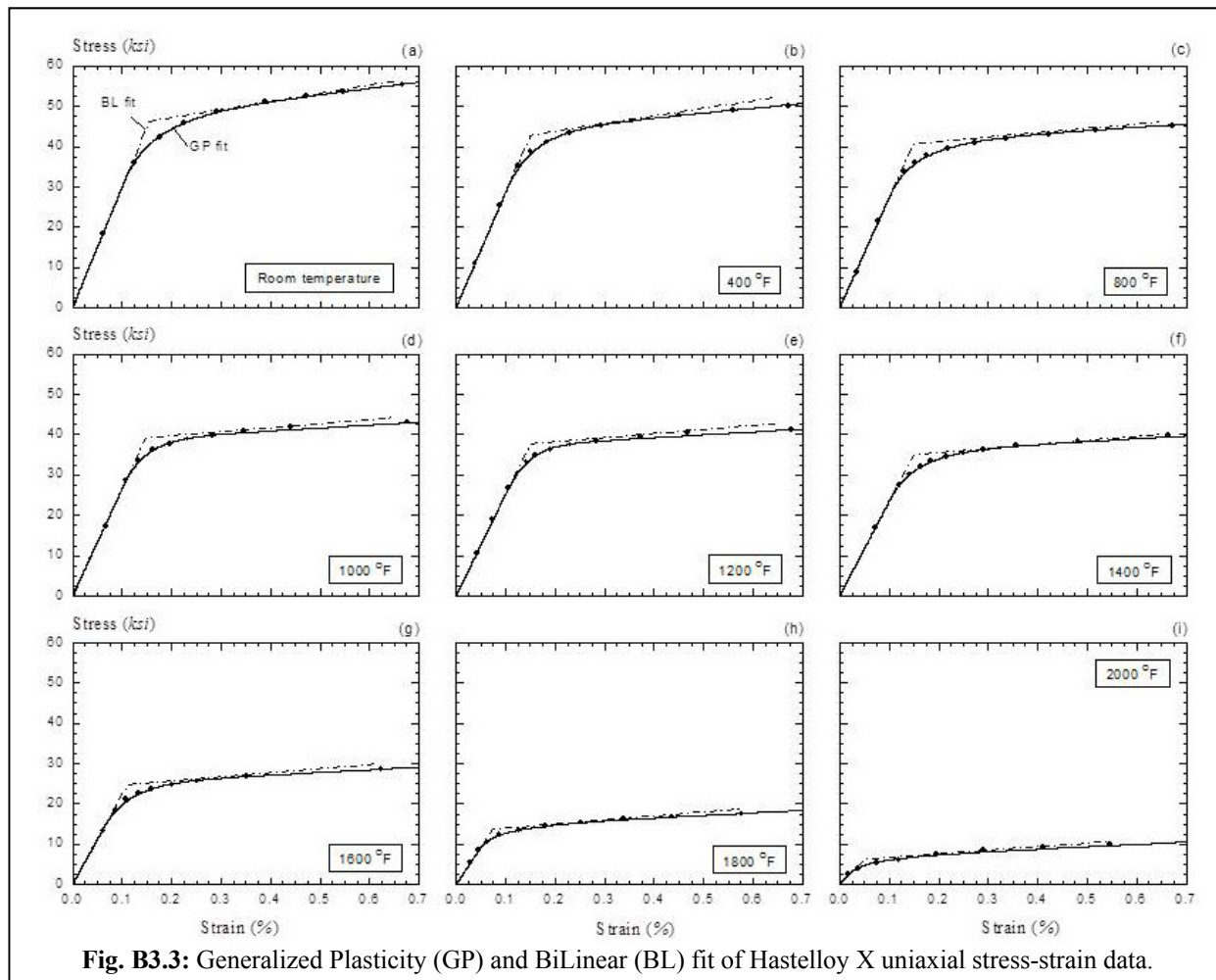
is repeated for two more high-low temperature cycles. Such loading histories show temperature-dependent responses that cannot be captured by existing thermo-cyclic material models, whereas they can be using the temperature-dependent GP model, as illustrated in Fig. B3.2.

Figure B3.3 shows that the GP model also improves fits to uniaxial stress-strain data at nine isothermal temperatures for Hastelloy X compared to the bilinear hardening model that has been employed in previous studies. The GP model was also exercised in a more complex stress field by comparing it to experimental results of Swaminathan *et al.* (2013b) on a double notched specimen subjected to tensile loading. In the double notch configuration the ligament between the two notch tips experiences highly biaxial stresses. In the experiments several Cottrell-Stokes type thermal cycles were performed for such a configuration and the measured strain results using the optical method of Digital Image Correlation agreed well with the GP prediction for the same loading cycles.

B.3.2 Incorporation in thermo-aero-acoustic structural solver

The inability to incorporate anticipated nonlinearities and coupling in hypersonic vehicle analysis and design has been a persistent, decades-long obstacle in eluding reusable hot-structure vehicles (Thornton, 1992; Blevins *et al.*, 1989). Two recent USAF funded industry studies on knowledge gaps in state-of-the-art design methods for hot-structure hypersonic vehicles (Tzong

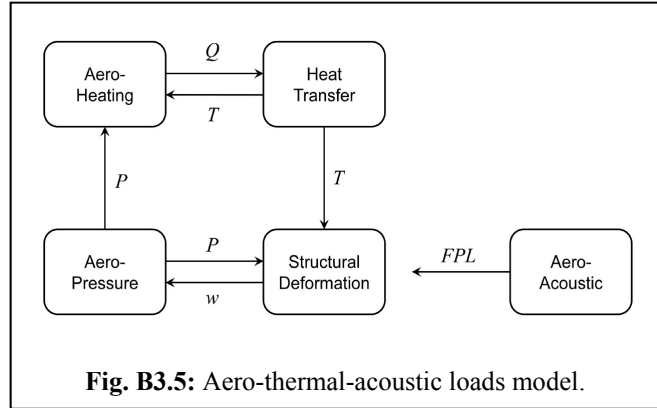
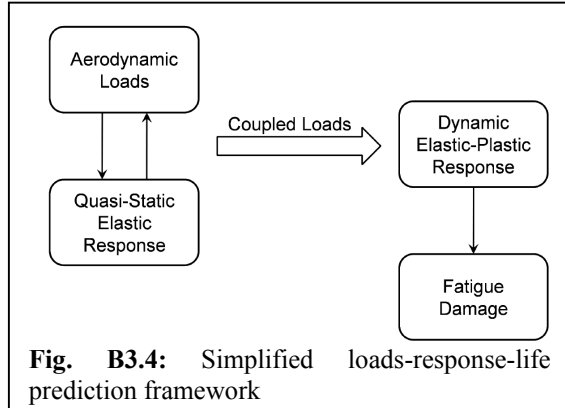
et al., 2010; Zuchowski, 2010) also suggest the need for a coupled, nonlinear computational framework to predict the loads, response, and life of these aerospace platforms. Current industry



best practices employ decoupled, linear analysis methods and presumably conservative assumptions on worst case loading conditions. This leads to highly uncertain predictions of structural response and life, and to structural designs with (presumably) excessive weight. These factors have a tremendously negative impact on closing the vehicle design and on optimizing its operational capabilities.

Here, in a closely collaborative effort with project B4 (described in detail below), the GP model was applied towards a high-fidelity, finite element analysis of structural components with a multi-physics/multi-scale approach similar to that adopted by the AFRL. A coupled fluid-thermal-structural analyses, performed by Dr. Adam Culler of AFRL (previously of Ohio State University) produced thermo-mechanical loading histories for ramp panel geometries. These loadings were then imposed on representative structural proxies to determine the thermo-plastic material response after repeated cycling. Spatially resolving the stress and strain state in the panels drove fatigue life prediction estimates using the model multiaxial temperature dependent fatigue failure model developed in project B4. Although currently at an early stage, this type of analysis demonstrates the viability of the computational framework developed to improve life prediction estimates for applications relevant to AFRL.

Preliminary studies are carried out using the simplified loads-response-life prediction framework illustrated in Fig. B3.4. In this framework, aerodynamic loads are coupled to the quasi-static elastic response of the structure throughout a given trajectory. These loads are then prescribed on a conjugate elastic-plastic dynamic response model of the structure. Lastly, the time history of the thermo-mechanical, elastic-plastic, dynamic response is used to assess the accumulated fatigue damage.

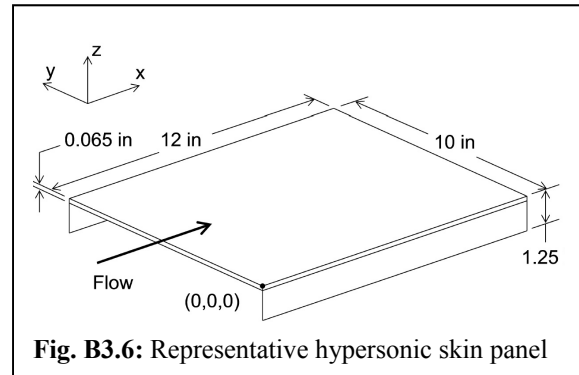


The current scheme employs post-processing routines to estimate damage introduced by thermo-cyclic loading during the flight profile, *i.e.*, structural elements do not weaken in “real-time”. Current procedures adopt a critical stress over a critical plane methodology (Findley, 1959) and thus require the entire response history to be known prior to evaluating damage. A simple, but crude, approach would reduce stiffness values at material points at the start of each major loading cycle relative to the critical stress achieved during the previous loading cycles. However, high computational costs and memory limits may necessitate the development of an accurate and physically-based incremental damage model, perhaps through the use of microstructural plasticity models. It is anticipated that this aspect of the coupled framework will require a substantial amount of future research.

Three types of structural loads are considered in this study, namely: (1) aerodynamic pressure, (2) thermal, and (3) aeroacoustic. Each of these loads is a result of the aerothermodynamics of high-speed flow. Aerodynamic pressure is caused by directional changes to the freestream flow that result from geometric parameters such as: angle of attack, curvature of external surfaces, and structural deformation. Thermal loads result from structural temperature changes, which are driven by aerodynamic heating. The aeroacoustic loads (fluctuating pressure loads) considered are those caused by turbulence in the boundary layer and shock-boundary layer interaction. The models used to predict the structural loads, and coupling of the various models, are depicted in Fig. B3.5. Details of this approach are given in Culler and McNamara (2010, 2011).

The loads-response-life prediction framework developed in this work is applied to a representative panel structure of an airbreathing hypersonic vehicle. The panel investigated is illustrated in Fig. B3.6 and corresponds to a portion of the stiffened-skin located on the inlet ramp of a concept vehicle (Blevins *et al.*, 1989, 1993). The inlet ramp forms a compression surface for the scramjet engine. This region of the vehicle is exposed to severe heating and pressure loading, thus the inlet ramp structure is an interesting test case for life prediction under combined loading.

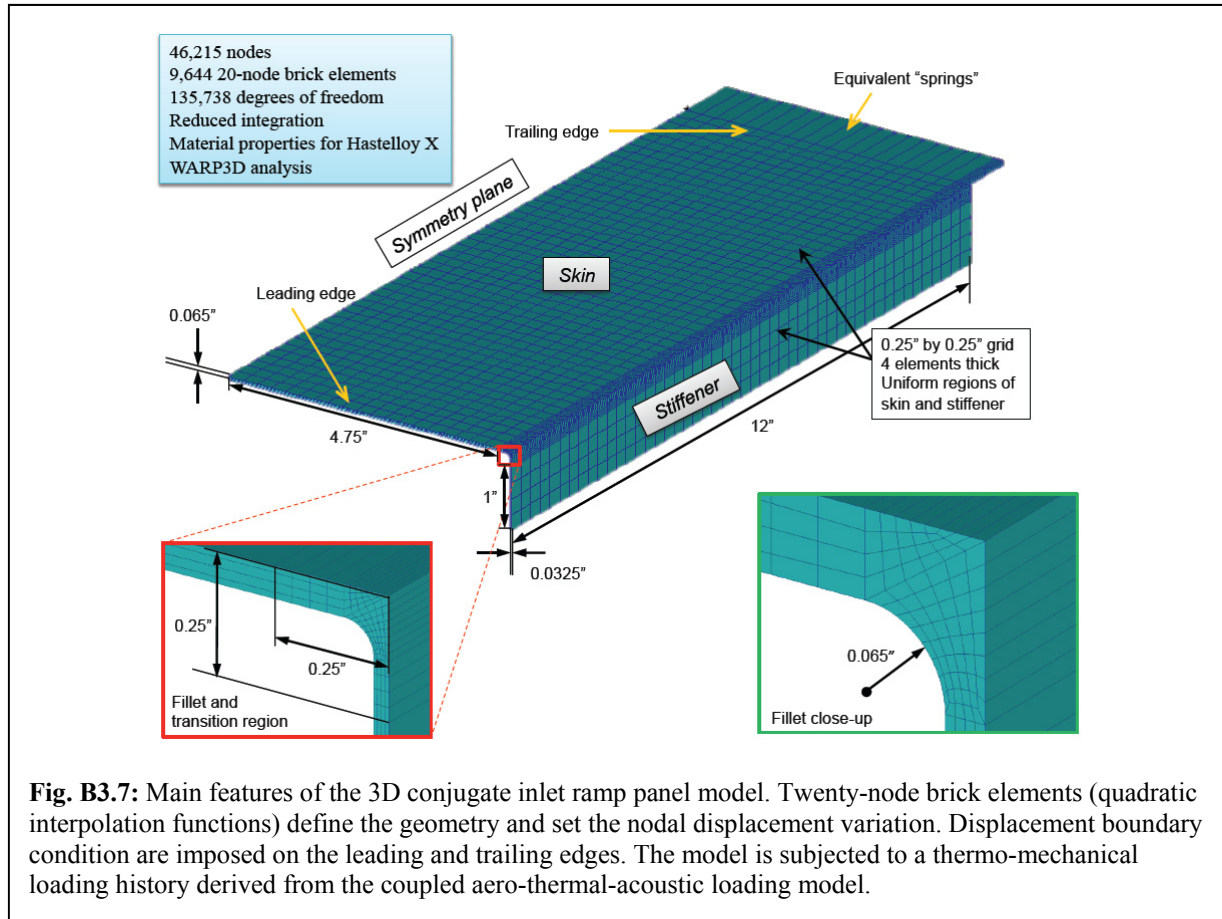
Heat transfer and structural finite element models are developed in MSC.Nastran for the panel geometry depicted in Fig. B3.6. For computational efficiency, the structural model consists entirely of shell elements. The heat transfer model uses shell elements for the stiffeners and brick elements for the skin to compute a through thickness temperature gradient. Both models use a 0.25x0.25 in grid. To accommodate moderate deformations with small strains, the structural model uses nonlinear strain-displacement relations and a linear-elastic material model with temperature dependent properties. Thermal loads are applied to the structural model by passing the temperature distribution from the heat transfer solution. Aerodynamic pressure and heating loads are applied to the skin of the structural and heat transfer models, respectively. Thermal radiation from the external skin surface to a low temperature environment is also included.



Structural boundary conditions are applied along the leading and trailing edges of the skin. The leading ($x = 0$) and trailing ($x = 12$ in) edges are fully-constrained in rotation and z -translation and the panel is free to expand in the y -direction. Resistance to in-plane expansion in the flow direction is included by constraining the leading edge in x -translation and placing independent linear springs at each node along the trailing edge. The total spring constant is set to 1% of the product of skin thickness and elastic modulus at 70°F and is divided uniformly among the individual springs.

Aeropressure loading is obtained assuming 1D piston theory (Lighthill, 1953; Ashley and Zartarian, 1956) over an inclined wedge with a flexible panel embedded on the top surface (Sobotka *et al.*, 2013). Aerodynamic heating from the boundary layer is computed using Eckert's reference enthalpy method (Eckert, 1956). The inviscid flow properties required for Eckert's reference enthalpy method are computed using the local pressure from piston theory in conjunction with isentropic flow relations (Thornton and Dechaumphai, 1955). Thus, aerodynamic heating computations include the effect of structural deformation on the boundary layer flow. Aeroacoustic loads resulting from both attached and separated turbulent boundary layer flow are considered. These fluctuating pressure loads are computed using the semi-empirical methods developed by Laganelli and Howe (1977) and Laganelli and Wolfe (1993) that extended an empirical relation for incompressible attached turbulent boundary layer flow to compressible flow using a transformation function, and to separated flow using empirically derived correlations. The equations in Laganelli and Wolfe (1993) are used in this work to compute root-mean-square (rms) pressure levels and power spectral densities in order to prescribe spatially uniform, temporally random fluctuating pressure loads on the panel.

Computational costs incurred during the iterative aero-thermal loading scheme currently limit the level of mesh refinement for structural and thermal analyses. Consequently, the thermo-mechanical loading history calculated during the iterative coupled analysis (shown in Fig. B3.5) provides boundary conditions to a conjugate finite element model shown in Fig. B3.7. This model is constructed using 20-node brick elements (quadratic interpolation functions for displacements) to capture the strong bending modes expected in these analyses. Reduced integration of the element stiffness matrices eliminates shear locking. Except near the connection, the mesh in the skin and stiffener regions have uniform element placement with



nodes coincident to the original panel model (shell elements). The four elements through the thickness for the skin and stiffener have been distributed non-uniformly over the thickness. Thinner elements near the free surfaces (top/bottom of the skin and sides of the stiffener) reveal higher stress gradients and plastic deformation during bending.

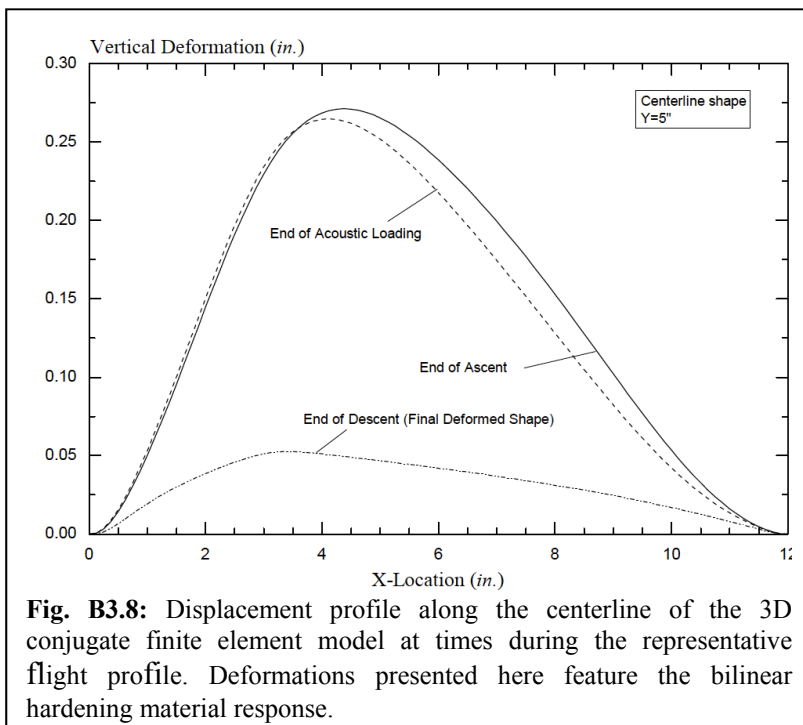
The coupled physics analysis generates a loading history of spatially and temporally non-uniform values for nodal pressures applied to the skin and temperatures at each node in the panel model (shell elements). A user-developed Matlab script linearly interpolates this loading history onto the conjugate mesh shown in Fig. B3.7. On the upper surface of the skin, interpolated pressure values provide a value for the average traction applied to each element's surface on the conjugate mesh. The resulting element traction represents the imposed mechanical loading, and the thermal loading history sets temperatures at each node. Structural analyses presented here employed the computational framework, WARP3D.

Thermo-mechanical loading histories determined from the coupled physics scheme described above drive 3D continuum analyses of the inlet ramp panel geometry. In these studies, we model elastic-plastic material response of the nickel-based superalloy Hastelloy X using two material models: the bilinear hardening (BL) model and the Generalized Plasticity (GP) model. Both models incorporate features to capture temperature-dependence of the material properties and cyclic loading (*e.g.*, ratcheting). We employed the BL and GP models due to 1) ease of fitting model parameters from available material databases, 2) computational efficiency (both

models have a symmetric algorithmic tangent), and 3) computational accuracy over long loading histories.

In order to demonstrate the elastic-plastic response and fatigue life prediction models, a Mach 2-7-2 trajectory is considered. This range of Mach numbers is selected based on heating effects being relatively insignificant below Mach 2 and the maximum useful temperature of Hastelloy X corresponding to approximately a Mach 7 cruise condition. At time zero the representative vehicle is exposed to Mach 2 flow at a dynamic pressure of 2000 psf. The dynamic pressure is held constant while the Mach number is increased at a constant rate to reach Mach 7 at 150 sec. Upon reaching Mach 7, the acoustic load is applied for a duration of 0.1 sec. During this time the thermal state is held constant. At 150.1 sec, the acoustic load is removed and the panel is unloaded by simply reversing the ascent loads. Thus, the panel is subject to the effects of both low-cycle thermal and high-cycle acoustic loading during the trajectory.

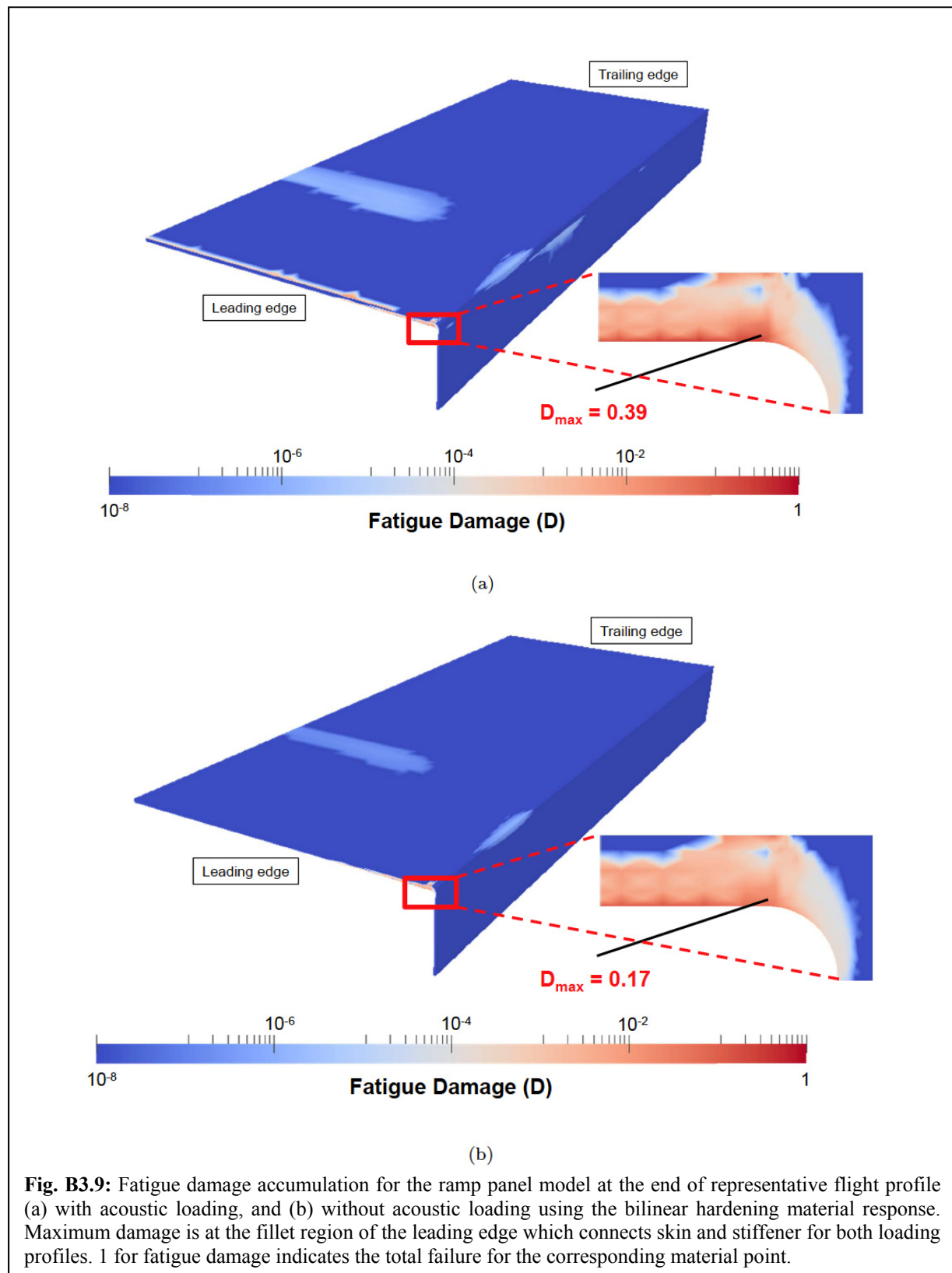
Figure B3.8 presents the centerline displacement profile for the 3D conjugate finite element model at three times during the representative flight profile: at the end of ascent; at the end of the acoustic loading; and at the end of descent, *i.e.*,



the final deformed shape. Residual plastic strain introduced by the aero-thermal-acoustic loading permanently deforms the ramp panel. This computational result implies that for the next flight, the panel has an initial shape defined by the final deformed shape in Fig. B3.8. The ascent/descent loading cycle primarily drives permanent deformation in the model. Acoustic loading has a relatively minor influence on the deformed shape, as shown by the difference between the displacement profile at the end of ascent and at the acoustic loading phase. Here, the ramp panel has the same imposed loading (thermal and mechanical), and any differences are attributed to plastic deformation accumulated during the acoustic loading.

Fatigue damage accumulation using the bilinear hardening material response is presented for the representative flight profile with acoustic loading in Fig. B3.9(a), and without acoustic loading in Fig. B3.9(b). Fatigue damage is quantified by the Findley parameter as detailed in the description of project B4. These results suggest that the most vulnerable region to crack nucleation is near the fillet at the leading edge. The maximum values of fatigue damage (D) with and without acoustic loading are 0.39 and 0.17, respectively. Note that a value of unity for D denotes total failure at the corresponding material point. These computational damage results imply that the next flight would begin with the material degradation shown in Fig. B3.9(a). As expected, acoustic loading, which exhibits highly cyclic behavior, has a significant influence on

fatigue damage. In contrast, the evolution of plastic deformation is governed by severe thermo-



mechanical loading during ascent/descent. This indicates that residual deformation alone is not a suitable proxy to estimate damage.

As was mentioned above, the transient loading regime in the model problem analyzed was of only a very small duration – 0.1 sec. Extending this type of analysis to longer transient loading times would be of interest. To some extent this is limited by computational cost considerations and additional work would be needed on this topic. However, the modeling approach adopted here utilizes several techniques to minimize computational costs. For an arbitrary thermo-mechanical increment, the modified GP model satisfies the consistency equation by solving a scalar quadratic equation (*i.e.*, no local Newton-iterations). This model includes a symmetric algorithmic tangent that minimizes the number of global iterations per time increment. By improving the rate of convergence, the adaptive integration scheme enables analyses to take relatively large time increments without sacrificing accuracy – an important consideration during transient acoustic loading. These considerations maximize the efficiency of computations performed in routines associated with the modified GP model. Comparable thermo-cyclic plasticity models (*e.g.*, the Frederick-Armstrong model) lack these features and incur additional computational costs. Furthermore, the modified GP model has been implemented (in these studies) within WARP3D – a highly parallelized and vectorized computational platform designed to facilitate large-scale finite element analyses.

In these preliminary studies, execution of the numerical analyses for the ramp panel analyses represented a fraction of the total time spent developing the computational approach. For example, on a server with two Xeon X5680 processors (6 cores each at 3333 MHz and 12 MB of L1 cache), the full analysis from ascent to descent (1650 time increments) completed in just under nine hours (wall clock time). The short acoustic loading phase (0.1 secs) requires 1000 time increments and reflects the bulk of the numerical analysis. Computations performed in the modified GP model remain a small fraction of the total analysis time relative to time spent during factorization of the global stiffness matrix.

Further studies in this area include: Sensitivity of the structural response to the thermo-cyclic material response, *i.e.*, the Generalized Plasticity model vs. the bilinear hardening model; Influence of the acoustic loading on the residual deformation levels and life predictions; Boundary condition matching between the conjugate finite element model and the original shell model of the inlet ramp panel; Displacement histories throughout the acoustic loading; Energy profiles over the flight profile; Inclusion of piston theory unsteady aerodynamics during acoustic loading; Loads-response-life prediction for subsequent flights with accumulated plastic deformation and fatigue damage.

B4 Towards a Fatigue Initiation Theory for Multiaxial Thermomechanical Fatigue
Personnel: Sehitoglu, Oral (Postdoc, UIUC), Penmetsa (AFRL)
Start: 2011, End: 2012

This project was started later in the progression of the center as a direct response to the need to increase center efforts in the area of fatigue life forecasting. The goal of the project was to provide a predictive model for fatigue damage nucleation, i.e., a regime that can be thought to encompass up to the instant of the initial formation of detectable fatigue microcracks, that could handle both multiaxial loading conditions, and also conditions that involved thermomechanical loading. The efforts of this project concentrated on two different length scales which correspond to levels 0 and 1 of the fatigue life forecasting plan outlined in Table 3.1. The first scale is a structural level scale where the material would be treated as a continuum that macroscopically follows some form of elasto-plastic constitutive law. The second scale is a microscale where the specific arrangement, orientation, size etc., of grains in the material influence fatigue damage accumulation and initiation. In the following two sections the methods used and results obtained at each length scale will be presented.

B.4.1 Macroscale Model

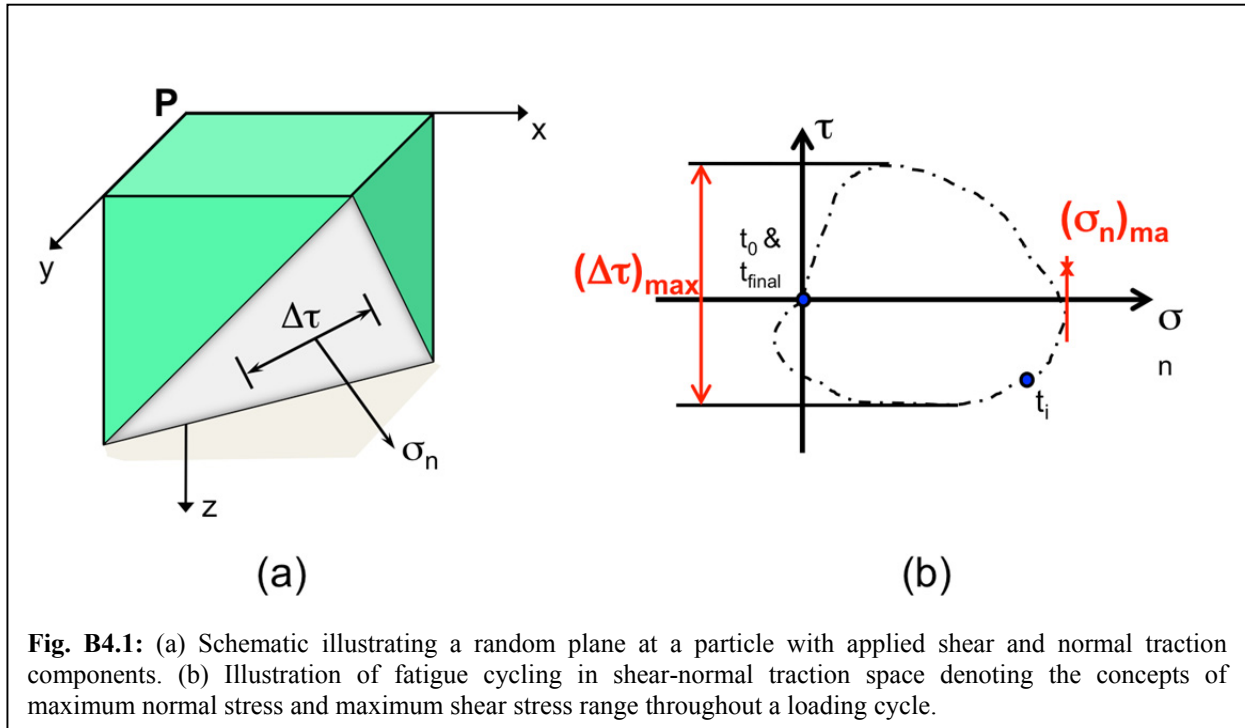
In the current study, it was decided, primarily because of time constraints imposed by the project end date and the delayed start of this effort, to use as a starting point an existing phenomenological multi-axial fatigue model, namely the Findley model (Findley, 1959) is chosen to assess the accumulation of fatigue damage and to predict fatigue crack nucleation due to 3D cyclic loadings. The model, however, did have to be modified for application to elevated temperatures, including thermal cycling, which would be present in the case study to be performed (see section B.3.2. above).

The Findley (1959) model suggests that fatigue damage is driven by a combination of the normal stress, σ_n , and the alternating shear stress, $\Delta\tau$, (both computed on the same shear plane) through the relationship:

$$f = \left(\frac{\Delta\tau}{2} + k\sigma_n \right)_{\max} \quad (\text{B.4-1})$$

where k represents the material sensitivity to σ_n . The value of the expression in parentheses in Eq. B.4-1 varies with shear plane orientation for each material point. Figure B4.1(a) shows a representation of the stress state on an arbitrary plane at a material point P by considering a random section of a plane on the infinitesimally small cube of material centered around point P. The magnitude of the shear stress on that plane is shown as $\Delta\tau$ and the normal stress there is σ_n . As the fatigue loading cycle progresses, both $\Delta\tau$ and σ_n vary. The history of a loading cycle in the $\Delta\tau$ - σ_n plane is schematically illustrated in Fig. B.4.1(b) for one complete loading cycle, i.e., where t_0 and t_{final} coincide. For a single loading cycle Fig. B.4.1(b) shows the definitions of these stress intervals for the purposes of the Findley model: the maximum normal stress σ_n is the magnitude of the largest tensile stress occurring anywhere in the fatigue cycle. The shear stress range however is the *entire* range of shear stress throughout the loading history of the cycle, i.e., from maximum positive shear stress to minimum negative shear stress. The reason for this is that

the shear effects will produce the same amount of material damage, *i.e.*, motion of dislocations *etc.*, no matter which direction the shear load is acting at, whereas compressive normal stress do



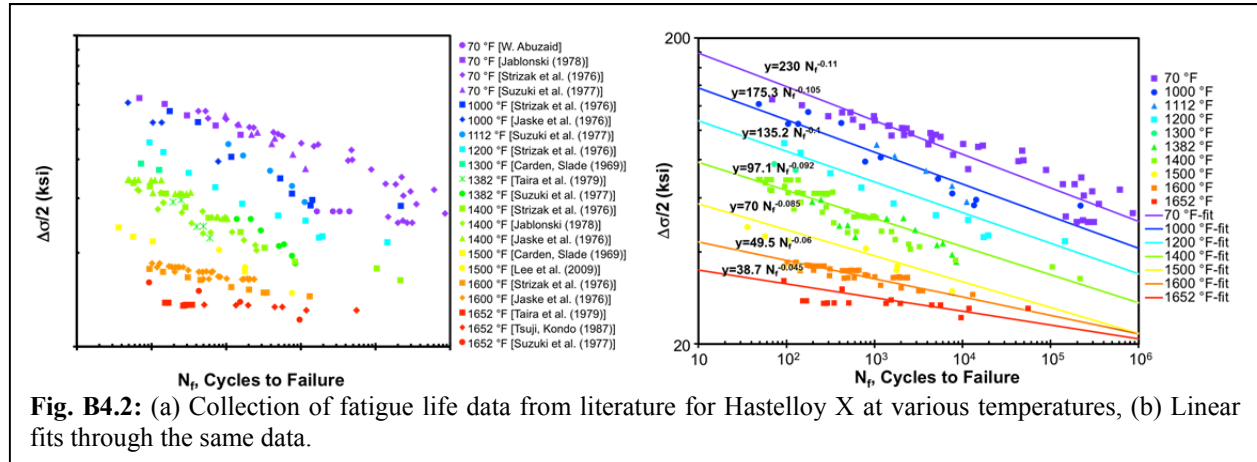
not tend to induce additional damage, certainly not when compared to tensile normal stresses. The maximum value over *all* shear planes throughout the *entire response history* is the Findley parameter, f , and the plane where it is observed is the critical plane.

In terms of implementation of the Findley model there was a close interaction between Drs. Sobotka, Oral and Culler to integrate the Findley model capability with the thermo-aero-acoustic simulation framework and Generalized Plasticity models discussed above. The GP model provides time varying inputs of stress to the Findley model, which then assess fatigue damage. When the Findley parameter reaches a critical value, fatigue failure is deemed to initiate. However, obtaining this critical parameter requires close correspondence with experiments so that it can be calibrated for multiaxial conditions. This was not done in the present work because of the magnitude of the activity's scope. Instead, we used literature results to both integrate thermal effects in the Findley model and to identify critical states. In addition, over multiple cycles a linear accumulation of damage was assumed (*i.e.*, Miner's rule was used for the Findley parameter). In the future, how damage accumulates over multiple cycles would be another possible area of research.

The specific material of interest in the life prediction modeling effort was the Ni-based superalloy Hastelloy X. This material has also been used in most of the experimental efforts in the Center (projects D2, D3 and D4 described later), because of its superior mechanical properties at elevated temperature (up to 1,000 °C). Another advantage of this material is that it has been widely characterized in the past, and a large amount of data on the fatigue response of this material already exist in the literature. Relationships between f and fatigue life, N_f , for the nickel-based superalloy Hastelloy X have been obtained at different temperatures from an extensive literature survey (Carden and Slade, 1969; Brinkman *et al.*, 1976; Jaske *et al.*, 1976; Suzuki *et al.*, 1977; Jablonski, 1978; Taira *et al.*, 1979; Strizak *et al.*, 1981; Tsuji and Kondo,

1987; Lee *et al.*, 2009). Figure B4.2(a) shows the collection of all this literature data for Hastelloy X in one plot of the half-maximum stress range as a function of cycles to failure. Note that the experimental results shown here are from a variety of experimental configurations including uniaxial and biaxial loading, each of which had to be converted to the equivalent stress range plotted in the figure. The temperature ranges from room temperature to about 900°C (1,650°F). Some of the data have been obtained in-house (by Dr. W. Abuzaid), but the vast majority are from the cited literature sources. Figure B4.2(b) shows best line fits to this data. These line fits are what was used when implementing the Findley model in the 3D ramp panel model discussed in B4.

In the model implementation, at a material point, *i.e.*, a node of the 3D model, rain-flow cycle counting (ASTM Standard E 1049, “Practices for Cycle Counting in Fatigue Analysis”) is



performed for the shear stress loading history over differently oriented planes. Fatigue damage is evaluated using the calculated Findley parameter, and the compiled temperature dependent $f-N_f$ relations for each loading cycle. As was mentioned a linear damage accumulation was used.

The macroscopic model based on the Findley parameter has been implemented in a computational framework as described in B.3.2. The results of the combined are shown in Fig. B3.7 where the damage accumulated during a particular flight is shown as a contour plot of the parameter D , defined as $D=1/N_f$. In a uniaxial tension setting $D=1$ would denote complete failure. In the structural context shown in Fig. B3.7 $D=1$ would denote local failure and would necessitate removal of the finite element at that location and replacement with a microcrack. The microcrack would then evolve according to a different law (not the Findley parameter), which was not pursued in this work which was only interested in fatigue crack initiation not growth. This issue however, of how a crack would replace an element and at what value of D this should be done, is an aspect that would need further study. It would have to be linked in some way to microstructural observations because even in a uniaxial setting when D reaches values below 1 local microcracking has begun.

B.4.2 Microscale Model

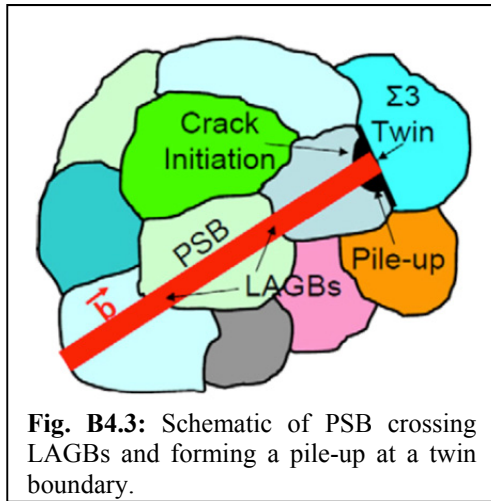
A second aspect of this work was an early incursion into the issues involved in Level 1 modeling and attempted to link a microscale-based model to macroscale quantities. In particular, fatigue crack initiation was assumed to start from the existence of persistent slip bands (PSBs)

that accumulate slip on pile up grain boundaries. Low angle grain boundaries (LAGBs) would allow slip to easily cross them, while high angle grain boundaries (*i.e.*, high misorientation) are more difficult for slip to cross, as is schematically illustrated in Fig. B4.3. As slip accumulates at a pile up, the associated stress concentration will eventually cause microcrack initiation.

The fatigue model used here (described in detail in Sangid *et al.* (2011a,b,c)), predicts fatigue crack initiation based on PSB-GB interaction. In the formulation of the model, the energy of a PSB interacting with a GB is described and its stability is used as a criterion for fatigue crack initiation. The energy expression of a PSB evolves with the number of loading cycles and includes both continuum and atomistic terms as shown in the following expression,

$$\begin{aligned}
 E = & \sum_i \left\{ \underbrace{\frac{\mu b h \pi}{d^2 (1-\nu) \left(\cosh \left(\frac{2\pi h}{d} \right) - 1 \right)}}_{\text{Dislocation pile-ups}} - \underbrace{\alpha \mu b \sqrt{\rho}}_{\text{Work hardening}} - \underbrace{m \Delta \sigma}_{\text{Applied work}} \right\} b L n^{\text{layers}} \partial X_i \quad \left\{ \text{Continuum based terms} \right. \\
 & + \underbrace{\sum_i \partial X_i \cdot \left\{ \sum_j E_{MD,j}^{nuc-GB} L_j^2 \right\} (\rho - \rho_o) b h}_{\text{Dislocation nucleation at GBs}} + \underbrace{\sum_i \partial X_i \cdot E_{MD}^{slip-GB} n_{dis}^{pen} b h}_{\text{Extrusion formation at GBs}} \quad \left\{ \text{Terms derived from atomistic simulations} \right. \\
 & + \underbrace{\sum_i \left(\partial X_i n_{eff}^{\text{layers}} \cdot \int_0^L \gamma_{SF} dL \right)}_{\text{Formation of PSB – Shearing } \gamma \text{ matrix}} \quad \left. \right\} \quad (B.4-2)
 \end{aligned}$$

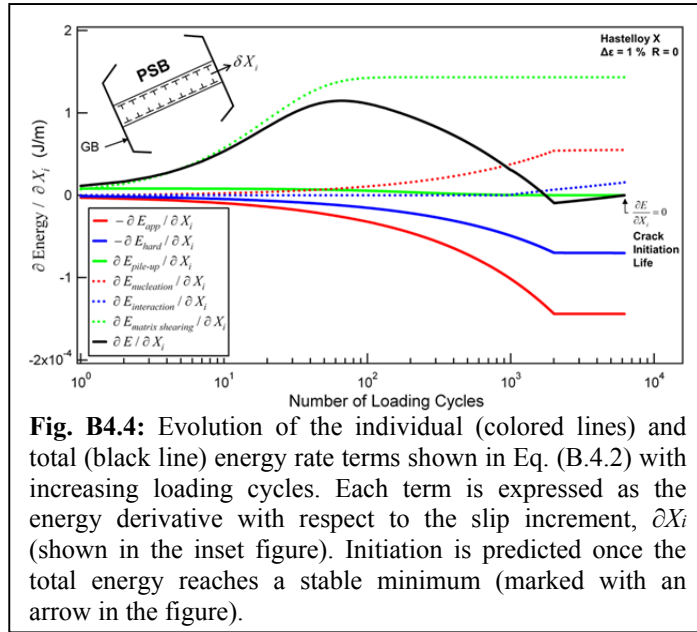
where σ is the applied stress, m is the Schmid factor of the grain containing the PSB, L is the grain size (also assumed to be the length of the PSB in cases where LAGBs allow easy PSB transmission as in Fig. B4.3), N is the number of cycles, ρ is the dislocation density within the PSB, h is the width of the PSB, and d is the mean dislocation spacing within the PSB, Σ is the character of GB in the coincident site lattice (CSL) notation. The three terms in the first parenthesis in Eq. (B.4-2) are those based on continuum mechanics concepts for modeling dislocations. These terms respectively represent the energy of the stress field due to the dislocation pile-ups at the PSB ($E_{pile-up}$), the work hardening energy of the material (E_{hard}), and the energy of the stress field due to the applied forces (E_{app}). The PSB structure consists of a number of dislocation layers (*i.e.*, planes at which dislocations glide), and each plane within the PSB has individual contribution to the continuum terms. Energy from these terms represents an internal barrier which should be overcome by dislocations in order to deform the material plastically. The remainder of the terms in Eq. (B.4-2) are computed from atomistic simulations and represent the energy to nucleate a dislocation from the GB ($E_{nucleation}$), the energy associated



internal barrier which should be overcome by dislocations in order to deform the material plastically. The remainder of the terms in Eq. (B.4-2) are computed from atomistic simulations and represent the energy to nucleate a dislocation from the GB ($E_{nucleation}$), the energy associated

with PSB-GB interaction resulting in dislocation pile-ups and steps/ledges at the GB ($E_{interaction}$), and the energy for the formation of the PSB by shearing the lattice ($E_{lattice\ shearing}$). GBs act as sources of dislocations which are agglomerated in the PSB, and they act as barriers for slip transmission. Each GB has a different energy barrier for dislocation nucleation and dislocation penetration depending on its character. These atomistic energies are incorporated into the evaluation of $E_{nucleation}$ and $E_{interaction}$. The dislocation must overcome an energy which can be associated with destroying the lattice stacking sequence in the matrix to form slip bands by cutting the matrix. This energy corresponds to the stacking fault energy which is incorporated into the evaluation of $E_{lattice\ shearing}$. Writing the energy expression as shown in Eq. (B.4-2) allows us to consider the main microstructural features that influence fatigue crack initiation. For example the Schmid factor, which is related to crystal orientation and loading direction, and grain size are included in the continuum terms of Eq. (B.4-2). By incorporating the atomistic terms, the differences in response between the various types of GBs (different CSL) are also accounted for. This is important if we want to accurately capture and explain some of the previous experimental results on certain types of GBs, particularly $\Sigma 3$ twin boundaries, which have been reported as preferred sites for fatigue crack initiation (Boettner *et al.*, 1964; Heinz and Neumann, 1990; Llanes and Laird, 1992; Miao *et al.*, 2009).

The criterion for when fatigue crack initiation occurs is based on the stability of the PSB. Each of the energy expressions in Eq. (B.4-2) can be expressed in terms of the slip increment



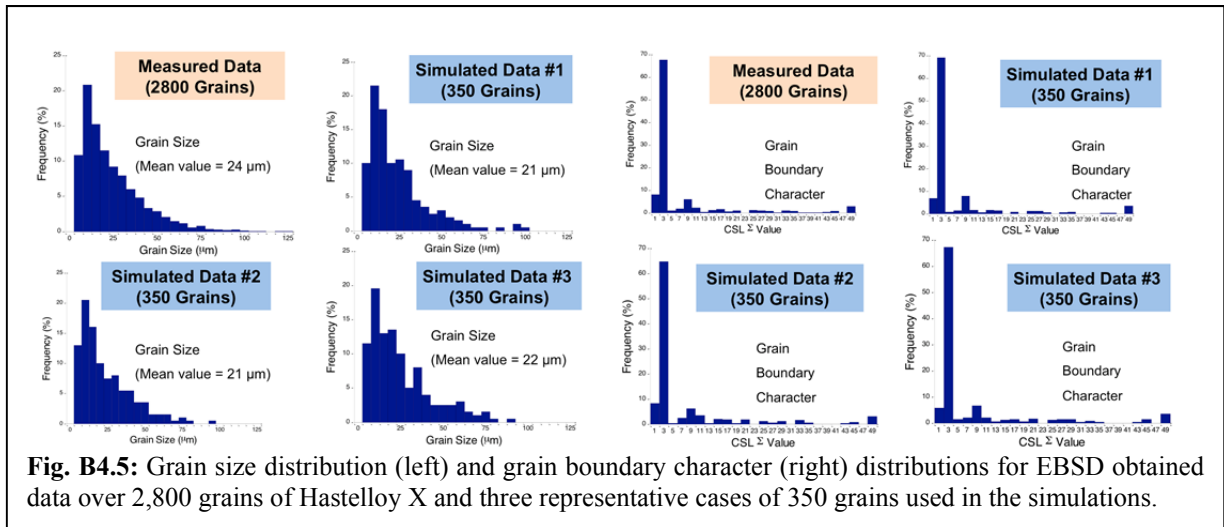
once the magnitude of the total energy derivative reaches zero in addition to the second derivative being positive in order to insure that the energy corresponds to a local and stable minimum, expressed by,

$$\frac{\partial E}{\partial X_i} = 0. \quad (B.4-3)$$

The methodology described above for predicting crack initiation based on PSB-GB interaction is also applicable to polycrystals. In this case, the energy equation is evaluated for

each grain in the aggregate or for each grain cluster, *i.e.*, group of grains connected with low angle GBs (LAGBs). LAGBs allow PSBs to traverse the GB (*i.e.*, slip transmission), thus increasing the length of the PSB and consequently influencing the energy terms in Eq. (B.4-2). Based on this condition for slip transmission (*i.e.*, slip passing through a LAGB), Electron Backscatter Diffraction (EBSD) measurements of grain orientations can be easily used to construct the grain clusters as detailed in Appendix D in Sangid *et al.* (2011c). It should be pointed out, however, that other types of GBs (*e.g.*, $\Sigma 3$ GBs) can under certain conditions (*e.g.*, high resolved shear stress and low residual dislocation as discussed in Lee *et al.* (1989)) allow slip to penetrate through the interface and potentially result in the creation of a grain cluster. In our application of the model for Hastelloy X, we do not account for this and the grain clusters are strictly defined using the concept of LAGBs. Once the grain clusters are defined based on EBSD measurements, the number of cycles to crack initiation for each grain or grain cluster is evaluated in the model, and the minimum calculated number of cycles is considered as a limiting case that determines the life of the aggregate.

The calculated life for a polycrystalline aggregate pertains to that particular microstructure, *i.e.*, the spatial distribution of grain size, orientation, and GB character that is established from EBSD. By spatially varying the microstructure through simulations and reevaluating the life for each of the simulated microstructures, the scatter in fatigue life can be predicted (here we strictly refer to the scatter introduced by the microstructure). In our application of this model, each of the simulated microstructures is derived from the *same* experimental EBSD measurements of Hastelloy X, but with the grains spatially rearranged. Using the EBSD data ($\sim 2,800$ grains in this study), the distribution of grain size, Schmid factor (which relates to grain orientations), number of neighboring grains (each grain is surrounded by a different number of grains), and the GB character (CSL Σ value) are established. These distributions are used to help generate simulated microstructures that are statistically equivalent to the EBSD measurements. Each simulated microstructure consists of a certain number of grains



(*i.e.*, a subset of the EBSD data, 350 grains in this study). For each grain, the grain size, Schmid factor, and number of neighboring grains are assigned and the information of the neighboring grains is selected from the measured distributions until the required number of grains is reached in the simulated aggregate (350 grains). Figure B.4.5 shows examples of the grain size distribution and grain boundary character from the original experimental data of 2800 grains and

for 3 representative microstructures (out of 300 different ones) consisting only of 350 grains. This process of creating a simulated microstructure is repeated to generate a large number of aggregates (300 in this study) which we evaluate the life for each.

Scatter in Fatigue Life

Figure B4.6(a) shows stress-strain curves for selected cycles of one of the Hastelloy X samples loaded in fatigue ($\Delta\epsilon = 1\%$, $R = 0$) that were obtained in terms of project D3 (see below). We observe material hardening in the initial (about 100) cycles, *i.e.*, the increase in the stress range seen in Fig. B4.6(a), and more clearly in Fig. B4.6(b), for cycles 1-100, followed by

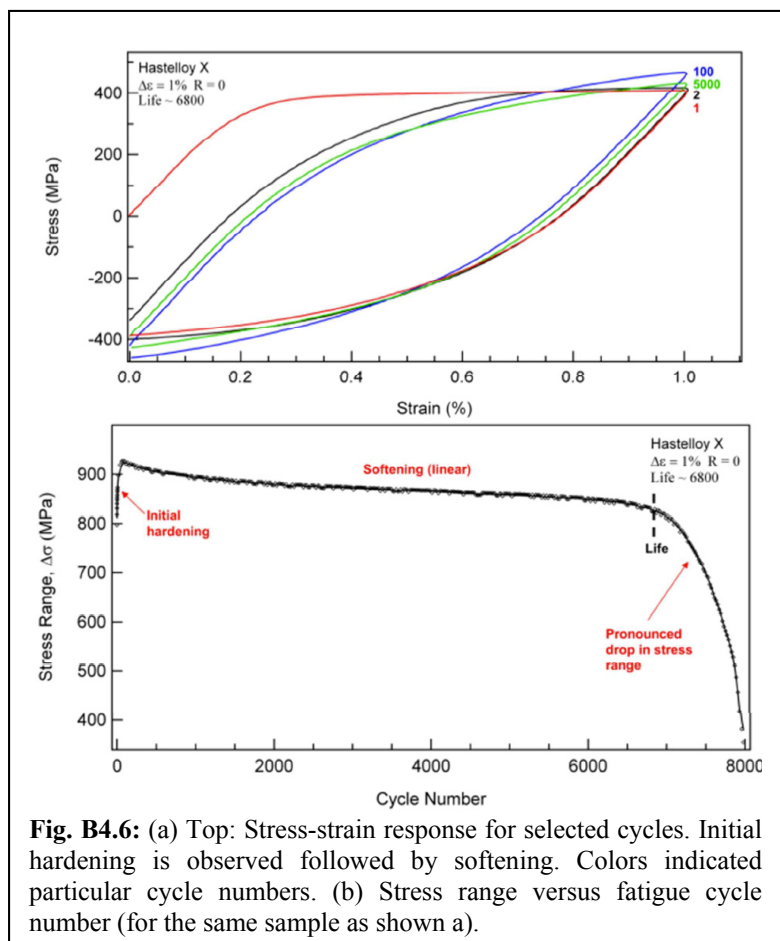
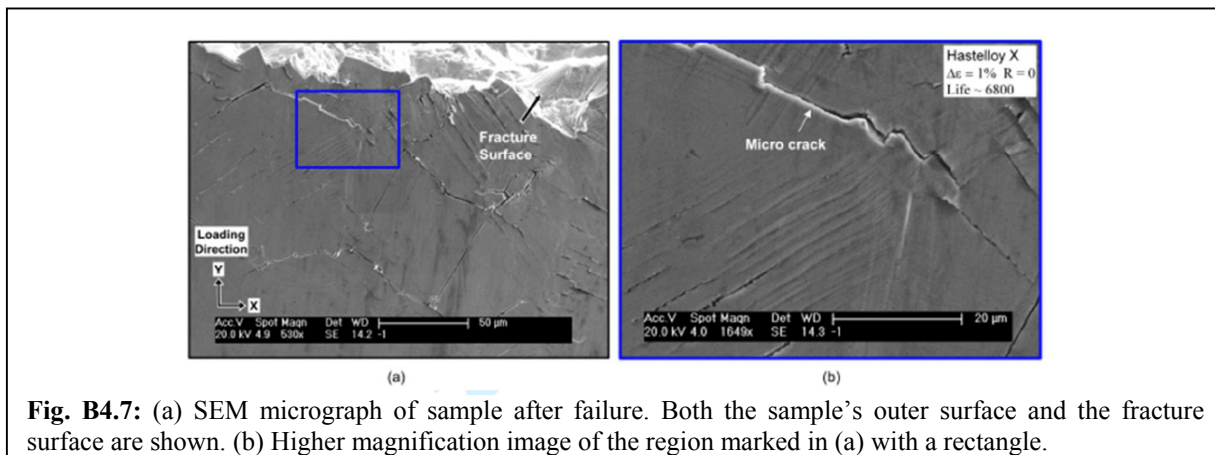


Fig. B4.6: (a) Top: Stress-strain response for selected cycles. Initial hardening is observed followed by softening. Colors indicated particular cycle numbers. (b) Stress range versus fatigue cycle number (for the same sample as shown a).

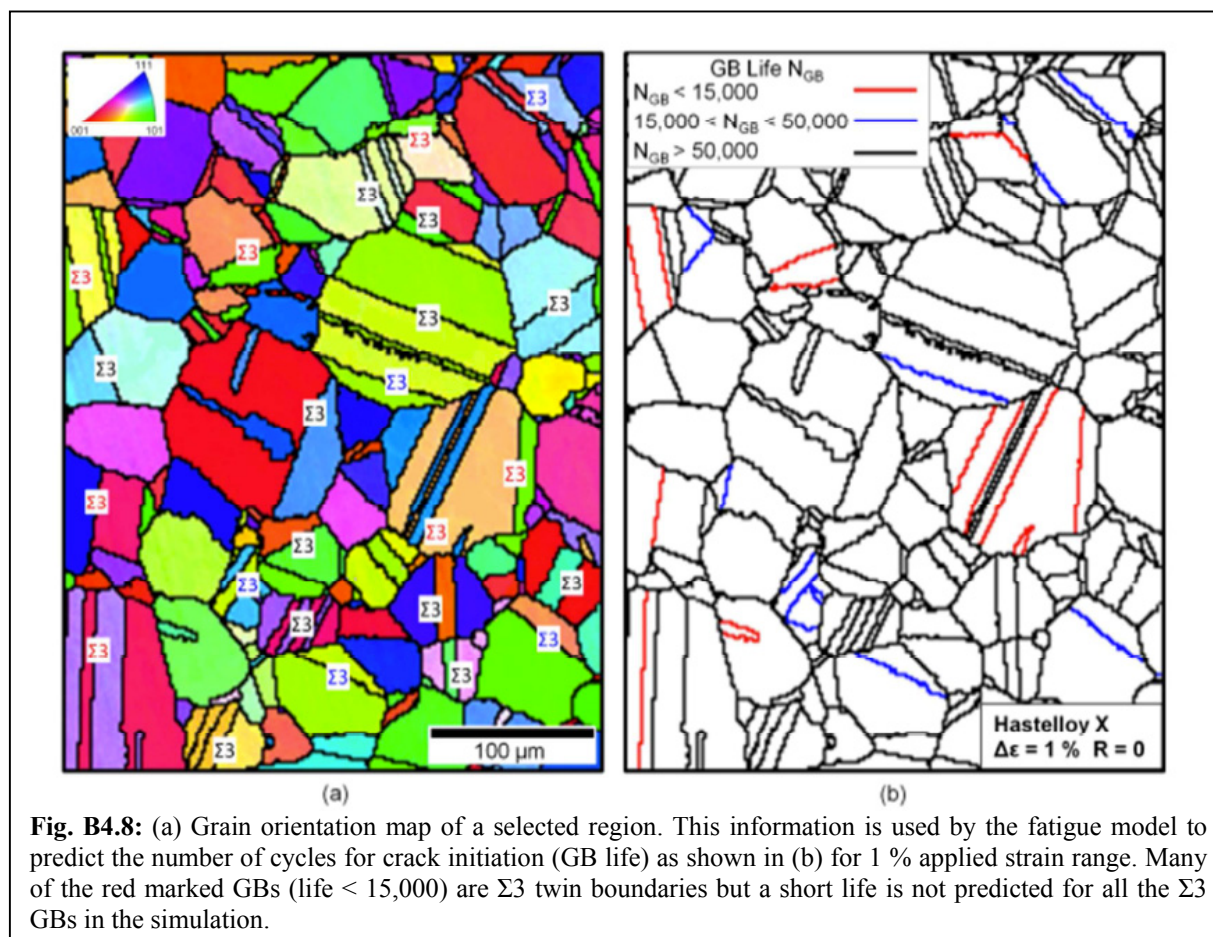
softening until failure. The rate of softening was linear up to the point where a major crack developed in the sample resulting in a sharper and more pronounced stress drop with additional loading cycles. The fatigue lives that we report represent the number of cycles at which this transition was observed, although all samples were fatigue loaded to complete failure (see Fig. B4.6(b) for a pictorial illustration of this definition of “fatigue life”). SEM analysis of the failed samples revealed numerous micro cracks on the sample’s surface (across the entire gage section) in addition to the main crack causing failure (a representative case for one of the tested samples is shown in Fig. B4.7(b)). These micro cracks (notice that no major/main crack has developed in that case) clearly initiate in the vicinity of GBs, *i.e.*, along slip bands and around slip band-GB interaction regions. Because of time and supply constraints only two different strain ranges were tested in D3, 0.8 % and 1.0 %. The fatigue lives for the 0.8 % strain amplitude ranged from 8,200 to 14,000 cycles and for the 1.0 % strain amplitude between 3,200 and 8,000 cycles.

Life Predictions from Simulations

Based on the microstructure characterized using EBSD (see project D3), we evaluated the number of cycles to nucleate a crack (GB life) for each grain cluster using the fatigue model described earlier. A selected region of the entire EBSD scan is shown in Fig. B4.8(a). The



predicted GB life (N_{GB}) is plotted spatially for this region in Fig. B4.8(b). Different GB colors indicate different life ranges which are defined in the legend of this figure. The GBs colored with



red correspond to lives less than 15,000 cycles, blue GBs represent lives between 15,000 and

50,000 cycles and finally the black boundaries have lives exceeding 50,000. Many of the red marked GBs (life < 15,000) are $\Sigma 3$ twin boundaries, which is consistent with experimental observations of their tendency to nucleate fatigue cracks. We emphasize that short lives are not predicted for all of the $\Sigma 3$ GBs. Depending on the energy terms described in Eq. (B.4-2), each particular $\Sigma 3$ GB, and each GB in general, will have a different predicted life.

Figure B4.8(b) displays the number of cycles to reach a critical state of initiation for each GB. The GB with minimum number of cycles to initiation dictates the life of the aggregate (from the simulation). This life corresponds to a PSB reaching a stable minimum energy configuration and resulting in crack initiation at the PSB-GB intersection region (due to the formation of steps/ledges). The crack length is not defined in the model formulation although one may expect

that following initiation at the PSB-GB interaction region, the crack will grow to the PSB length (cluster length) within a relatively short number of cycles. In this work, we compare the life from simulations with experimental life results, which as defined above (Fig. B4.6) is not really the life to complete failure. Since a crack length is not defined in both cases, some deviation between the lives established experimentally and through simulation is likely. Nevertheless, we expect that the difference between the number of cycles to generate a crack length on the order of the cluster size (multiple grains) to be close to the life as defined in our experiments. The microstructure characterized using EBSD is then varied to create simulated microstructures as discussed above. By reevaluating the life for each of the simulated aggregates, we *predicted* a scatter in fatigue life. The number of cycles for fatigue crack initiation, as predicted from the model (red diamonds), and the

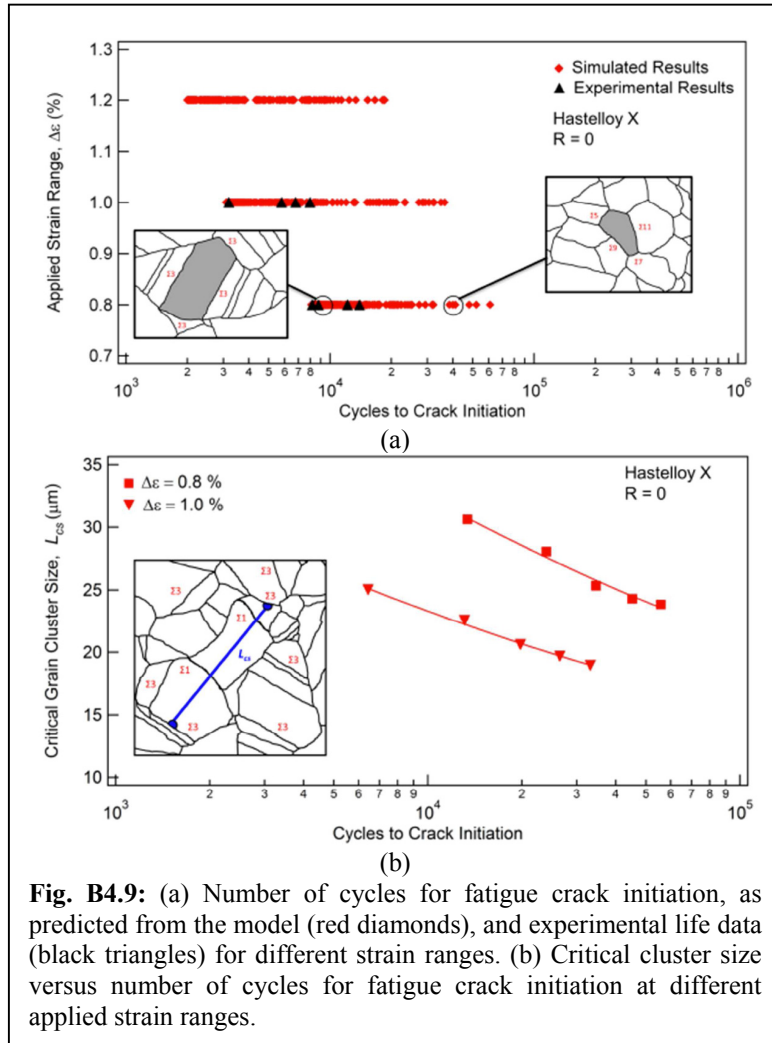


Fig. B4.9: (a) Number of cycles for fatigue crack initiation, as predicted from the model (red diamonds), and experimental life data (black triangles) for different strain ranges. (b) Critical cluster size versus number of cycles for fatigue crack initiation at different applied strain ranges.

experimental life data (black triangles) for different strain ranges are plotted together in Fig. 4.9(a).

The simulations are established from 300 different simulated aggregates at three different strain ranges; 1.2, 1.0 and 0.8 % applied strains. The experimental results from D3 are given for 1.0 and 0.8 % applied strain ranges. Experiments at 1.2 % were not possible with the sample dimensions used in D3. The 1.2% simulations are included to show the prediction capability of

the model outside the range tested. The modeling approach yields good predictions of the experimental scatter in fatigue life (about 85 % of the simulated life predictions are within the range of the set of experimental values).

The scatter in life from simulations is introduced by *variations in the simulated microstructures* (i.e., difference in grain size, grain boundary character, grain boundary neighbor information, Schmid factor, etc.). The critical grain clusters which exhibit the minimum life can be in the form of a single grain or a group of grains that are connected with slip transmission permitted at low angle grain boundaries. Slip transmission through multiple GBs increases the cluster size and continues until slip is impeded, thus creating a pile-up, by a blocking high angle GB. Therefore, critical grain clusters are typically surrounded by high angle grain boundaries (e.g., $\Sigma 3$) where blockage occurs. The implication of the increase in cluster size as stated earlier is that it increases the length of the PSB and consequently, the energy terms in Eq. (B.4-2). The shaded grain clusters shown in the insets of Fig. 4.9(a) show the extreme cases where crack initiation is predicted. The grain cluster on the left with lower cycles to crack initiation corresponds to a large grain surrounded by smaller grains, and its grain boundary characteristics are mainly $\Sigma 3$ twin boundaries which exhibit the highest energy barrier for slip transmission. The grain cluster on the right with higher cycles to crack initiation is surrounded by almost equiaxed grains, and with no $\Sigma 3$ twin boundaries.

The effect of the critical grain cluster size, L_{cs} on fatigue crack initiation is illustrated in Fig. 4.9(b). In this figure, the inset schematically shows a representative grain cluster and its size, L_{cs} . This grain cluster consists of three grains which are connected by $\Sigma 1$ low angle grain boundaries. To obtain the data points in Fig. 4.9(b), the entire range of cycles to crack initiation for each strain range in Fig. 4.9(a) is divided into five equal intervals (binned based on number of cycles to crack initiation). Then, mean values of critical grain cluster size and mean values for cycles to crack initiation within each interval are plotted in Fig. 4.9(b). The size of the grain cluster where fatigue crack initiation is predicted decreases with increasing number of cycles to crack initiation. The following equation is obtained by fitting to the simulations results in Fig. 4.9(b),

$$\Delta \varepsilon = 0.128 N_{in}^{-0.09} L_{cs}^{-0.55}, \quad (B.4-4)$$

where ε is the applied strain range, N_{in} is the number of cycles to crack initiation to a critical size, and L_{cs} is the critical grain cluster size in μm . Similar to the Hall-Petch type relation, Eq. (B.4-4) exhibits almost a square root dependence for the grain cluster size. The results presented in Fig. 4.9(b), which lead to Eq. (B.4-4), represent a statistical approach to examining the importance of the microstructural attributes considered in the fatigue model, in this case the cluster size, on the number of cycles to crack initiation. Similar analysis on the other contributing factors can help us identify the key parameters that have the largest influence on the calculated life.

Summary

In this project a recently developed crack initiation fatigue model and novel high resolution experimental measurements were combined to investigate the scatter in fatigue life for the nickel based superalloy, Hastelloy X. The major contributions and outcomes of this project are summarized as follows:

- The fatigue model developed by Sangid *et al.* (2011a,b,c) and applied here to Hastelloy X can predict the experimentally observed scatter in fatigue life *relying only on the microstructural variations established through simulated microstructures* (based on EBSD measurements but with grains rearranged spatially).
- The variation in fatigue life was linked to a grain cluster size L_{cs} , defined as a series of grains bounded by GBs unfavorable for slip transmission. Experimental observation from DIC showed evidence of strain localization in grain clusters which supports the modeling approach. The critical grain cluster size L_{cs} is an *outcome* of the model used and provides a possible means for the statistical “upscaling” of the microstructurally based life predictions to a macroscale model. For example, a macroscale model that wants to include fatigue life variability can do so by including a dependence of fatigue life on the parameter L_{cs} – grain cluster size – which can then either be furnished by a lower order set of simulations (as those described here), or for a specific alloy could be determined by microscopy experiments on a number of samples extracted from various places of the material microstructure.

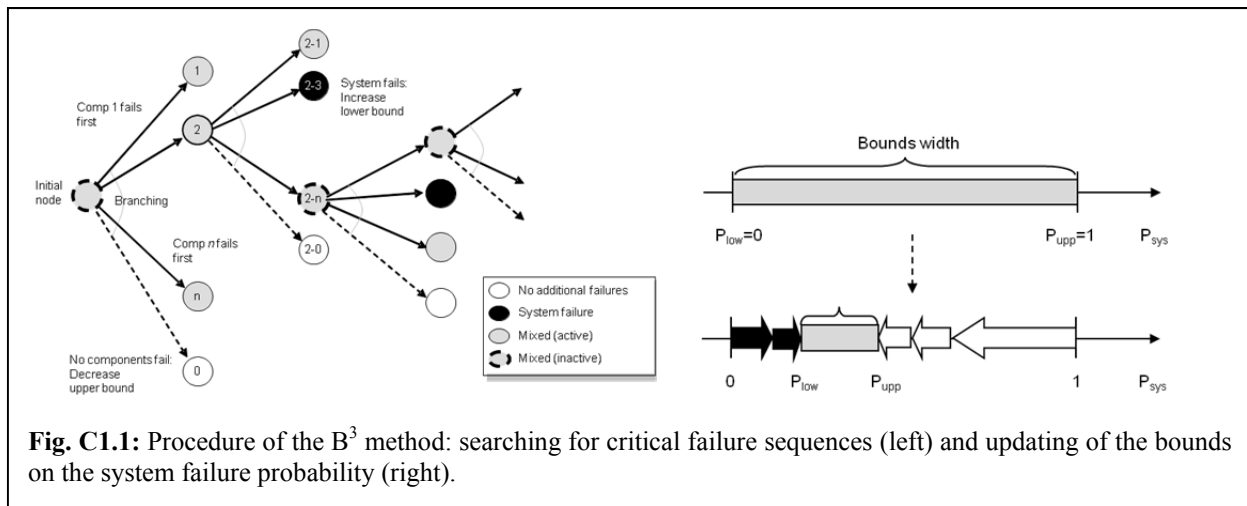
C1 Uncertainty/Risk Quantification Methods for STATS

Personnel: Song, Lee (Graduate student, UIUC), Tuegel (AFRL)

Start: 2006; End: 2010

Aircraft structures are often subjected to the risk of progressive failure caused by fatigue crack growth under repeated loadings. However, due to uncertainties in material, loadings and mathematical models, and the complex effects of load re-distributions, it is a challenging task to estimate the reliability of aging aircraft pertaining to crack growth. The goals of this research project are: (i) to develop novel system reliability analysis methods for estimating the probability of system-level failure caused by fatigue and for identifying critical failure sequences; (ii) to integrate the developed methods with advanced finite element (FE) simulations of aircraft structural systems; and (iii) to suggest a new framework for updating the estimated failure probability based on inspection results. The outcomes of the research will make crucial contribution to the risk-based life forecasting and condition-based maintenance of aircraft structures.

Based on a literature review and discussions with other researchers in MSSC, we developed a new Branch and Bound method employing system reliability Bounds, termed the “B³ method.” Fig. C1.1 illustrates the procedure of searching for critical failure sequences (left) and the corresponding updating of the bounds on the system failure probability (right). The method



enables us to estimate the risk of progressive failure accurately while minimizing the cost of finite element (FE) analysis. In addition, the method can identify most critical failure sequences in the decreasing order of their probabilities. The B³ method was successfully demonstrated by a three-dimensional truss structure.

The B³ method was subsequently generalized for continuum structures. In order to test the applicability of the generalized B³ method to continuum aircraft structures, an FE model of an aircraft longeron system was developed through collaboration with other MSSC researchers including Prof. Harry Millwater (University of Texas at San Antonio) and Luciano Smith (Southwest Research Institute) who were responsible for project C4. A detailed mechanism of fatigue-induced sequential failures of the generic aircraft longeron was formulated through collaborations as well. The developed FE model simulated fatigue-induced local failures so that the load re-distributions caused by sequential failures could be considered during the B³ analysis.

Fig. C1.2 shows the details of the developed FE model including locations of the fastener holes (left) and an example of stress re-distribution caused by a local cracking occurred around a fastener hole (right). The generalized B^3 method was successfully applied to the longeron structure, and Table C1.1 shows a variety of critical system-failure modes identified by the B^3 analysis.

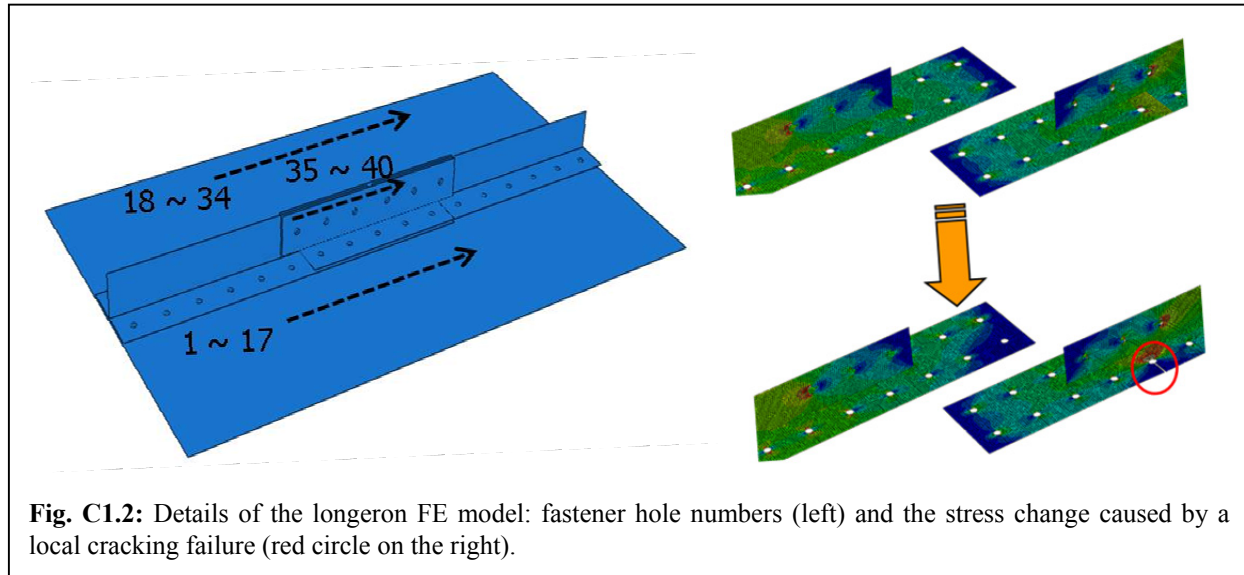


Fig. C1.2: Details of the longeron FE model: fastener hole numbers (left) and the stress change caused by a local cracking failure (red circle on the right).

Table C1.1: Critical failure sequences in the longeron identified by the generalized B^3 method

Failure sequence	Probability ($\times 10^{-3}$)	Yielding material	Yielding location
11	4.448	aluminum	around #11 hole
28	4.448	aluminum	around #28 hole
22 \rightarrow 5	0.480	steel	#35 fastener
5 \rightarrow 22	0.480	steel	#35 fastener
23 \rightarrow 11	0.282	aluminum	around #11 hole
6 \rightarrow 28	0.282	aluminum	around #28 hole
6 \rightarrow 22 \rightarrow 4	0.109	steel	#35 fastener
23 \rightarrow 5 \rightarrow 21	0.109	steel	#35 fastener

Currently, the generalized B^3 method is being integrated with a Bayesian approach to update the reliability estimates by the B^3 method based on the results of inspection on fatigue crack growth. Tests by discrete structural systems showed that the B^3 method enables the Bayesian approach to update the probability of the system-level failure based on various types of inspection results efficiently and accurately. The new updating approach is being tested by the developed longeron FE model under a variety of inspection scenarios. The developed method is expected to provide an effective probabilistic framework for condition-based maintenance of aircraft systems.

C2a Validation of Simulations Having Uncertainties in Both Simulation and Experiments

Personnel: Brandyberry, Gruenwald (Graduate student, UIUC), Haney(AFRL), Smarslok (AFRL)

Start: 2006; Completed: 2012

The goal of this project was the development of a robust methodology for the validation of complex structures simulations under the presence of uncertainty. This methodology allows the propagation of uncertainties through a computational model for comparison with experimental

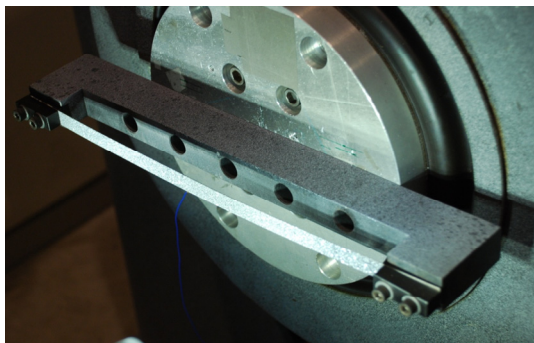


Fig. C2.1: The beam fixed in the testing apparatus and mounted on the electromagnetic shaker.

data, while minimizing the computational expense. A curved beam under harmonic loading was selected as a simple surrogate problem that is similar to the vibration of thin-skinned panels on aircraft. Experiments on curved beams, Fig. C2.1, were conducted at WPAFB to generate data for the methodology.

The process uses the *Reduced Order Clustering Uncertainty Quantification (ROCUQ)* methodology developed at Illinois (Bradyberry, 2008). The ROCUQ method allows for uncertainties in simulation input parameters to be efficiently propagated through computationally expensive simulation models, in order to generate distributions of output parameters of interest (System Response Quantities, or SRQs). These simulation distributions can be created and compared to experimental data (which also

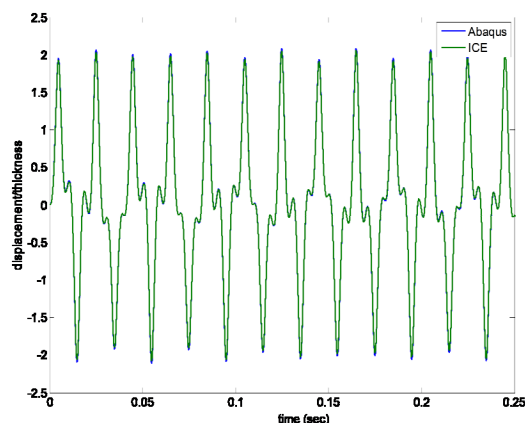


Fig. C2.2: Center displacement/thickness vs time plot for straight beam under 0.2 psi harmonic loading at 50 Hz. Simulations conducted by Abaqus and Matlab ICE program are compared and are nearly identical.

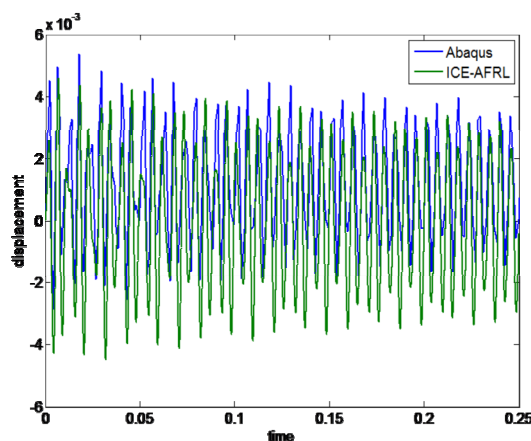


Fig. C2.3: Center displacement vs time plot for curved beam under 0.1 psi harmonic loading at 180 Hz. Simulations conducted by Abaqus and Matlab ICE program are compared.

has uncertainty associated with it). The foundation of the ROCUQ method is the use of Reduced Order Models (ROMs) to decrease computational expense and, most importantly, model the trends in SRQs.

Progress has been made in creating a ROM for the vibrating beam. The Implicit Condensation and Expansion (ICE) method was chosen for the ROM (Hollkamp and Gordon, 2008). This method satisfies the requirements of ROCUQ – it is fast running and has the ability to model all of the uncertain parameters in the simulation. The ICE method has also been shown to model nonlinear displacements accurately for a similar problem (Hollkamp and Gordon, 2008). ICE leverages commercial FEA programs to perform a regression analysis of static nonlinear test cases to find nonlinear equations of motion. Direct integration is then used on the equations of motion to determine displacements, strains, and stresses. Using straight and curved beam problems as described in (Hollkamp and Gordon, 2008), Abaqus simulations were performed and compared to ICE results. Figs. C2.1 and C2.3 show the comparison for harmonic loading for the straight and curved beams, respectively. The results are nearly exact for the straight beam case, whereas, there are discrepancies in the curved beam. These discrepancies are being investigated and once resolved, the ROM will be considered verified. The uncertain parameters that are going to be modeled in the simulation include: geometric parameters (width, thickness, radius of curvature); material properties (Young's modulus, Poisson's ratio, density); and the loading amplitude and frequency.

The experimental setup is described in Ehrhardt *et al.* (2001). A clamped-clamped curved beam was subjected to swept sine tests with a base excitation of 9g's and at a rate of 55 Hz/s over the frequency range of 60-430 Hz. Two high-speed cameras with a resolution of 1024x512 pixels operating at 3000 fps were used to capture the images. Data from these experiments will be used to validate the simulations and ROCUQ methodology.

With the completion of the ROM, the ROCUQ methodology will be used to perform an uncertainty propagation through the simulation, with an SRQ of the RMS value of the beam center displacement. The resulting cumulative distribution function(s) (CDF) for the SRQ(s) will be compared to similar CDF(s) from the experimental data, including the uncertainty estimates in both.

C2b Tudor Simulation and Force Analysis of a T-38 Performing a Touch-And-Go Maneuver

Personnel: Brandyberry, Tudor (Graduate student, UIUC), Tuegel (AFRL)

Start: 2011; Completed: 2012

This project involved deriving a framework for taking aircraft flight recorder data and simulating aircraft surface loading along a flight path using computational fluid dynamics (CFD), and then developing force information from the CFD surface pressure results for a USAF T-38. The force data was used to simulate forces on the aircraft in a structural mechanics program, ultimately to obtain stress information at several key locations. The CFD simulations were performed in a static sense where the T-38 is simulated at specific "points in the sky" without the inclusion of changing orientation or velocity during each CFD simulation. A series of 10 points were chosen from a 51 second touch-and-go maneuver by observing points along the flight-path where the speed and/or orientation of the aircraft changed significantly. Simulation results were then compared with thin airfoil theory to assess the reasonableness of the simulation.

The flight profile used in the current work was taken from an actual touch-and-go landing performed by a T-38. A suite of sensors on board the aircraft comprise the data collection process. In order to obtain a flight profile the following variables were examined: translational accelerations, angular rates, angle of attack, time and landing gear up/down. Using these variables the T-38 body frame translational velocities as a function of time may be derived.

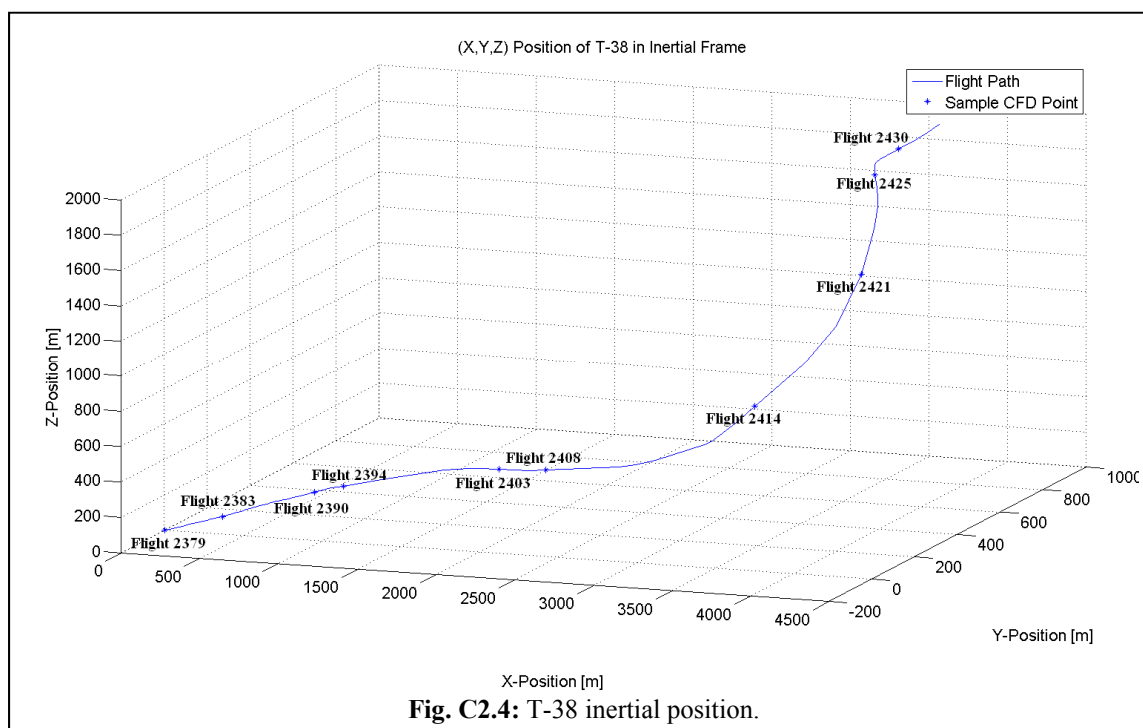
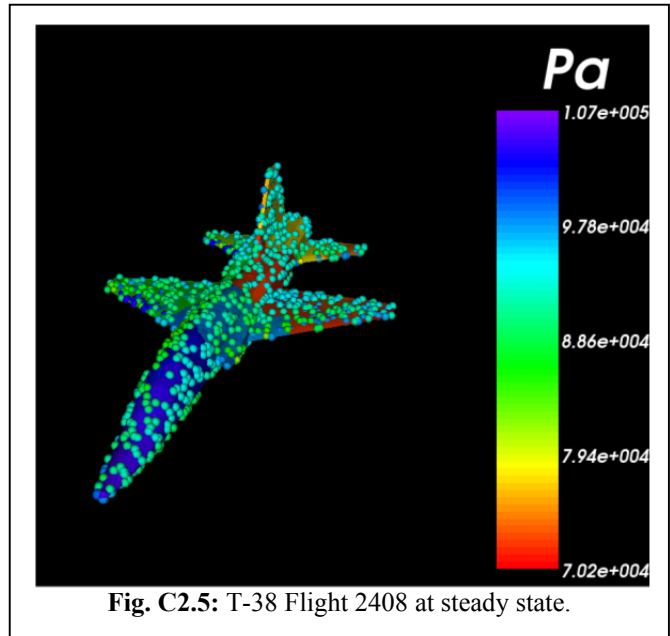


Fig. C2.4: T-38 inertial position.

Fig. C2.4 shows the Cartesian coordinate flight path for the takeoff and initial turn of the aircraft in the touch and go run. The points along the flight path where CFD simulations were performed are noted on the line with the four digit numbers denoting a number of seconds since recording began for the flight. Notice the aircraft begins its flight with a small angle of attack then begins to turn at 2408 seconds (the “Flight 2408” point in Fig. C2.4). The aircraft first performs a roll then begins to pitch causing the aircraft to turn. Using the orientation of the T-38, the translational velocity of the aircraft in its body frame was calculated. The translational velocity is the essential information for performing a CFD simulation at a specific time in the sky. Since the aircraft was not changing orientation or velocity quickly along this flight-path the points chosen along the path will generate a reasonable first-order approximation to the surface pressure loads on the aircraft.

These velocities were input as boundary conditions directly into the CFD solver (The *Rocflu* unstructured mixed-mesh solver in the *Rocstar Simulation Suite*). At each CFD point-in-the-sky, the T-38 flow field was run to steady-state in order to produce the resulting pressures, and thus surface forces on the aircraft. The CFD grid was composed of 126737 unstructured four-node tetrahedral elements. This generated 49588 elements on the surface of the aircraft. This grid was then enclosed in a cube where the inflow velocity and orientation boundary conditions can be specified. The boundary conditions used are the body frame translational velocities as discussed previously. As a result, the only differences between the 10 simulations are the boundary conditions that control the simulated orientation and velocity of the aircraft. When each simulation of a point in the sky was complete, the tractions were stripped off of the surface of the

aircraft and converted to element based forces. These forces were then provided to AFRL analysts for computation of the structural response of the aircraft. Fig. C2.5 shows one simulated pressure distribution on the surface of the aircraft for point-in-the-sky 2408. A variety of drag, lift and force checks were performed on the CFD pressure field results to ensure that reasonable values are being generated by the calculated flow field. The *Rocstar* CFD results are compared to results from *Aeromatic*, *XFOIL* (Anderson, 2005) to grossly verify the CFD simulations. Ongoing work involves simulating further points in the sky to generate a better characterization of the flight path, performing a grid refinement study, and investigating the use of overset mesh/moving grid CFD technologies in the *Rocstar Simulation Suite* to perform a continuous flight path simulation of the touch and go maneuver.



C3 Risk-Based Design Plots for Aircraft Damage Tolerant Design

Personnel: Penmetsa

Start: 2007; End: 2008

Traditional risk-based design process involves designing a structure based on risk estimates obtained during several iterations of an optimization routine. This approach is computationally expensive for large-scale aircraft structural systems. Therefore, this research introduces the concept of risk based design plots that can be used for both structural sizing and risk assessment. These plots are obtained using normalized probability distribution functions (PDF) of load and material properties and are parameterized to be applicable for a wide range of structural configurations. Risk based design plots serve as a tool for failure probability assessment given geometry and applied load or they can determine geometric constraints to be used in sizing given acceptable failure probability. This approach would transform a reliability based optimization problem into a deterministic optimization problem with geometric constraints that implicitly incorporate risk into the design.

A key concept that was developed during this research was the “distance factor”, which is a measure of the magnitude of separation between load and resistance probability distribution functions. The mathematical definition of this distance factor depends on the failure criteria being considered, as shown in Fig. C3.1. These variations are introduced into the definitions in order to incorporate the general design values adopted in the aerospace industry for load and material property definitions. Typically load is defined using limit load (LL), yield strength is defined using A or B basis allowables (F_{ty}), and fracture toughness (K_C) is defined using a nominal value. Therefore, if the failure criterion is based on load and yield strength like in net-section yield, then the distance factor is a measure of distance between the limit load and A or B basis strength value. On the other hand for fracture criteria the distance factor is a measure of separation of stress at limit load and mean residual strength.

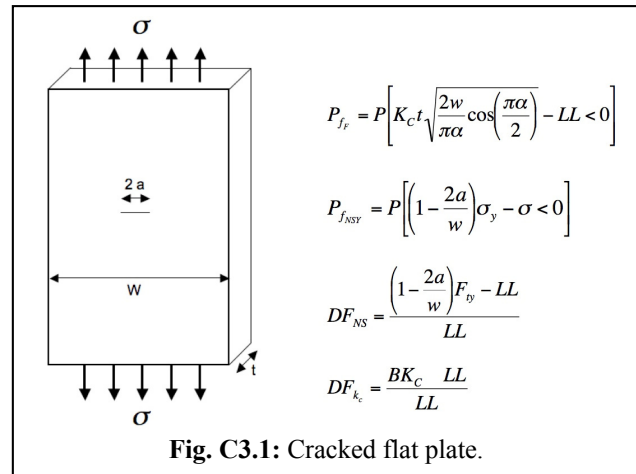
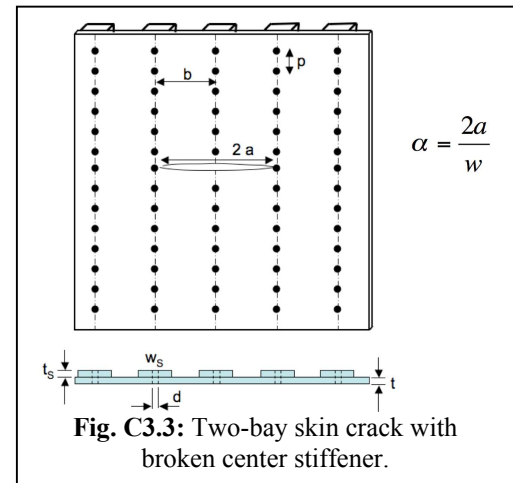
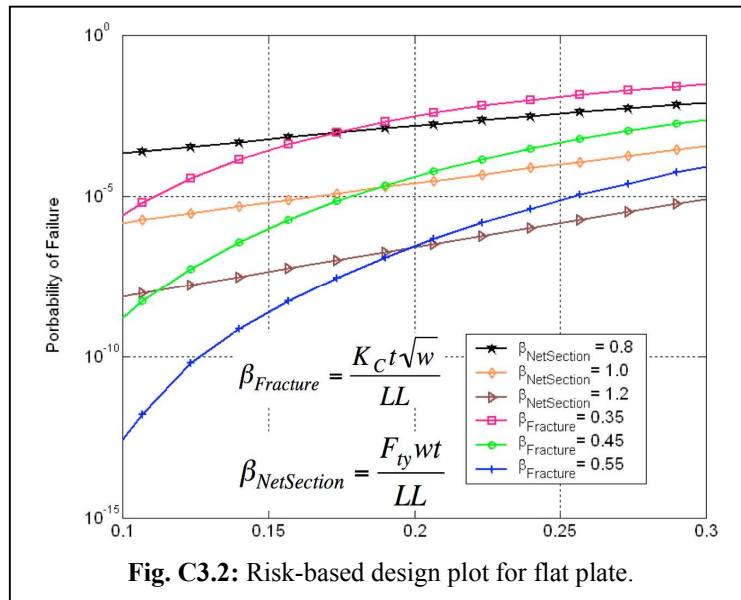


Fig. C3.1: Cracked flat plate.

The discovery of this important factor enabled successful development of risk based design plots (Fig. C3.2) for flat plates under uniaxial tension for the two failure criteria, net section yielding and fracture. Once these plots are generated further analysis of various structural configurations (geometry and crack length) that are made of the same material and subjected to the same loading spectrum would require no additional risk analysis. Therefore, these design plots can be generated for combinations of materials and loading spectrum to perform risk based comparative studies with minimal computational effort.

In order to demonstrate this technology on other aircraft structural components, a riveted stiffened panel, Fig. C3.3, was considered as the next test case. This stiffened panel was analyzed using displacement compatibility method, which solves for unknown fastener forces by equating the displacements in the plate and stiffener due to applied loads. This semi-analytical method estimates the fastener forces numerically using minimal computational effort and then uses

analytical expressions to determine the stress intensity factors. The stiffened panel was also modeled using ABAQUS and FRANC2DL to compare the accuracy of the semi-analytical method. After verifying its accuracy this method was selected to develop risk based design plots because of the ease of modeling various stiffener configurations. This method does not require any finite element meshing and re-meshing and also automatically analyzes both intact and broken stiffener configurations.



C4 System Reliability with Correlated Failure Modes

Personnel: Millwater, Smith, Sparkman, Wieland, Tuegel

Start: 2008; End: 2011

New aircraft systems are also likely to be constructed of novel materials, operate in extreme environments, and be of limited productions runs. As a result, experience-based methods for determining critical failure locations and failure modes may be lacking. Therefore, a systemic reliability-based methodology was developed to supplement engineering judgment and determine critical locations that are candidates for careful analysis and monitoring during testing and operation. Calculation of system reliability of large-scale aircraft structures is frequently intractable because of the potentially thousands of failure locations, hundreds of load cases and multiple failure modes. Consequently, a probability-based filtering technique – referred to as the Correlation-Conditional Probability (CCP) filtering method – was developed to complement engineering judgment by algorithmically determining the failure locations, load cases, and failure modes that will contribute to the estimation of the system reliability, thereby significantly reducing the complexity of the system reliability analysis. These locations may also serve as key monitoring points for structural certification and structural health monitoring. The central theme of the research is to let the structure define the failure modes and locations as opposed to human-developed cut sets and fault trees.

The method is based on three fundamental tenets: (i) Identify local probability-based “hot spots” using approximate, fast-to-compute probability of failure estimates at multiple locations, (ii) use correlation estimates between hot spots and joint probabilities to down select to a set of uncorrelated, or nearly so, important failure locations, and (iii) perform more sophisticated analysis on this limited number of failure locations using more accurate system reliability methods to calculate probabilities of failure on this reduced number of failure locations. The same methodology will be extended to

multiple load cases, failure modes and progressive failure. An example is shown in Fig. C4.1 which illustrates the failure domain for two load cases that can potentially generate failure at 30 possible locations (*i.e.*, “hot spots”). Of the 30 possible failure modes only 4 (namely, 1, 5, 26 and 30) control the entire failure domain of the structure and therefore are the only four necessary to be considered (*i.e.*, uncorrelated failure modes). It is worth pointing out that if failure mode 5 were excluded from this set the error in the failure domain is illustrated in purple in Fig. C4.1.

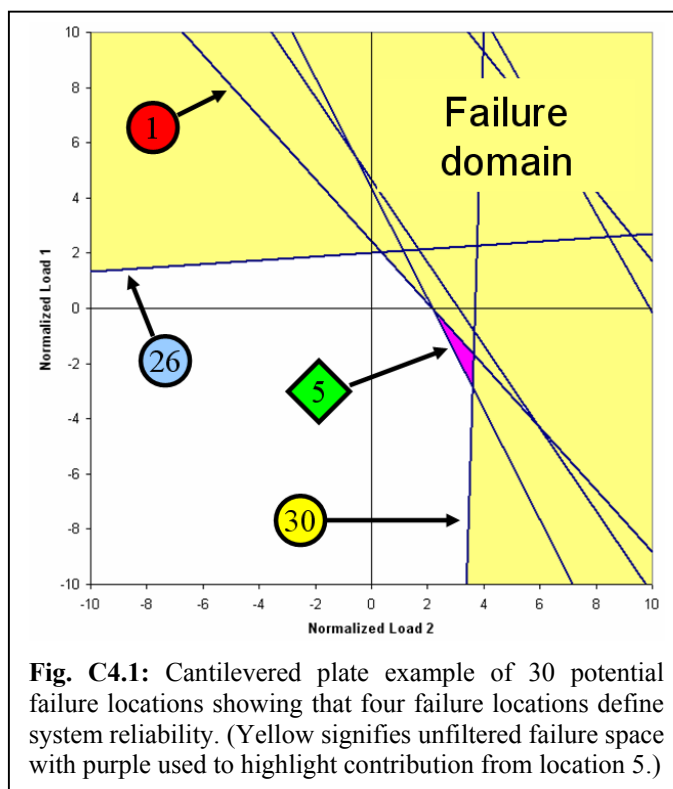


Fig. C4.1: Cantilevered plate example of 30 potential failure locations showing that four failure locations define system reliability. (Yellow signifies unfiltered failure space with purple used to highlight contribution from location 5.)

This methodology uses a formal pairwise error metric that determines the relative error in the system reliability should a limit state be filtered. The error metric considers the relative probabilities of failure and the correlation between limit states. Limit states with a filtering error above a threshold are kept and those below filtered. An efficient numerical method to evaluate the relative error was implemented that obtains accuracy to approximately 10^{-16} . Second order bounds are used to estimate the cumulative effect of all limit states. Both FORM (First Order Reliability Method) and sampling approaches have been developed that use the error metric as a bases for determining critical limit states.

The methodology was demonstrated using a T-38 lower wing skin analysis among others. Four different load cases were created and analyzed: (i) ultimate flight condition, which represented the greatest loading expected to be seen by the wing and included both bending and torsion, (ii) subsonic fatigue, (iii) supersonic fatigue, and (iv) landing. Random variables were the stiffnesses of the nine different materials in the model (10% coefficient of variation) and the yield strength of the lower wing skin (3.3% coefficient of variation). The methodology indicated that the root radius was the critical location. Figure C4.2 shows the correlation between all other locations and the root radius. Continuing studies concern the damage tolerance analysis of 133 holes located in a T-38 longeron as shown in Fig. C4.3 (longeron region highlighted in red).

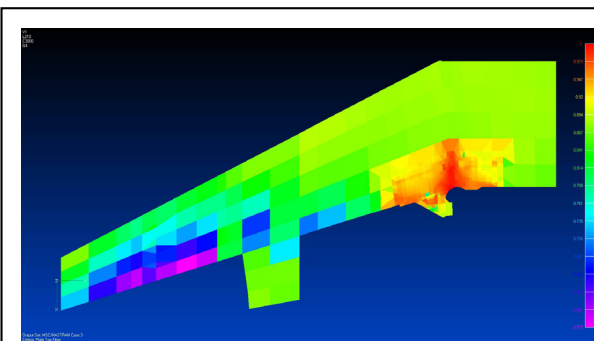


Fig. C4.2: Correlation of stresses to high stress location in root radius.

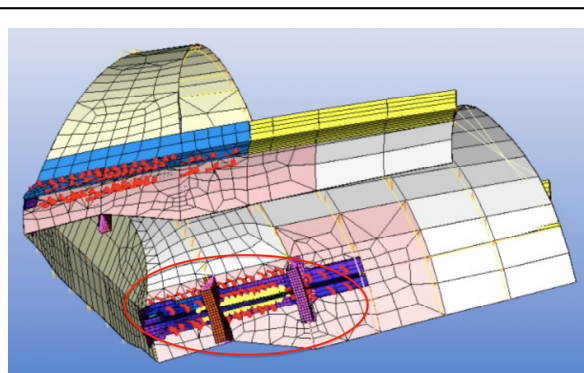


Fig. C4.3: T-38 longeron damage tolerance analysis.

C5 Probabilistic Cohesive Zone Model for Fiber Bridging

Personel: Penmetsa, Kable, Shanmugam, Tuegel (AFRL)

Start: 2008; End: 2010

Delamination between plies is the most common failure mode encountered in composite laminates and usually originates at edges such as at holes and notches. Interply delamination can cause fiber breakage and reduce the ultimate life of the composite. Generally Mode-I interlaminar fracture toughness or critical energy release rate of a composite is measured using a double cantilever beam (DCB) geometry with unidirectional composites (ASTM D5528). Unlike metals, the energy plot of a composite's DCB specimen shows an increase in energy release rate with increase in crack length. This is because of fiber cross-over bridging at the interface between the top and bottom arm of the DCB. During fiber bridging, shown in Fig. C5.1, a crack jumps from one fiber/matrix interface to another without breaking the fiber. This occurs only in unidirectional composites where the fibers migrate during the curing process of composite

preparation. The increase in energy release rate with respect to crack length is called R-curve effect as shown in Fig. C5.2.

The behavior of R-curves depends on specimen geometry and therefore an R-curve cannot be considered as material property when large-scale bridging occurs. Large-scale bridging occurs whenever the length of the crack at fiber bridging is equal to or greater than the geometry size.

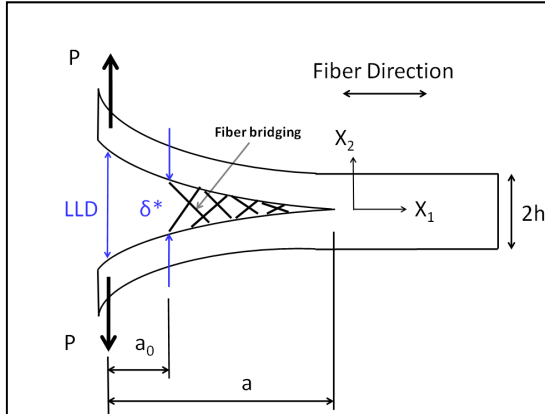


Fig. C5.1: DCB specimen with bridging.

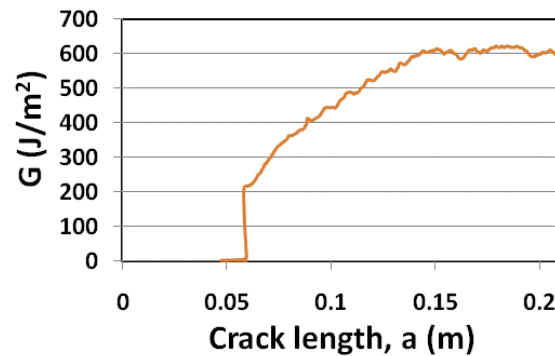


Fig. C5.2: R-Curve effect in bridged composite.

Since unidirectional composite DCB specimen test results are available from AFRL, this research used the known test data to develop a probabilistic cohesive zone model for fiber bridging. In the recent years cohesive zone models (CZM) have gained increasing popularity for modeling the fracture process and also in other applications like composite delamination, solder failures in circuits, *etc.* This can be attributed to the ability of the CZM to adapt to the nonlinearities in the process it represents by adjusting the model parameters. These parameters that are selected to represent the material behavior in the vicinity of the crack or a damage zone are non-deterministic in nature resulting in random fracture strength estimates. Currently there are no standardized tests for measuring the CZM parameters and their random scatter. Numerous researchers in the literature suggest values for the CZM parameters based on their experience from limited test data. Traditionally fracture toughness is determined through coupon tests for any material system that is being analyzed using Linear Elastic Fracture Mechanics (LEFM) to determine the fracture strength of a specimen. Since data for fracture toughness is available, this research is aimed at determining the probability density functions for the cohesive zone parameters that would give the same scatter in fracture strength as

provided material.

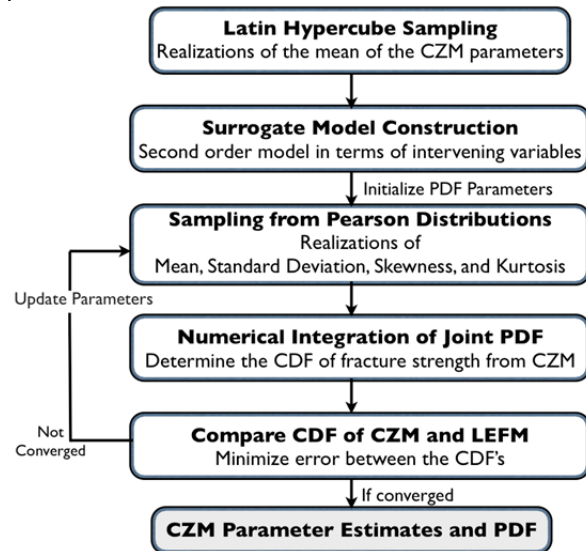
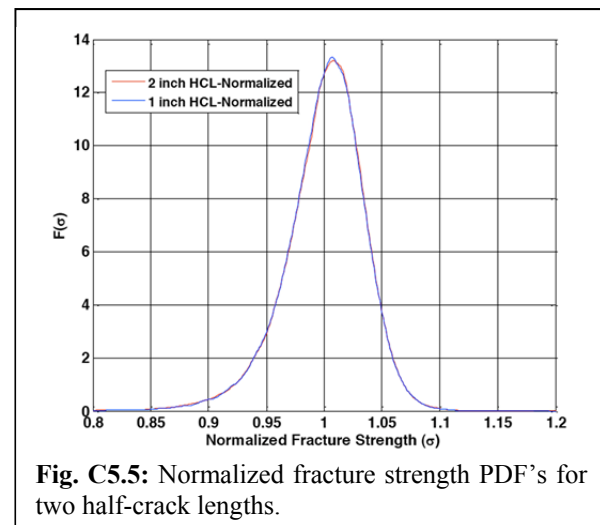
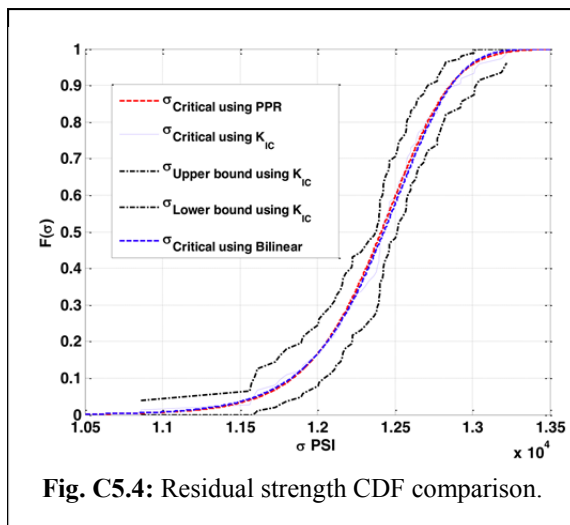


Fig. C5.3: Flow chart for determining CZM parameters and PDF's.

that obtained from the test statistics. Correlations between the model parameters were introduced to improve the accuracy of the fracture strength PDF. A finite width cracked plate is the test case to demonstrate the process. Figure C5.3 shows the flow chart that identifies all the steps involved in calibrating the probabilistic CZM.

In this research, bi-linear and PPR cohesive zone models were used to demonstrate the process and their cumulative distribution functions are shown in Fig. C5.4. Clearly both the models were able to capture the test data accurately. Another key finding of this research is the normalized fracture strength PDF. This normalized PDF represents the scatter in material strength and can be scaled to determine strength at any crack length. Two different half-crack lengths, 1 inch and 2 inch, were selected to demonstrate this feature. For both 1 inch and 2 inch half-crack lengths the normalized PDF's are shown in Fig. C5.5. Even though these distributions are visually the same, two analytical measures were used to ensure that they represent the same level of uncertainty. One was the Bhattacharya distance and the other was the entropy measure. Both the measures indicate that these distributions represent the same level of uncertainty. Therefore, this proves that the material randomness is independent of the geometric variables and



can be calibrated separately. This finding will enable construction of a nomograph for rapid risk assessment, which will be the focus of future efforts.

C6 Enriched Space-time Finite Element Method

Personell: Qian, Yang, Chirptukar, Alpert, Eason (AFRL), Spottswood (AFRL)

Start: 2010; End: 2011

Professor Qian and his colleagues developed a general formulation of the enriched space-time finite element method for solving structural dynamics applications that are of interest to the Air Force. By formulating the multiscale approximation within the context of the extended space-time finite element method, the goal is to integrate the physics that are governed by different characteristic temporal scales. Compared with the implementations without the enrichment, the proposed method provides extended capabilities in multiscaling in both the spatial and temporal domains. For the analysis of structural dynamics problem, the use of enriched space-time method not only inherits some of the basic features of space-time FEM in reducing the oscillations and producing stable results that are high-order accurate, it also provides extended capabilities in capturing multiscale temporal responses. In particular, it alleviates the need for temporal mesh refinement, which can be tedious in implementation without the enrichments.

We have developed a set of benchmark problems in both one-dimension and two-dimension (example problem shown next page, Fig. C6.1 and C6.2) to evaluate the robustness of the proposed approach. The accuracy is measured in terms of the error estimates, i.e., the difference between the analytical and numerical solution. It is shown that multiscale space-time FEM enjoys superior convergence properties over the traditional space-time FEM (Fig. C6.3) and the proposed method represent a new paradigm towards resolving structural and solid mechanics problems with strong temporal nonlinearity.



Fig. C6.1: Slender curved beam subjected to dynamic transverse pressure.

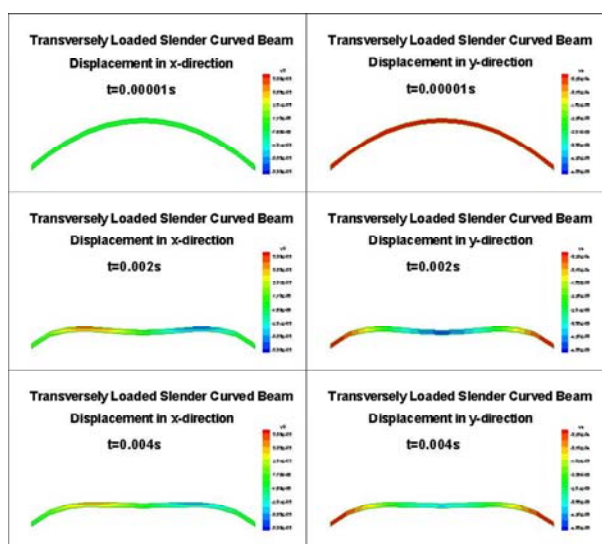


Fig. C6.2: Simulation of transversely loaded slender curved beam subjected to pressure load.

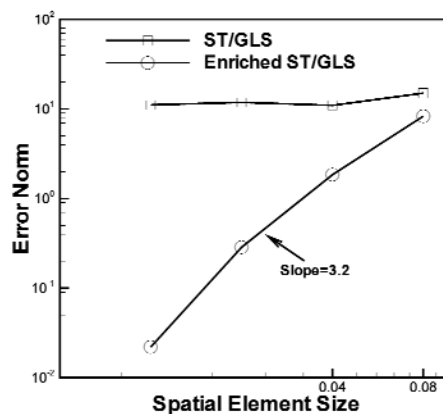


Fig. C6.3: Error norm vs. spatial element size between regular and enriched space-time solutions.

D1 Experimental Investigation of Thermomechanical Fatigue Failure Modes

Personnel: Sehitoğlu, Efstathiou (Graduate student, UIUC), Hauber (AFRL)

Start: 2006; End: 2009

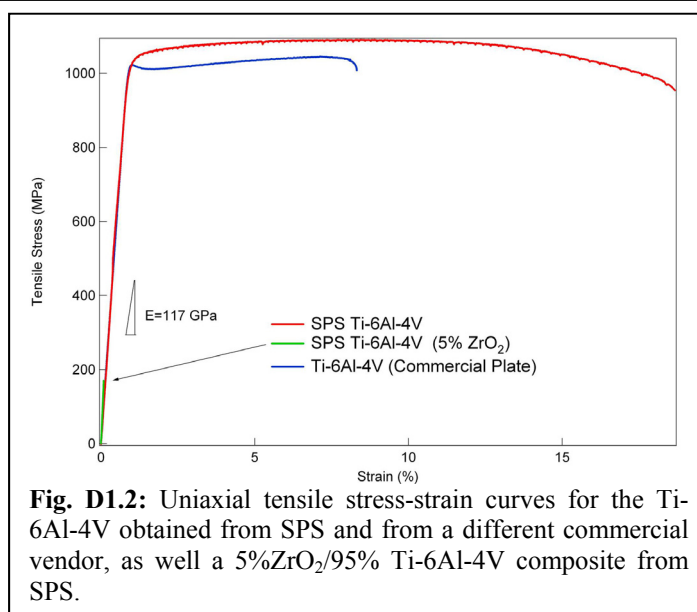
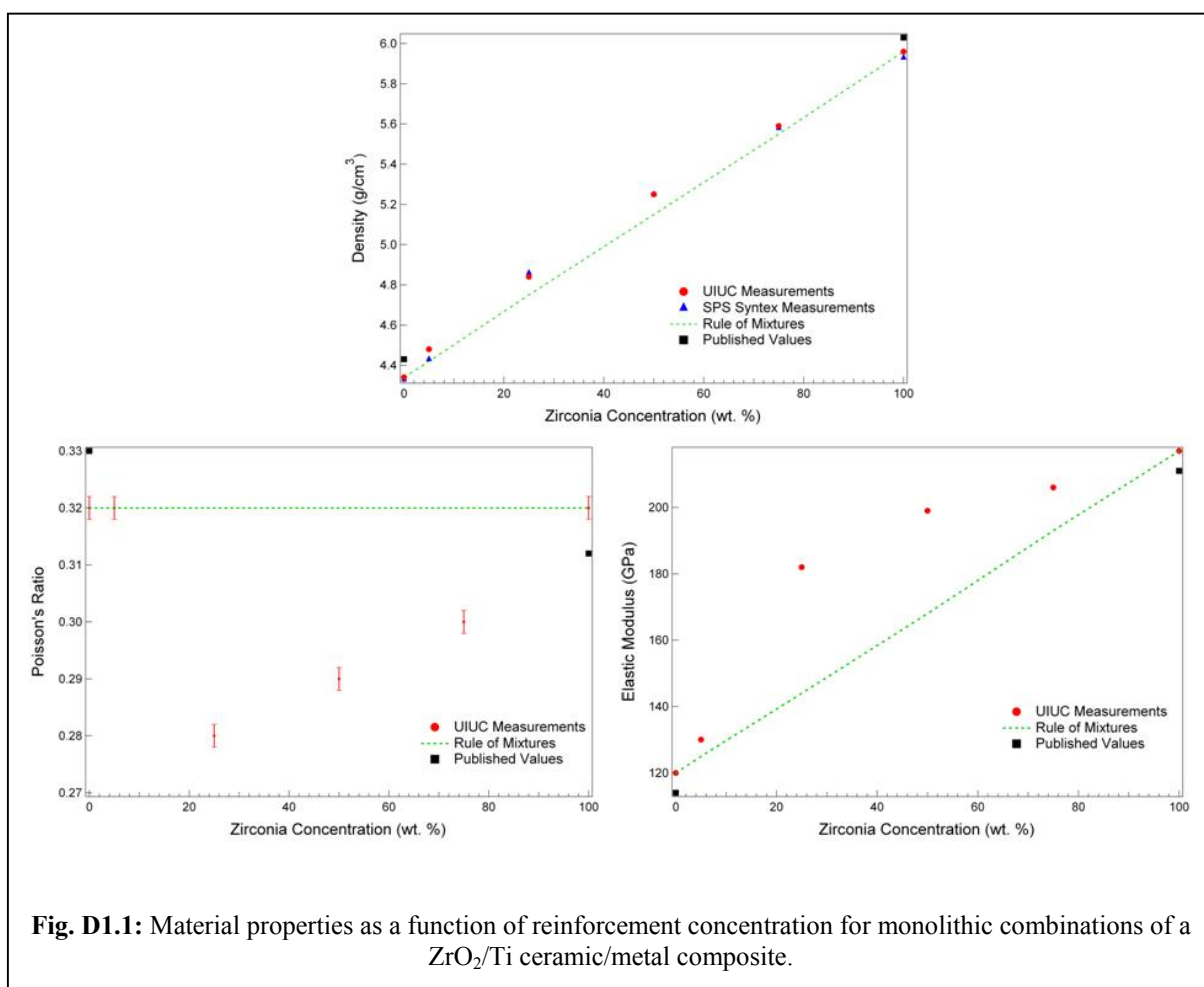
Functionally Graded Materials

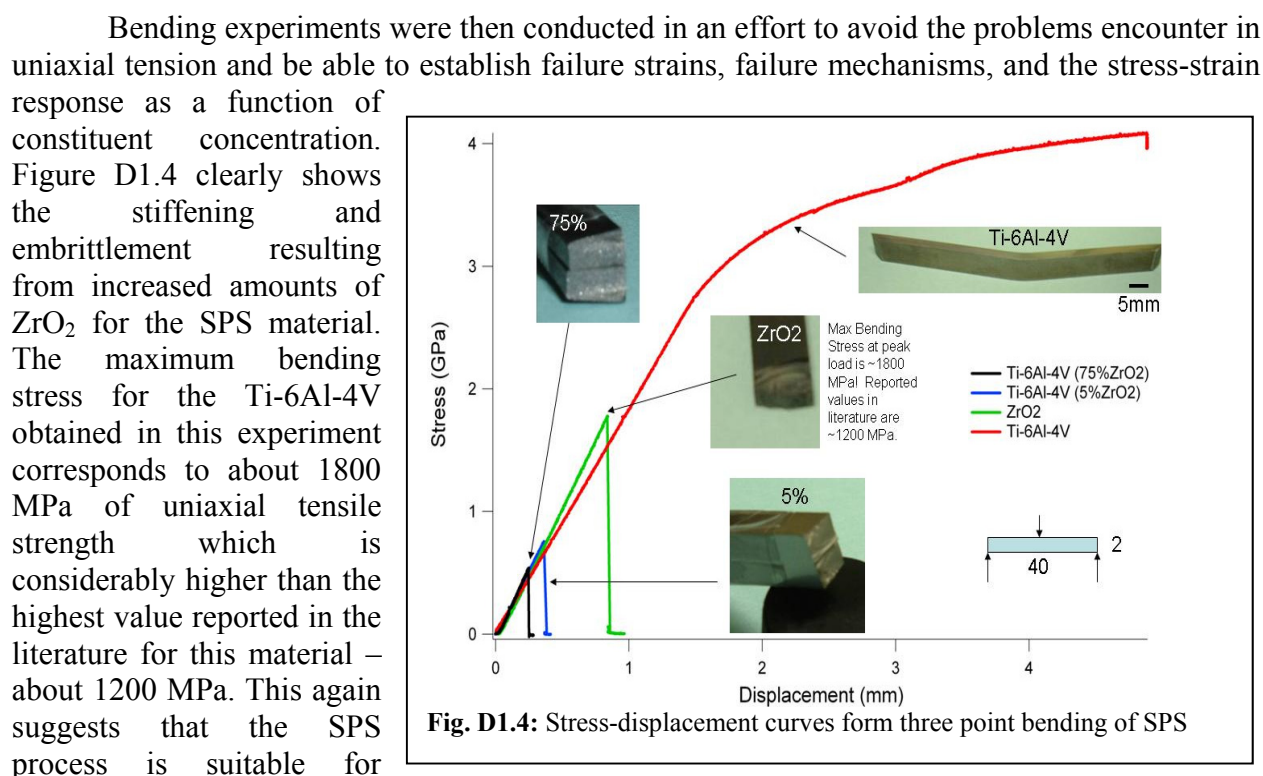
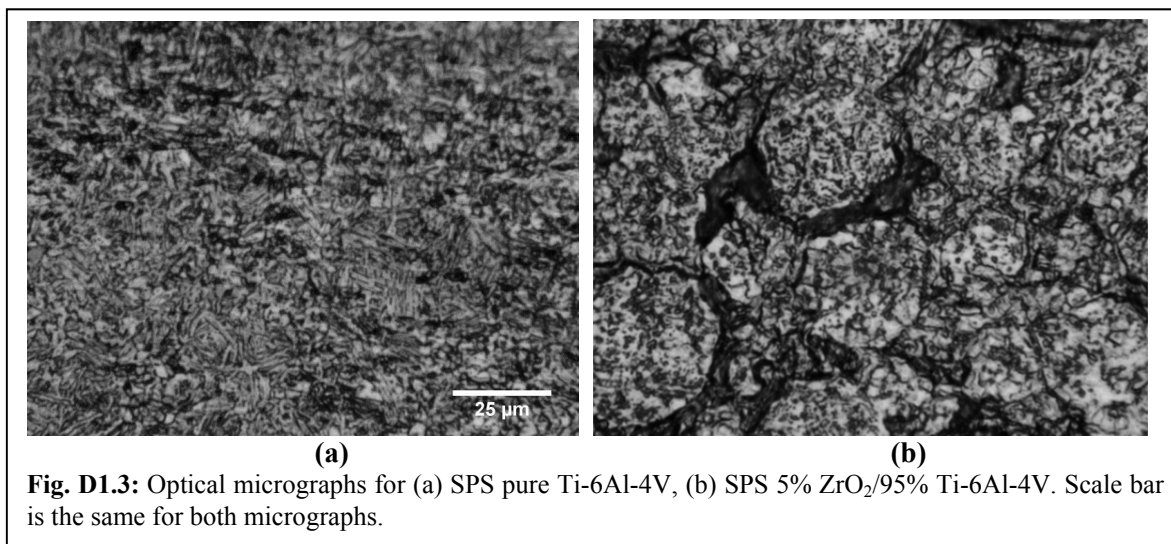
In the first part of this effort we investigated the mechanical and thermal behavior of functionally graded materials based on a gradual microstructural transition from zirconia ceramic to titanium metal. The material was custom made for this study from SPS Syntex, a subsidiary of Sumitomo Inc. in Japan. A set of monolithic samples of single $\text{ZrO}_2/\text{Ti-6Al-4V}$ concentration was obtained (namely percentages of $\text{ZrO}_2/\text{Ti-6Al-4V}$ of: 100/0, 95/5, 75/25, 50/50, 25/75 and 0/100) as well as several graded samples with 25 mm of layered graded thickness. The goal was to use the monolithic samples to measure thermomechanical and failure properties as a function of constituent phase concentration and then predict based on the monolithic results, the failure properties of the FGM material. Experimentation on the FGMs would then serve a validation for the models used to predict the FGM response (that would have been provided by interaction with project B1).

Initially, non-destructive testing was employed to determine the Young's modulus, Poisson's ratio, and density of the six different compositions of monolithic material. The results of these measurements appear in Fig. D1.1. The modulus and Poisson's ratio measurements for the 0%, 5% and 100% ZrO_2 concentrations appear close to the rule of mixtures whereas the 25%, 50% and 75% do not. As we would generally expect the elastic properties to follow the rules of mixtures fairly well (unlike failure properties which can deviate significant from the rule of mixtures for microstructural failure mode reasons), this deviation from rule of mixtures was an early sign that perhaps material consistency was not satisfactory.

Subsequently to these non-destructive experiments, samples for use in uniaxial tensile test and bending tests were cut from the original plates using water jet cutting. Figure D1.2 shows the uniaxial tensile test data for a Ti-6Al-4V commercially purchased alloy from a generic source and the equivalent one (100% Ti-6Al-4V) obtained from SPS Syntex manufactured using Spark Plasma Sintering (SPS). The two curves are fairly close to each other in the elastic range, while in the plastic range the SPS material exhibits a slightly reduced yield stress (which may have to do with the prior heat treatment and/or grain size) and, more importantly, a significantly lower ductility. The microstructure of the SPS Ti-6Al-4V alloy is shown in Fig. D1.3(a) and shows the expected form, and is comparable to that of the commercially bought alloy.

Uniaxial tension tests results are also shown in Fig. D1.2 for the sample containing 95% Ti-6Al-4V and 5% ZrO_2 . Despite such a small concentration of ceramic, the sample was extremely brittle and failed very early in the loading, compared to 100% Ti-6Al-4V. Fig. D1.3(b) shows the microstructure of the 5% ZrO_2 material where dark areas of what appears to be a second phase surround each grain. It is likely that these SPS reaction by products are responsible for such a dramatic decrease in failure stress and strain. The next sample to be tested in uniaxial tension consisted of 25% ZrO_2 and 75% Ti-6Al-4V. However it proved impossible to generate uniaxial tensile data for this material, and for higher concentrations of ZrO_2 , as the samples would consistently fail in the grip region under minute amounts of load.





Looking at the result for pure ZrO₂ obtained from SPS, we see a reasonable trend of increasing stiffness and embrittlement. However peak strength is dramatically reduced. In addition the monolithic composites with even small concentrations of ZrO₂ are not bracketed by the pure Ti-6Al-4V and ZrO₂ results. This, in addition to the findings in Fig. D1.3(b), implies that perhaps the SPS process used to manufacture these materials was not satisfactory.

Attempts to experiment at higher temperatures were even more unsuccessful due to premature failure of the specimens during heating. We subsequently explored the effects of temperature on the oxidation behavior and found that, reinforcement concentrations greater than

5% were extremely unstable at temperatures greater than approximately 600°C. The summary shown in Fig. D1.5 shows which concentrations managed to survive heating to 600°C and which to 1,100°C. Only the 100% Ti-6Al-4V and 100% ZrO₂ survived heating to such an elevated temperature. The 5% ZrO₂ sample also appeared to survive the heating but was not structurally sound after returning to room temperature. Since the SPS material displayed unsatisfactory thermomechanical response and oxidation behavior, we continued to develop a set of multiscale analysis tools by investigating metallic materials.

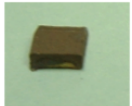
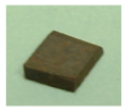


Syntex Material	600C	630C<T<1100C
Ti-6Al-4V	OK	OK 
Ti-6Al-4V 5%ZrO2	OK	OK 
Ti-6Al-4V 25%ZrO2	OK	NG; @630C-1min 
Ti-6Al-4V 50%ZrO2		NG
Ti-6Al-4V 75%ZrO2		NG
ZrO2	OK	OK 

Fig. D1.5: Summary of SPS materials subjected to different temperature ranges.

Multiscale study of cyclic plastic response of Ti

Since securing FGMs of sufficient quality in bulk to withstand the thermomechanical fatigue loading relevant to this work proved difficult, we continued the development of relevant optical techniques using metallic materials, such as the monolithic Ti-6Al-4V alloy or pure α -Ti. Grade 2 pure α -Ti has a hexagonal close-packed crystal structure. It is known that these low-symmetry crystal structures do not have sufficient slip systems to accommodate an arbitrary deformation, and therefore the collective behavior of grains, and grain–grain interactions become increasingly important, especially under extreme loading conditions. This can lead to heterogeneous deformation which may appear as networks of intersecting slip bands inclined to the loading direction. Although traditional continuum plasticity calculations do not capture this

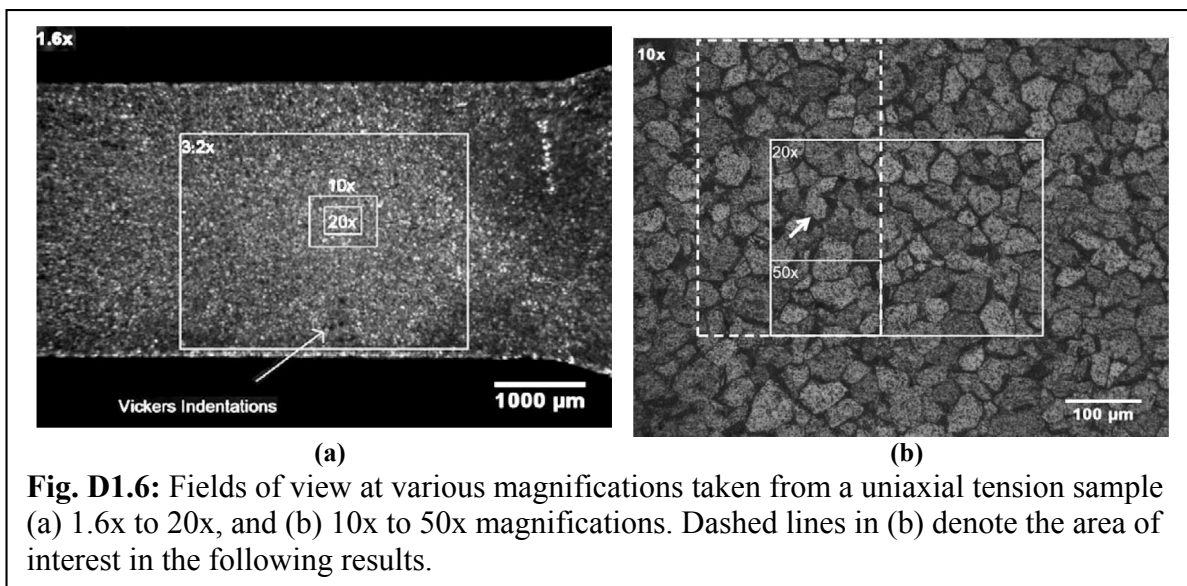
phenomenon, more rigorous finite element calculations (with crystal plasticity formulations) have been able to capture some aspects of the experimentally observed heterogeneous deformation, see Beaudoin *et al.* (1998), Mika and Dawson (1999), Delaire *et al.* (2000), Barbe *et al.* (2001), Raabe *et al.* (2001), Clayton *et al.* (2002) among others. Experimentally observing such microstructural inhomogeneities will require a multiscale measurement both at the scale of a large aggregate of grains and at the scale of a single grain or less.

Digital image correlation (DIC) is highly suitable for multiscale experimental studies because it does not possess an inherent length scale. In most previous work, the DIC technique has been used at a single length scale, and has proved to be very useful in investigating strain heterogeneities (Efsthathiou *et al.*, 2008). However, extending DIC to smaller length scales requires careful sample preparation and a more sophisticated experimental apparatus. Although the DIC algorithm has no inherent length scale, the camera and lens combination define a length scale which bounds the measurement resolution. The measurement resolution is effectively the number of displacement measurements per unit length; this is typically proportional to the optical resolution (pixels/unit length). A multiscale assessment of the deformation field is important because, as it will be shown, low optical resolutions tend to “smear-out” the details of the strain field measurements. This “smearing” is shown to affect the general characteristics of the strain field as well as the representative volume element (RVE) determination. A goal of the current multiscale investigation is to determine how mesoscale and macroscale deformation fields are related, and how measurement resolutions influence sub-grain level strain measurements. This work is unique because we utilize optical imaging to describe the strain distribution on a grain level for large numbers of grains, and we report the experimental and analytical requirements for obtaining full-field measurements which could be used for validating plasticity models.

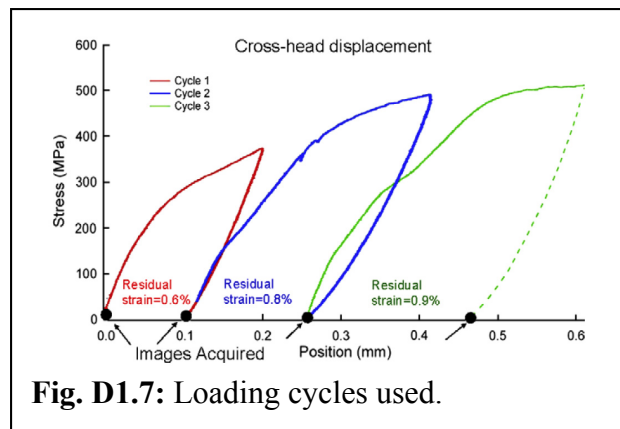
The existence of such strain heterogeneities occurring on different length scales imply that great care must be taken when applying homogenization techniques. At the heart of homogenization techniques is the RVE. Although many definitions of a RVE exist, and numerous experimental and numerical studies characterize RVEs based on microstructure and/or elastic deformation, no experimental measurements exist on what constitutes a RVE for plastic deformation. Furthermore, experimental determination of the RVE length scale is not generally possible unless internal 3D measurements are available. However, most studies in experimental mechanics, including the present one, involve 2D surface measurements. In this study, the 2D strain measurements from DIC were used, and therefore the results provide what can be thought of as a representative surface element (RSE) rather than a RVE. There is no universal relation between a RSE and a RVE. In fact simulating 3D microstructures based on surface measurements is an active area of research as was shown by St-Pierre *et al.* (2008).

Commercially available Grade 2 pure Ti was electro-discharged machined from an annealed cold-rolled plate. Specimen dimensions in the gauge section were 3x1x10 mm. A subsequent recrystallization treatment was conducted at 800°C for 24 h in a pressurized Ar environment to avoid surface oxidation. To reveal grain boundaries, the sample was polished using 800 grit, and subsequently etched in Kroll’s reagent. Using optical microscopy, the average grain size was estimated as 30 μm . A small region of the specimen surface was marked with Vickers indentations as reference points. This region was imaged using an Olympus microscope (model BX51M optical) at 1.6x magnification and is shown in Fig. D1.6(a). Also shown in Fig. D1.6 are the approximate field-of-views (FOVs) at several other magnifications for which results will be presented. The approximate dimensions of each FOV, and the corresponding optical

resolution ranges from 3x2 mm and 1.36 $\mu\text{m}/\text{pixel}$ for 3.2x to 140x100 μm and 87 nm/pixel for 50x. The Vickers indentations shown in Fig. D1.6(a) were used to uniquely identify the relative location of the FOV between different magnifications in order to accurately compare the results between magnifications. Since the FOV decreases considerably from 3.2x to 50x magnification, Fig. D1.6(b) is included to point out the particular region which was investigated at higher optical magnifications. The dashed white box outlines the particular region where measurements at 10x, 25x, and 50x will be compared.



A motion control system consisting of three stepper motors, each attached to a slide which was controlled by Labview software developed in-house. This system allowed the sample to be translated underneath the microscope lens with a resolution of 2 $\mu\text{m}/\text{step}$, thus enabling an array of images (for example, 3 columns by 4 rows at 50x; *i.e.*, 12 images) to be obtained in the region of the dashed white box in Fig. D1.6(b). Each image overlapped its neighbor by approximately 30% to ensure the image correlation results were continuous over the region.



(Note: In project D2 this methodology was developed further and far larger number of images are now routinely collected in this method.) Uniaxial tensile testing was conducted at room temperature on a servohydraulic load frame. The specimen was loaded with a constant cross-head displacement rate of 5×10^{-3} mm/s in three increments to an approximate nominal residual strain of 0.6%, 0.8%, and 0.9% (measured from the cross-head displacement, see Fig. D1.7). After each increment of deformation, the specimen was removed from the load

frame and imaged using the microscope at 3.2x, 10x, 20x, 25x, and 50x magnification. All images were oriented with the horizontal direction aligned with the loading axis, and were

obtained with a IMI model 202FT digital camera (1600x1200 pixels). These images were used to measure the strain fields by digital image correlation (DIC).

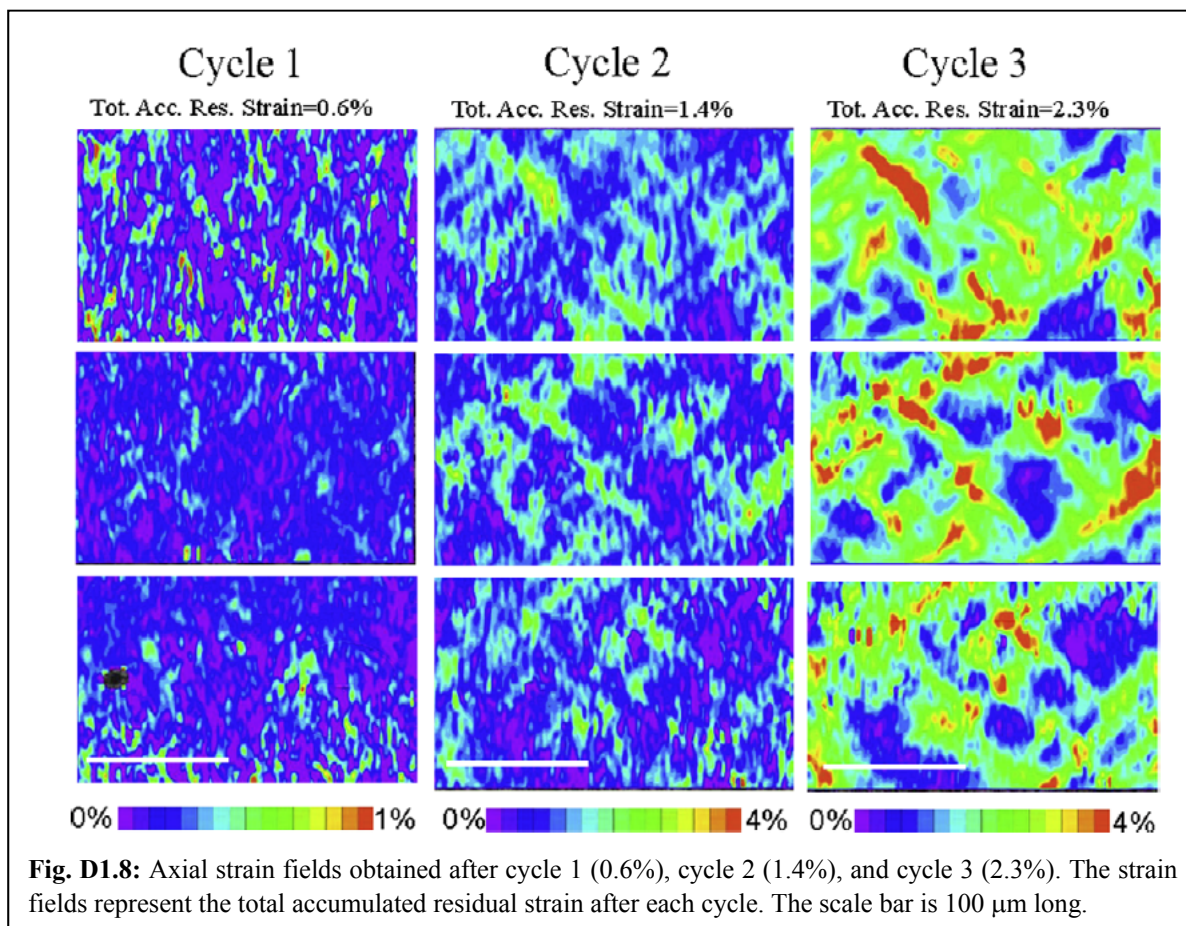
To provide a full-field description of displacements or strain, it is necessary to have many correlation points (*i.e.*, the center point of each subset) within the area-of-interest, and therefore the subsets are usually spaced every 10 pixels. Using a central-difference scheme, implemented in the commercial software (see VIC-2D, Correlated Solutions, 2008), the strain field was computed at the center of each subset. The strain averaging scheme is based on strain averaging over a window. The window size is characterized by a number of measurements for which 3x3 is a minimum value for the software employed. The imposed minimum value on the window size is due to the central-difference scheme implemented in the software. All of the results reported are averaged with a window size of 3x3, and step sizes of 10 pixels. Thus, an estimate of the strain confidence level can be calculated as $\pm 0.1\%$, where ± 0.02 is the sub-pixel accuracy and 20 pixels is the length over which the differentiation is conducted.

Digital image correlation was performed on the image-pairs obtained at each magnification to compare the magnitude and distribution of residual strain. Digital image correlation at 25x and 50x magnification was conducted by two different methods to produce continuous strain fields over a FOV which was comparable to lower magnifications. The first method was to correlate individual image-pairs, and then assemble the results to form a single continuous strain field representing the entire region in the white dashed box outlined region in Fig. D1.6(b). The second method required first assembling individual images to form several larger images that were used in the correlation. The results were then assembled to form a continuous strain field representing the region outlined by the dashed white box in Fig. D1.6(b).

Results

Fig. D1.8 shows the total accumulated residual strain distribution at the end of each loading increment as measured using DIC at 25x. The total accumulated residual strain refers to the effect of successive loading cycles as described earlier with reference to Fig. D1.7. Since measurements are made after each unloading, the accumulated strain represents residual plastic strain permanently “locked” into the microstructure. It is possible, especially for the lower load level cycles and for the slip restricted hcp material, that after unloading some grains may remain in a state of elastic straining, even at zero load, because of the local constraint provided by its neighboring grains of differing texture which had undergone plastic straining. This type of “locked-in” elastic strains would also be included in the DIC measurement, and for this reason we have employed the term “accumulated residual strain” rather than “accumulated plastic strain” in this work. In Fig. D1.8, the first column represents the residual strain after the first loading increment, the second column represents the total accumulated residual strain of the first plus the second load increment, and the third column represents the total accumulated residual strain of the first plus the second and the third load increment. Each strain field in the first column is the result of a correlation, and they represent a different area along the sample width. Note that these images could be assembled together (top to bottom) to form a single continuous strain field as described in the previous section, but they were not assembled to make this point clear.

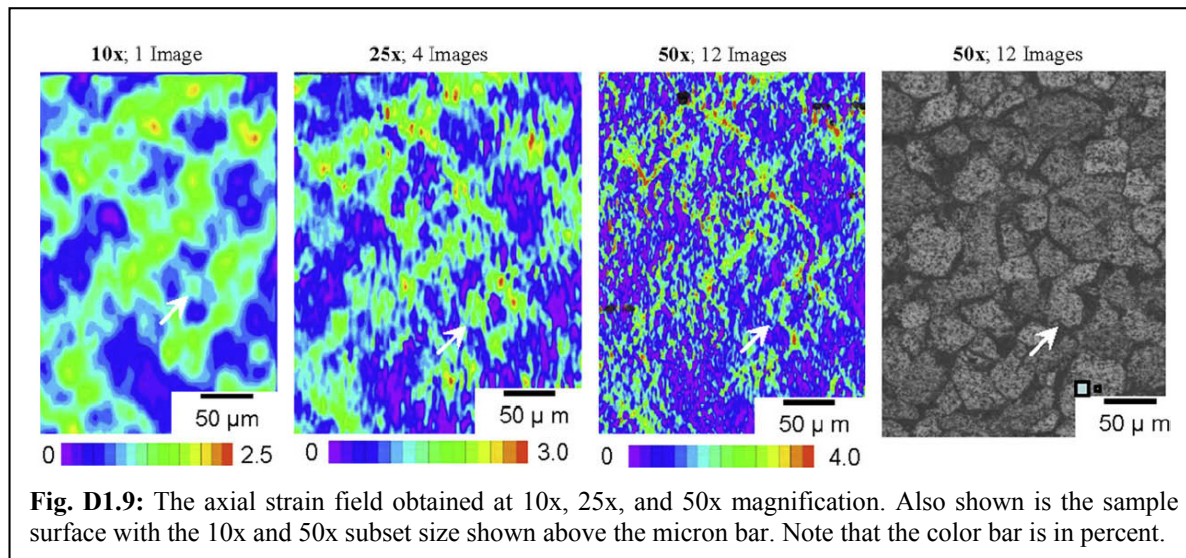
These results indicate that the plastic deformation initially appears somewhat uniform after the first load increment, and becomes nonuniform after the second. Note that the first increment is shown with a color bar up to 1% strain. If this figure were plotted on a common



scale for all three loadings, the first loading would appear as one solid color, and therefore the conclusion would be that it is completely homogeneous. By using this color scale it is clear that the strain field possess some smaller scale heterogeneity even after the first load increment. The strain fields corresponding to the second load increment appear to show strain heterogeneities in patterns that are inclined approximately $\pm 45^\circ$ to the loading direction. At the completion of the third load increment, the strain field appears to have developed regions with significantly larger strains, and consequently at this length scale it appears spatially somewhat more homogeneous again. Note, however, that the deformation pattern after the third load increment has a significant numerical strain heterogeneity which ranges from approximately 0–4%.

In order to assess the influence of the optical magnification, the strain fields must be measured over the same sample area or field-of-view (FOV). As previously mentioned, the FOV is considerably smaller at high magnification, and therefore comparing results over the same FOV requires assembling images prior to correlation, or assembling results of individual correlations. In Fig. D1.9, a comparison of the strain field measurements at 10x, 25x, and 50x optical magnifications is presented for the region encompassed by the dashed white box in Fig. D1.6(b). Each strain field represents the same FOV, but they are made up of 1 image at 10x, 4 at 25x, and 12 at 50x magnification. Also shown, in the rightmost image of Fig. D1.9, is the sample surface with an arrow pointing to the reference grain, and the subset size for the 10x and 50x magnification. The 10x and 50x subset sizes appear over the micron bar, and they show that they are smaller than the average grain size, but note that the 50x subset size is considerably smaller

(almost a spec) compared to the grain size. At 10x magnification, three green bands nearly 50 μm wide are visible, and inclined approximately 45° to the loading direction. With increased



optical magnification, these bands become narrower, and considerably more detail emerges between them.

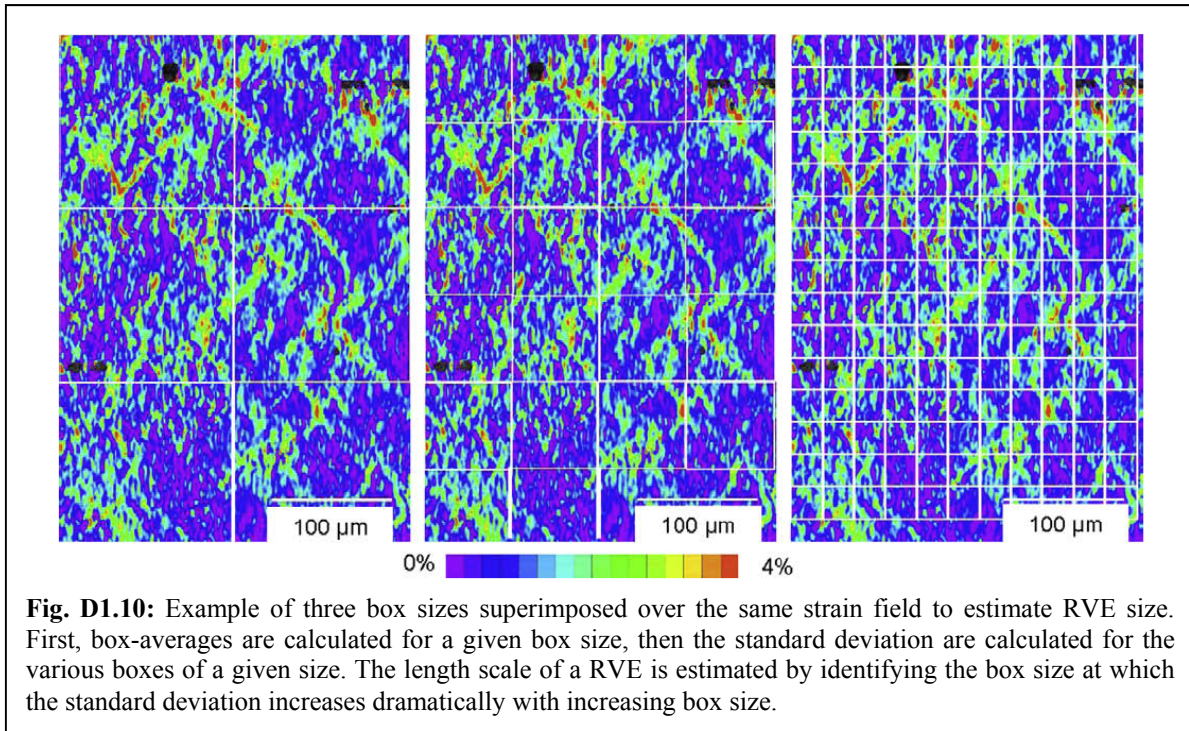
Representative Volume Element (RVE)

In modeling techniques such as crystal plasticity, it is commonly assumed that such lattice effects are averaged or homogenized. The length scale at which homogenization is implemented raises the question which motivates this work; what is the length scale of a representative volume element (RVE) under plastic deformation conditions? In this work, the determination of the length scale of a RVE is based on residual strain, and the RVE length scale is estimated by calculating the standard deviation (SD) of the average strain at various length scales for the same strain field. The length scales are defined by the size of a square box which encompasses regions in the strain field. Note that although the RVE refers to a “volume”, it is common to describe the RVE as “length scale” or a “size” that is simply the length of one of its dimensions in space. In this work it will prove useful to reserve “length scale” for the RVE, and “size” for the length of the square box that is used to determine the RVE.

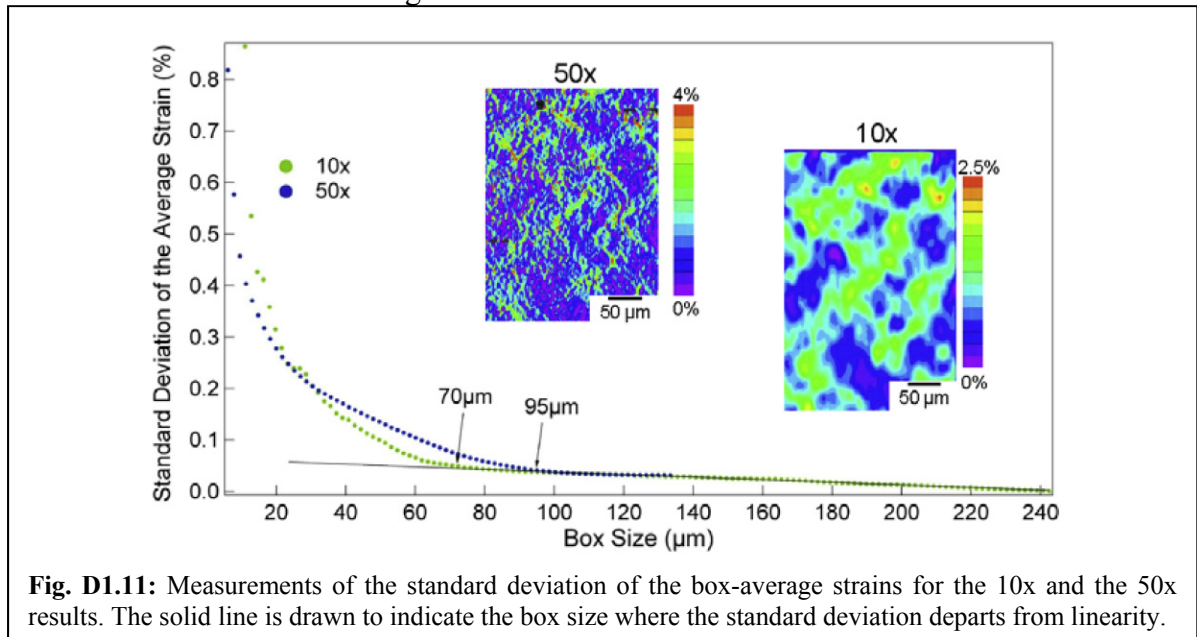
Figure D1.10 shows how the length scale of a RVE is estimated in this work based on the above description. In the figure, an example of three differently sized white boxes are superimposed over the *same* 50x strain field. The first step was to determine the average strain within each box for a given box size. These averages will be referred to as box-averages. For example, 6 box-averages are calculated for the left most strain field, whereas 154 are calculated for the right most strain field. A simple algorithm was implemented to do this for box sizes ranging as large as the entire width of the strain field to as small as a DIC subset size. Then the standard deviation (SD) of these box-averages was calculated for a given box size. The length scale of the RVE was then determined by identifying the box size at which the SD increases dramatically with increasing box size.

The results of this analysis are presented in Fig. D1.11 for the 10x and the 50x strain field. In Fig. D1.11, the SD is small at large box sizes, whereas the SD is large at small box sizes.

To determine the length scale of a RVE, a line is fit to the tail end of the data where the standard deviation of average strain is small, and then the RVE length scale is determined by the box size at which the SD departs from this line. The corresponding RVE length scale is approximately 95



μm for the 50x strain field, and approximately 70 μm for the 10x strain field. The difference between the estimates of RVE length scale originates from the different measurement resolution. By visually inspecting the strain fields presented in Fig. D1.11, it is obvious that the “smeared” 10x strain field has a smaller SD for a given box size.



The primary goal of estimating the length scale of a RVE using the simple box-average technique was to show how it would differ for strain field measurements obtained with medium and high optical resolution (10x and 50x). It was shown that if a RVE is estimated based on the results obtained with medium optical resolution, the estimated RVE length scale will effectively be smaller due to a “smearing” of the strain fields. The implications are significant for models using homogenization techniques which utilize macroscale strain field measurements for input or verification and validation.

D2 Development of Experimental Techniques for Validating a Coupled Thermomechanical Fatigue Simulation Framework

Personnel: Lambros, Carroll (graduate student, UIUC), Chona (AFRL)

Start: 2006; End: 2010

D.2.1 Material Selection

As the early aspects of this work involved the development of experimental techniques for use at high temperature, a material suitable for work at high temperatures was sought. Initial work on this project also involved the SPS Syntex Functionally Graded Materials (FGMs) discussed in project D1. A number of preliminary experiments were undertaken in applying DIC to brittle materials. The monolithic SPS Syntex composite consisting of 5% Zirconia (yttria stabilized ZrO_2) and 95% titanium was used. While the majority of this material is actually metallic, it exhibits brittle behavior common in ceramic materials, as seen in Figs. D1.2 and D1.4. This material had an advantage in machinability since it is electrically conductive and can be machined by EDM, unlike typical ceramics which are not conductive and require techniques such as waterjet cutting or diamond sawing. A specimen was cut and notched using EDM and put into a four-point bending configuration as shown in Fig. D2.1(a). Monotonically increasing load was applied to the specimen and images were captured throughout the test at a magnification of 1.9x. The specimen exhibited brittle behavior, and very little deformation was visible at the notch before failure. However DIC strain measurements just before fracture show some localized behavior developing at the notch (see Fig. D2.1(b)). However continued work with this material was ended once it was found that its high temperature capabilities had actually been compromised because of issues with manufacturing (Fig. D1.5).

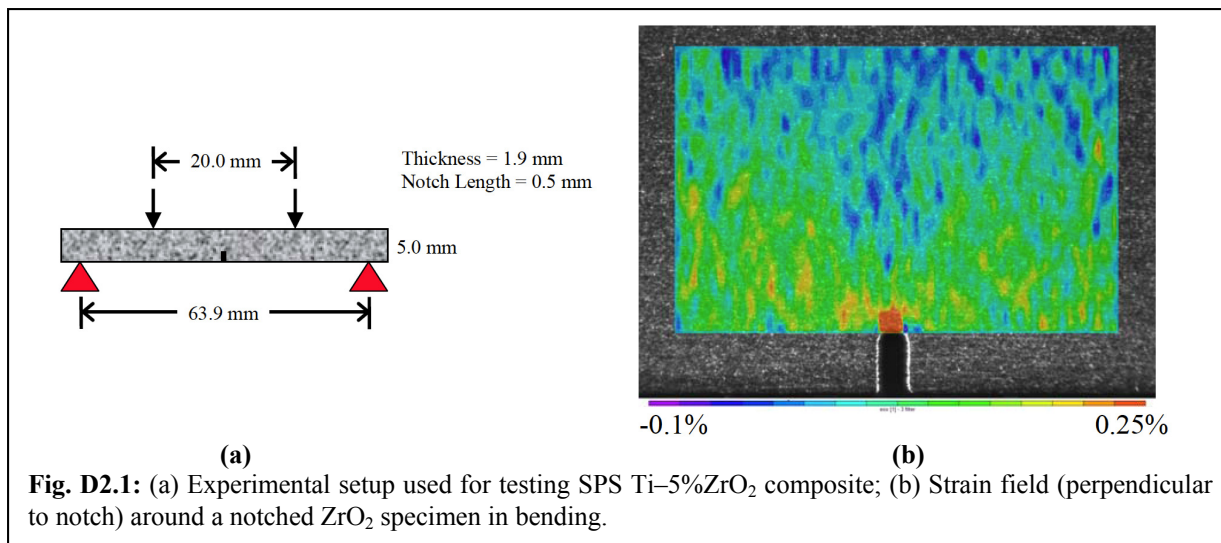
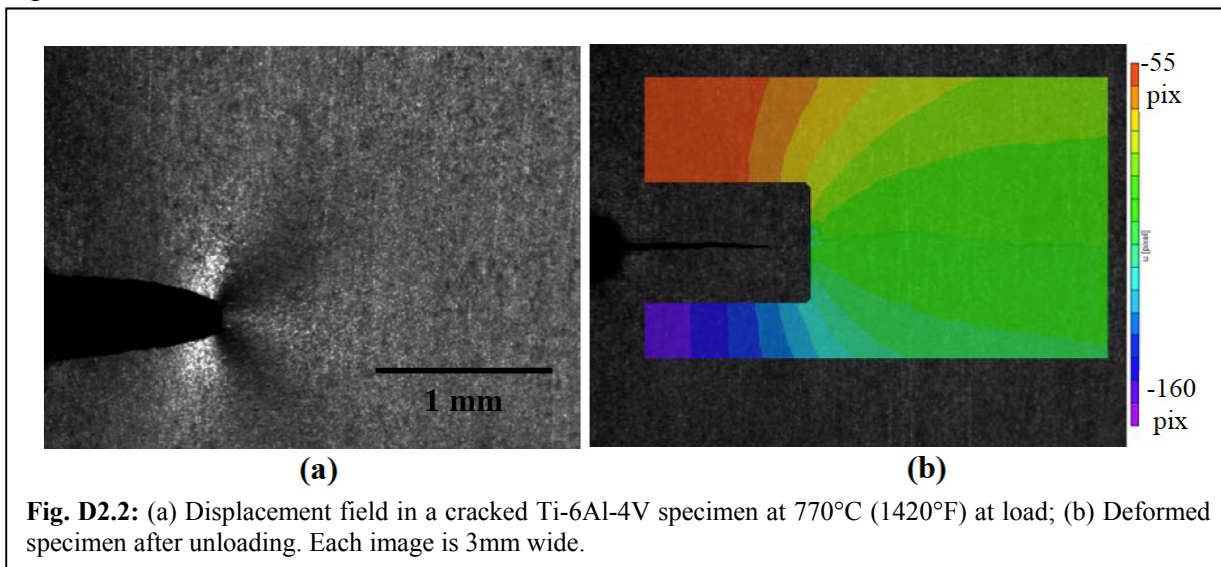


Fig. D2.1: (a) Experimental setup used for testing SPS Ti–5%ZrO₂ composite; (b) Strain field (perpendicular to notch) around a notched ZrO₂ specimen in bending.

At that stage we turned to the use of metallic materials as platforms for development of our techniques that would later be transferred in some fashion to newer, more thermally resistant, materials that would be developed in the future. Since we were also interested in using materials relevant in some fashion to the aerospace industry, our early studies turned to Ti and Ti alloys. DIC was used to measure the coefficient of thermal expansion, modulus of elasticity, and yield strength of pure titanium as a function of temperature up to 730°C (1346°F). For some experiments, DIC reference and deformed images were taken at the same temperature, but for

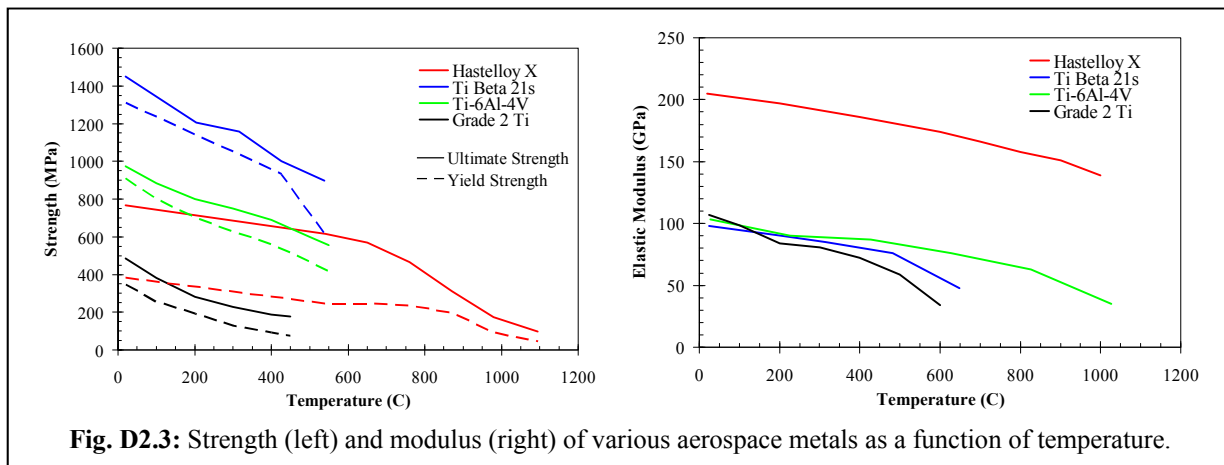
others (such as finding coefficient of thermal expansion or thermal fatigue experiments) reference and deformed images are necessarily captured at different temperatures. As specimens are heated, oxide layers are formed with oxide color dependent on temperature. Therefore, the specimen's appearance changes with heating causing DIC to fail for correlations between temperatures. To solve this problem, specimens were "preheated" to temperatures higher than those achieved during the actual experiment. This allowed the specimen to develop a high temperature oxide layer that remains unchanged with changing temperature (as long as the temperature is kept below the preheating temperature).

The DIC technique gave suitable measurements for these experiments, but pure titanium loses its structural rigidity above 500°C (932°F). The alloy Ti-6Al-4V displays higher strength than pure titanium at elevated temperatures and was therefore used in elevated temperature experiments on cracked specimens. In one experiment, a crack was initiated and grown from an EDM notch in a Ti-6Al-4V specimen (with loading parameters of $\Delta K=10 \text{ MPa}\sqrt{\text{m}}$, $R=0.1$). The specimen was heated to 770°C (1420°F) and a mechanical fatigue cycle, with the same load levels as before, was applied to the specimen at a slower frequency of 1 cycle in 120 seconds. Images were captured throughout this cycle. For the temperatures in this experiment Ti-6Al-4V loses its structural rigidity and excessive plastic deformation took place before the peak load of the cycle could be achieved. As Fig. D2.2(a) shows, significant plastic deformation occurred throughout the test. Even though Ti-6Al-4V may not be structurally useful at these temperatures, the displacement field around the crack was still measured with reasonable accuracy. Figure D2.2(b) shows the displacement field with a portion of the correlation area removed since the correlation fails in the open-crack region due to crack tip blunting. Materials with better resistance to elevated temperatures will be required to perform experiments at higher temperatures.



Some early work at room temperature was performed on Ti and Ti alloys (e.g. the RVE work in D1 and the closure work in section D.2.2). However it was of interest to eventually move to higher temperatures and therefore we had to investigate other possible metallic materials as well that were capable of achieving temperatures higher than the 770°C of Ti-6Al-4V. Candidates for such materials were Ti Beta 21s or nickel super alloys, such as Hastelloy X, for which the dependence of mechanical properties with temperature is shown in Fig. D2.3. Based

on these data, and on the earlier proposed use of nickel based super alloys (e.g., Inconel 718 and 625) in designs such as the X-33 (Zuchowski, 2010). Hastelloy X was selected as a material to continue our technique development work on. Therefore subsequent studies in project D2, as well as all the work in D3 and D4 were done on the Hastelloy X material.



D.2.2 Multiscale Measurements of Fatigue Crack Closure

The work of most aspects of this project involved the use of experimental techniques at the macroscale and the microscale to measure the deformation fields arising during (thermo)mechanical fatigue crack growth. Most of the remaining work in this project focused on the room temperature studies necessary to develop the techniques and to understand the material that we were working with. The **macroscale is defined** as the scale at which the details of the microstructure can be ignored and the deformation fields can be thought of as arising from a continuum that can be described by some continuous constitutive law. At this scale, for example, the material may be well described by the Generalized Plasticity theory discussed in project B3. “Homogenized” quantities, such as the stress intensity factor, can also be used to characterize the field as a whole. In the context of this work the **microscale is defined** as the length scale where details of the material structure, such as grain shape, orientation, morphology, *etc.* cannot be ignored when describing deformation fields. In such a case homogenized quantities are not valid, and rather a pointwise characterization of local response is needed. Clearly in some fashion the microscale is related to, *i.e.*, affects, the macroscale and it is precisely this relation that we are seeking to investigate. Therefore, experiments were designed to quantify deformation fields at both the macroscale and the microscale and relate the two through homogenization concepts, such as the RVE described earlier in project D1 or the fatigue life prediction scatter described in project B4.

In this project it was decided to use the optical technique of digital image correlation (DIC) both at the macroscale and microscale since DIC does not possess an inherent length scale. DIC was applied either at magnifications that were zoomed-out enough to be considered macroscale measurements, or zoomed-in enough to reveal microstructural details. In this section we will discuss macroscale measurements of stress intensity factor compared to microscale measurements made *behind* the growing crack. In this fashion we investigate crack closure phenomena. Below we will compare macroscale measurements with microscale measurements

ahead of the growing crack tip. With these measurements we will investigate the influence of microstructure on fatigue crack growth.

In the early 1970s, Elber (1970, 1971), discovered the crack closure phenomenon which involved the reduction of fatigue crack growth rates stemming from the residual compression generated by the plastic wake of the growing fatigue crack. As loading is applied, the crack tip does not accumulate new damage until this residual lateral compression is overcome and the crack starts opening – hence the naming “closure”. Elber modified the well known Paris relationship (Paris and Erdogan, 1963) to use only the portion of the stress intensity factor range above the crack opening level, ($\Delta K_{eff} = K_{max} - K_{open}$), as follows:

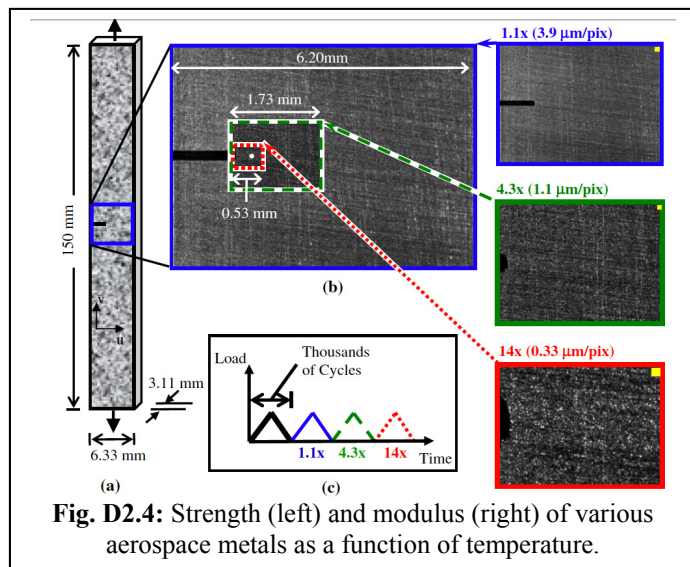
$$\frac{da}{dN} = C(\Delta K_{eff})^m. \quad (D.2.1)$$

Using ΔK_{eff} largely eliminated the direct dependence of crack growth rate on the load ratio such that one parameter, ΔK_{eff} , could be used instead of two (K and R), thereby demonstrating that plasticity-induced crack closure was the mechanism responsible for the effect of load ratio on crack growth rates. Crack closure acts as a shielding mechanism that reduces the effective stress intensity factor range at the crack tip, thereby decreasing crack growth rates.

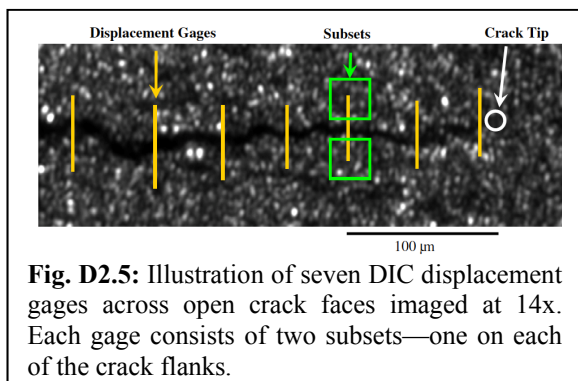
The objective of this part of our work was to combine some of the techniques that have individually been used in the past in a multiscale framework that would allow experimentally linking measures of crack closure at locations close to and far from the crack tip. Specifically, full-field displacement measurements at the macroscale (order of mm) can be used to calculate the effective stress intensity factor range and, in turn, calculate closure levels. At the microscale, (order of μm) non-contact displacement gages can be used to quantify crack tip closure. The DIC technique, which does not possess an inherent length scale, is highly suitable for such multiscale experimentation and will facilitate direct linking between the scales.

Edge-notched tension specimens were cut from a plate of grade 2 (commercially pure) titanium with electrical discharge machining (EDM); a 0.30 mm EDM wire was used to machine the notch (see Fig. D2.4(a)). The modulus of elasticity and Poisson’s ratio were found to be 109 GPa and 0.33, and a yield stress of 400 MPa was also determined from tension tests. Microscopy on etched specimens indicated a grain size of roughly 10 μm . Each specimen was rough polished using abrasive paper up to 800 grit. The natural texture of the specimen surface after rough polishing provided a suitable speckle pattern for using DIC; **therefore, the specimens were not painted** (see Fig. D2.4(b) for a comparison of the resulting speckle patterns at each magnification). Specimens were fatigued at rates between 2 and 8 Hz to initiate and grow a crack from the EDM notch tip at constant load amplitude and a load ratio of roughly zero. Consequently, the stress intensity factor slowly increased throughout the crack growth process. After a period of crack growth, the fatigue loading was stopped and several “measurement” cycles were applied to the specimen at a much slower rate of 240 s per cycle. This slower rate allowed 120 images to be captured throughout the loading cycle so that a typical fatigue cycle could be studied in detail.

A digital camera with a resolution of 1600 by 1200 pixels was used to capture images throughout measurement cycles. Optical magnifications from 1.1x to 28x (3.8 to 0.17 $\mu\text{m}/\text{pixel}$, respectively) were achieved with an adjustable lens with a 12x magnification range and a 2x adapter tube. Each measurement cycle was viewed with a different magnification as illustrated in Fig. D2.4(c). In all, three magnifications were used in measurement cycles: two “macroscopic”



Several gages were placed along the crack length as shown in Fig. D2.5, which illustrates a 14x image of a fully open crack at peak load. Subset sizes of 81 by 81 pixels were used corresponding to a gage width of 27 μm . A typical gage length was 40 μm , and gages used in this work were placed from 10 μm ahead of the crack tip to 700 μm behind the crack tip. For



ignoring in plane shearing displacements. Shearing displacements were found to be extremely small (less than one pixel), were about two orders of magnitude less than opening displacements, and were in fact near the lower resolution limit of DIC. A load versus displacement plot, such as the one shown in Fig. D2.6, was created for each DIC displacement gage. Each data point in Fig. D2.6 represents gage displacement at a specified load level (one image per point) with the loading portion of the cycle represented by circles and the unloading portion by triangles. The local crack opening level is identified by the load at which the gage displacement begins to increase significantly. This load level is computed by fitting a straight line to the upper linear portion of the loading curve in Fig. D2.6 and visually determining where the gage displacement first deviates from this line.

Several subsets were placed along the crack flanks and load vs. displacement curves where obtained for each. This showed that local crack opening loads vary with position and increase as the crack tip is approached. This behavior is expected since cracks generally open first at the mouth and last at the crack tip. Local crack opening and closure values determined from DIC displacement gages for three load levels are presented in Fig. D2.7. The low, medium,

magnifications of 1.1x and 4.3x (3.8 and 1.1 $\mu\text{m}/\text{pixel}$, respectively) and one microscopic magnification of 14x (0.33 $\mu\text{m}/\text{pixel}$) as illustrated in Fig. D2.4(b).

DIC was performed on images from each of the measurement cycles using a commercially available image correlation program. The first image in the measurement cycle (at minimum load) was used as the reference image, and terms up to first order displacement gradients were used in all correlations. For loading cycles observed at the microscopic magnification (14x), DIC displacement gages spanning the crack faces (Riddell *et al.*, 1999) were used.

For both of the macroscopic loading cycles (1.1x and 4.3x), DIC was used to obtain full-field displacements for each image throughout the cycle. Correlations were performed using a subset size of 41 by 41 pixels and a spacing of 15 pixels between subset centers.

At the microscopic magnification, DIC displacement gages were used to measure crack opening displacements along the crack length. Gage displacement is defined here as the relative vertical displacement of the gage's two subsets

and high K experiments are shown as squares, triangles, and diamonds, respectively. Filled symbols represent opening levels and empty symbols represent closure levels so that each pair of filled and empty symbols represents one displacement gage. Note that the data from the low K experiment cover a larger distance behind the crack tip because two measurement cycles were

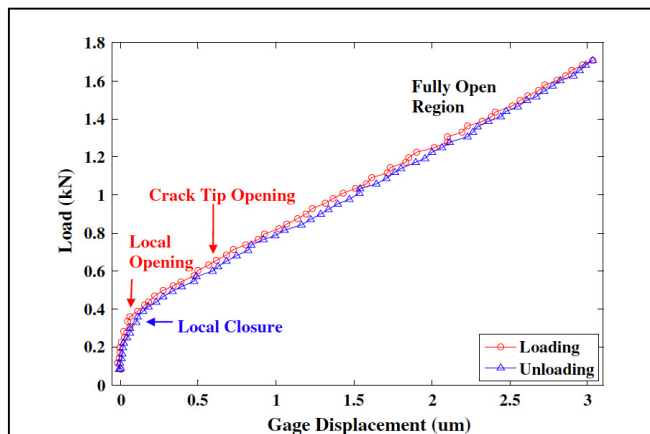


Fig. D2.6: Load versus displacement for a typical DIC displacement gage. Local opening levels are defined by the sharp knee in the curve while the compliance offset method is required to detect the more gradual compliance change caused by crack tip opening. Local closure values are found from the sharp knee of the unloading portion of the curve.

estimate of the crack tip opening level. Extrapolating local low K opening values provides a crack tip opening estimate of 35% of the peak load. This value is in agreement with crack profile observations (31%) and with the crack tip opening level calculated from the ASTM compliance offset method within experimental error.

In the macroscale experiments, full-field displacements were obtained from DIC, such as the contour plots of v -displacements (perpendicular to the crack line) shown in Fig. D2.8. The origin is placed at the crack tip, and a positive displacement contour means material moved upwards (rigid motion has been subtracted from these plots using the KT regression discussed later). Fig. D2.8(a) shows the v -displacement field measured at a magnification of 1.1x while Fig. D2.8(b) shows results from the 4.3x field of view, measured independently

performed at a magnification of 14x for the low K experiment: one with the imaged area near the crack tip, and a second with the imaged area behind the crack tip by several hundred micrometers.

In agreement with Macha *et al.* (1979) and Riddell *et al.* (1999), the local crack opening (and closure) levels for the low K experiment exhibit two regions. The first region is far behind the crack tip (between 350 and 700 μm behind the tip) where closure levels remain constant. This implies that a large portion of the crack opens at roughly 16% of the peak load. The second region of crack opening is near the crack tip (within 350 μm) where closure levels increase as the crack tip is approached. If local crack opening levels are extrapolated to the crack tip location, they can provide an

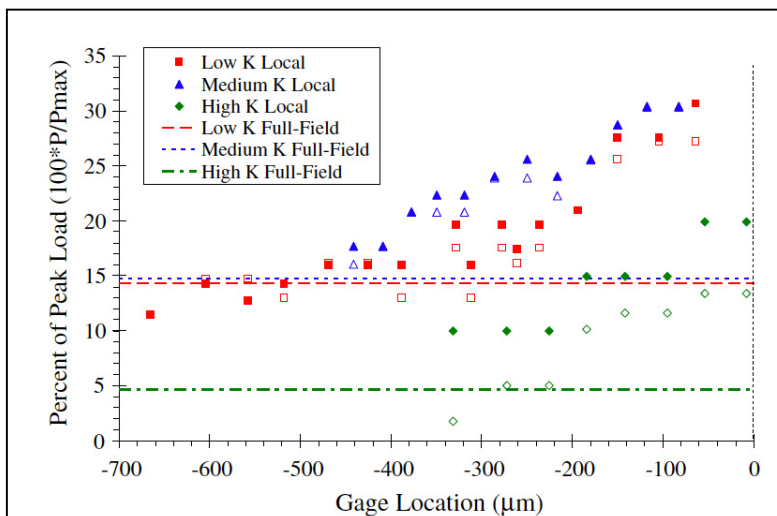


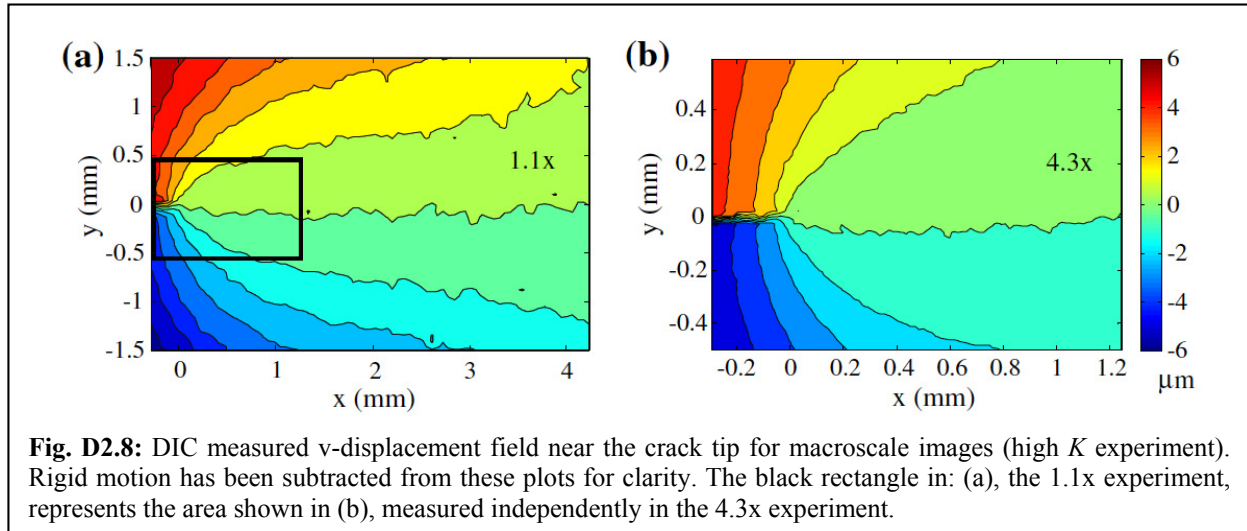
Fig. D2.7: Local opening and closure levels from microscale measurements (points) and macroscale measurements (lines) for three different K values. 0 μm denotes the crack tip location. Symbols indicate displacement gage measurements while lines indicate measurements from the full-field effective K method.

during two consecutive cycles. The black rectangle in Fig. D2.8(a) represents the area shown in Fig. D2.8(b).

Asymptotic theoretical solutions exist for full-field displacements near a crack tip. To determine what stress intensity factor the specimen actually experiences, which could be different than the theoretical load-based stress intensity factor primarily due to crack closure, a least squares regression was performed on the DIC measured v -displacements (v) (Fig. D2.8), and the stress intensity factor (K), T -stress (T), rigid rotation (A), and rigid translation (B) as given by the asymptotic result:

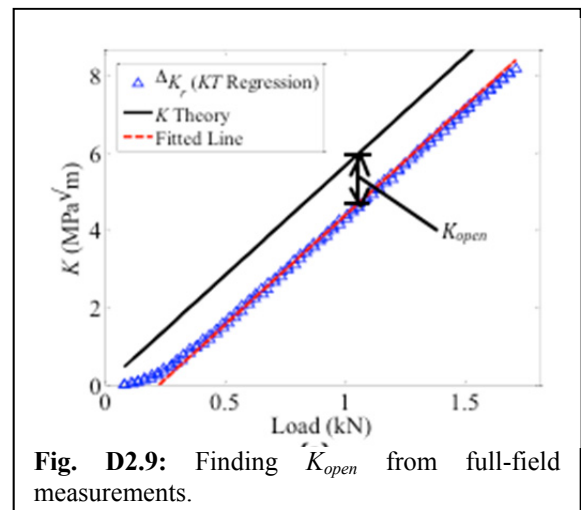
$$v = \frac{K_I}{\mu} \sqrt{\frac{r}{2\pi}} \sin\left(\frac{\theta}{2}\right) \left[\frac{1}{2}(\kappa + 1) - \cos\left(\frac{\theta}{2}\right) \right] - \frac{1}{2\mu} \left(\frac{v}{1+\nu} \right) T r \sin(\theta) + A r \cos(\theta) + B. \quad (\text{D.2.2})$$

In Eq. D.2.2 r is the distance from the crack tip, θ is the angle from the crack line ahead of the tip, μ is the shear modulus, and κ is given by $(3 - \nu)/(1 + \nu)$ for plane stress (where ν is Poisson's



ratio). Figure D2.9 shows the stress intensity factor measured in this way, along with the theoretical prediction from 2D elasticity for a monotonically loaded crack tip of the same material and geometry. As can be seen the measured K is less than the theoretical value, indicating the presence of closure, and therefore crack tip shielding. The amount of closure at the macroscale can be estimated either as the difference between the theoretical and measured result, or by applying at the macroscale a technique similar to the compliance change methodology proposed by Elber for the microscale results. The latter is shown in Fig. D2.7 as the dashed lines, of which there is only one per experiment since it is an aggregate full-field measurement.

In summary, two full-field DIC methods for measuring crack closure levels during fatigue



crack growth in Ti were introduced and compared to a DIC based displacement gage method. Including the T -stress term in the least squares regression was necessary for reliable results from the full-field techniques. Results from the three techniques were compared for low, medium and high K experiments (with maximum K values of $9.7 \text{ MPa}\sqrt{\text{m}}$ (with $R = 0.05$), $15.4 \text{ MPa}\sqrt{\text{m}}$ (with $R = 0.05$), and $18.9 \text{ MPa}\sqrt{\text{m}}$ (with $R = 0$), respectively). Crack opening levels calculated from the full-field effective K method agree with displacement gage closure levels far from the crack tip in the constant opening level region. The second full-field method, the full-field K -compliance method, gives crack opening levels that are an average of local values over the correlated region. The use of these full-field methods would allow effective stress intensity factors to be measured on a full-field basis circumventing some of the drawbacks of placing displacement gages in contact with the sample near the crack tip. Our focus here was to introduce full-field crack closure measurement techniques and to use a multiscale experimental approach to compare closure levels obtained through microscale and macroscale experiments on the same sample. The full-field crack closure techniques demonstrated here use lower magnification images than the DIC displacement gage technique (in this case, $1.1\times$ compared to $14\times$). Since high quality, high magnification images for DIC can be difficult to obtain, these full-field techniques could be a valuable, easier method for estimating closure levels. This could be of great use in many engineering applications where obtaining approximate answers with less effort is desired.

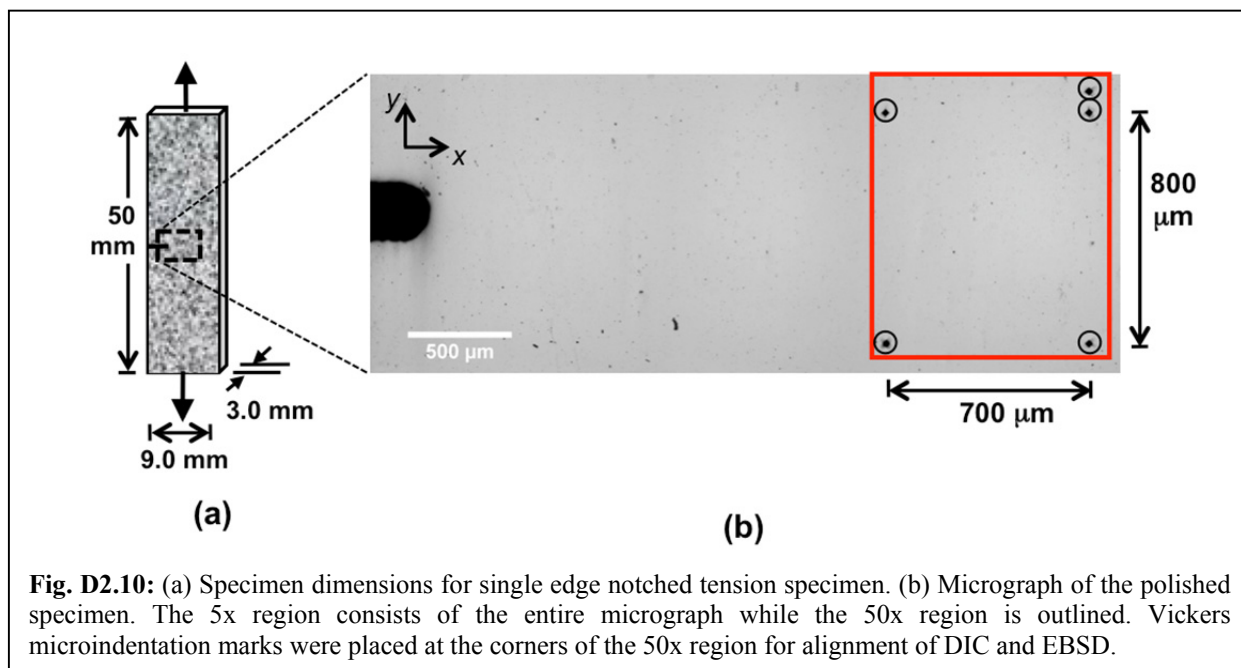
D.2.3 *Ex Situ* Methodology for Ultra-high Resolution Strain Measurement

A second set of experiments were conducted where the area that was zoomed into was now ahead of the fatigue crack tip rather than behind. The goal of this set of experiments was to develop an understanding of how strain accumulates at the microscales (*i.e.*, on a size scale comparable to the material grain structure) and how this deformation can be related to macroscale measurements of quantities such as the stress intensity factor. Two types of multiscale measurements were made in this part of the work: *ex situ* and *in situ*. *Ex situ* measurements involved removing the sample from the load frame and taking high resolution images using an optical microscope. *In situ* involved taking images as the fatigue crack was growing, which means that only one area could be imaged. In this section we will discuss the *ex situ* ultra-high resolution experiments, while the *in situ* experiments will be covered in the next section.

Microstructural measurements from electron backscatter diffraction (EBSD) were aligned with deformation measurements from digital image correlation (DIC). A brief description of the testing procedures will be given here. More details of the experimental procedures for sample preparation, experimentation, acquisition of high resolution DIC data, and linking multiple data sets, along with a discussion of the benefits and drawbacks of the procedure are given in Carroll *et al.* (2010). A single-edge-notch tension specimen of Hastelloy X was machined with dimensions of $50 \times 9 \times 3 \text{ mm}$ as shown schematically in Fig. D2.10(a). A 1.5 mm , through-thickness notch was machined using electrical discharge machining with a wire diameter of $150 \text{ }\mu\text{m}$ resulting in a notch width of $200 \text{ }\mu\text{m}$. The specimen was then polished to a finish acceptable for EBSD using rough polishing, alumina polishing powder down to $0.3 \text{ }\mu\text{m}$, and finally, vibratory polishing with $0.05 \text{ }\mu\text{m}$ colloidal silica. This work consists of multiscale DIC measurements over two regions of interest shown in the micrograph of the polished specimen in Fig. D2.10(b). The first region of interest is the entire area shown in Fig. D2.10(b)

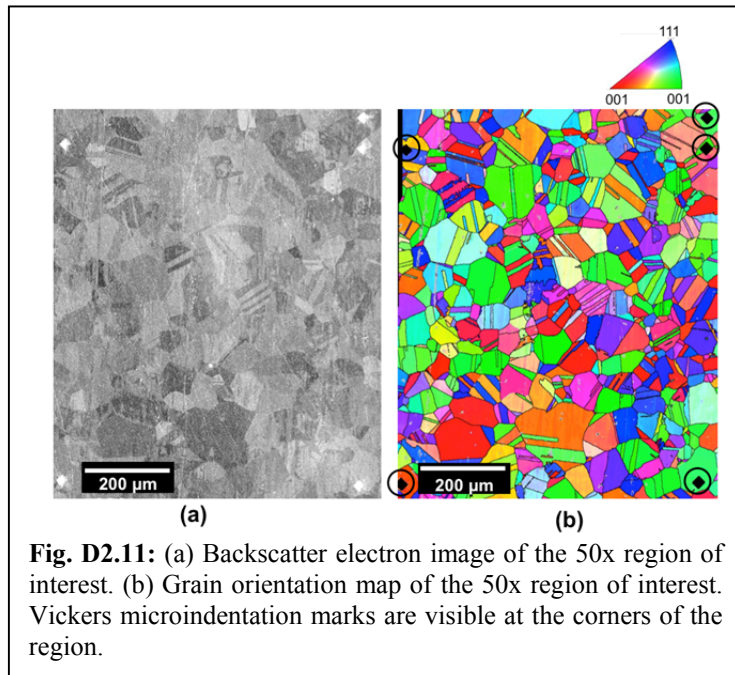
(approximately 2.7 mm x 0.9 mm) including the notch tip. This region was examined at 5x magnification with digital image correlation (DIC) at a resolution of 0.87 $\mu\text{m}/\text{pix}$. The second region of interest, which is a subset of the first, is outlined on the right side of Fig. D2.10(b) and was imaged at 50x magnification (0.087 $\mu\text{m}/\text{pix}$). The 50x region is 700 μm x 800 μm and is located 3.05 to 3.75 mm ahead of the notch mouth. At both 5x (0.87 $\mu\text{m}/\text{pix}$) and 50x (0.087 $\mu\text{m}/\text{pix}$) magnifications, arrays of images were collected to cover the respective regions of interest. An optical microscope, Olympus model BX51M, was used with 5x and 50x objectives, respectively. Digital image correlation was performed using Vic2D (version 2009.1.0), a commercially available DIC program from Correlated Solutions, Inc.

DIC-measured residual plastic strain fields, obtained from each image as described below, were stitched together to provide high-resolution strain field measurements over the

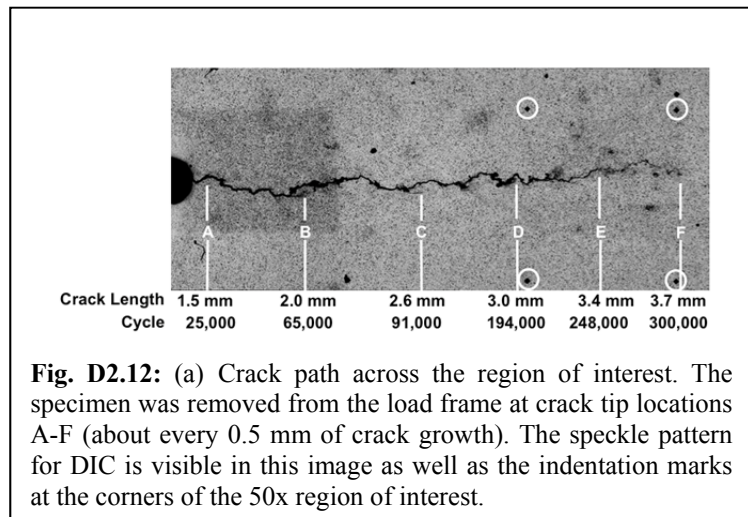


entire region of interest (Carroll *et al.*, 2010). Two images at 5x magnification (each with an image width of 1.39 mm) were used to cover the entire region of Fig. D2.10(b). The smaller region in Fig. D2.10(b) was covered with 112 images (8 x 12) at 50x magnification (each with an image width of 139 μm). The stitching technique allowed for ultra-high resolution DIC results over relatively large regions of interest.

Additionally, microstructural measurements were captured throughout the 50x region using EBSD (Fig. D2.11). Fiducial markers, in the form of Vickers microindentation marks, were placed on the specimen at the corners of the 50x region of interest to provide alignment between EBSD and DIC measurements; these are pointed out by circles in both Fig. D2.10(b) and Fig. D2.11(b). An SEM micrograph of the 50x region of interest is shown in Figure 2a. The grain orientation map shown in Fig. D2.11(b) illustrates that the material used here is relatively untextured with equiaxed grains. Although the average grain size of Hastelloy X is 95 μm , the presence of annealing twins that divide nearly every grain makes the effective grain size closer to 50 μm .

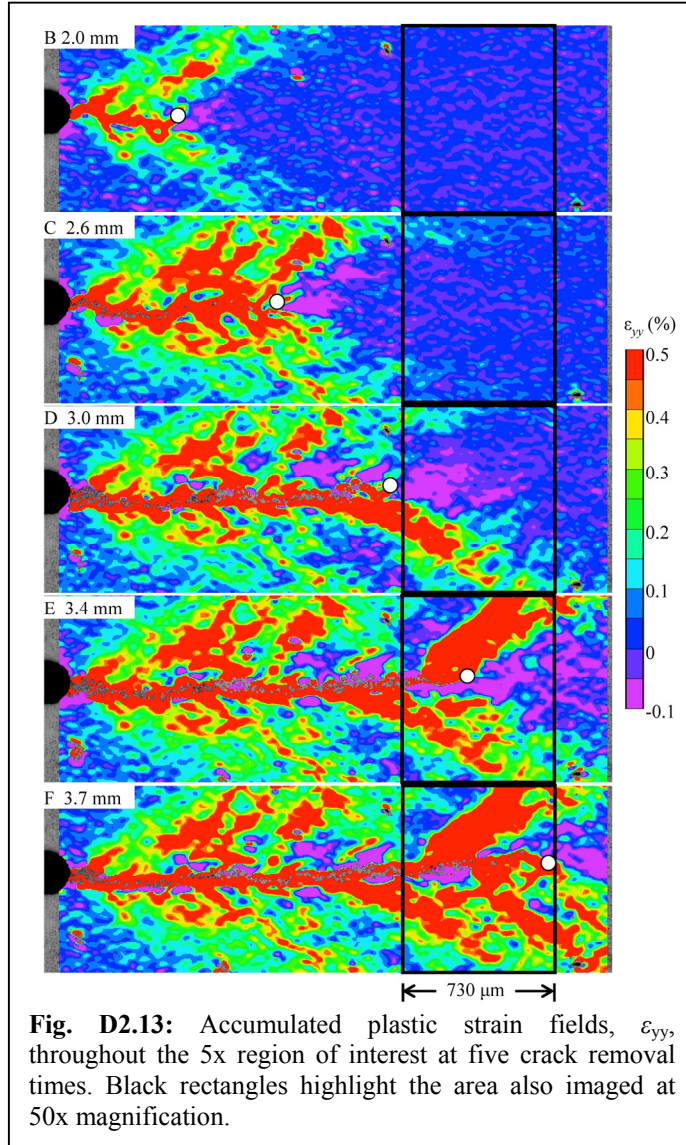


regions of interest were imaged in the optical microscope at multiple resolutions using imaging techniques described above. The crack path and speckle pattern are shown in the micrograph in Fig. D2.12. The crack length and number of cycles for each of the specimen removal times, labeled A-F, are shown below the micrograph. DIC was performed on image sets B-F, with image set A as the reference, for both regions of interest, the larger one at 5x and the smaller one at 50x. It is important to note that all images (both reference and deformed) were captured at zero load, and consequently the strain measured by such *ex situ* DIC only includes fatigue strain accumulation (*i.e.*, predominantly plastic strains) as opposed to strain due to a current load on the specimen which would be measured using what we term *in situ* DIC.



The strain field perpendicular to the crack line, ϵ_{yy} , at each removal time, B-F, is plotted for the two-image 5x region in Fig. D2.13. The crack tip in each plot is represented by a white circle. DIC subset sizes and spacings, two measures of DIC spatial resolution, were $18 \times 18 \mu\text{m}$ (21 x 21 pix), and $4.3 \mu\text{m}$ (5 pix), respectively. These plots clearly show an inhomogeneous wake of plastic strain accumulation left behind the propagating fatigue crack. When a crack is loaded monotonically, the plastic zone consists of two lobes of high strain emanating at some angle from the crack tip on each side of the crack line. As a fatigue crack grows under what are thought of as steady state conditions, it is expected to leave behind a plastic wake with a height dictated by these lobes. However, as is

seen in Fig. D2.13, the plastic wake consists of lobes of accumulated strain interspersed with areas of little or no accumulated strain. These strain localizations are remnants of plastic zones associated with specific past crack tip locations. These lobes of accumulated strain are often asymmetric, although the crack path itself is macroscopically straight. In addition, the strain accumulated as the crack tip passes a particular material point appears to be largely unaffected by further crack growth beyond that point, so that behind the crack tip, all of the strain fields in



crack tip, only the one below the crack line is apparent in strain field D. When the crack is at point E, a high-strain lobe above the crack tip has also developed. By the time the crack tip reaches the end of the region of interest, time F, another lobe below the crack line appears. Within this region of interest, the strain localizations are in an asymmetric, staggered pattern (*i.e.*, the lobes formed at D, E, and F are on alternating sides of the crack line).

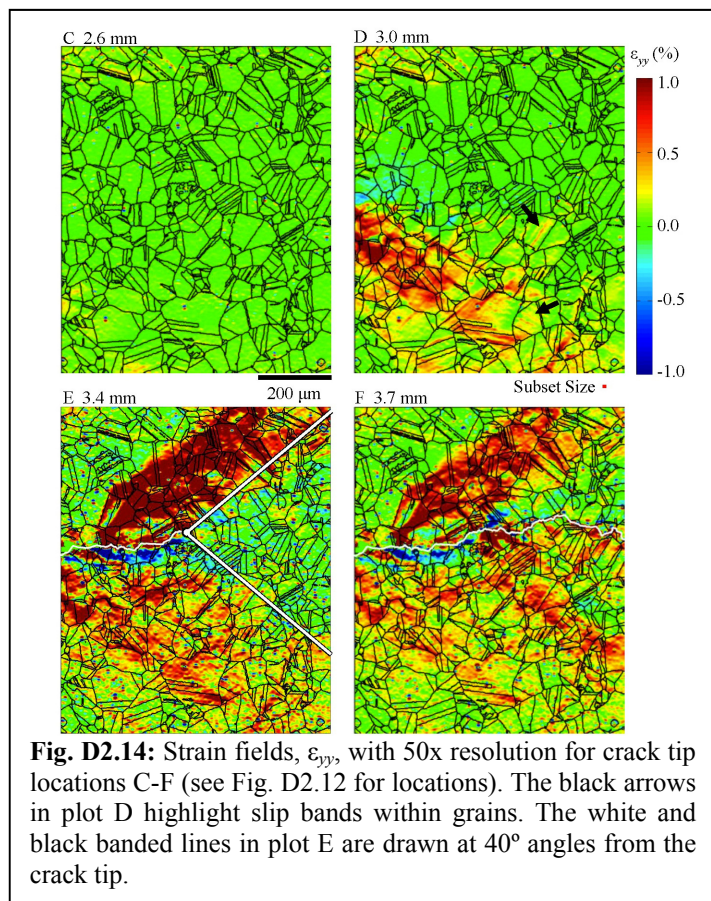
The strain lobes at time E appear to form at angles of roughly 40° (as do the majority of the strain lobes shown in Figs. D2.13 and D2.14). Lines at angles of $\pm 40^\circ$ are drawn on plot E in Fig. D2.14 to illustrate this point. Because strain accumulates in lobes, the material directly

Fig. D2.13 essentially look the same.

The black rectangle in Fig. D2.13 represents the region of interest that was also imaged at 50x magnification for DIC. At 50x magnification, DIC results were obtained using a subset size of $8.8 \mu\text{m} \times 8.8 \mu\text{m}$ (101×101 pix) and a subset spacing of $0.87 \mu\text{m}$ (10 pix) producing 2400 correlation points within a typical $50 \mu\text{m}$ diameter grain. DIC was performed separately on each of the 112 pairs of images and the resulting strain fields were stitched together to obtain the strain fields over the entire region of interest. The improved resolution obtained by image stitching is demonstrated in Carroll *et al.* (2010)

The stitched, 50x magnification ϵ_{yy} strain fields for crack tip locations C through F are shown in Fig. D2.14 with grain boundaries from EBSD results overlaid on top. For comparison, the crack path is drawn in white on plots E and F. At time C, the region is relatively strain free with the high strain lobes only beginning to enter at the corners. At time D, as the crack enters the region of interest, a lobe of high strain ahead of the crack tip appears within the region of interest. While there are generally two lobes of high strain ahead of the

ahead of the crack tip (to the right of these lines) accumulates very little strain. Slip emanating from the crack tip at angles has also been observed and predicted by other researchers (Tomkins



and Biggs, 1969; Peralta and Laird, 1998; Peralta *et al.*, 2007) for fatigue crack growth. In particular, a kinematical model for fatigue crack growth by Peralta and Laird (1998) predicts slip at an angle of 54.7° ahead of the crack tip.

In addition to the lobes of macroscopic strain localization discussed earlier, the strain fields in Figs. D2.13 and D2.14 have inhomogeneities at the sub-grain level. There are localizations that occur on grain (and twin) boundaries, slip bands within grains, and grains that accumulate different levels of strain than their neighbors. There are few studies of direct measurements of accumulated strain associated with fatigue crack growth with which the present results (either low or high resolution) can be compared. Sangid *et al.* (2011d) discuss the interaction of slip bands associated with fatigue crack growth and grain and twin boundaries;

and they show two DIC strain fields that appear to be a combination of accumulation from fatigue crack growth and monotonic loading. Although their resolution is relatively low compared to that used here, there does appear to be heterogeneity in the wake of the crack. Peralta *et al.* (2007) shows a single lobe of strain following slip bands near a crack tip, but this lobe is on the order of one or two grains as opposed to dozens seen here. More commonly, researchers obtain measurements throughout a single cycle resulting from an increase in load as in a monotonic fracture experiment or unstable crack propagation within a single cycle. Although obtaining strain fields in such cases is informative, both of these types of strain measurements are inherently different from those shown in this paper because they do not capture strain accumulation resulting from fatigue crack growth.

In addition to strain heterogeneities in the form of lobes, strain localizations also were observed at the subgrain level. Some grains accumulated more strain than others (although the strain within a grain was rarely homogeneous), and strain localizations were found on grain and twin boundaries. One example these subgrain level strain localizations is shown in Fig. D2.15 (from a similar experiment). The backscatter electron image in Figure 11a shows slip bands within a few grains near a crack line. Of particular interest are a few slip bands (indicated by arrows) within the highlighted grain that change direction as they cross two twin boundaries. This change in direction is caused by the change in orientation between the twinned and untwinned material. The slip bands generally form on the most favorable slip system in each

grain, *i.e.*, the system with the highest resolved shear stress. DIC provides quantitative measurements of the strains associated with these slip bands. The plot of ϵ_{yy} strain in Fig. D2.15(b) shows that the vertical strain increases dramatically at slip band locations. Furthermore,

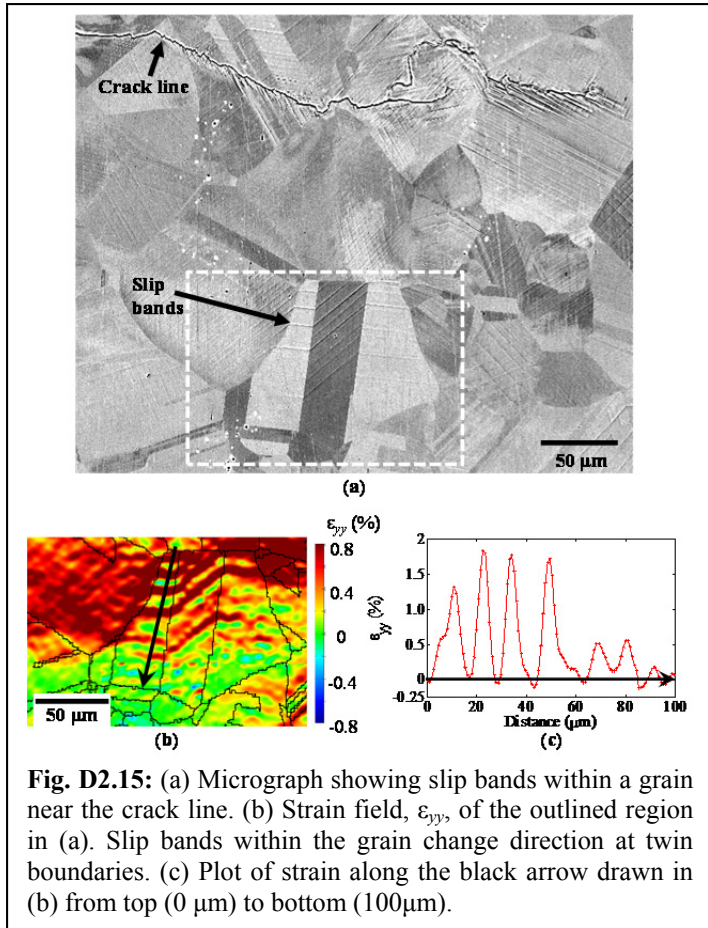


Fig. D2.15: (a) Micrograph showing slip bands within a grain near the crack line. (b) Strain field, ϵ_{yy} , of the outlined region in (a). Slip bands within the grain change direction at twin boundaries. (c) Plot of strain along the black arrow drawn in (b) from top (0 μm) to bottom (100 μm).

the spatial alignment of DIC results with microstructure is further confirmed by comparing Fig. D2.15(a) to (b). A line plot of the strain along the black arrow in Fig. D2.15(b) (from top to bottom) is shown in Fig. D2.15(c). It reveals that the residual plastic strain within these slip bands reaches up to 1.8% (perhaps more since this is a lower bound of the maximum) while the material between slip bands is entirely undeformed, even though the —macroscopic stress generated by the crack tip at that location is still significant (this location is well within the plastic zone predicted by linear elastic fracture mechanics). It is important to note that the strain could be higher than the values shown in this plot since the strain is calculated over the finite distance determined by the subset size and spacing (in this case, 7 μm and 0.9 μm, respectively).

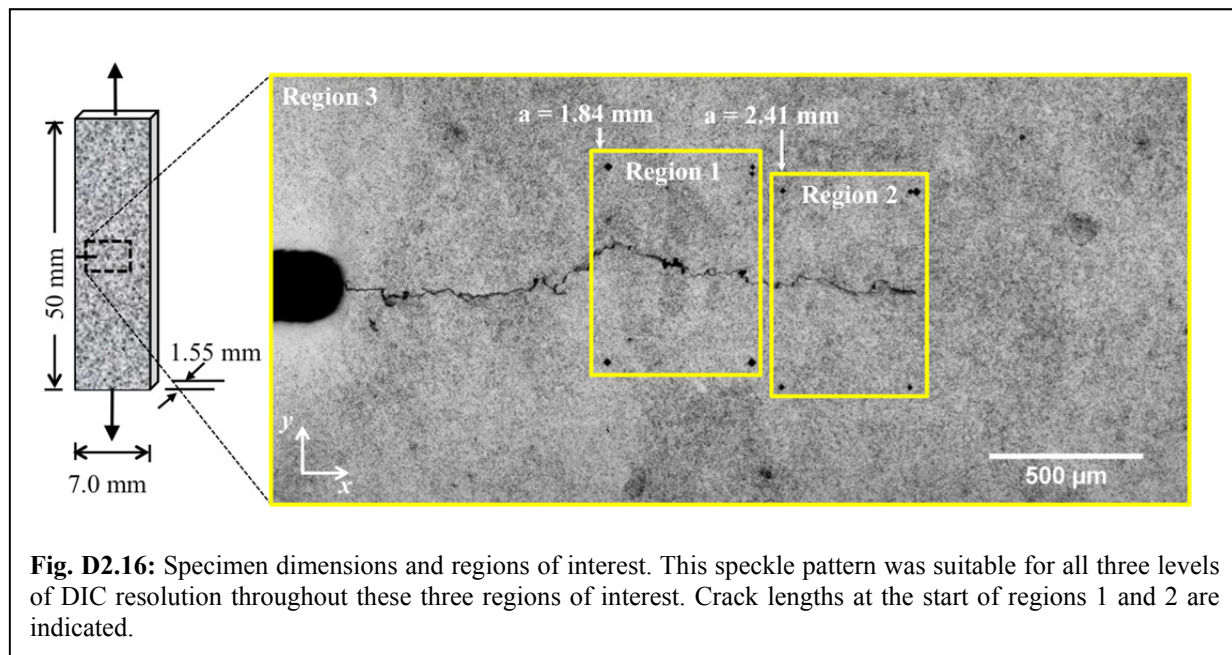
The measurements performed in this work combine an extraordinary

amount of data from various sources, but there is still some information not captured here. Both strain and microstructure measurements in this paper are two-dimensional surface measurements. Subsurface microstructure undoubtedly influences both the crack path and the surface deformation. Thus, one extension of this work that would overcome this limitation is the acquisition of 3D measurements, both in regards to microstructure characterization and displacement/strain. Microstructural characterization could be improved by obtaining subsurface measurements of microstructure (after crack growth) through serial sectioning (Groeber *et al.*, 2008; Field *et al.*, 2010). A non-destructive approach is the use of diffraction contrast tomography, which can be used to measure both microstructure and crack path three-dimensionally. However, to our knowledge, the experiments described here provide the first subgrain level, full-field measurements of plastic strain accumulation near a growing fatigue crack. The spatial resolution of these DIC measurements is also unprecedented for the large area covered.

D.2.4 *In Situ* High Resolution Strain Measurement during Fatigue Crack Growth

In this part of our effort, we employed a similar approach to investigate the relationships between crack path, microstructure, crack growth rate, and strain field in fatigue crack growth. High resolution DIC measurements of strain accumulation in fatigue crack growth were obtained, and these plastic strains were related to grain structure measured by electron backscatter diffraction (EBSD). *In situ* DIC measurements in a servohydraulic load frame show the development of grain-level strain fields over time, and subgrain level measurements of strain accumulation in the same regions are made using the high resolution, *ex situ* DIC technique. Additionally, crack path and crack growth rate were examined in relation to these microstructure and strain measurements.

The material studied was again Hastelloy X with the following pertinent material properties: yield strength = 348 MPa, ultimate strength = 730 MPa, ductility = 54%, elastic modulus = 205 GPa, Poisson's ratio = 0.32 (Haynes International, Inc.). A single edge notch tension specimen with dimensions 50 x 7.0 x 1.55 mm and a 0.99 mm notch (Fig. D2.16) was machined using Electrical Discharge Machining (EDM). The specimen was prepared as described above to produce a surface finish suitable for EBSD. Material deformation associated



with fatigue crack growth was studied in three regions of the specimen as shown in Fig. D2.16. Region 3 comprises an area that includes the entire crack line from the notch tip to the final crack tip position (approximately 2.0 mm wide by 1.0 mm tall). DIC measurements of full-field strain accumulation were made throughout this region after the last load cycle (cycle number 208,434) was applied to the specimen (using a DIC reference image captured before fatigue loading). Regions 1 and 2, the smaller regions in Fig. D2.16, measure 630 x 470 μm and 630 x 410 μm , respectively. The crack length, as it entered regions 1 and 2, was 1.84 and 2.41 mm as annotated in Fig. D2.16. These two smaller regions were studied in greater detail as the crack passed through each region. The full-field strain accumulation within each region was measured, *in situ*, every 64 cycles by DIC (using commercially available software, Vic2d, from Correlated Solutions, Inc.). This was accomplished by correlating minimum-load images captured at the measurement cycle to the reference image captured before fatigue loading. After the crack had

grown through regions 1 and 2, cycling was stopped, the specimen was unloaded, and high resolution, full-field DIC measurements of strain accumulation between the initial and final states were obtained using the techniques described in Carroll *et al.* (2010).

Two microscopes were used to capture images for this experiment. A microscope mounted on a 3-axis stage near the load frame was used to acquire *in situ* images of regions 1 and 2 every 16 cycles. The major advantage of this *in situ* optical microscope setup is that it allows a large number of cycles to be accumulated through the use of a servohydraulic load frame (in contrast to using a screw-driven *in situ* load frame in a scanning electron microscope). A 10x magnification objective was used to obtain an image scale of 0.43 $\mu\text{m}/\text{pix}$ (corresponding to an image size of 688 x 516 μm). A separate microscope was used for *ex situ* imaging of the unloaded specimen before and after fatigue loading. High resolution DIC results for regions 1 and 2 were obtained by stitching 36 images (per region) at a scale of 0.087 $\mu\text{m}/\text{pix}$ (50 \times magnification with an image size of 139 x 104 μm). *Ex situ* imaging of region 3 was performed at a scale of 0.87 $\mu\text{m}/\text{pix}$ (5 \times magnification with an image width of 1.39 x 1.04 mm) using a montage of three images.

Although images were captured every 16 cycles, DIC was performed on the *in situ* images in regions 1 and 2 at intervals of 64 cycles to reduce the computational load. The speckle pattern allowed a subset size of 9 x 9 μm (21 x 21 pix) and a subset spacing of 2.2 μm (5 pix) to be used. As a result, full-field DIC measurements of the strain field were obtained for roughly 1,200 measurement cycles as the crack grew across the region 1. Similarly, strain fields for 900 measurement cycles were obtained for region 2. These measurements show the evolution of the strain field with crack growth, and its relationship to grain structure. Using *ex situ* images, high resolution DIC was performed throughout regions 1 and 2 using a subset size of 7 x 7 μm (81 x 81 pix) and a subset spacing of 0.9 μm (10 pix). These high resolution measurements allow the strains inside grains and across multiple grains to be visualized. The DIC results for region 3

were calculated using a subset size of 27 x 27 μm (31 x 31 pix) and a subset spacing of 4.4 μm (5 pix). The measurements throughout this region provide a larger view of the strain field surrounding regions 1 and 2.

Before loading the specimen, microstructural measurements were acquired throughout regions 1 and 2 using electron backscatter diffraction (EBSD). Grain orientation maps of these two regions are shown in Fig. D2.17; each map is a compilation of four EBSD scans. As before, the five Vickers indentation markers in the corners of each map, and at corresponding locations in Fig. D2.16, were used as fiducial markers to spatially overlay DIC strain measurements (both *in*

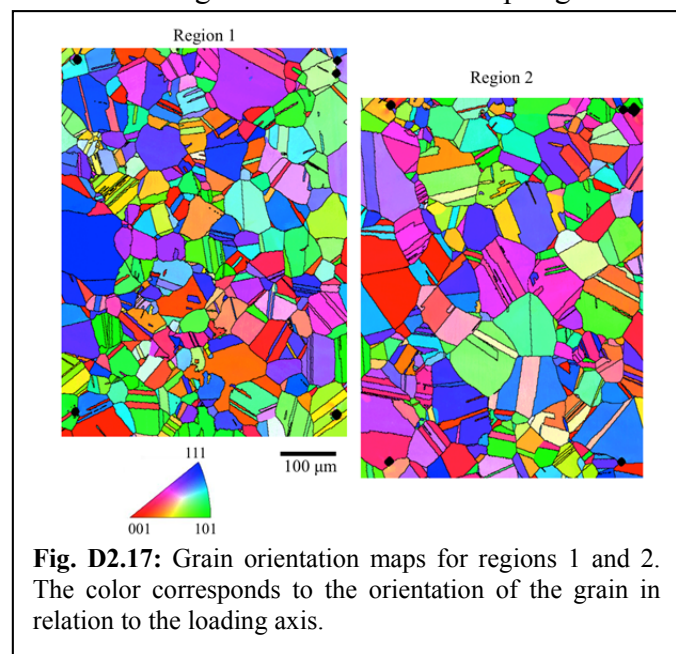
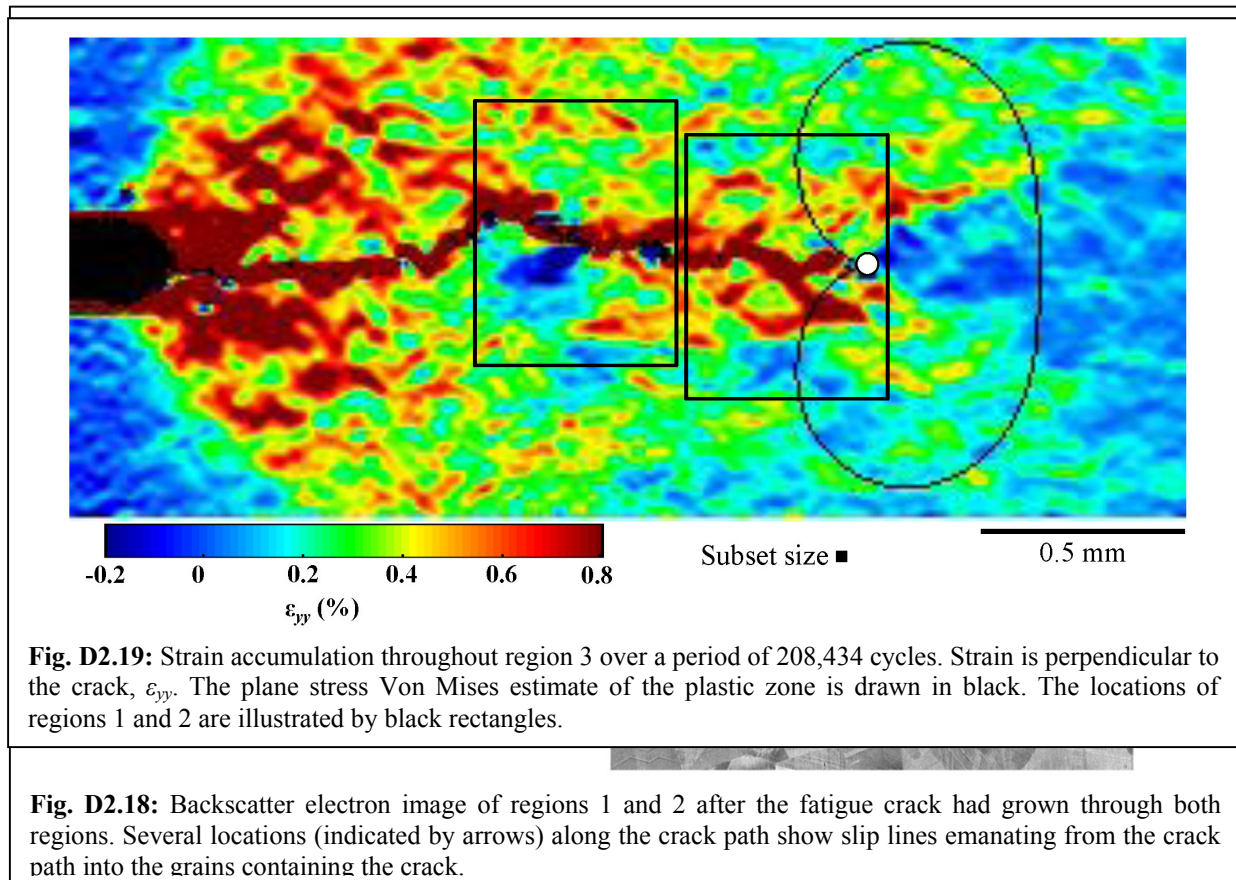


Fig. D2.17: Grain orientation maps for regions 1 and 2. The color corresponds to the orientation of the grain in relation to the loading axis.

situ and *ex situ*) with EBSD measurements of microstructure. After EBSD was performed, a speckle pattern was applied to the specimen by depositing 1 μm silicon powder on the surface. This speckle pattern, visible in Fig. D2.16, was suitable for all three levels of DIC resolution.

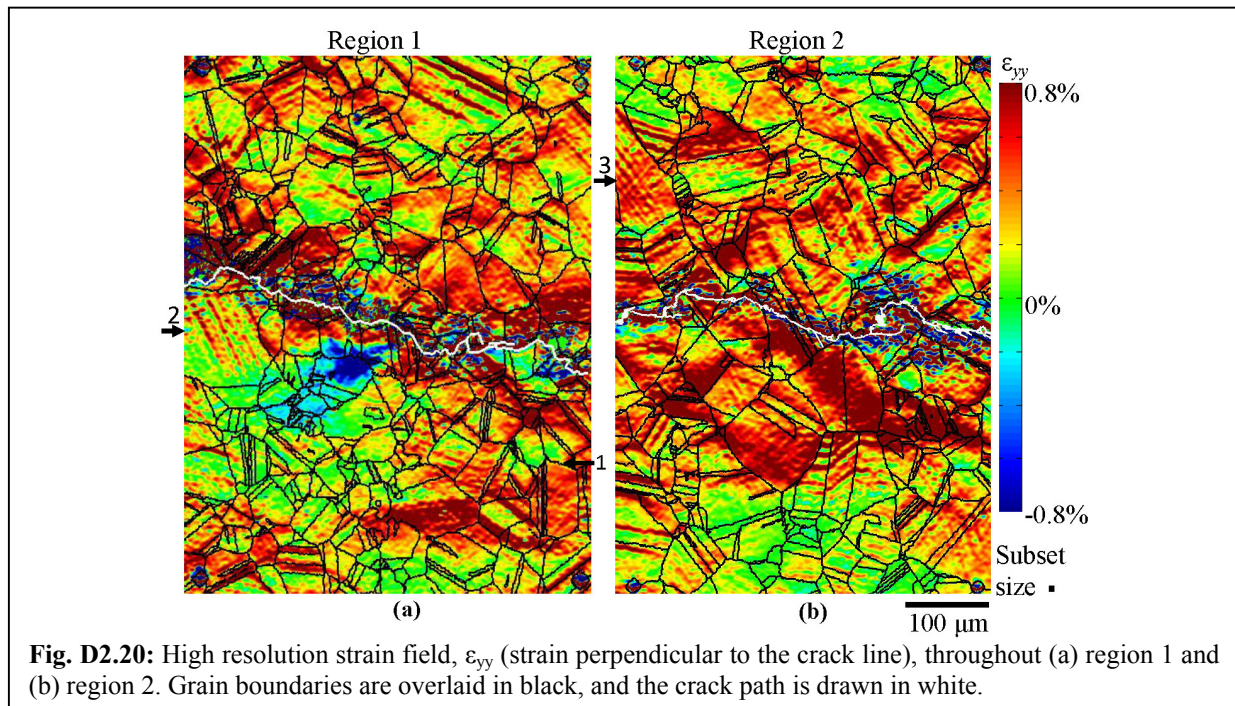
Fatigue loading was applied at a rate of 1 Hz. The crack initiated at the notch tip after 9,000 cycles and grew until entering region 1 around cycle 72,000. As the crack grew across the first region of interest, the change in stress intensity factor, ΔK , was held constant at 18.3 ± 0.3 MPa $\sqrt{\text{m}}$ by load shedding. The crack finished growing through region 1 around cycle 149,000, spending a total of 77,000 cycles within the region. The crack entered region 2 around cycle 166,000 and grew through the region for 42,000 cycles until exiting around cycle 208,000. While the crack tip was within the second region of interest, the fatigue loading was held at a constant



load amplitude so that ΔK increased from 18.2 to 22.7 MPa $\sqrt{\text{m}}$ (at 1 Hz) as the crack length increased. The minimum load was held constant at 0.2 kN throughout the entire fatigue loading so that the loading ratio, R , rose from 0.07 to 0.14 throughout the test. The difference in load amplitude between regions 1 and 2 did not appear to have a significant effect except in long-term crack growth rates. After the crack had grown through regions 1 and 2, fatigue loading was stopped and the specimen was imaged in the scanning electron microscope. A backscatter electron image of regions 1 and 2 after fatigue loading is shown in Fig. D2.18. This image shows the crack path, and grain geometry near the crack. Furthermore, slip bands generated by the growing fatigue crack are visible. Some slip bands develop in grains that are relatively far from the crack path. Other slip bands develop on the crack flanks and appear to influence crack path and crack growth rate (discussed later). These crack-flank slip bands are indicated by arrows in Fig. D2.18.

The strain throughout region 3, which accumulates over the entire period of fatigue crack initiation and growth (208,434 cycles), is plotted in Fig. D2.19. In essence, this is a quantitative

measure of the plastic wake produced during fatigue crack growth. This figure shows the strain field component perpendicular to the crack, ϵ_{yy} . The starter notch tip is shown in black at the left edge of the plot, the final crack tip position is highlighted by a white circle, and the subset size is



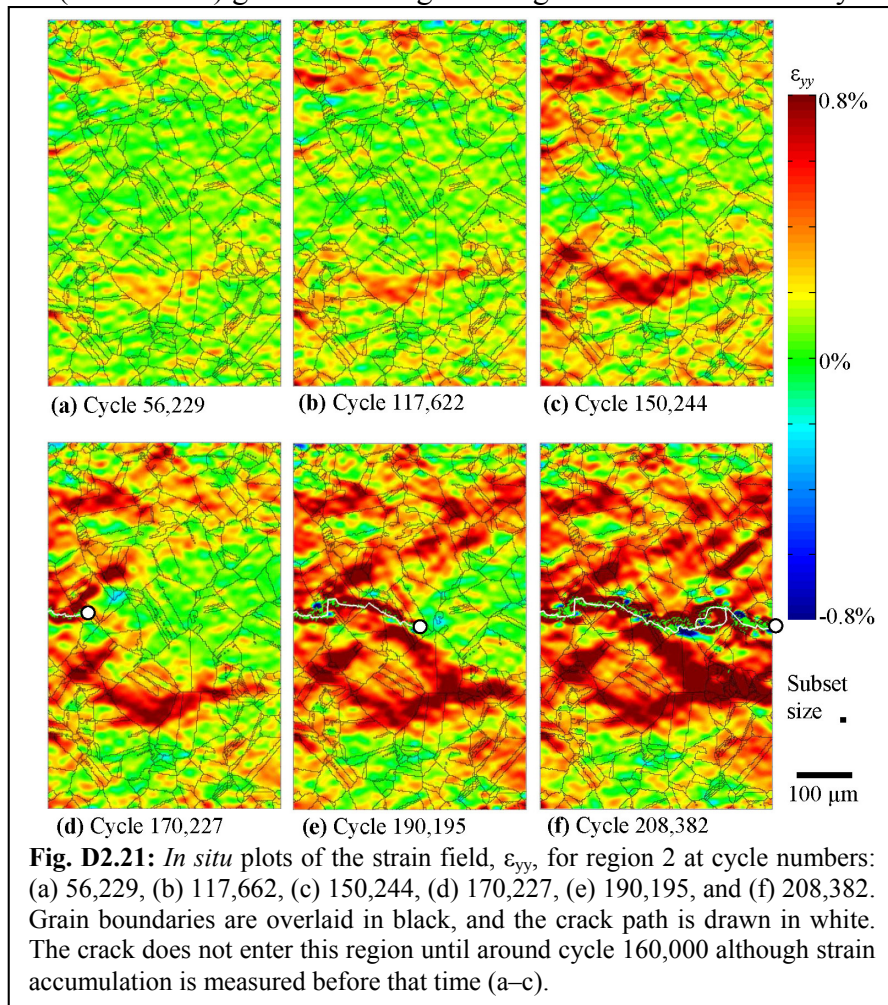
shown below the plot as an estimate of the spatial resolution of these measurements. As the crack grew, the material on the crack flanks separated so that the DIC algorithm detected a strain along the crack line; consequently, the crack path is apparent from the high measured strain levels associated with it. This path is also verified by comparison with the image of Fig. D2.18. The plane stress Von Mises estimate of the plastic zone is drawn in black in Fig. D2.19 (estimated for a stress intensity factor, K , of $20.5 \text{ MPa}\sqrt{\text{m}}$ and a yield stress of 385 MPa), and has a height of roughly 1.1 mm .

Plots of the high resolution strain fields, ϵ_{yy} , throughout regions 1 and 2 are shown in Fig. D2.20. The crack path is illustrated in white and grain boundaries from EBSD are shown in black. The subset size, an estimate of the spatial resolution of DIC measurements, is shown at the bottom right. These plots show a considerable amount of inhomogeneity at the grain and subgrain levels. On the scale of multiple grains, there is considerable variation in average strain levels from one grain to another (as indicated at point number 1 in Fig. D2.20). In some locations, significant strain accumulation occurs within a grain near the grain boundary while the neighboring grain exhibits relatively little strain near the same grain boundary (number 1). This indicates a grain boundary that has blocked dislocation motion between grains. While some grains accumulate more strain than others, there are very few grains in which the strain is homogeneous. Much of the strain variation within grains is in the form of slip bands within grains (number 2). A few locations also show evidence of multiple active slip systems within a single grain indicated by lines of strain localizations at multiple angles (point 3).

The strain plots in Figure D2.20 show the final strain accumulation field after crack growth has finished (*i.e.*, after cycle 208,434), but they contain little information on how those strain fields developed. The *in situ* strain fields that were captured every 64 cycles are better

suited to provide information on the change in strain fields with time. Six of these ϵ_{yy} strain fields are shown in Fig. D2.21 as the crack grows through region 2. The crack path is shown in white and the crack tip is illustrated by a white dot. The first three of the plots in Fig. D2.21(a–c) show that strain accumulation starts well before the crack tip enters the region indicating some fatigue damage is accumulating due to the far-field stress. The last three of these plots (Fig. D2.21(d–f)) show the strain field development as the crack grows through the region. In these last three plots, the majority of the strain accumulation is observed to travel with the crack tip in two lobes angled approximately 40° ahead of the crack tip. The plot in Fig. D2.21(e) demonstrates that the extent of these lobes of plastic strain is not only far from the crack tip, but also within one grain of the crack tip. Regions that accumulated strain well ahead of the crack tip saw strain levels intensify as the crack traveled through the region. The accuracy of the plots in Fig. D2.21 can be evaluated by comparing Fig. D2.21(f) to Fig. D2.20(b). These *in situ* and *ex situ* measurements of strain are independent of one another, yet they show strain localizations in the same locations (with an obvious difference in spatial resolution)

Crack tip position can be identified in each *in situ* image to measure the crack length at each cycle. A plot of crack length versus cycle number as the crack grew through region 1 is shown in Fig. D2.22(a). The slope of this plot represents the crack growth rate. A linear fit to the data (the red line) gives an average crack growth rate of 6.8 nm/cycle. Because this is constant- K



crack growth in the Paris regime, the crack growth rate is fairly constant. However, there are a few variations in the crack growth rate at the numbered locations. The causes for these deviations can be explained by crack path, microstructure, and strain accumulation in Fig. D2.22(b–g). At point number 1 in Fig. D2.22, the crack pauses until resuming its average growth rate at point number 2. A dead end branch is observed at point 1 in Fig. D2.22(b) indicating that this crack path became less energetically favorable than a competing crack path; consequently, crack growth paused as an alternate path was

formed. Fig. D2.22(d) indicates that this pause at point number 1 could also be due to strain accumulation above the crack line that reduced the driving force for the crack. This strain accumulation and associated crack pause can be seen in the first video included in supplemental material. This video shows the crack length vs. cycle number plot and the strain field as the crack grows through region 1. A comparison of Fig. D2.22(d) with Fig. D2.22(c) shows that this strain accumulation occurred within a grain containing several annealing twins (alternating orange/green in Fig. D2.22(c)). It is possible that annealing twins affect crack growth rates and local strain accumulation, but further study would be necessary to confirm or reject this hypothesis.

After the brief pause in crack growth between points 1 and 2, the crack continues to grow at the global average crack growth rate until slowing just before point 3, probably due to the deviation in crack path at that time. At point 3 (Fig. D2.22(a)), crack growth accelerates. The cause of this acceleration is not immediately clear from the image in Fig. D2.22(e), but the series of *in situ* images reveals the cause. After the crack decelerates slightly at point 3, it appears to

jump ahead to the point indicated by the arrow in Fig. D2.22(e). From this point, the crack appears to grow both forward and backward (to link back to point 3) simultaneously. This crack growth can be seen in the second video included in supplemental material. Of course, the crack is not truly growing backward. In reality, the subsurface crack front has grown ahead of the surface

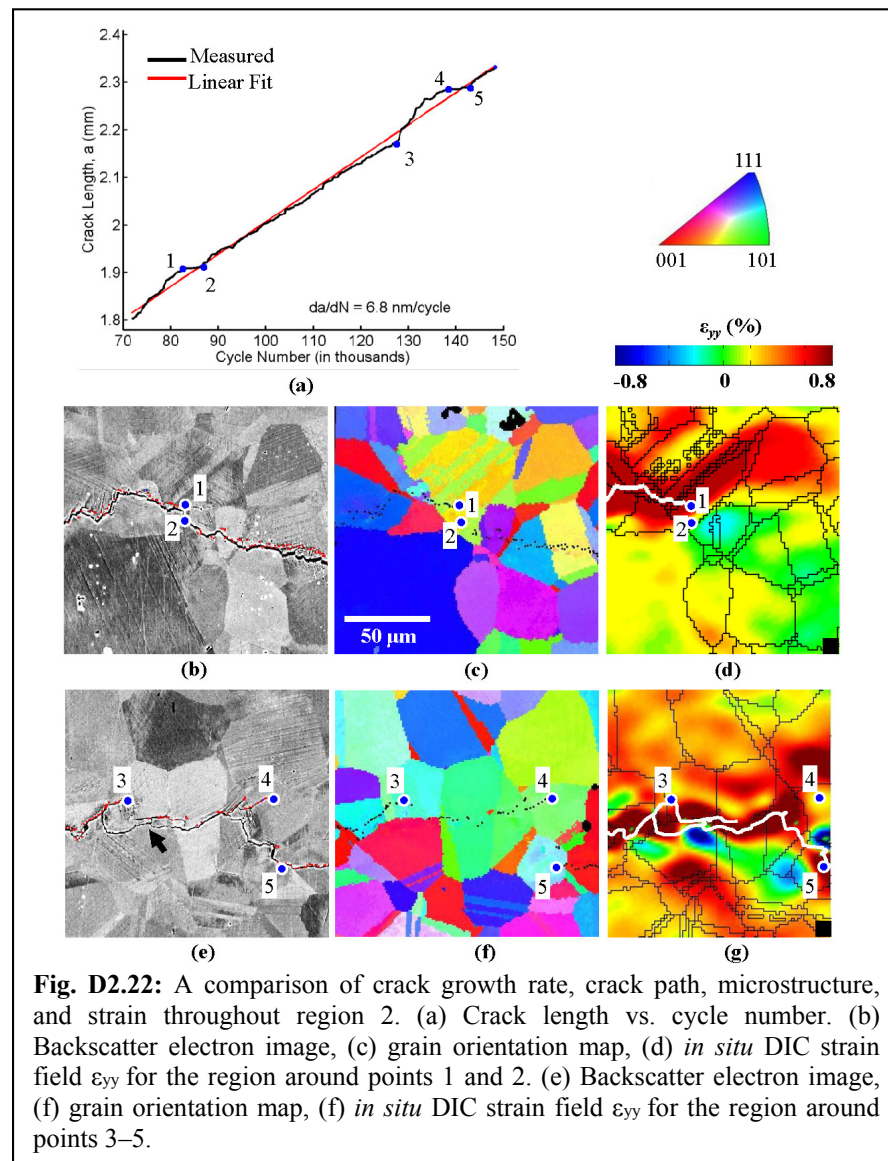


Fig. D2.22: A comparison of crack growth rate, crack path, microstructure, and strain throughout region 2. (a) Crack length vs. cycle number. (b) Backscatter electron image, (c) grain orientation map, (d) *in situ* DIC strain field ϵ_{yy} for the region around points 1 and 2. (e) Backscatter electron image, (f) grain orientation map, (f) *in situ* DIC strain field ϵ_{yy} for the region around points 3–5.

crack front (which may have also contributed to the slight deceleration before point 3). As the crack grows forward, the subsurface crack front also grows out to the surface. After this fast surface crack growth, the crack pauses again at point 4 as it forms a crack branch (Fig. D2.22(e)). This branching pauses crack propagation until a more favorable branch forms and becomes the primary crack path (point 5 in Fig. D2.22). This branching is due to slip systems in local grains that provide favorable conditions for crack growth, but only on a temporary basis. The grain orientation map and *in situ* strain field throughout the region near the crack branching is shown in Fig. D2.22(f,g).

Combined *ex situ* and *in situ* DIC

techniques provided measurements of the strain field near a growing fatigue crack with sub-grain level resolution. The *in situ* measurements also showed how these strains developed over time with crack propagation. The plastic strain field traveled in two lobes angled ahead of the crack tip with almost no strain accumulation directly ahead of the crack. A considerable amount of inhomogeneity, which was strongly influenced by microstructure, was observed in the plastic wake behind the crack tip.

This work examined the local relationships between four variables in fatigue crack growth: crack path, microstructure, crack growth rate, and strain field. The following relationships were observed: (i) The local crack growth rate is affected by the local strain field, crack path, and microstructure. Local strain accumulation can reduce the crack growth driving

force, branches and tortuosity in the crack path can slow crack growth, and grain orientation can favor faster or slower local crack growth rates. The long-term crack growth rate over many cycles represents an average of many of these factors, sometimes competing. (ii) The strain field within the crack tip plastic region is influenced by both location relative to the crack path and microstructure. (iii) The local crack path was shown to depend on microstructure. In particular, the crack deviated significantly in order to go around a large grain that was unfavorably oriented for slip (*i.e.*, had a low Schmid factor). Microscale slip lines at the crack tip are determined largely by local grain orientation and influence the crack growth direction. However, crack growth was rarely along a single slip plane within a grain; it alternated between multiple planes and sometimes appeared to grow in directions not associated with any obvious slip plane. The favorability of crystallographic slip planes may also affect local crack growth rates, but not in a straightforward manner. (iv) The strain field was shown to have some effect on crack path and crack growth rate. In one instance, strain accumulation in a twinned region may have contributed to retardation of the crack growth rate. In contrast, strains associated with crystallographic slip may create conditions favorable for faster crack growth and may influence crack path.

Although these experiments produced an unprecedented amount of data, both in terms of extent and resolution, it is inevitable that data have limitations. There are a few aspects of these experiments that could benefit from further optimization. Better resolution for *in situ* measurements could be obtained by improving lighting, increasing magnification, and reducing system noise (*e.g.*, vibration). *In situ* measurements also have the potential for simultaneously measuring strain fields within cycles and between cycles if the images can be kept in focus throughout the loading cycle.

Additionally, measurements such as these could also be analyzed on a statistical basis to infer the effects of microstructure on strain localizations. A statistical correlation would provide a quantitative measure of the effects of microstructural variables such as grain orientation (perhaps based on the global or local Schmid factor), grain geometry (large vs. small grains), and grain boundary misorientation among others. Padilla *et al.* (2012) used a Spearman rank correlation to compare strain fields to microstructural properties. They found a correlation between Schmid factor and maximum shear strain in uniaxial tension experiments in Zirconium. A statistical analysis of the transmission of persistent slip bands was performed by Sangid *et al.*, (2011a) by performing molecular dynamics simulations over a large number of grains. They found that twin boundaries are stronger barriers to slip transmission between grains than other coincidental site lattice grain boundaries. Also, as happened with the crack closure work in project D4, it would be useful to extend this work to high temperature applications.

Both strain and microstructure measurements in these experiments are two-dimensional and take place only on the specimen surface. However, one factor that potentially influences the crack path and surface deformation is microstructural effects below the surface. Thus, one extension of this work that would overcome this limitation is the acquisition of 3D measurements, both in regards to microstructure characterization and displacement/stain. Microstructural characterization could be partially improved by obtaining sub-surface measurements of microstructure (after crack growth) through serial sectioning as, for example, in the work of Groeber *et al.*, 2008, and Field *et al.*, 2010. A more thorough approach is the use of diffraction contrast tomography (Herbig *et al.*, 2011), which can be used non-destructively to measure both microstructure and crack path three dimensionally.

Another piece of data that would improve understanding of these experiments is the stress field. Although the global stress is known, microstructure and crack path geometry alter

these fields locally. It is rare for experimental techniques to capture both stress and strain. Some estimation of stress values could possibly be obtained through simulations such as crystal plasticity models. Multiple studies on these models have shown them to be qualitatively accurate in some situations, but their reliability still has room for improvement. The fidelity of these models could be improved if they were given three dimensional microstructure measurements of the sample to be experimentally tested. Simulation strain fields on the specimen surface could then be compared to experimental measurements to validate the model and improve the credibility of simulated stress fields.

D3 Thermomechanical Fatigue of Hastelloy X: Role of Combined Loading on Material Response

Personnel: Sehitoğlu, Abuzaid (graduate student, UIUC), Penmetsa (AFRL)

Start: 2008; End: 2012

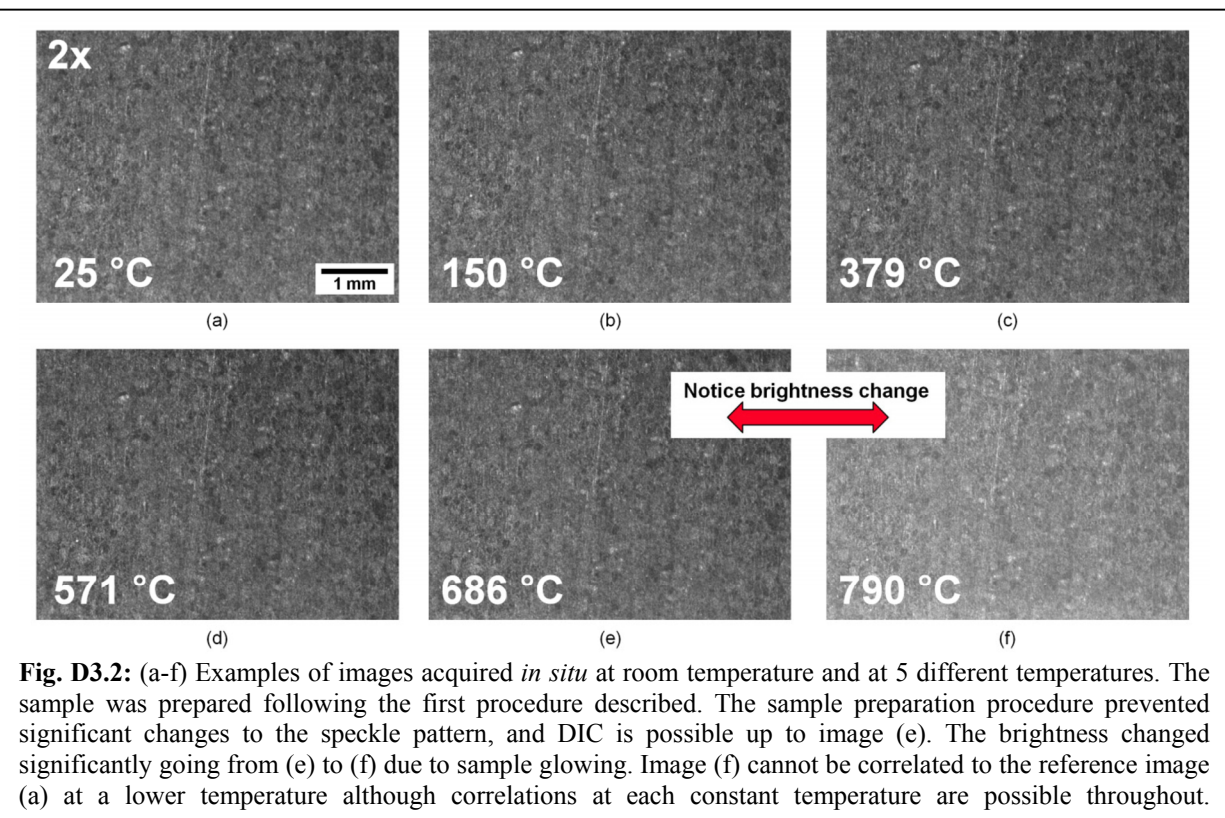
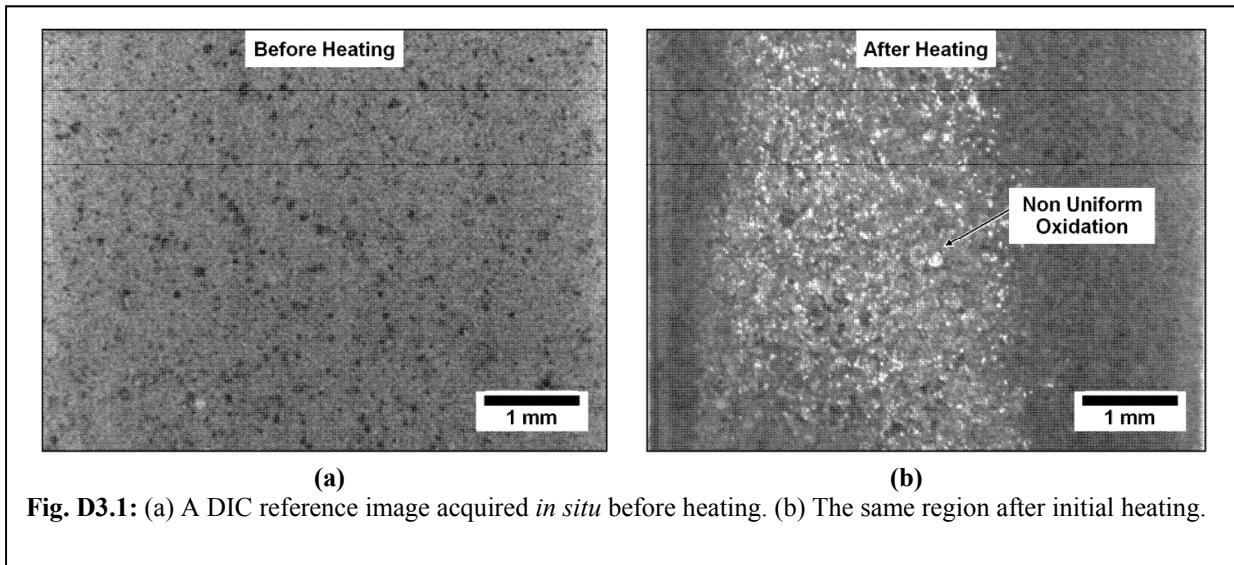
This project was formed as a continuation of project D1 and was initially slated to study thermomechanical fatigue of Hastelloy X. An early series of macroscopic experiments investigated the relative effects of thermomechanical fatigue on Hastelloy X and dealt with the challenges of using DIC at elevated temperatures. After several such macroscale experiments, the focus of the project was shifted onto a more microstructural understanding of how fatigue damage evolved in Hastelloy X in order to provide experimental data for projects B3 and B4. In these microscale efforts it became of interest to explore the role of grain and twin boundaries in fatigue damage accumulation in Hastelloy X. Since this material is quite pristine and devoid of inclusions, interstitials and other second phase particles that could act as fatigue crack initiators, fatigue damage in this case accumulates at grain/twin boundaries as dislocations pile-ups forming at the end of PSBs (see Fig. B4.1). Therefore a closer scrutiny of such boundaries became necessary. Initially this was done at room temperature, but the eventual goal of the project was to perform microscale experiments at elevated temperatures. In the rest of this section a summary of these results is presented.

D.3.1 Elevated Temperature Experiments

One of the problems encountered when using DIC at elevated temperature has been related to oxidation upon heating which drastically changes the sample's surface and therefore the DIC speckle pattern (an example is shown in Fig. D3.1). Another challenge is associated with surface glowing which was observed around 650°C for Hastelloy X and also affects imaging of the DIC pattern (see Fig. D3.2). Attempts to address the previous issues were made. Mainly the sample preparation procedure had to be adjusted. The following two approaches were followed:

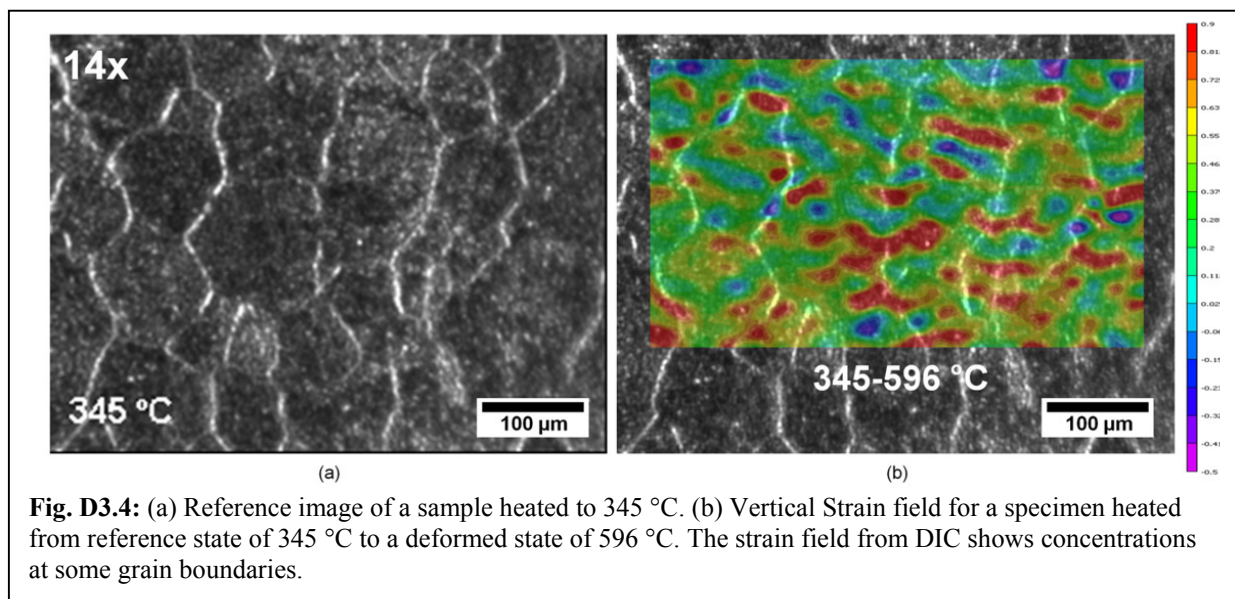
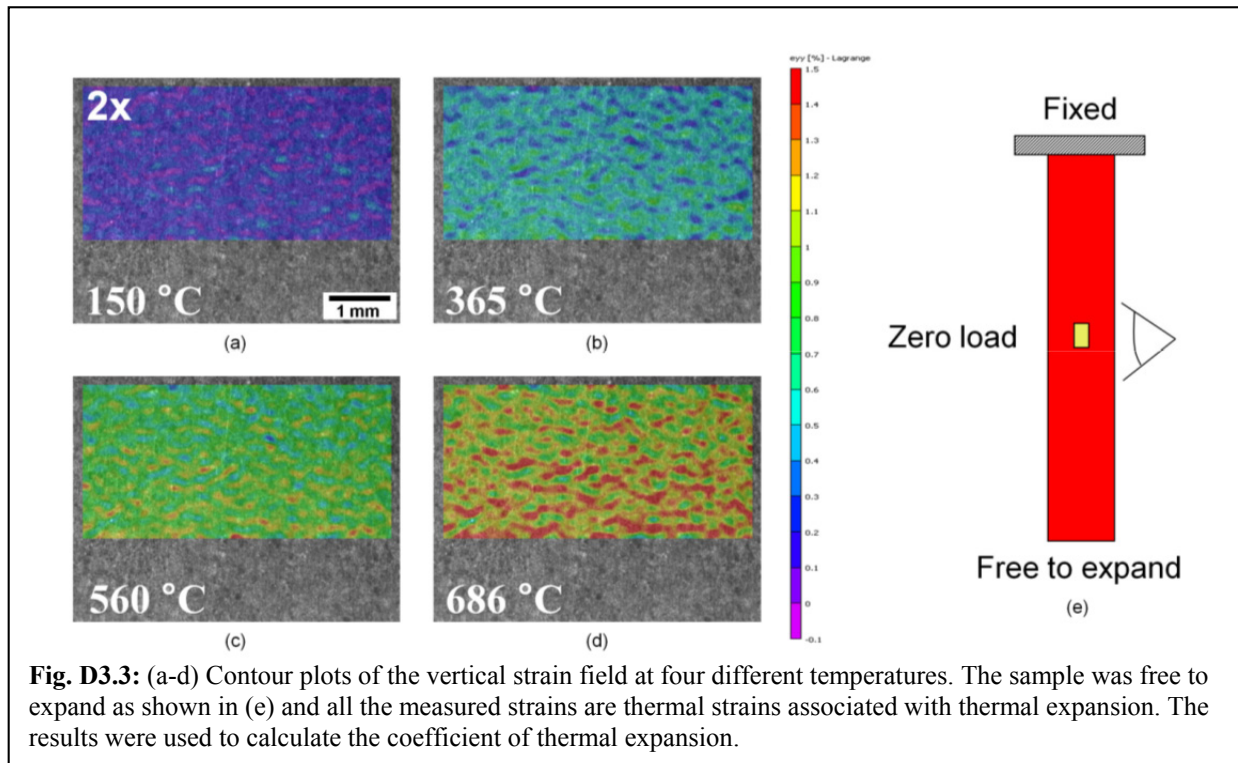
1.—In the first approach, samples were finely polished to 0.3 μm , heated in an oven to 1000°C with a 5 minute hold time, and finally quenched in water. The uniformity of surface oxidation in different regions of the sample was improved following these steps. After quenching in water, a fine speckle pattern was applied to the surface using a Si powder. This procedure prevented significant pattern changes due to additional oxidation when the sample was then heated in the load frame. This procedure was adequate for relatively short experiments (*e.g.*, monotonic tension experiments) since additional surface changes due to oxidation became significant with continuous heating of the sample for longer times. Temperature cycling was also possible up to temperatures where surface glowing did not induce significant changes to image brightness (acquired for DIC).

2.—In the second procedure, samples were painted with high temperature white paint and then speckled with high temperature black paint (using an airbrush). Adding a layer of paint on the surface helped reduce surface changes due to oxidation. Consequently, longer experiments were made possible using this procedure.



The previous two procedures were utilized to make DIC strain measurements for selected examples as explained below. To validate the DIC measurements between 30 and 650°C, the thermal expansion coefficient of Hastelloy X was measured over this entire range. The reference image was captured at room temperature. Images of the heated sample (surface) were acquired at four different temperatures. Figure D3.3 shows contour plots of the vertical strain field at these four different states. The field average results in the vertical and horizontal direction are summarized in Table D3.1. In general, the measurements made are in good agreement with

literature values for Hastelloy X (around 15-20 $\mu\text{strain}/\text{C}^\circ$). An additional feature of the first sample preparation procedure was that it revealed the grain boundaries by oxidation. This allowed *in situ* high magnification measurements (14x magnification) at the grain level and at high temperature (up to 650°C), as shown in Fig. D3.4. The strain field from DIC shows concentrations at some grain boundaries.

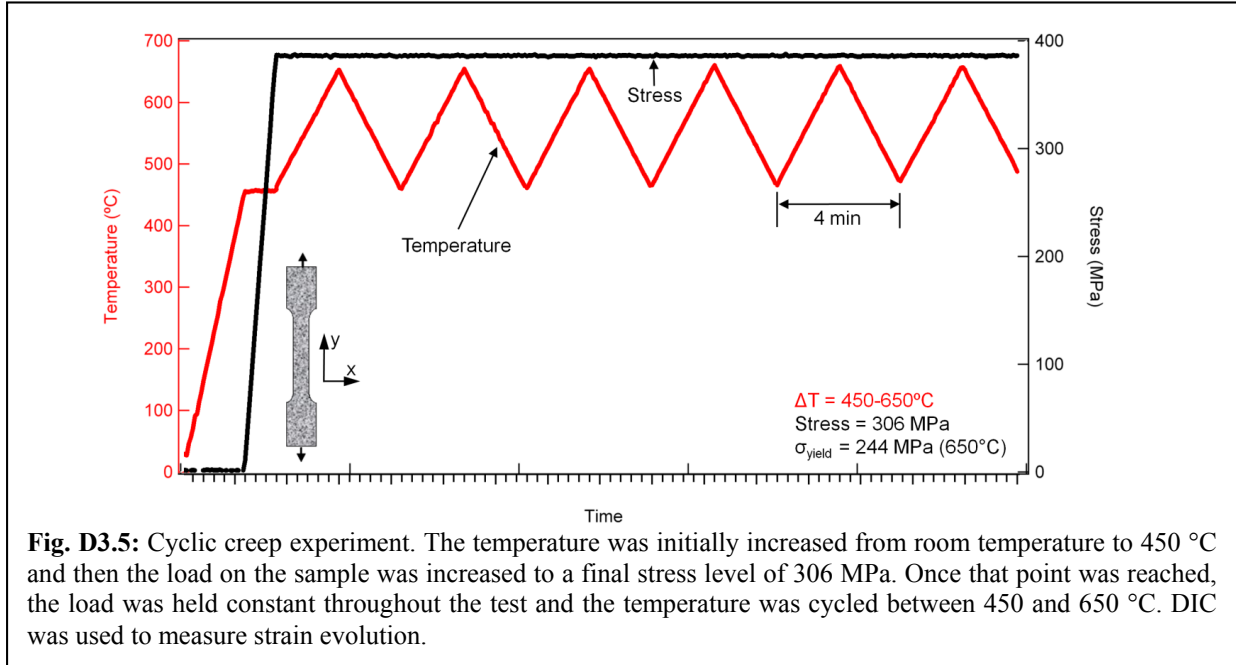


Temp Range °C	Thermal Expansion Y μ strain/°C	Thermal Expansion X μ strain/C°
25-150	14.58	15.40
150-379	16.30	16.55
379-571	17.81	17.68
571-686	22.75	23.30

Table D3.1: Summary of the thermal expansion coefficients obtained from DIC.

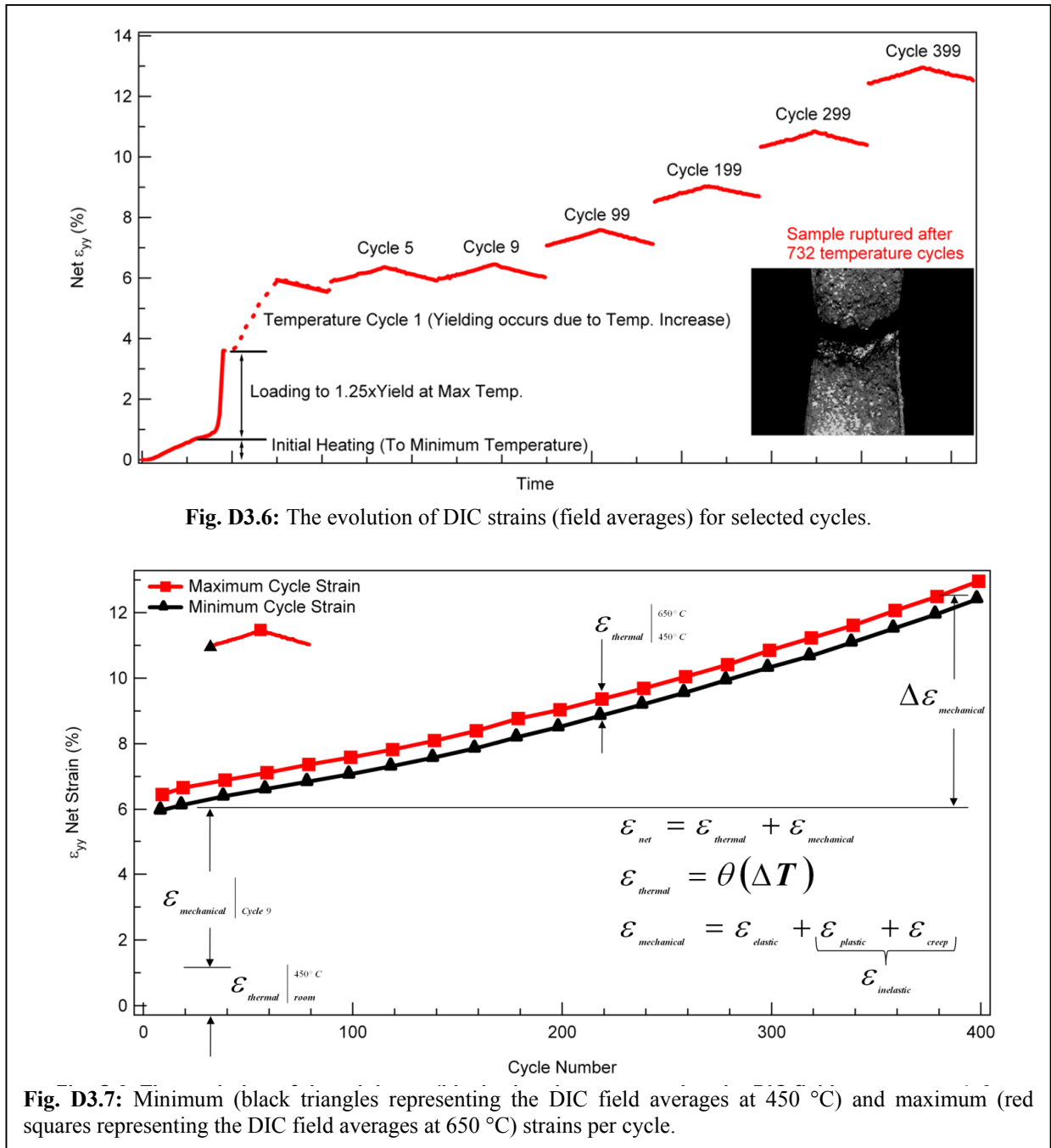
For a cyclic creep experiment, the stress was held constant and the temperature was cycled to failure. The sample was initially prepared following the second sample preparation procedure. Heating was done in the load frame via induction heating. The test started by increasing the sample's temperature from room temperature to 450 °C. After initial heating, the sample was loaded in uniaxial tension to a stress level of 306 MPa. Once this stress level was reached it was held constant throughout the experiment while the temperature was cycled between 450 °C and 650 °C. Figure D3.5 shows the stress and temperature loading conditions.

DIC measurements were made *in situ* during the test. The DIC field average values for selected cycles are shown in Fig. D3.6. Notice that yielding takes place once the load on the



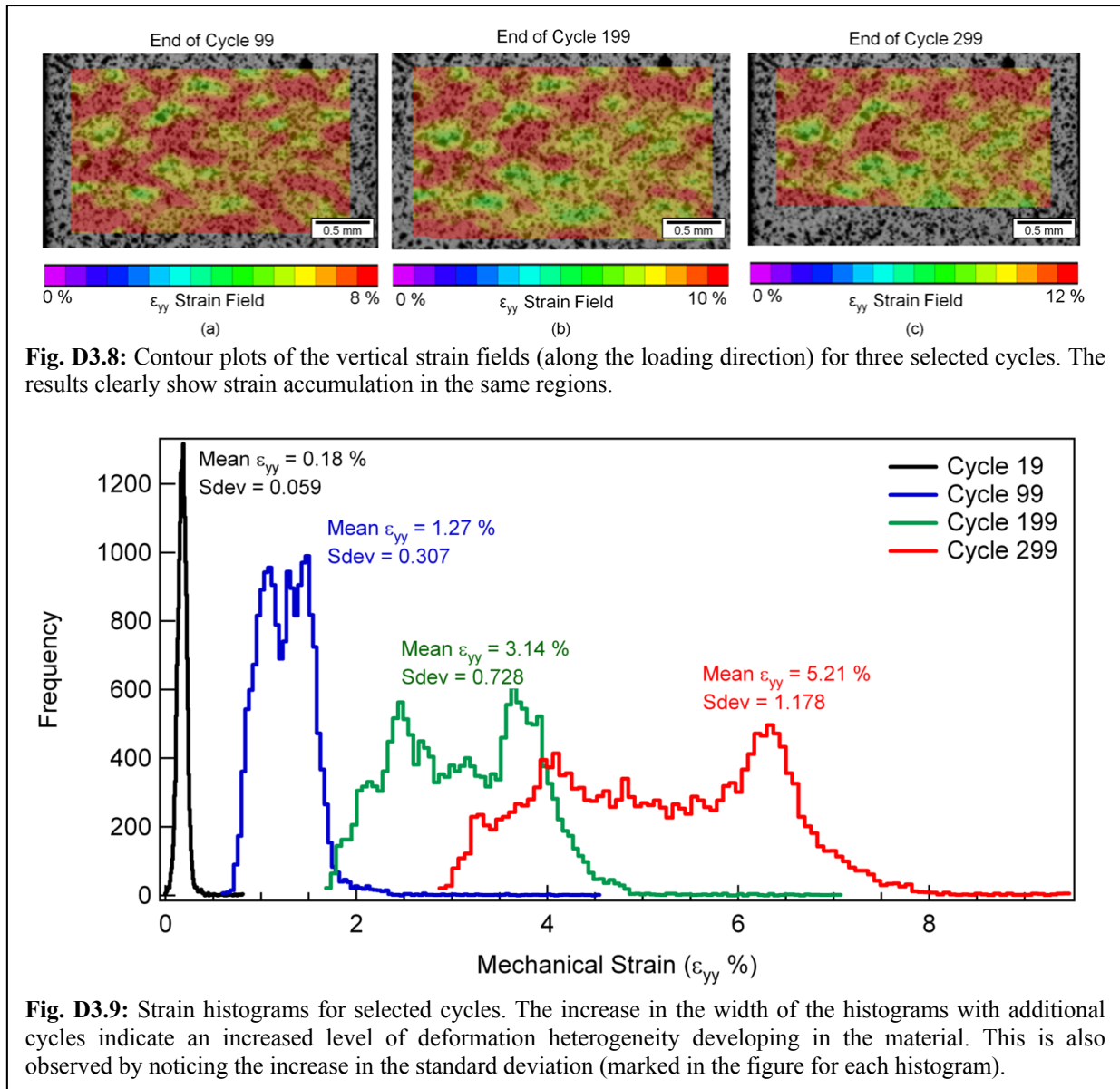
sample was initially increased from 0 to 306 MPa. Additional accumulation of plastic strains was also measured in the first temperature cycle (*i.e.*, heating from 450 °C to 650 °C) due to changes in material properties. The evolution of strains beyond that point was gradual and a function of

cycle number. DIC measurements beyond cycle 399 were not possible due to significant damage to the surface.



Contour plots of the vertical strain fields (along the loading direction) for three selected cycles are shown in Fig. D3.8. The results clearly show strain accumulation in the same regions. Notice the similarity in the contour plot features. The scale was adjusted in each of the contour plots to enable a better visitation of the high strain regions. Strain histograms were also constructed from the DIC strain measurements. Selected cases are shown in Fig. D3.9. The

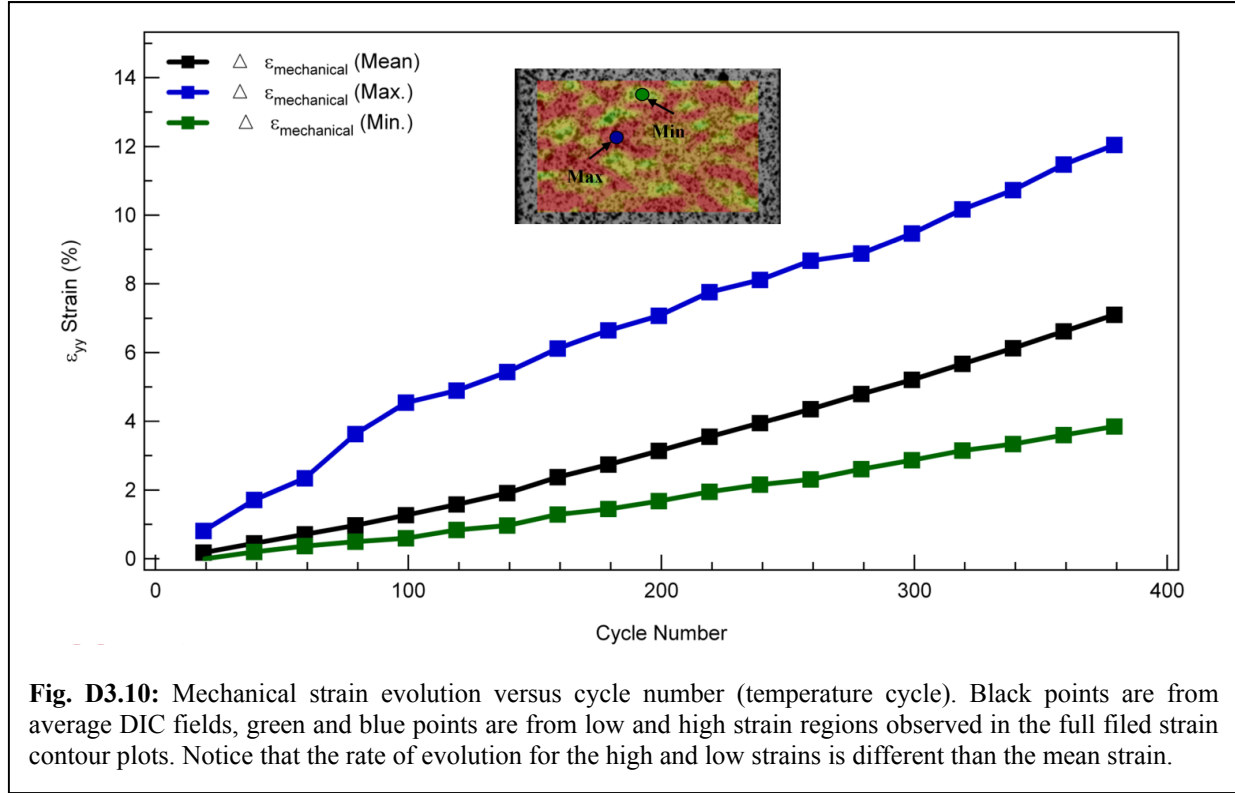
results presented in Figs. D3.8 and D3.9 indicate that an increased level of deformation heterogeneity was developing in the material with the continuous accumulation of creep strains.



The evolution of the mechanical strains versus cycle number is plotted in Fig. D3.10. The black points represent the mean strain evolution obtained from averaged DIC fields; this quantity is comparable to measurements obtained utilizing a high temperature extensometer. The additional blue and green points represent the evolution of high and low strains in the region of interest and are captured by observing the full field contour plots. We notice that the rate of evolution of high strains is larger than that of the mean strains.

In summary, the results from this experiment indicate that the accumulation of creep strains takes place in the same spatial regions on the sample's surface. This suggests that the local microstructure has a major influence in defining the critical location for strain accumulation. This observation, which will also be seen below for room temperature

experiments, requires further investigation. Higher resolution strain measurements and microstructural characterization, similar to what will be discussed below, can provide further insight into this issue. However, the tools required for making these measurements have not been fully developed yet.



D.3.2 Local plastic strain accumulation under uniaxial loading

In this part of the work, the material investigated is again Hastelloy X, a nickel based super alloy which is designed for high temperature applications. In previous studies, researchers have investigated HastelloyX under static (*e.g.*, Rowley and Thornton, 1996), fatigue (*e.g.*, Miner and Castelli, 1992), crack growth (*e.g.*, Huang and Pelloux, 1980) and creep loading conditions (*e.g.*, Kim *et al.*, 2008). However, the local material response at a microstructural level has not been previously studied. Since this level is important for the creation of fatigue microcracks in this material such a microstructural level study will be pursued in the current work, with emphasis on the slip transmission across GBs. High resolution *ex situ* digital image correlation (DIC) was used to measure plastic strain accumulation with sub-grain level spatial resolution in uniaxial tension experiments. In addition, the underlying microstructure was characterized with similar spatial resolution using electron backscatter diffraction (EBSD). With this combination of crystallographic orientation data and plastic strain measurements, the resolved shear strains on individual slip systems were spatially calculated across a substantial region of interest, *i.e.*, we determined the local slip system activity in an aggregate of ~600 grains and annealing twins. The full-field DIC measurements showed a high level of

heterogeneity in the plastic response with large variations in strain magnitudes within grains and across grain boundaries (GBs). We used the experimental results to study these variations in strain, focusing in particular on the role of slip transmission across GBs in the development of strain heterogeneities. For every GB in the polycrystalline aggregate, we have established the most likely dislocation reaction and used that information to calculate the residual Burgers vector and plastic strain magnitudes due to slip transmission across each interface.

Commercially available polycrystalline HastelloyX, a nickel-based superalloy, was investigated in this study. The alloy was solution heat treated by the manufacturer at 1177 °C. Dog bone specimens with 4.0x3.2 mm cross sectional gage area were electric discharge machined from a 3.2 mm thick sheet in the as received condition. The overall sample size was selected based on the load frame loading capacity and the maximum sample size that can be investigated using the EBSD system. The surface of the specimen was mechanically polished using SiC paper (up to P1200) followed by finer polishing using alumina polishing powder (up to 0.3 μm) and vibro-polishing with colloidal silica (0.05 μm). The final surface finish was adequate for microstructural surface characterization using EBSD. After sample preparation, a 1.0x0.6 mm region of interest was outlined on the specimen's surface using Vickers indentation marks (fiducial markers as discussed in Carroll *et al.* (2010)). A Scanning Electron Microscope (SEM) equipped with an EBSD detector was used to characterize the microstructure of the specimen in the region of interest. Measurement spacing of 1 μm was selected, and a total of eight area scans were necessary to cover the region of interest at the selected magnification (300x). Fig. D3.11(a) shows a grain orientation map of the selected region of interest. No texture was observed in the aggregate consisting of approximately 600 grains. The percentage of

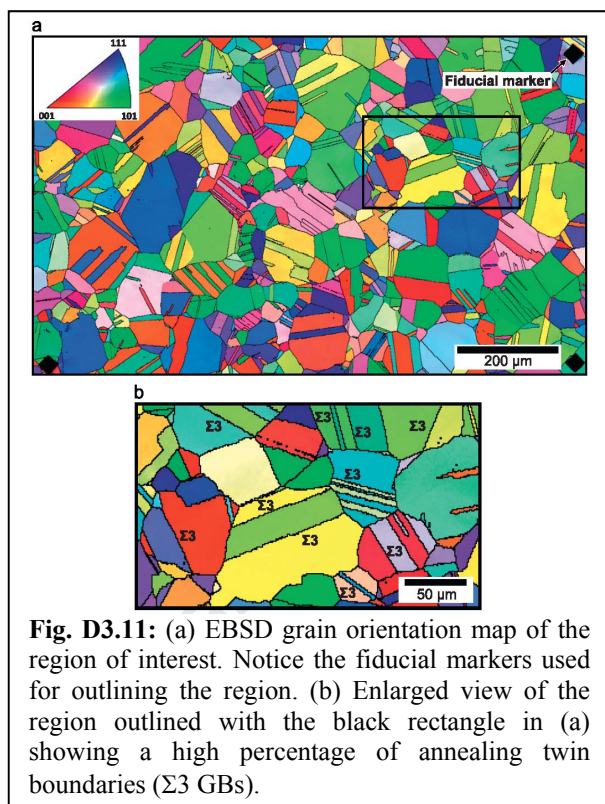


Fig. D3.11: (a) EBSD grain orientation map of the region of interest. Notice the fiducial markers used for outlining the region. (b) Enlarged view of the region outlined with the black rectangle in (a) showing a high percentage of annealing twin boundaries ($\Sigma 3$ GBs).

annealing twin boundaries ($\Sigma 3$ type GBs using the coincident site lattice, CSL, notation) was about 30% of the total number of GBs, as seen in the enlarged view of Fig. D3.11(b).

To obtain accurate strain measurements with sub-grain level resolution using DIC, it is necessary to increase the magnification at which reference and deformed images are captured (Efsthathiou *et al.*, 2010). This reduces the field of view and thus imposes limitations on the area/number of grains that can be studied. The *ex situ* technique used in this study, described in detail in Carroll *et al.* (2010), addresses this problem and enables high resolution measurements over relatively large areas by capturing and stitching enough high magnification images to cover the required region of interest.

Following EBSD, a fine speckle pattern was applied to the sample's surface for DIC measurements. Reference images were captured using an optical microscope at 31x magnification (0.14 $\mu\text{m}/\text{pix}$). Fig. D3.12 shows

an example of a reference image with the speckle pattern and subset size (101x101 pixels) used

in the current work. A total of 316 overlapping images were required to cover the region of interest outlined by the indentation marks. These reference images were stitched together to generate one ultra-high resolution reference image that covered the complete region of interest. The specimen was then deformed in uniaxial tension using a servo-hydraulic load frame to 2.2%

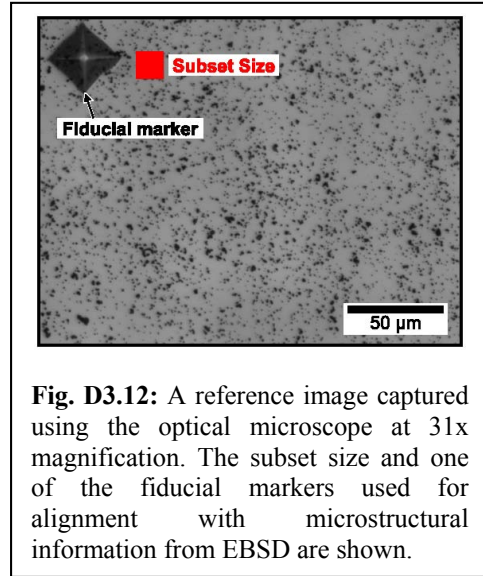


Fig. D3.12: A reference image captured using the optical microscope at 31x magnification. The subset size and one of the fiducial markers used for alignment with microstructural information from EBSD are shown.

nominal strain (using strain control at $1.83 \times 10^{-4} \text{ s}^{-1}$ strain rate) and unloaded (using load control). After unloading, the total residual strain was 2% nominal strain measured using a 12.7mm ($\frac{1}{2}$ in) gage length extensometer. Subsequently, 316 deformed images were captured and stitched, following the same procedure used for the reference images. In plane displacements were obtained from DIC and the results were differentiated to obtain the high resolution strain fields. The subset size used for DIC (14 μm) is smaller than the average grain size (50 μm) allowing for sub-grain level deformation measurement resolution (average number of DIC correlation points per grain ~ 350). The fiducial markers visible in both the EBSD orientation map and DIC contour plots, allow for accurate alignment of the measured strain fields and the underlying microstructure in the region of interest

(Carroll *et al.*, 2010). The advantage of such a measurement procedure is that it enables quantitative analysis of the plastic strain fields in relation to the underlying microstructure of the polycrystalline specimen.

Figure D3.13(a) shows a contour plot of the vertical strain field ϵ_{yy} (along the loading direction). This component of the strain tensor along with two other components, the horizontal strain field ϵ_{xx} and the shear strain field ϵ_{xy} , were acquired using DIC. By assuming plastic incompressibility, the component in the residual plastic normal strain along the third direction, ϵ_{zz} , was calculated using

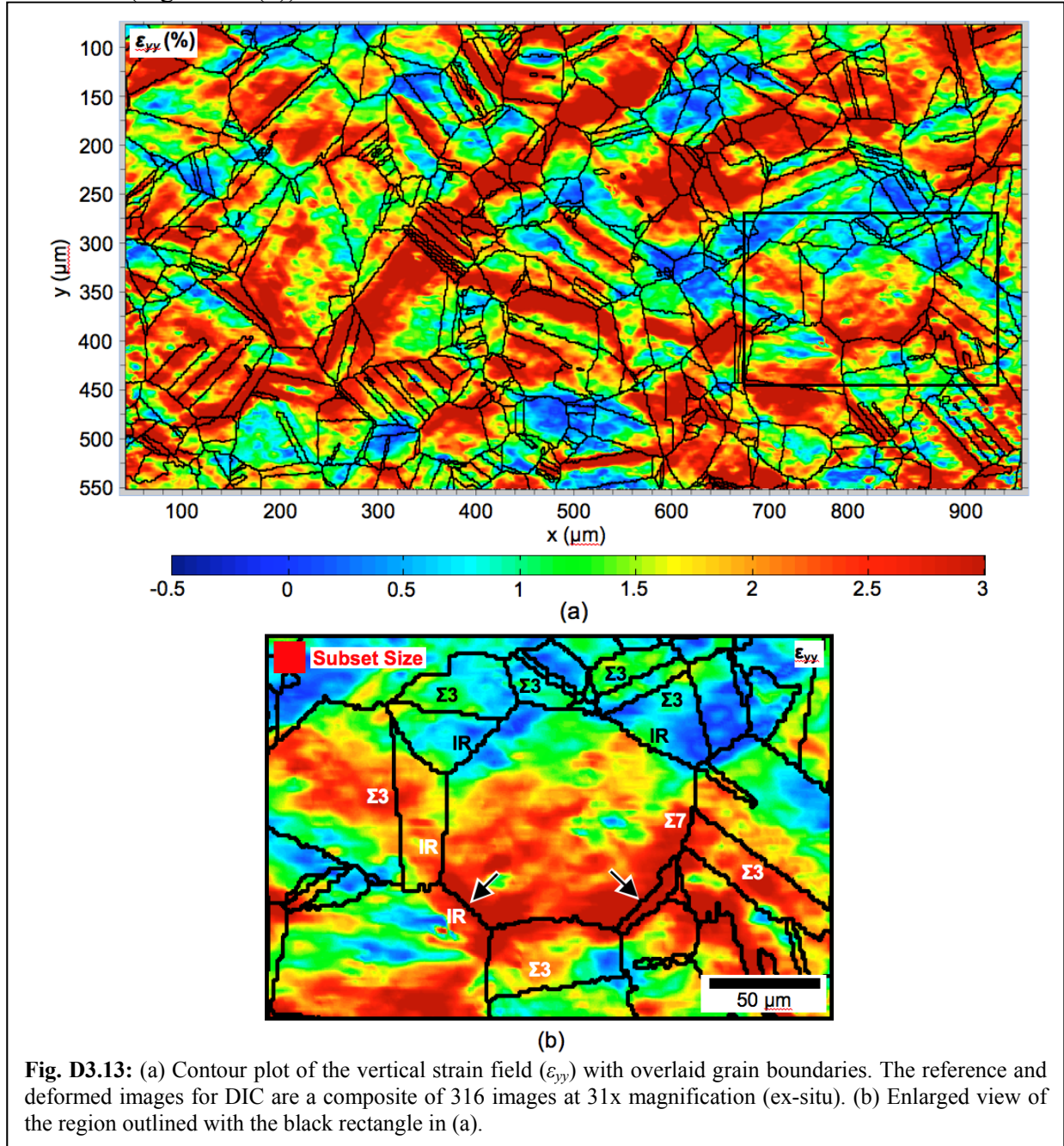
$$\epsilon_{zz} = -1 \times (\epsilon_{xx} + \epsilon_{yy}) \quad (\text{D.3-1})$$

The shear strain components in the third direction, ϵ_{xz} and ϵ_{yz} remain unknown in our analysis (as in any surface measurement technique). Using the measured and calculated components of the plastic strain tensor and by assuming the unknown components as zero, an estimate of the effective plastic strain, ϵ_{eff}^p , was calculated spatially using the following equation:

$$\epsilon_{eff}^p = \sqrt{\frac{2}{3} (\epsilon_{ij} \times \epsilon_{ij})} \quad (\text{D.3-2})$$

To assess and analyze the effect of microstructure, local crystallographic orientations from EBSD were numerically overlaid on the DIC strain data, *i.e.*, for each point, spatial strain and orientation data were consolidated. Eventually, each point in the field has four components of the strain tensor (ϵ_{xx} , ϵ_{yy} , ϵ_{xy} , and ϵ_{zz}), the effective plastic strain, and an associated local crystallographic orientation. This allowed for a superposition of the grain boundaries on all the strain contour plots as shown for example for the ϵ_{yy} in Fig. D3.13(a).

A significant level of heterogeneity is observed from the strain contour plots. In Fig. D3.13(a), regions rendered in dark red have strains higher than 3% (ϵ_{yy} field average = 2%), while regions rendered in dark blue have strains around 0%, and some are even negative, *i.e.*, compressive, in certain areas. This variation in strain appears to be associated with the local microstructure. For example, high strains were visually detected in the vicinity of many grain boundaries (Fig. D3.13(b)).



Such high-resolution full-field strain measurements at the grain level enable us to address the specific regions of grains, which facilitate accumulation of heterogeneous strains. This is accomplished through separating each grain into a core and mantle demarcation. The core refers

to the interior of the grain and the mantle to the region in the vicinity of the neighboring grain, *i.e.*, the region of the grain near the GB (Meyers and Ashworth, 1982). Hence, each grain has several mantles corresponding to the number of neighboring grains. Mantle regions, which exhibit high strains on both sides of the interface, can be associated with slip transmission across the GB, while boundaries that block slip, *i.e.*, shielding, have high strains in one of the mantles and low strains in the other mantle across the interface. We establish an experimental estimate of the GB mantle size from DIC strain measurements and grain boundary locations. To do so, we calculated the spatial distance from each DIC measurement point to the nearest grain boundary, as shown schematically in the inset of Fig. D3.14(a). This facilitates binning the strain data based on distance from the GBs. As the focus in this study is on high strain regions that can be associated with slip transmission across GBs, only points with high strains were considered (ϵ_{eff}^p field average = 2.08%). These points were then binned based on their distance from the nearest GB, and the average strain in each bin was computed. Figure D3.14(a) shows a plot of

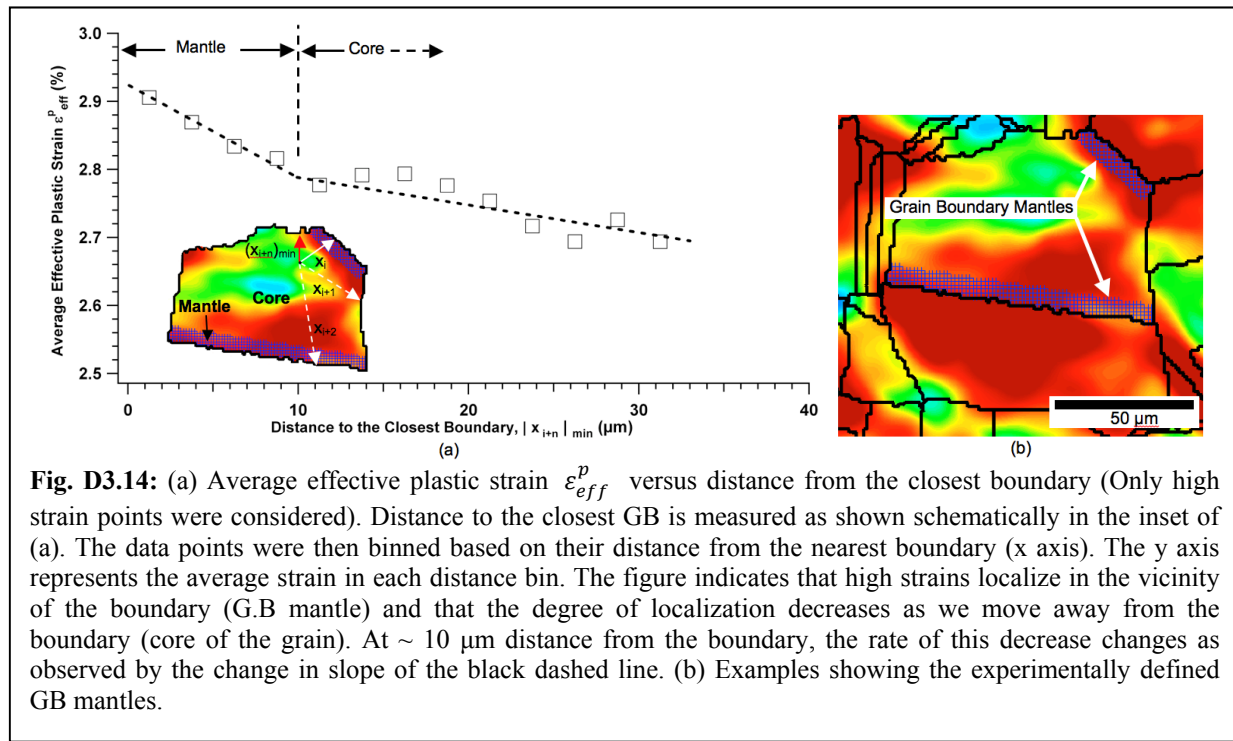


Fig. D3.14: (a) Average effective plastic strain ϵ_{eff}^p versus distance from the closest boundary (Only high strain points were considered). Distance to the closest GB is measured as shown schematically in the inset of (a). The data points were then binned based on their distance from the nearest boundary (x axis). The y axis represents the average strain in each distance bin. The figure indicates that high strains localize in the vicinity of the boundary (G.B mantle) and that the degree of localization decreases as we move away from the boundary (core of the grain). At $\sim 10 \mu\text{m}$ distance from the boundary, the rate of this decrease changes as observed by the change in slope of the black dashed line. (b) Examples showing the experimentally defined GB mantles.

the average effective plastic strain ϵ_{eff}^p versus distance from the closest boundary (only points $> \epsilon_{eff}^p$ field average = 2.08% were considered in this figure). We observe that the magnitude of the elevated strains decrease as we move away from the GBs (mantle regions) and approach the grain interior regions (core).

At a distance of $\sim 10 \mu\text{m}$ from the boundary, there is an inflection point in the change of strain with respect to distance from the GB as observed from the change in slope of the black dashed lines in Fig. D3.14(a). This point was used as an experimentally measured estimate of the GB mantle size, since it marks a transition in slip response while moving away from the GB and approaching the core of the grain. Once the mantle size was determined, mantle points were selected for each specific boundary across the *entire* microstructure, *i.e.*, select points within $10 \mu\text{m}$ from the GBs. Each GB has two mantles associated with it; one on each side of the GB across the interface. Figure D3.14(b) shows an example of GB mantles defined in this work.

Delineating the mantle regions helps determine the core points for each specific grain by subtracting all the mantle points from the total number of points in each grain.

Strain histograms of ε_{eff}^p in cores and mantles over the entire microstructure, in the area of interest, approximately 600 grains, are shown in Fig. D3.15. The histogram of the points belonging to mantles, *i.e.*, red histogram, shows a range of strains between 0 and 6%, while points belonging to cores, *i.e.*, black histogram, show a smaller strain range between 0.1 and 4.2%.

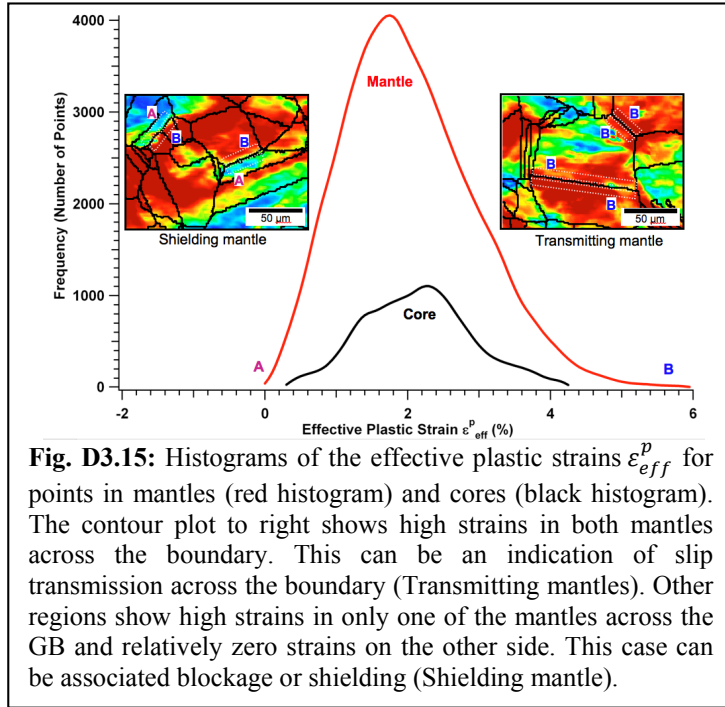


Fig. D3.15: Histograms of the effective plastic strains ε_{eff}^p for points in mantles (red histogram) and cores (black histogram). The contour plot to right shows high strains in both mantles across the boundary. This can be an indication of slip transmission across the boundary (Transmitting mantles). Other regions show high strains in only one of the mantles across the GB and relatively zero strains on the other side. This case can be associated blockage or shielding (Shielding mantle).

Less scatter around the mean was also observed for the core histogram (standard deviation = 0.8) compared to mantle histogram (standard deviation = 0.9). We also notice in Fig. D3.15 that the mean strain for mantle points (2.05%) is less than the mean strain for core points (2.18%). This is primarily attributed to the low strains in some of the mantle regions which lower the mean strain of the mantle points. We emphasize that the presence of mantle points with low strains does not contradict the results presented in Fig. D3.14(a) as only points with relatively high strains were used to construct that figure as opposed to considering all the points, regardless of their magnitude, in the results

presented in Fig. D3.15.

In addition, with such detailed high-resolution DIC information we can obtain slip activity on individual slip systems within each grain. The local change in the macroscopic plastic strain due to crystallographic slip is achieved through increments of shear, $d\gamma^\alpha$, in the activated slip systems (Kocks and Chandra, 1982). The individual components of the plastic strain tensor are given by the following equation:

$$d\varepsilon_{ij}^p = \frac{1}{2} \sum_{\alpha=1}^s (n_i^\alpha l_j^\alpha + n_j^\alpha l_i^\alpha) d\gamma^\alpha = \sum_{\alpha=1}^s (m_{ij}^\alpha) d\gamma^\alpha \quad (\text{D.3-3})$$

where α is the slip system number, s is the number of slip systems (12 for fcc), n^α is the vector defining the normal to slip plane for system α , and l^α is the vector defining the slip direction. Three components of the plastic strain tensor were measured from DIC (ε_{xx} , ε_{yy} , ε_{xy}). The fourth component, ε_{zz} , was calculated by assuming plastic incompressibility (Eq. (D.3-1)). Also, n^α and l^α are known for fcc crystals. Solving for the scalar quantities $d\gamma^\alpha$ at each spatial point provides local information about slip system activation across the entire region of interest.

The difficulty that arises when attempting to solve Eq. (D.3-3) is that the number of activated slip systems is not generally known. Also, if the number of activated systems is assumed, five has been proposed as sufficient number of systems necessary to satisfy compatibility (Taylor, 1938), the problem of which combination to select from the twelve possible systems arises. Taylor proposed a model to solve this problem. In his formulation, the

combination which minimizes the sum of the absolute values of the shear increments is considered to be the combination that is actually operative (Taylor, 1938). Since then, different models and constitutive formulations, that are more physically based, have been proposed to solve this problem (Roters *et al.*, 2010). In the current work, a visco-plastic constitutive model was used to solve for the shear strain increments spatially across the entire microstructure. In the formulation used, which is standard in many crystal plasticity frameworks, the shear strain rate is written as a function of the resolved shear stress on each slip system (Hutchinson, 1976):

$$\frac{\dot{\gamma}^\alpha}{\dot{\gamma}_0} = \left| \frac{\tau^\alpha}{\bar{\tau}} \right|^n \text{sgn}(\tau^\alpha) \quad (\text{D.3-4})$$

where $\dot{\gamma}^\alpha$ is the shear rate on slip system α , τ^α is the resolved shear stress, $\bar{\tau}$ is a reference stress state, and $\dot{\gamma}_0$ and n are material parameters that describe the reference strain rate and the slip rate sensitivity, respectively. The term “sign of τ^α ” in Eq. (D.3-4) is present in order to ensure that $\dot{\gamma}^\alpha$ and τ^α have the same sign (*i.e.*, positive work is being done). As the emphasis in our analysis is to obtain the shear strain increments, $d\gamma^\alpha$, and not solving for the exact kinetics, *i.e.*, the shear stress τ^α , we take $\dot{\gamma}_0 = \bar{\tau} = 1$ and $n = 20$, *i.e.*, rate insensitive.

If we make the simplification that $d\gamma^\alpha = \dot{\gamma}^\alpha$, we can substitute for the shear increments from Eq. (D.3-4) into the net strain Eq. (D.3-3), producing a relation between the total plastic strain and resolved shear stresses

$$\dot{\epsilon}_{ij}^p = \sum_{\alpha=1}^s \left(\frac{\dot{\gamma}_0}{\bar{\tau}} \left| \frac{\tau^\alpha}{\bar{\tau}} \right|^{n-1} \tau^\alpha \right) (m_{ij}^\alpha) \quad (\text{D.3-5})$$

The resolved shear stress on each slip system (τ^α) is related to the stress tensor (σ_{ij}) through the following equation:

$$\tau^\alpha = m_{pq}^\alpha \sigma_{pq} \quad (\text{D.3-6})$$

Substituting Eq. (D.3-6) into Eq. (D.3-5):

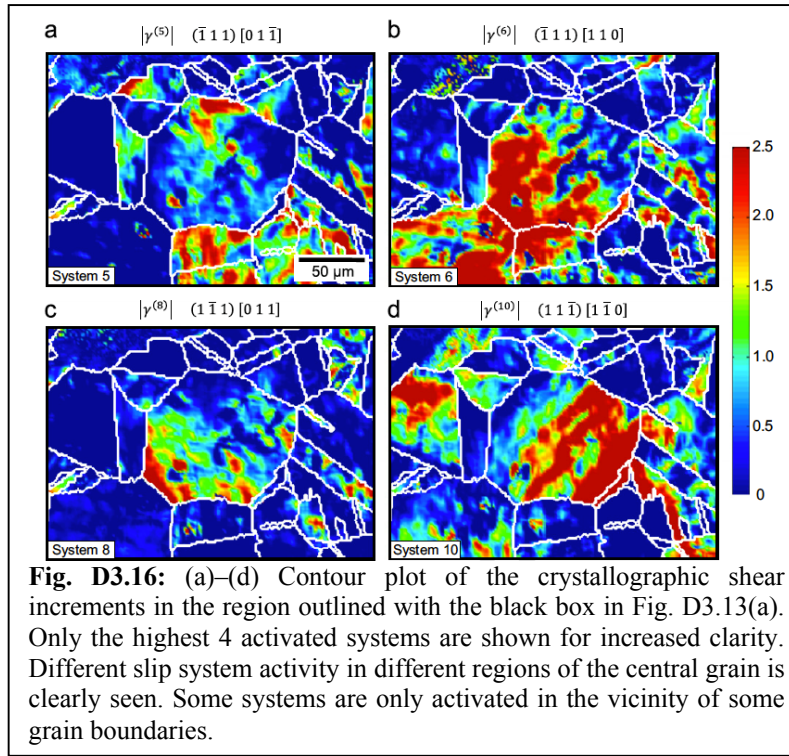
$$\dot{\epsilon}_{ij}^p = \left[\sum_{\alpha=1}^s \left(\frac{\dot{\gamma}_0}{\bar{\tau}} \left| \frac{\tau^\alpha}{\bar{\tau}} \right|^{n-1} m_{ij}^\alpha m_{pq}^\alpha \right) \right] \sigma_{pq}. \quad (\text{D.3-7})$$

Given the macroscopic plastic strain rate (here we make the simplification that $\dot{\epsilon}_{ij}^p = d\epsilon_{ij}^p$) and the orientation data (to be able to transform from sample frame to crystal frame) we solved Eq. (D.3-7) - the non-linear system of equations was solved using an iterative solver - for the stresses σ_{pq} . Subsequently, the resolved shear stresses τ^α were calculated using Eq. (D.3-6). Finally, Eq. (D.3-4) was used to back-substitute for the shear strain rates. Following this procedure, the shear strain increments can be specified on all the 12 slip systems (*i.e.*, no question of choosing the active slip systems arises; all systems with nonvanishing resolved shear stress are potentially active). By performing this calculation for each spatial point across the region of interest, we acquired spatial information about slip system activation across the entire microstructure.

Contour plots of residual plastic strain slip system activity were generated for all twelve slip systems. For the sake of brevity, in Fig. D3.16, we only show the ones with the highest shear

increments in the same region shown earlier in Fig. D3.13(b). Different slip systems were activated in various spatial regions of the central grain, while certain slip systems, such as 5 and 8, show activity only in the vicinity of some grain boundaries, *i.e.*, mantle regions. This spatial information, regarding activated slip systems on both sides of every grain boundary in the region of interest (approximately 1600 GBs), along with crystallographic grain orientation was used to provide insight into the local deformation behavior in grain boundary regions.

This information is the used to study the role of the residual Burgers vector in slip transmission and strain accumulation across grain boundaries. One of the possible outcomes of



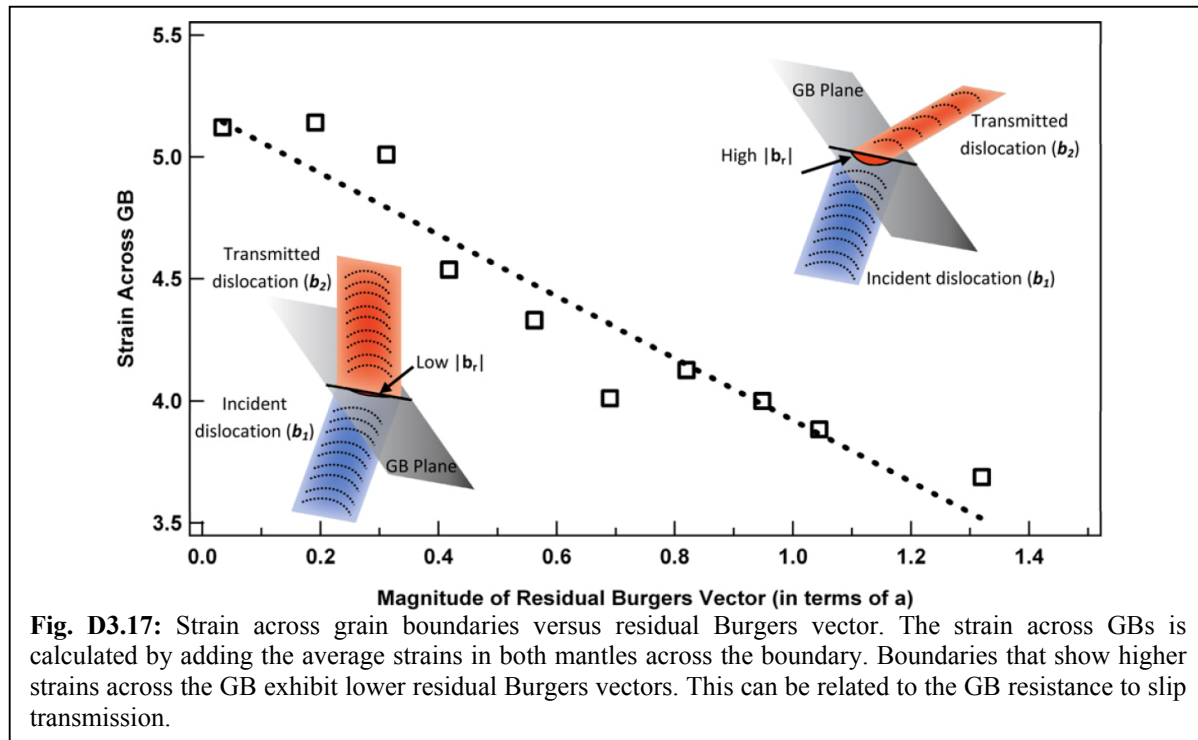
dislocation-grain boundary interaction is partial slip transmission of the incoming slip across the GB, which leaves behind a residual dislocation in the GB plane. The following dislocation reaction equation is used to define \mathbf{b}_r based on the Burgers vectors of the dislocations on both sides of the GB (Sutton and Balluffi, 2006):

$$\mathbf{b}_r = \mathbf{b}_1 - \mathbf{b}_2 \quad (\text{D.3.8})$$

where \mathbf{b}_1 and \mathbf{b}_2 are the Burgers vectors of the incident and transmitted dislocations across the GB, respectively. In the most general case, 144 possible interactions exist for slip

transmission at each GB. This number of possible interactions is obtained by considering the 12 slip systems (fcc material) within grain 1 (incident) and 12 slip systems within grain 2 (transmitted). Note that the same reaction is obtained by reversing the order of the incoming and outgoing dislocations.

In our analysis, we have individually selected each GB and interrogated the 144 possible slip transmission interactions by checking if both of the slip systems associated with each interaction were activated in the mantle regions of that GB. In the case of confirmed activation of both slip systems, through the DIC strain measurements, an experimental estimate of \mathbf{b}_r was calculated for that specific GB. If multiple slip systems were activated in the mantles, several estimates of \mathbf{b}_r were calculated. To investigate the relation between \mathbf{b}_r and the accumulation of strain due to slip transmission, we used the experimentally determined estimates of \mathbf{b}_r and the strain measurements across GBs (mantle regions). First, we calculated the strain across each transmitting mantle in the region of interest, and then binned the GBs based on the minimum estimate of \mathbf{b}_r and finally calculated the average strain across the GBs for each bin. Fig. D3.17 shows a plot of strain across GBs versus \mathbf{b}_r . Higher strains were measured across those GBs that have low \mathbf{b}_r indicating a lower GB resistance to slip transmission.



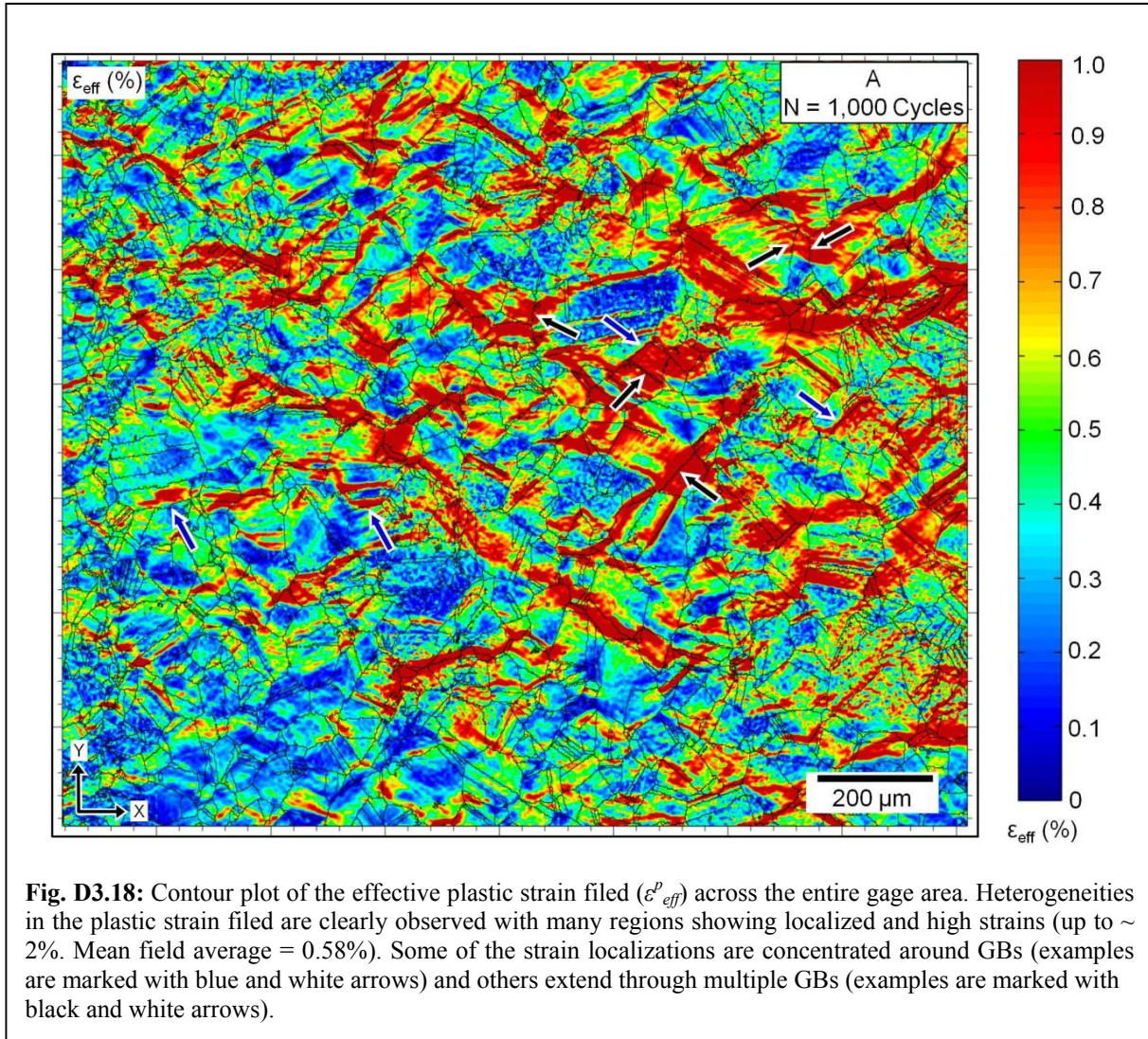
D.3.3 Fatigue crack initiation dependent on plastic strain accumulation

In the case of pristine materials, the formation of persistent slip bands (PSBs) and their interactions with grain boundaries (GBs) have been identified as a primary source of crack initiation. In general, it is widely accepted that localized plastic deformation, which is a precursor to PSB formation, is essential for fatigue crack initiation. However, it is less clear how the localization of plastic strains influences the length of the fatigue cracks which initiate later in the fatigue life after strain localization has occurred. Generally speaking, grain size, grain orientation, orientation of neighboring grains, and the presence of grain boundaries all influence the local material response leading to heterogeneous stress and strain fields at the microstructural scale, as was shown earlier. Grain boundaries are particularly important and their role has been a subject of extensive research. The manifestation of the deformation heterogeneities introduced by GBs at the mesoscale can be in the form of strain localization (Abuzaid *et al.*, 2012), also as seen above. An example, and also a focus in the current work, is the interaction of slip with a GB which may lead either to transmission across the boundary or to the creation of a pile-up and blockage of slip.

One may generally expect high strains across the GB interface in the case of transmission and high strains on only the pile-up side in the case of blockage. Fatigue cracks initiating in the vicinity of transmitting and shielding GBs can potentially be different due to variation in the area, *i.e.*, number of grains, with localized plasticity. The correlation between these two different deformation mechanisms (shielding and slip transmission) in the vicinity of GBs and fatigue crack initiation, particularly the length of fatigue cracks that form upon transformation of the slip band to a finite crack size, requires further investigation. Here we use the techniques described earlier to study strain concentrations at the microscale in Hastelloy X subjected to fatigue loading

early in the loading process and correlate the results with cracks developed later on during loading.

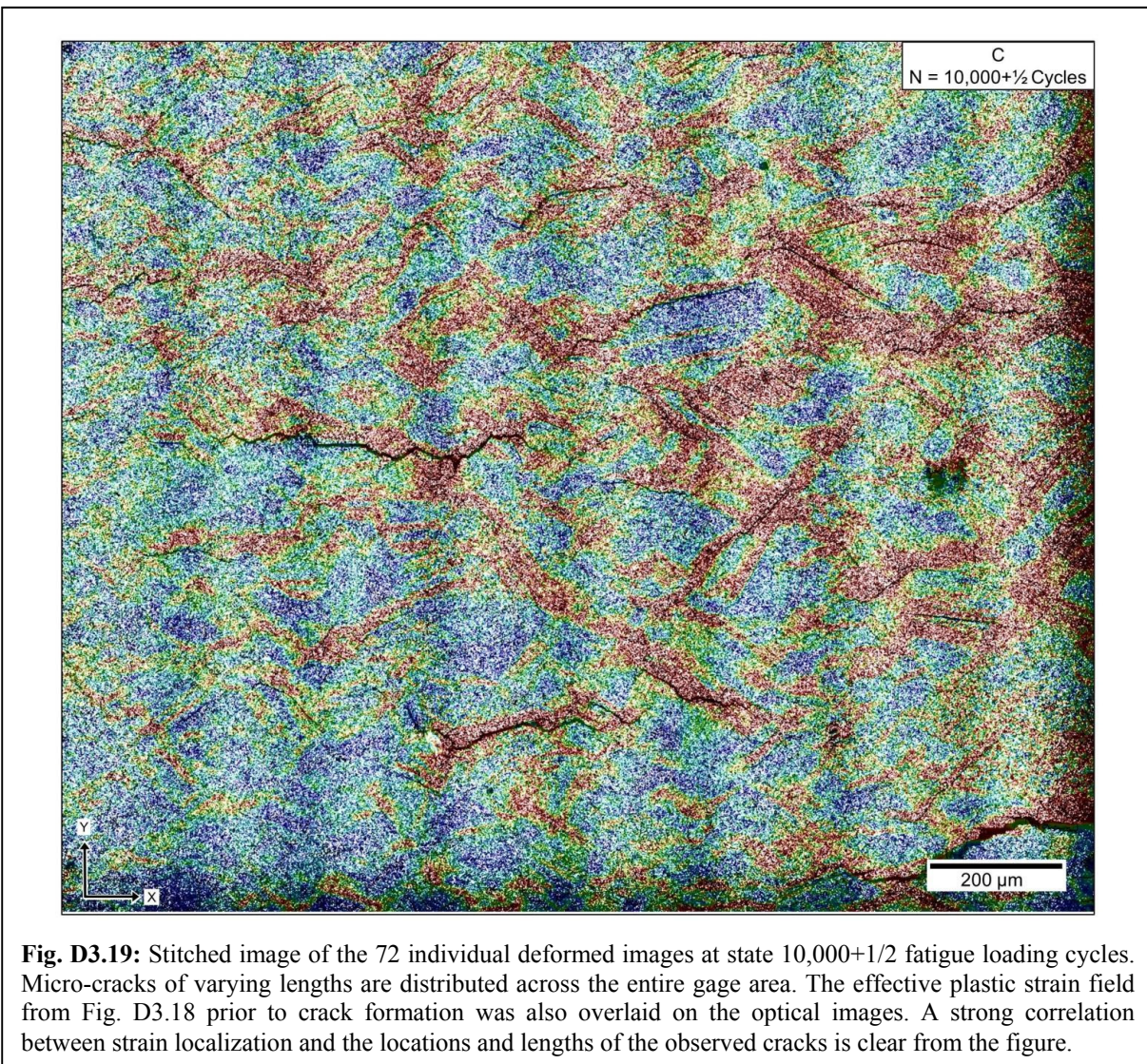
After characterizing the microstructure and capturing reference images for DIC, the Hastelloy X sample was fatigued in load control at a rate of 0.4 Hz, loading ratio, R , of -1, and stress range of 900 MPa (using a servohydraulic load frame). After 1,000 cycles, the test was stopped and the sample removed from the load frame to capture deformed images for *ex situ* DIC. The DIC strain measurements reported here (Fig. D3.18) are for this deformed state for



which no cracks were observed under an optical microscope. Loading was resumed with an additional 9,000 cycles (a total of 10,000 cycles). Optical images at this deformed state revealed numerous micro-cracks covering the entire gage area and therefore no additional loading cycles were applied except for a half tensile cycle to open the initiated micro-cracks for better visualization.

Figure D3.19 shows a stitched image of 72 high magnification optical images at deformed state of 10,000. The ε_{eff}^p plastic strain field from Fig. D3.18 prior to crack formation at 1,000 is also overlaid on the optical images. Visually, we observe many microcracks distributed

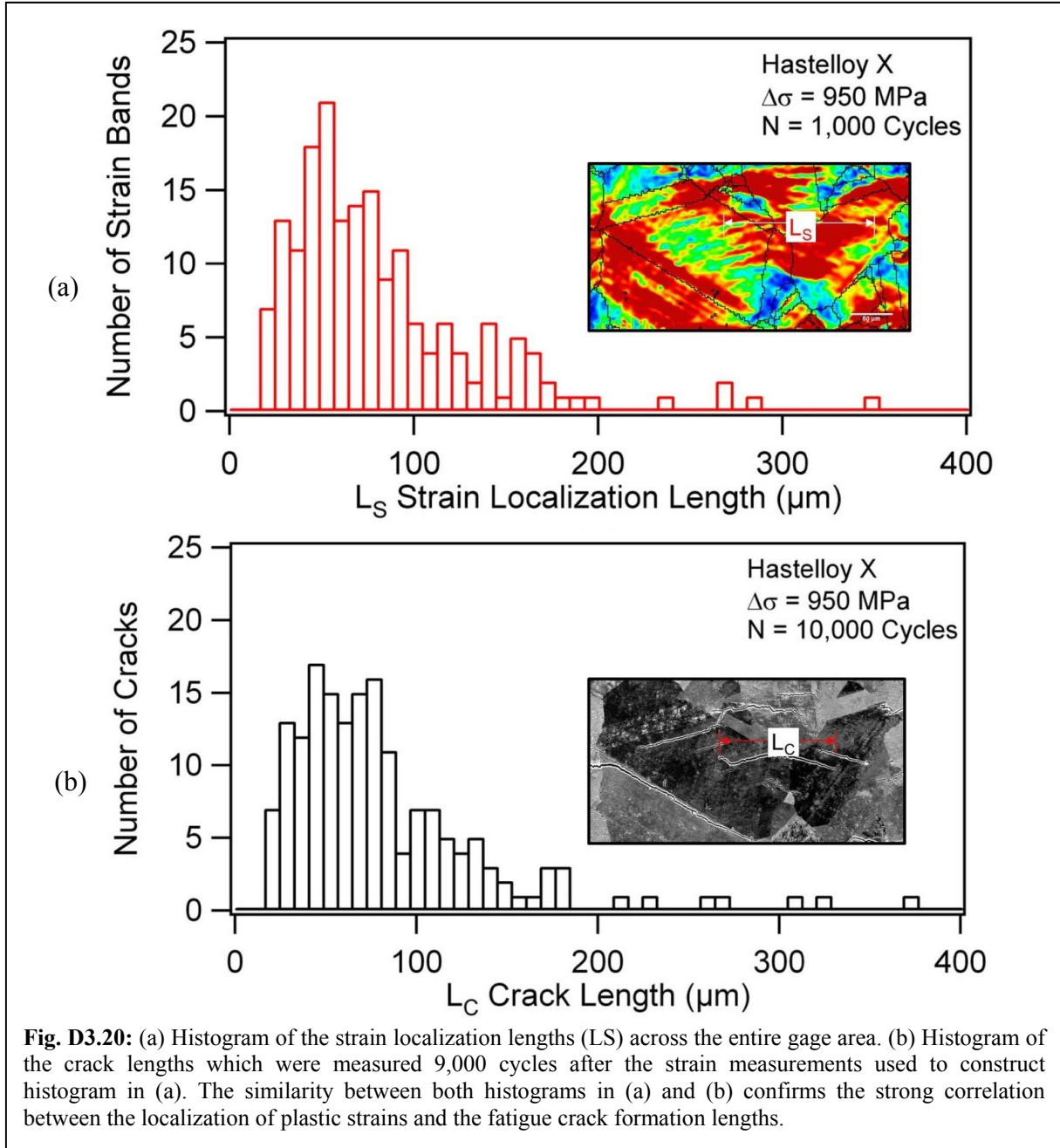
across the entire gage area. The cracks vary in length and no single crack seems to dominate the field. The strains overlay reveals a strong correlation between not only the locations of the observed cracks, but also the crack formation lengths and the high strain regions.



For a more quantitative assessment of the correlation between the fatigue crack formation lengths and the length of the localized slip bands (*i.e.*, strain localization length), all the lengths of the strain localization regions and fatigue cracks were measured across the entire gage area. A histogram of the strain localization lengths (LS) at 1,000 loading cycles is shown in Fig. D3.20(a). The corresponding histogram of the crack lengths at 10,000 loading cycles is shown in Fig. D3.20(b) (recall that these measurements were made 9,000 cycles *after* the strain measurements). The similarity between both histograms confirms the strong correlation between the localization of plastic strains and the fatigue crack formation lengths. The crack formation lengths were easily measured from the SEM images. We note that every crack *type* was measured and not every crack in the region. For example, several parallel cracks similar to each other may exist. Only the length of the longest of these similar and parallel cracks is included.

The strain localization lengths were based on the generally sharp gradients in strain magnitudes around the regions with strain localization (*i.e.*, sharp drop/rise in strain magnitudes).

The experimental results and analysis support the following conclusions: 1- The localization of plastic strains at the microstructural level prior to fatigue crack formation determines the *location and length* of micro-cracks which form later in the fatigue life. 2- The deformation mechanisms (*i.e.*, *shielding* and *transmission*) in the vicinity of GBs influence strain localization in the vicinity of GBs and thus affect fatigue crack formation. 3- A better assessment of the critical conditions for fatigue crack formation requires not only knowledge of the local strain magnitudes, but also an evaluation of the role of GBs in blocking or transmitting slip.



D4 Thermomechanical Fatigue of Hastelloy X: Role of Defects

Personnel: Lambros, Casperson, (Graduate student, UIUC), Chona (AFRL)

Start: 2010, Completed: 2012

The work in this project dealt with the effects of elevated temperature on fatigue crack closure. As a fatigue crack grows in a ductile material, it leaves behind a plastic wake, or a region of permanent plastic deformation on either side of the crack faces. This plastic wake produces compressive forces serving to shield the crack from external loading (Elber, 1970, 1971). As explained in D2, the crack therefore, does not fully open until a specific load, the opening load, is reached. The conventional Paris relationship was thus modified by Elber to incorporate only the portion of the loading range, or the stress intensity factor range, experienced by the opened crack. This was illustrated by Equation (D.2.1). Consequently, fatigue life prediction of a structure or component can be dramatically affected by the presence or absence of crack closure. This can be especially true in the context of high temperature, where yield properties can vary significantly. However the effects of high temperature on fatigue crack closure have gone largely unstudied. It was the goal of this work to investigate the role of increasing temperature on fatigue crack closure limits in a nickel-based superalloy.

The specimens used in this investigation were 75 mm by 7.0 mm by 1.28 mm, sections of Hastelloy X, a nickel-based superalloy. Along one edge of the rectangular sample, a 1 mm long, 0.15 mm wide notch was cut. The specimen was then polished and a speckle pattern of Si particles was applied to the surface. The back surface was painted with a high temperature, flat black paint allowing the use of an IR thermometer to monitor the specimen's temperature. To initiate and grow a crack from the notch tip, the specimen was fatigue loaded in axial tension at a frequency of 2 Hz. During loading, the stress ratio R , the ratio of minimum to maximum load, was maintained at 0.05 to facilitate the presence of crack closure. After reaching a crack length of about 2.3 mm the specimen was subjected to several “measurement cycles” cycles at the same load amplitude as the fatigue precracking but at a lower frequency of 0.125 Hz. During these lower frequency cycles, images were taken at 15 fps (frames per second), totaling 120 images per cycle, at a resolution of 490 pix/ μm (macroscale, 2x magnification) or 2440 pix/ μm (microscale, 10x magnification).

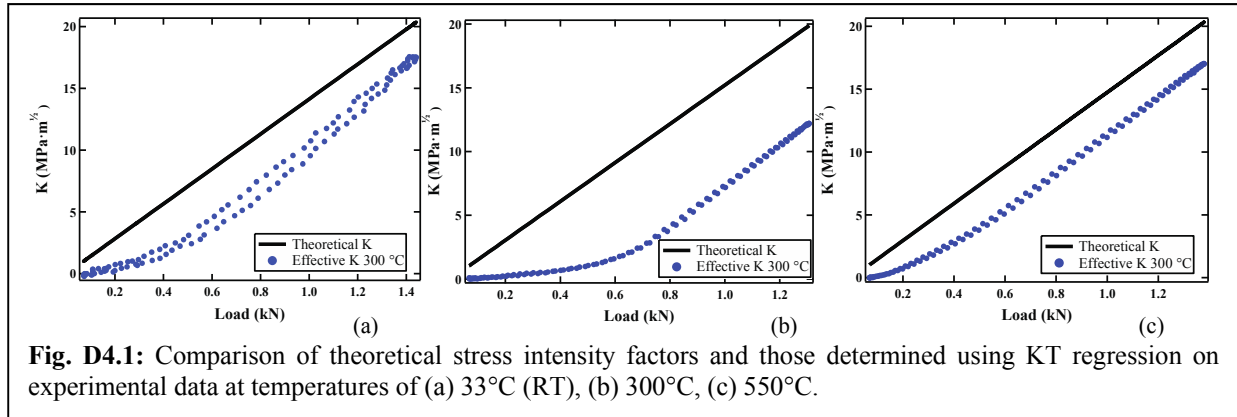
Adapting the room temperature methods of Carroll *et al.* (2009), which we described in Section D.2.2, to high temperature crack closure, isothermal experiments were run at 33°C (RT), 250°C, 300°C, 400°C, and 550°C. Denoting this initial temperature as T_1 , two types of experiments were run (i) temperature jump experiments, where the specimen was fatigue loaded at T_1 , subjected to measurement cycles, then raised to an elevated temperature, T_2 and measurement cycles at this new temperature were made, and (ii) temperature overload experiments in which, following the same procedure as before, the temperature was raised to T_2 for a single cycle, and was then returned to T_1 , where fatigue loading was continued. During the measurement cycles, no further growth of the crack occurred.

Isothermal Crack Closure Results

Full-field displacements were measured using DIC. When analyzing the images, a full-field (macro-scale) crack opening (and closure level) was calculated by examining a stress intensity factor as a function of load (Carroll *et al.*, 2009). Figure D4.1 shows the variation of measured stress intensity factor throughout an entire measurement cycle – both loading and unloading – for temperatures of (a) 33°C, (b) 300°C, and (c) 550°C. The theoretical stress

intensity factor, K_{theor} , fails to account for the presence of crack closure within the specimen. Deviation between the theoretical and the experimental K_I curves therefore directly demonstrates the existence of crack closure which reduces the effective (DIC measured) stress intensity factor experienced by the crack tip – note the curvature of the applied stress intensity factor at low loads in most of the curves. Here, the linear portion of the experimental K_I curve corresponded to a fully open crack while the portion of the curve with a change in slope denoted the portion of the loading cycle where crack closure was present (Carroll *et al.*, 2009). The slope of the linear portion of the experimental K_I in most cases agreed with that of K_{theor} . This demonstrated that once the crack fully opened, the cracked specimen had the predicted compliance, thus indicating primarily elastic deformation outside of the area of the crack region affected by closure. In some cases however, a small error in the estimation of the crack tip location may have caused differences in the measured and predicted specimen stiffness, consequently causing differences in the maximum value of the experimental K_I .

As shown by Fig. D4.1(a), at 33 °C, a closure level of 34% of the peak load was calculated using the “full field effective K ” method (Carroll *et al.*, 2009). Results were similar at elevated temperatures. Under isothermal conditions of 300°C (Fig. D4.1(b)), the calculated closure level was 39%. Moving to higher temperatures, an isothermal experiment at 550°C (Fig.



D4.1(c)) resulted in a closure level of 27% of peak. These closure levels are, in fact, very similar since variability between closure levels at the same temperature can be within $\pm 10\%$ as will be demonstrated later.

Thermal Jump Crack Closure Results

Figure D4.2(a) shows a K_I vs. load plot for fatigue cracking at 33°C where the amount of crack closure was calculated at 27.4%. Following the temperature jump from RT (33°C) to 250°C, the specimen no longer experienced *any crack closure*. As seen from Fig. D4.2 (b), the experimental stress intensity factor vs. load curve was completely collinear with the theoretical curve. Figure D4.2(c) shows a specimen that at 300°C experienced a level of crack closure of 19% of peak whereas after a change in temperature of 100°C (T_2 of 400°C), the closure level decreased to 17.6%. These two crack closure levels are very similar, suggesting that a temperature jump of 100°C, is not sufficient to affect the level of crack closure. Note that the elastic modulus reduces by 5 GPa while the yield stress reduces by 20 MPa due to the temperature jump. Figure D4.2(e) shows that in a separate 300°C experiment, a crack closure level of 39% of peak load was measured and at 550°C, the closure level significantly decreased to 15%. The temperature change from 300°C, to 550°C, is accompanied by a decrease in the

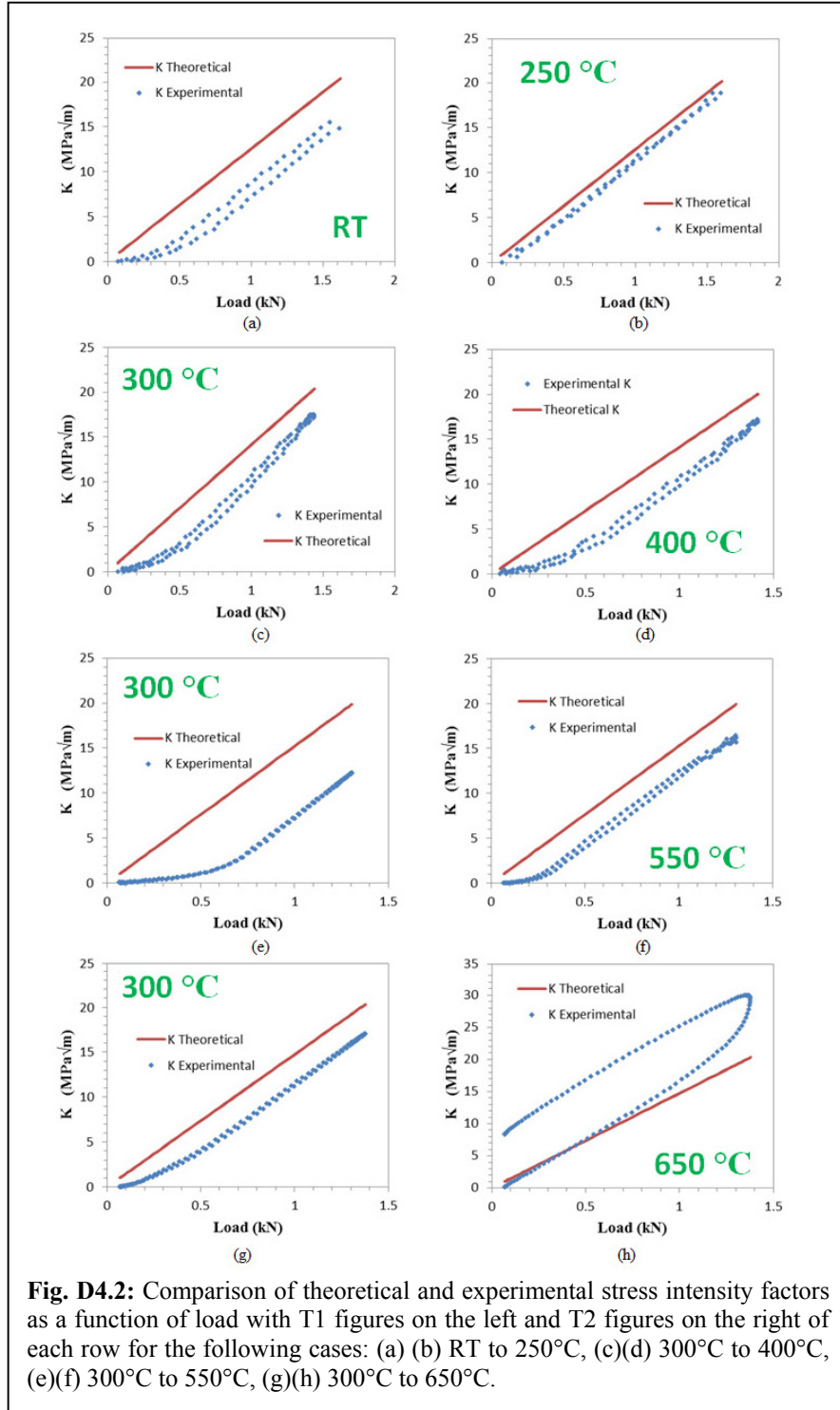
elastic modulus (15 GPa) and in the yield stress (50 MPa) - both larger reductions than were seen for the jump from 33°C to 250°C. Another specimen, shown in Fig. D4.2(g), at T_1 of 300°C experienced a 28% closure level and then at T_2 of 650°C, experienced no closure. The change in yield stress is constant between the experiments shown in Fig. D4.2 (e, f) and (g, h). The elastic

modulus, however, decreases by 20 GPa upon a jump from 300°C and 650°C. Consequently, the change in yield stress alone, or the amount of thermal jump alone, are inadequate for prediction of crack closure levels.

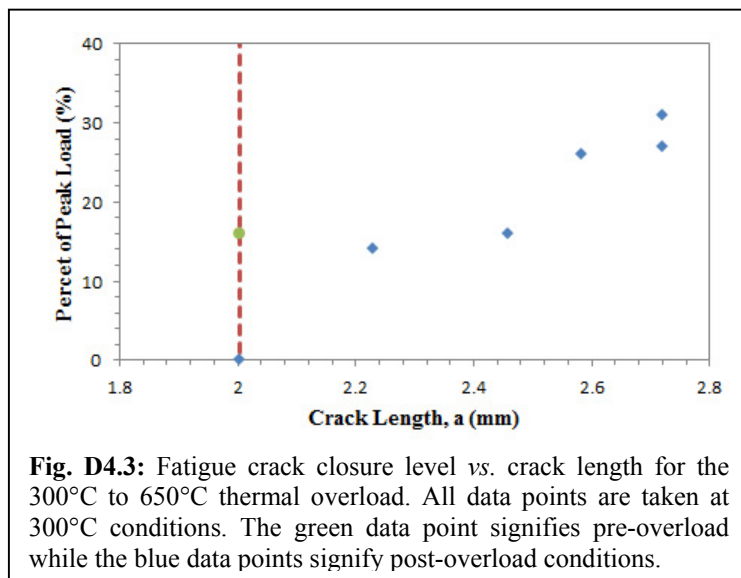
Thermal Overload Crack Closure Results

The thermal overload experiments begin the same way as thermal jump experiments, only after one or more measurement cycles are taken at the elevated temperature T_2 , the temperature is again reduced back to the original level T_1 and fatigue crack growth is continued. This is done in analogy to a single mechanical overload cycle with the intent to investigate how crack growth continues after the return to T_1 . In analogy to a mechanical overload experiment, in the thermal overload experiment performed in this work, the crack was grown at a T_1 of 300°C until a total crack length

of 2.004 mm was reached, a three cycle thermal overload at a T_2 temperature of 650°C was



performed at this same crack length, and finally, crack growth was continued at the original T_I . Crack closure was quantified at various crack lengths while growing the fatigue crack post-overload by performing a few measurement cycles (the reduced frequency cycles) periodically as the crack advanced. Prior to the overload, the crack closure was quantified at a crack length of 2.004 mm and a T_I of 300°C as 0.16 (Fig. D4.2(g)). At the overload temperature of 650°C the crack closure was found to be eliminated as shown by Fig. D4.2(h). In Fig. D4.3 the entire overload history (both pre- and postoverload) is summarized. The vertical, dashed line illustrates the crack length where the thermal overload occurred. The green data point was measured prior



to the overload while the blue data points were measured following the overload. There are two data points at the crack length of 2.004 mm because one (the green point) represents the closure level prior to thermal overload while the other (the blue point) represents the closure level just following the overload once the thermal conditions were reestablished at the T_I level. Figure D4.3 shows that the crack closure levels began to increase once the thermal conditions were reestablished at T_I and fatigue loading was restarted.

At a crack length of 2.229 mm, the closure level was quantified as 0.14. Once the crack grew to a total length of 2.458 mm, the closure level had increased to 0.16. At $a = 2.584$ mm, closure was 0.26 and at $a = 2.719$ mm, closure was calculated to be 0.31. The crack remained at a crack length of $a = 2.719$ mm for another 100,000 cycles before the experiment was halted. As fatigue crack growth rates have been shown to return to nominal, post-overload levels when grown outside of the effected plastic zone caused by a tensile overload, the closure level gradually increased as the fatigue crack was grown past the overload point. Here, crack closure levels post overload increased past the levels which were seen prior to the overload. This is potentially due to a lack of experimental data points outside of the enlarged, overload plastic zone. As seen in Roychowdhury and Dodds (2005), in the case of a simulated mechanical overload, crack closure levels have been seen to increase above the original steady state levels after the crack has grown out of the enlarged overload plastic zone, and then to evolve back to original steady state levels.

Figure D4.4 shows a crack length, a , vs. number of cycles, N curve. Each data point was taken after approximately the same amount of crack advance. The dashed red line represents the crack length, $a = 2.004$ mm, where the thermal overload occurred and the dashed green line represents the crack length, $a = 2.9$ mm, where the crack should have (based on an elastic palne stress estimate) grown out of the enlarged plastic zone created by the thermal overload of 650°C. Figure 15 shows a slight retardation in crack growth rate until a little before the estimated boundary of the elasto-plastic zone. As stated earlier, the crack ceased propagating after this. Crack tip blunting leads to the change in crack growth propagation rate. The blunted crack needed to reinitiate before further growth could occur.

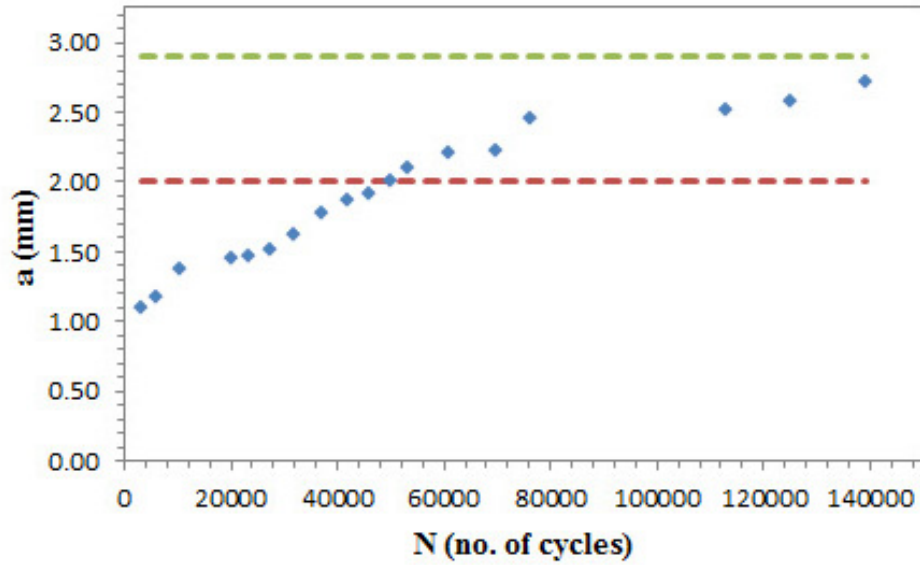


Fig. D4.4: a vs. N for the thermal overload at 300°C. The red dashed line signifies where the thermal overload to 650°C occurred and the green dashed line signifies where the crack should have grown out of the plastic zone created by the thermal overload.

5. Collaborative Aspects

The work performed in this center was in the context of collaborative activities with AFRL researchers from the Aerospace Systems Directorate (AFRL/RQHF). Each project had a primary UIUC advisor and a primary AFRL collaborator from the time of its inception. A project description for each project proposal was generated by both these lead PIs (Principal Investigators) and then submitted to the center's steering committee for discussion and approval. The steering committee, which consisted of 3 people from AFRL and 3 from UIUC to the strengthen collaborative decision-making process, then either approved projects or in some (rare) cases requested modifications and resubmission. Depending on the project, other researchers from both UIUC and AFRL may have been involved in addition to the two main PIs. The existence of project supervisors and participants from both AFRL and UIUC gave the graduate students involved a unique perspective in education as they were also directly involved with practical aspects of application of their research to AFRL needs.

Although naturally the level of collaboration in each joint project varied, some being more integrated than others, overall a highly interactive environment between UIUC and AFRL researchers existed. In several cases there was close coupling between UIUC researchers performing simulations of experimental data gathered by AFRL personnel. An example is the collaborative activities between Geubelle and Bodony from the UIUC side and Gordon, Hollkamp and Beberniss from AFRL, where the UIUC team performed integrated simulations of the facilities and experiments conducted at AFRL. This was a particularly useful application of collaborative efforts. However, the collaboration evolved over time as center activities progressed. Prof. Bodony for example joined the MSSC effort several months after the initial team was formed. After a number of visits and interactions with Joe Hollkamp and Bob Gordon the entire group investigated in detail the operation of the SEF facility at AFRL. Input provided by the UIUC student's research was incorporated into the SEF facility test plan. This was a tangible example of knowledge transfer, and represents a particularly strong aspect of the UIUC/AFRL collaboration. The collaboration worked both ways in that Hollkamp and Gordon were very helpful in guiding Mahesh Sucheendran, the Ph.D. student working on this project, through his research. In late 2008, stemming from conversations between Dan Bodony, Mike Spotswood and Tom Eason during one of the center's external reviews, a new project that focused more fundamentally on the loads a flexible structure would feel in a representative hypersonic environment was started. Such interaction that would lead to significant directional changes and even introduction of new projects was not uncommon and in many cases shaped the details of the continued research in various projects. (The most significant example of this is perhaps the March 29, 2010 meeting which is discussed in more detail later on.) However on occasion communication lines could break down, causing the collaborating parties to perhaps view the evolution of a project differently. Such obstacles were often overcome by in person visits to AFRL or detailed teleconferences. For example, in the case of Chris Ostoich's project part of the collaboration challenges arose because of the ambiguity of the initial project plan: milestones were vague and progress was sometimes slow as Chris had to develop a considerable number of new computational tools. In the latter half of this project, however, there was a very close collaboration which eventually resulted into UIUC researchers becoming external advisors to AFRL-centered efforts such as the new RC19 tunnel tests.

In some other cases the interests and expertise of UIUC and AFRL collaborators lined up more directly, with both sides having expertise in similar areas. For example initial

collaborations between Lambros and Sehitoglu, and Hauber, Spotswood and Chona were very close, with weekly teleconferences, to discuss in detail experimental developments. Some collaborations over time transformed in nature as the team changed or individuals' duties varied, with for example such teleconferences diminishing in number after Dr. Hauber's move to a different branch of AFRL and Dr. Spotswood's change of position.

A very close interaction with AFRL personnel, in particular Dr. Eason, took place with Prof. Duarte's group. Dr. Eason played a critical role in defining the target research problem for several of Prof. Duarte's projects – one that was both relevant to the US Air Force and at the same time leveraged the expertise and ongoing research in Prof. Duarte's group. Furthermore, Dr. Eason was, during the seven years of the center, deeply involved in all technical aspects of this research. This was helpful in keeping the work focused on a path to solve target problems and also in transitioning findings and developed computational tools to AFRL personnel and industries. This tight collaboration also proved important for the expansion of the funding required to AFOSR sponsored efforts. Other such strong coupling between UIUC/AFRL and other external researchers also resulted in additional AFOSR funding and can be viewed as a significant success of the center as additional funds were made possible beyond the base AFRL funding. This fact was reflected in the center meetings which were very well attended with researchers from a large number of institutions.

An overarching factor that was crucial for the success of many of the research efforts of the MSSC, was the high quality and dedication of the students that were recruited for this effort. At any given time many students (between 6-9) were supported directly through the MSSC, with several more 2-3 being supported indirectly either through matching funds or through additional external funding from AFRL or AFOSR. In many cases students worked as a team that shared their experiences and research methodologies. This was true for both the numerical and experimental aspects of the center where, for example, Prof. Duarte's three students shared a software platform, Prof. Geubelle's and Bodony's students worked very closely, and Prof. Lambros's and Sehitoglu's students were essentially co-advised by both faculty. As a result, students benefited from each other's progress and attained excellent productivity.

Individual collaborations proceeded through regular meetings either in person or through teleconferencing. However, in terms of group interaction, the Technical Interchange Meetings (TIM) which were held about every 6 months proved invaluable for outlining progress of the entire group, to the entire group. Once every 6 months such face to face interaction took place where the entire group got to hear updates from all participants. Although the format of the TIMs changed for almost every meeting, each meeting really achieved its main purpose. In this sense TIMs were vital a part of the collaborative nature of the center. In addition, meetings between the primary researchers in the center, especially the meeting of March 29 2010 that launched the Life Forecasting efforts of the center, proved instrumental in developing technical guidance for the center activities. In fact it would probably have been even more instructive to hold such meetings perhaps at the frequency of TIM meetings (*i.e.*, once every 6 months) or at least once a year.

Another successful collaborative interaction was the inclusion of some of the more senior AFRL researchers into Ph.D. students' preliminary and/or defense examinations. In most departments at UIUC the preliminary examination consists of a thesis proposal in which the students first present their work to that point (typically after the completion of at least one journal publication) and then present future plans for competing a Ph.D. In this exam the role of the committee is critical in providing input not only on the quality for the research to that point, but also on the student's future plans. Often the committee provides suggestions for major re-routes

of the student's work and redefines the student's project. This definitely was the case for all the committees which involved AFRL personnel and not only helped focus the student's work onto topics of technical relevance to the Air Force, but also showed the students different perspectives of approaching the problem under consideration. This collaboration was another significantly successful feature of the MSSC collaborative activities.

6. References

- Abuzaid W., Sangid M.D., Carroll J.D., Sehitoglu H. and Lambros J. (2012), "Slip transfer and plastic strain accumulation across grain boundaries in Hastelloy X", *Journal of the Mechanics and Physics of Solids*, Vol. 60, p. 1201-1220.
- Adams N. and Kleiser L. (1996), "Subharmonic transition to turbulence in a flat-plate boundary layer at Mach number 4.5," *Journal of Fluid Mechanics*, Vol. 317, No. 1, pp. 301–335.
- Anderson J.D. (2005), "Fundamentals of Aerodynamics", Fourth Edition, McGraw-Hill Series in Aeronautical and Aerospace Engineering.
- Ashley H. and Zartarian G. (1956), "Piston Theory - A New Aerodynamic Tool for the Aeroelastician", *Journal of the Aeronautical Sciences*, Vol. 23, No. 12, pp. 1109-1118.
- Auricchio F. and Taylor R.L. (1995), "Two material models for cyclic plasticity: nonlinear kinematic hardening and generalized plasticity", *Int. J. Plas.*, Vol. 11, pp. 65–98.
- Barbe F., Forest S. and Cailletaud G. (2001), "Intergranular and intragranular behavior of polycrystalline aggregates. 2. Results", *International Journal of Plasticity*, Vol. 17, No. 4, pp. 537–563.
- Beaudoin A., Bryant J. and Korzekwa D. (1998), "Analysis of ridging in aluminum auto body sheet metal", *Metallurgical and Materials Transactions A*, Vol. 29, No. 9, pp. 2323–2332.
- Bebernis T., Spottswood M. and Eason T. (2011), "High-Speed Digital Image Correlation Measurements of Random Non- linear Dynamic Response," *Experimental and Applied Mechanics*, Volume 6, edited by T. Proulx, Vol. 9999 of Conference Proceedings of the Society for Experimental Mechanics Series, Springer New York, pp. 171–186.
- Blevins R.D., Bolios D., Holehouse I., Hwa V.W., Tratt M.D., Laganelli A.L., Pozefsky P. and Pierucci M. (1989), "Thermo-Vibro-Acoustic Loads and Fatigue of Hypersonic Flight Vehicle Structure - Phase II Report", Rohr Industries, Inc., RHR 89-202, November 1989.
- Blevins R.D., Holehouse I. and Wentz K.R. (1993), "Thermoacoustic Loads and Fatigue of Hypersonic Vehicle Skin Panels", *Journal of Aircraft*, Vol. 30, No. 6, pp. 971-978.
- Bodony D.J. (2009), "Heating effects on the structure of noise sources of high-speed jets," AIAA Paper 2009-0291, Presented at the 47th Aerospace Sciences Meeting & Exhibit, Orlando, Florida, Jan. 5-8.
- Bodony D.J. (2010), "Accuracy of the simultaneous-approximation-term boundary condition for time-dependent problems," *J. Sci. Comput.*, Vol. 43, No. 1, pp. 118–133.
- Bodony D.J., Zagaris G., Reichert A. and Zhang Q. (2010), "Aeroacoustic predictions in complex geometries," *IUTAM Symposium on Computational Aero-Acoustics for Aircraft Noise Prediction*, edited by R. J. Astley and G. Gabard, Vol. 6, *Procedia Engineering*, pp. 234–243.
- Boettner R.C., McEvily A.J. and Liu Y.C. (1964), "On the Formation of Fatigue Cracks at Twin Boundaries", *Philosophical Magazine*, Vol. 10, p. 95.
- Brandyberry M.D. (2008), "Thermal Problem Solution Using a Surrogate Model Clustering Technique," *Computer Methods in Applied Mechanics and Engineering*, Vol. 197(29-32), pp. 2390-2407.
- Brinkman C.R., Rittenhouse P.L., Corwin W.R., Strizak J.P., Lystrup A. and DiStefano J.R. (1976), "Application of Hastelloy X in Gas-Cooled Reactor Systems", Report Number: ORNL/TM-5405, 1976.
- Carden A.E. and Slade T.B. (1969), "High-Temperature Low-Cycle Fatigue Experiments on Hastelloy X," *Fatigue at High Temperature*, ASTM STP 459, 1969.

- Carpenter M.H., Gottlieb D. and Abarbenel S. (1994), "Time-stable boundary conditions for finite difference schemes involving hyperbolic systems: Methodology and application for high-order compact schemes," *J. Comp. Phys.*, Vol. 111, pp. 220–236.
- Carroll J., Efstathiou C., Lambros J., Sehitoglu H., Hauber B., Spotswood S. and Chona R., 2009 "Investigation of Fatigue Crack Closure Using Multiscale Image Correlation Experiments," *Engineering Fracture Mechanics*, Vo. 76, No. 15, pp: 2384-2398, DOI: 10.1016/j.engfracmech.2009.08.002.
- Carroll J., Abuzaid W., Lambros J. and Sehitoglu H. (2010), "An experimental methodology to relate local strain to microstructural texture", *Review of Scientific Instruments*, Vol. 81, 083703.
- Cassenti B.N. (1983), "Research and development program for the development of advanced time-temperature dependent constitutive relationships - Vol. 1 - Theoretical discussion", Contractor Final Report NASA CR-168191.
- Clayton J., Schroeter B., McDowell D. and Graham S. (2002) "Distributions of stretch and rotation in polycrystalline OFHC Cu", *Journal of Engineering Materials and Technology*, Transactions of the ASME, Vol. 124, No. 3, pp. 302–312.
- Cottrell A.H. and Stokes R.J. (1955), "Effects of temperature on the plastic properties of aluminum crystals", *Proc. Royal Soc. A* Vol. 233, pp. 17–34.
- Crisfield M. (1997), "Non-linear Finite Element Analysis of Solids and Structures, Volume 2: Advanced Topics", Baffins Lane, Chichester, West Sussex PO19 1UD, England: John Wiley & Sons Ltd.
- Crowell A., Miller B. and McNamara J. (2011), "Computational modeling for conjugate heat transfer of shock-surface interactions on compliant skin panels," No. AIAA-2011-2017, 52nd AIAA/ASME/ASCE/AHS/ASC Structures, Structural Dynamics and Materials Conference, Denver, Colorado, Apr. 4-7.
- Culler A.J. (2012), "Coupled fluid-thermal-structural modeling and analysis of hypersonic flight vehicle structures", Ph.D. thesis, Ohio State University.
- Culler A.J. and McNamara J.J. (2010), "Studies on Fluid-Thermal-Structural Coupling for Aerothermoelasticity in Hypersonic Flow", *AIAA Journal*, Vol. 48, No. 8, pp. 1721-1738.
- Culler A.J. and McNamara J. (2011), "Impact of Fluid-Thermal-Structural Coupling on Response Prediction of Hypersonic Skin Panels," *AIAA J.*, Vol. 49, No. 11, pp. 2393–2406.
- DARPA (2010), "Falcon HTV-2 Launch Tests Hypersonic Vehicle Flight Capabilities," DARPA News Release, April 23, 2010, www.darpa.mil/WorkArea/DownloadAsset.aspx?id=2147484133, Accessed: December 1, 2012.
- DARPA (2011), "DARPA HYPERSONIC VEHICLE SPLASH DOWN CONFIRMED," DARPA News Release, August 14, 2011, <http://www.darpa.mil/NewsEvents/Releases/2011/08/14>, Accessed: December 1, 2012.
- De Graaff D. and Eaton J. (2000), "Reynolds-number scaling of the flat-plate turbulent boundary layer," *Journal of Fluid Mechanics*, Vol. 422, No. 1, pp. 319–346.
- Delaire F., Raphanel J., and Rey C. (2000) "Plastic heterogeneities of a copper multicrystal deformed in uniaxial tension: experimental study and finite element simulations", *Acta Materialia*, Vol. 48, No. 5, pp. 1075–1087.
- Eckert E. (1956), "Engineering relations for heat transfer and friction in high-velocity laminar and turbulent boundary-layer flow over surfaces with constant pressure and temperature", *Transactions of the ASME*, Vol. 78, No. 6, pp. 1273-1283.

- Efstathiou C., Sehitoglu H., Carroll J., Lambros J. and Maier H. (2008), "Full-field strain evolution during intermartensitic transformations in single-crystal NiFeGa", *Acta Materialia*, Vol. 56, pp. 3791–3799.
- Efstathiou C., Sehitoglu H., Lambros J., (2010), "Multiscale strain measurements of plastically deforming polycrystalline titanium: role of deformation heterogeneities", *International Journal of Plasticity*, Vol. 26, p. 93.
- Ehrhardt, David, et al., (2011), "Non-Contact Experimental Modal Analysis of a Curved Beam Using a Full Field Optical Technique", 52nd AIAA/ASME/ASCE/AHS/ASC Structures, Structural Dynamics and Materials Conference, AIAA, Denver, Colorado.
- Elber W. (1970), "Fatigue crack closure under cyclic tension", *Engineering Fracture Mechanics*, Vol. 2, pp. 37–45.
- Elber W. (1971), "The significance of fatigue crack closure", *ASTM – STP 486*, pp. 230–42.
- Field D.P., Magid K.R., Mastorakos I.N., Florando J.N., Lassila D.H. and Morris J.W. Jr. (2010), "Mesoscale strain measurement in deformed crystals: A comparison of X-ray microdiffraction with electron backscatter diffraction", *Philosophical Magazine*, Vol. 90, pp. 1451-1464.
- Findley W.N. (1959), "A theory for the effect of mean stress on fatigue of metals under combined torsion and axial load or Bending", *Journal of Engineering for Industry*, pp. 301-306.
- Frederick C.O. and Armstrong P.J. (2007), "A mathematical representation of the multiaxial Bauschinger effect", *Mats. at High Temp.*, Vol. 24, pp. 1–26.
- Fries T.P. and Andreas Zilian A. (2009), "On time integration in the XFEM", *International Journal For Numerical Methods In Engineering*, Vol. 79, pp. 69–93□.
- Glass C. and Hunt L. (1986), "Aerothermal tests of spherical dome protuberances on a flat plate at a Mach number of 6.5," *NASA STI/Recon Technical Report N*, Vol. 87.
- Glass C. and Hunt L. (1988), "Aerothermal tests of quilted dome models on a flat plate at a Mach number of 6.5," *NASA STI/Recon Technical Report N*, Vol. 88.
- Groeber M., Ghosh S., Uchic M.D. and Dimiduk D.M. (2008), "A framework for automated analysis and simulation of 3D polycrystalline micro structures. Part 1: Statistical characterization", *Acta Materialia*, Vol. 56, pp. 1257-1273.
- Heinz A. and Neumann P. (1990), "Crack initiation during high cycle fatigue of an austenitic steel", *Acta Metallurgica et Materialia*, Vol. 38, p. 1933.
- Herbig, M., King A., Reischig P., Proudhon H., Lauridsen EM., Marrow J., Buffière JY., Ludwig W. (2011), "3-D growth of a short fatigue crack within a polycrystalline microstructure studied using combined diffraction and phase-contrast X-ray tomography", *Acta Materialia*, Vol. 59, pp. 590-601.
- Hollkamp J.J. and Gordon R.W. (2008), "Reduced-order models for nonlinear response prediction: Implicit condensation and expansion", *Journal of Sound and Vibration*, Vol. 318.
- Huang J. and Pelloux R. (1980), "Low cycle fatigue crack propagation in hastelloy-X at 25 and 760 °C", *Metallurgical and Materials Transactions A*, Vol. 11, p. 899.
- Huang L. (2006), "Broadband sound reflection by plates covering side-branch cavities in a duct", *Journal of Acoustical Society of America*, Vol. 119, No. 5, pp. 2628-2638
- Hutchinson J.W. (1976), "Bounds and Self-consistent estimates for creep of polycrystalline materials", *Proceedings of the Royal Society of London Series A, Ser. C*, Vol. 348, p. 101.
- Jablonski D.A. (1978), "Fatigue Behavior of Hastelloy-X at Elevated Temperatures in Air", *Vacuum and Oxygen Environments*, Ph.D. Thesis, Massachusetts Institute of Technology, Cambridge, Massachusetts.

- Jaske C.E., Rice R.C., Buchheit R.D., Roach D.B. and Porfilio T. L. (1976), "Low-Cycle Fatigue of Type 347 Stainless Steel and Hastelloy Alloy X in Hydrogen Gas and in Air at Elevated Temperatures", Report Number: NASA-CR-135022.
- Johnson G.R. and Cook W.H. (1983), "A constitutive model and data for metals subjected to large strains, high strain rates and high temperatures", *Proceedings of Seventh International Symposium on Ballistics*, pp. 541–548.
- Kim W.-G., Yin S.-N., Kim Y.-W. and Chang J.-H. (2008), "Creep characterization of a Ni-based Hastelloy-X alloy by using the ta projection method", *Engineering Fracture Mechanics*, Vol. 75, p. 4985.
- Kim J., Bodony D.J. and Freund J.B. (2009), "LES investigation of a Mach 1.3 jet with and without plasma actuators," *AIAA Paper 2009-0290*, Presented at the 47th Aerospace Sciences Meeting & Exhibit.
- Kim J., Natarajan M., Bodony D.J. and Freund J.B. (2010), "A high-order, overset mesh algorithm for adjoint-based optimization for aeroacoustics control," *AIAA Paper 2010-3818*, Presented at the 16th AIAA/CEAS Aeroacoustics Conference.
- Kim D.-J., Duarte C.A. and Sobh N.A. (2011), "Parallel Simulations of Three-dimensional Cracks Using the Generalized Finite Element Method", *Computational Mechanics*, Vol. 47, No. 3, pp. 265-282.
- Kocks U.F. and Chandra H. (1982), "Slip geometry in partially constrained deformation", *Acta Metallurgica*, Vol. 30, p. 695.
- Laganelli A.L. and Howe J.R. (1977), "Prediction of Pressure Fluctuations Associated with Maneuvering Re-entry Weapons", *AFFDL-TR-77-59*, July 1977.
- Laganelli A.L. and Wolfe H.F. (1993), "Prediction of Fluctuating Pressure in Attached and Separated Turbulent Boundary-Layer Flow", *Journal of Aircraft*, Vol. 30, No. 6, pp. 962-970.
- Lee T.C., Robertson I.M. and Birnbaum H.K. (1989), "Prediction of slip transfer mechanisms across grain boundaries", *Scripta Metallurgica*, Vol. 23, p. 799.
- Lee S., Lu Y., Liaw P., Chen L., Thompson S., Blust J., Browning P., Bhattacharya A., Aurrecoechea J. and Klarstrom D. (2009), "Tensile-Hold Low-Cycle-Fatigue Properties of Solid-Solution-Strengthened Superalloys at Elevated Temperatures", *Materials Science and Engineering: A*, Vol. 504, No. 1-2, pp. 64-72.
- Lighthill M.J. (1953), "Oscillating airfoils at high Mach numbers," *Journal of the Aeronautical Sciences*, Vol. 20, No. 6, pp. 402–406.
- Llanes L. and Laird C. (1992), "The role of annealing twin boundaries in the cyclic deformation of f.c.c. materials", *Materials Science and Engineering: A*, Vol. 157, p. 21.
- Lubliner J. (1974), "A simple theory of plasticity", *Int. J. Solids and Struc.*, Vol. 10, pp. 313–319.
- Lubliner J., Taylor R.L. and Auricchio F. (1993), "A new model of generalized plasticity and its numerical implementation", *Int. J. Solids and Struc.*, Vol. 22, pp. 3171–3184.
- Macha D.E., Corbly D.M. and Jones J.W. (1979), "On the Variation of fatigue-crack-opening load with measurement location", *Experimental Mechanics*, Vol. 19, No. 6, pp. 207–13.
- Malik M.R. (1990), "Numerical methods for hypersonic boundary-layer stability," *J. Comp. Phys.*, Vol. 86, pp. 376–413.
- Mattsson K., Svärd M. and Nordström J. (2004), "Stable and accurate artificial dissipation," *J. Sci. Comput.*, Vol. 21, No. 1, pp. 57–79.
- Merle R. and Dolbow J. (2002), "Solving thermal and phase change problems with the eXtended finite element method", *Computational Mechanics*, Vol. 28, No. 5, pp. 339-350.

- Meyers M.A. and Ashworth E. (1982), "Model for the effect of grain size on the yield stress of metals", *Philosophical Magazine A*, Vol. 46, p. 737.
- Miao J., Pollock T.M. and Wayne Jones J. (2009), "Crystallographic fatigue crack initiation in nickel-based superalloy Rene 88DT at elevated temperature", *Acta Materialia*, Vol. 57, p. 5964.
- Mika D. and Dawson P. (1999), "Polycrystal plasticity modeling of intracrystalline boundary textures", *Acta Materialia*, Vol. 47, No. 4, pp. 1355–1369.
- Miner R. and Castelli M. (1992), "Hardening mechanisms in a dynamic strain aging alloy, HASTELLOY X, during isothermal and thermomechanical cyclic deformation", *Metallurgical and Material Transactions A*, Vol. 23, p. 551.
- National Research Council (1998), "Review and evaluation of the air force hyper-sonic technology program", Technical Report AFSB-J-97-01-A.
- Nordström J., Gong J., der Weide E.V. and Svärd M. (2009), "A stable and conservative high order multi-block method for the compressible Navier-Stokes equations," *J. Comp. Phys.*, Vol. 228, pp. 9020–9035.
- O'Hara P.J. (2010), "A multi-scale generalized finite element method for sharp, transient thermal gradients", Ph.D. Thesis, University of Illinois.
- O'Hara P.J., Duarte C.A., Eason T. and Garzon J. (2012), "Efficient analysis of transient heat transfer problems exhibiting sharp thermal gradients", *Computational Mechanics*, DOI 10.1007/s00466-012-0750-6.
- Ostoich C.M., Bodony D.J. and Geubelle P.H. (2012), "Fluid-Thermal Response of Spherical Dome Under a Mach 6.59 Laminar Boundary Layer," *AIAA Journal*, Vol. 50, No. 12, 2012/11/29, pp. 2791–2808.
- Padilla H., Lambros J., Beaudoin A. and Robertson I. (2012), "Relating inhomogeneous deformation to local texture in zirconium through multiscale digital image correlation experiments", *International Journal of Solids and Structures*, Vol. 49, No. 1, pp. 18–31.
- Paris P, Erdogan F. (1963), "A critical analysis of crack propagation laws", *Basic Engineering Transactions ASME Series D*, Vol. 85, pp. 528–34.
- Park K., Paulino G.H. and Roesler J.R. (2009), "A unified potential-based cohesive model of mixed-mode fracture", *J Mech Phy Solids*, Vol. 57, pp. 891-908.
- Peralta P. and Laird C. (1998), "Fatigue fracture at bicrystal interfaces: Experiment and theory", *Acta Materialia*, Vol. 46, pp. 2001-2020
- Peralta P., Choi S.H. and Gee J. (2007), "Experimental quantification of the plastic blunting process for stage II fatigue crack growth in one-phase metallic materials", *International Journal of Plasticity*, Vol. 23, pp. 1763-1795.
- Pereira J.P., Kim D.-J. and Duarte C.A. (2012), "A Two-Scale Approach for the Analysis of Propagating Three-Dimensional Fractures", *Computational Mechanics*, Vol. 49, No. 1, pp. 99-121.
- Pirozzoli S., Grasso F. and Gatski T. (2004), "Direct numerical simulation and analysis of a spatially evolving supersonic turbulent boundary layer at $M=2.25$," *Phys. Fluids*, Vol. 16, pp. 530.
- Pirozzoli S. and Grasso F. (2006), "Direct numerical simulation of impinging shock wave/turbulent boundary layer interaction at $M=2.25$," *Phys. Fluids*, Vol. 18.
- Plews J.A. (2011), "Non-intrusive extension of a generalized finite element method for multiscale problems to the ABAQUS analysis platform", MS Thesis, University of Illinois.
- Pope S. B. (2000), *Turbulent Flows*, Cambridge University Press, Cambridge, U.K.

- Pulliam T.H. and Chaussee D.S. (1981), "A diagonal form of an implicit approximate-factorization algorithm," J. Comp. Phys., Vol. 43, pp. 357–372.
- Raabe D., Sachtleber M., Zhao Z., Roters F. and Zaefferer S. (2001), "Micromechanical and macromechanical effects in grain scale polycrystal plasticity experimentation and simulation", Acta Materialia, Vol. 49, No. 17, pp. 3433–3441.
- Riddell W.T., Piascik R.S., Sutton M.A., Zhao W., McNeill S.R. and Helm J.D. (1999), "Determining fatigue crack opening loads from near-crack-tip displacement measurements", ASTM – STP 1343, pp. 157–74.
- Roters F., Eisenlohr P., Hantcherli L., Tjahjanto D.D., Bieler T.R. and Raabe D. (2010), "Overview of constitutive laws, kinematics, homogenization and multiscale methods in crystal plasticity finite-element modeling: theory, experiments, applications", Acta Materialia, Vol. 58, p. 1152.
- Rowley, M.A., Thornton, E.A., 1996. Constitutive modeling of the visco-plastic response of Hastelloy-X and aluminum alloy 8009. J. Eng. Mater. Technol. 118, 19.
- Roychowdhury S. and Dodds J.R.H. (2005), "Effects of an overload event on crack closure in 3-d small-scale yielding: finite element studies", Fatigue & Fracture of Engineering Materials & Structures, Vol. 28, pp. 891–907.
- Sandham N.D., Yao Y.F. and Lawal A.A. (2003), "Large-eddy simulation of transonic turbulent flow over a bump," Int. J. Heat and Fluid Flow, Vol. 24, pp. 584–595.
- Sangid M.D., Maier H.J. and Sehitoglu H. (2011a), "An energy-based microstructure model to account for fatigue scatter in polycrystals", Journal of the Mechanics and Physics of Solids, Vol. 59, p. 595.
- Sangid M.D., Maier H.J. and Sehitoglu H. (2011b), "A physically based fatigue model for prediction of crack initiation from persistent slip bands in polycrystals", Acta Materialia, Vol. 59, p. 328.
- Sangid M.D., Maier H.J. and Sehitoglu H. (2011c), "The role of grain boundaries on fatigue crack initiation – An energy approach", International Journal of Plasticity, Vol. 27, p. 801.
- Sangid M.D., Pataky G.J., Sehitoglu H., Rateick R.G., Niendorf T. and Maier H.J. (2011d), "Superior fatigue crack growth resistance, irreversibility, and fatigue crack growth-microstructure relationship of nanocrystalline alloys", Acta Materialia, Vol. 59, pp. 7340–7355.
- Sobotka J.C., Oral A. and Culler A.J. (2013), "Towards a Coupled Loads-Response-Life Prediction Framework for Hypersonic Structures in Combined Extreme Environments", 54th AIAA/ASME/ASCE/AHS/ASC Structures, Structural Dynamics, and Materials Conference.
- Spottswood M., Eason T. and Bebernis T. (2012), "Influence of shock-boundary layer interactions on the dynamic response of a flexible panel," proceedings of the International Conference on Noise and Vibration Engineering, Leuven, Belgium.
- St-Pierre L., Hérissé E., Dexet M., Crépin J., Bertolino G. and Bilger N. (2008), "3D simulations of microstructure and comparison with experimental microstructure coming from O.I.M. analysis", International Journal of Plasticity, Vol. 24, No. 9, pp. 1516–1532.
- Strand B. (1994), "Summation by parts for finite difference approximations for d/dx ," J. Comp. Phys., Vol. 110, pp. 47–67.
- Strizak J. P., Brinkman C. R. and Rittenhouse P. L. (1981), "High-Temperature Low-Cycle Fatigue and Tensile Properties of Hastelloy X and Alloy 617 in Air and HTGR-Helium", IAEA Specialists' Meeting on High-Temperature Metallic Materials for Application in Gas-Cooled Reactors, CONF-810530-4.

- Succheendran M., Bodony D.J. and Geubelle P.H. (2009), "Structural-acoustic interaction of a cavity-backed, clamped, elastic plate with sound in a duct," *Bull. Am. Phys. Soc.*, Vol. 54, No. 19.
- Suzuki H., Iseki T. and Shoda Y. (1977), "High-Temperature Low-Cycle Fatigue Tests on Hastelloy X", *Journal of Nuclear Science and Technology*, Vol. 14, No. 5, pp. 381-386.
- Svärd M., Carpenter M.H. and Nordström J. (2007), "A stable high-order finite difference scheme for the compressible Navier-Stokes equations, far-field boundary conditions," *J. Comp. Phys.*, Vol. 225, pp. 1020–1038.
- Svärd M. and Nordström J. (2008), "A stable high-order finite difference scheme for the compressible Navier-Stokes equations: No-slip wall boundary conditions," *J. Comp. Phys.*, Vol. 227, pp. 4805–4824.
- Swaminathan B., Abuzaid W., Lambros J. and Sehitoglu H. (2013a), "Investigation of Portevin-Le Chatelier effect at elevated temperatures in Hastelloy X", submitted to *International Journal of Plasticity*.
- Swaminathan B., Lambros J. and Sehitoglu H. (2013b), "Mechanical response of a nickel superalloy under thermal and mechanical cycling: uniaxial and biaxial stress states", submitted to *Journal of Strain Analysis for Engineering Design*.
- Taira S., Fujino M. and Ohtani R. (1979), "Collaborative Study on Thermal Fatigue of Properties of High Temperature Alloys in Japan", *Fatigue of Engineering Materials and Structures*, Vol. 1, No. 4, pp. 495-508.
- Taylor G.I. (1938), "Plastic strain in metals", *Journal of the Institute of Metals*, Vol. 62, pp. 307–325.
- Thornton E.A. (1992), "Thermal Structures: Four Decades of Progress", *Journal of Aircraft*, Vol. 29, No. 3, pp. 485-498.
- Thornton E.A. and Dechaumphai P. (1988), "Coupled Flow, Thermal, and Structural Analysis of Aerodynamically Heated Panels", *Journal of Aircraft*, Vol. 25, No. 11, pp. 1052-1059.
- Tomkins B. and Biggs W.D. (1969), "Low endurance fatigue in metals and polymers, Part 3: Mechanisms of failure", *Journal of Materials Science*, Vol. 4, pp. 544-553.
- Tsuji H. and Kondo T. (1987), "Strain-Time Effects in Low-Cycle Fatigue of Nickel-Base Heat-Resistant Alloys at High Temperature", *Journal of Nuclear Materials*, Vol. 150, No. 3, pp. 259-265.
- Tzong G., Jacobs R. and Liguore S. (2010), "Air Vehicle Integration and Technology Research (AVIATR) Task Order 0015: Predictive Capability for Hypersonic Structural Response and Life Prediction: Phase I - Identification of Knowledge Gaps", Volume 1 - Nonproprietary Version," AFRL-RB-WP-TR-2010-3068, V1, September 2010.
- Vinokur M. (1974), "Conservation equations of gasdynamics in curvilinear coordinate systems," *J. Comp. Phys.*, Vol. 14, pp. 105–125.
- Visbal M. (2012), "On the interaction of an oblique shock with a flexible panel," *Journal of Fluids and Structures*, Vol. 30, pp. 219 – 225.
- Zagaris G., Bodony D.J., Brandyberry M., Campbell M.T., Shaffer E.G. and Freund J.B. (2010), "A collision detection approach to chimera grid assembly for high fidelity simulations of turbofan noise," 48th AIAA Aerospace Sciences Meeting, No. 2010–836, AIAA.
- Zuchowski B. (2010), "Air Vehicle Integration and Technology Research (AVIATR) Task Order 0015: Predictive Capability for Hypersonic Structural Response and Life Prediction: Phase I - Identification of Knowledge Gaps," AFRL-RB-WP-TR-2010-3069, August 2010.

Appendix I – List of all MSSC projects

A—Response Prediction: Coupled Aero-Thermo-Mechanical-Acoustic Analysis and Simulation

A1 Design of STATS using Topology Optimization

Personnel: Paulino, Stump (Graduate student, UIUC), Byrd, Haney (AFRL)
Start: 2006; End: 2008

A2 Generalized FEM Analysis for Transient Simulations

Personnel: Duarte, O'Hara (Graduate student, UIUC), Eason (AFRL)
Start: 2006; End: 2010

A3 Integrated Fluid/Structure Interaction Simulation

Personnel: Geubelle, Bodony, Joumaa (Graduate student, UIUC) Sucheendran (Graduate student, UIUC), Kuester (Undergraduate student, UIUC), Halvorson (Undergraduate student, UIUC), Hollkamp (AFRL), Gordon (AFRL)
Start 2006; End: 2010

A4 Analytical Prediction of Dynamic Response of Functionally Graded Material (FGM)

Personnel: Palazotto, Larson (AFIT student)
Start 2007; End: 2008

A5 Multiphysics, Coupled Analysis of Extreme-Environment Structures

Personnel: Bodony, Geubelle, Ostoich (Graduate student UIUC), Spottswood (AFRL)
Start: 2008, End: 2013

A6 Non-Intrusive Implementation of Multiscale Capabilities in a General Purpose FEA Platform

Personnel: Duarte, Pereira (Graduate student, UIUC), Plews (Graduate student, UIUC), Eason (AFRL)
Start: 2008, End: 2010

A7 Multiscale Thermo/Strain Field Coupling

Personnel: Duarte, Plews (Graduate student, UIUC), Eason (AFRL)
Start: 2009; End: 2010

B—Life Prediction: Identification and Definition of Structural Limit States

B1(x) Failure Analysis of Functionally Graded Aircraft Components in Combined Environments

Personnel: Huang, Xiao (Graduate student, UIUC), Tuegel (AFRL)
Start: 2006; End: 2007

B1 Mechanism-Based Cohesive Failure Model for Functionally Graded Aircraft Components and Structures

Personnel: Paulino, Park (Postdoc UIUC), Gain (Graduate student, UIUC), Tuegel (AFRL)
Start: 2008; End: 2010

B2 Imperfections and Defect Tolerance of Aircraft Shells and Structures

Personnel: Tortorelli, Watts (Graduate student, UIUC), Eason (AFRL)
Start 2009; End: 2011

B3 3D Cyclic Plasticity Model for Thermomechanical Loading in Large-scale Analyses

Personnel: Dodds, Sobotka (Postdoc, UIUC), Gockel (AFRL)
Start: 2010, End: 2012

B4 Towards a Fatigue Initiation Theory for Multiaxial Thermomechanical Fatigue

Personnel: Sehitoglu, Oral (Postdoc, UIUC), Penmetsa (AFRL)
Start: 2011, End: 2012

C—Life Prediction: Framework and Methodologies for Risk-quantified Structural Assessment

C1 Uncertainty/Risk Quantification Methods for STATS

Personnel: Song, Lee (Graduate student, UIUC), Tuegel (AFRL)
Start: 2006; End: 2010

C2 Validation of Simulations Having Uncertainties in Both Simulation and Experiments

Personnel: Brandyberry, Tudor (Undergraduate student UIUC), Gruenwald (Graduate student UIUC), Haney (AFRL)
Start 2006; End: 2009

C3 Risk-Based Design Plots for Aircraft Damage Tolerant Design

Personnel: Penmetsa
Start: 2007; End: 2008

C4 System Reliability with Correlated Failure Mode

Personnel: Millwater, Smith (Graduate student, Texas San Antonio), Sparkman, Wieland, Tuegel (AFRL)
Start: 2008; End: 2011

C5 Probabilistic Cohesive Zone Model for Fiber Bridging

Personnel: Penmetsa, Kable, Shanmugam, Tuegel (AFRL)
Start: 2008; End: 2010

C6 Enriched Space-time Finite Element Method

Personnel: Qian, Yang, Chirptukar, Alpert, Eason (AFRL), Spottswood (AFRL)
Start: 2010; End: 2011

D—Experimental Discovery and Limit State Characterization

D1 Experimental Investigation of Thermomechanical Fatigue Failure Modes

Personnel: Sehitoglu, Efstathiou (Graduate student, UIUC), Hauber (AFRL)
Start: 2006; End: 2009

D2 Development of Experimental Techniques for Validating a Coupled Thermomechanical Fatigue Simulation Framework

Personnel: Lambros, Carroll (graduate student, UIUC), Chona (AFRL)
Start: 2006; End: 2010

D3 Thermomechanical Fatigue of Hastelloy X: Role of Combined Loading on Material

Response

Personnel: Sehitoglu, Abuzaid (graduate student, UIUC), Penmetsa (AFRL)
Start: 2008; End: 2012

D4 Thermomechanical Fatigue of Hastelloy X: Role of Defects

Personnel: Lambros, Casperson (graduate student, UIUC), Chona (AFRL)
Start: 2010; End: 2012

Appendix II – List of MSSC sponsored Journal Publications

2013

- Casperson M.C., Carroll J., Lambros J., Sehitoglu H. and Dodds R.H., (2013), “Investigation of thermal effects on fatigue crack closure using multiscale digital image correlation experiments”, submitted to International Journal of Fracture.
- Shanmugam V., Penmetsa R., Tuegel E. and Clay S., (2013), “Stochastic Modeling of Delamination Growth in Unidirectional Composite DCB Specimens using Cohesive Zone Models”, in press Composite Structures.
- Sobotka J.C., Oral A., Culler A.J., (2013), “Towards a Coupled Loads-Response-Life Prediction Framework for Hypersonic Structures in Combined Extreme Environments”, submitted to AIAA journal.

2012

- Abuzaid W.Z., Oral A., Sehitoglu H., Lambros J. and Maier H., (2012), “Fatigue Crack Initiation in Hastelloy X – The Role of Boundaries”, accepted Fatigue and Fracture of Engineering Materials and Structures.
- Abuzaid W.Z., Sehitoglu H., Lambros J., (2012), “Plastic Strain Localization and Fatigue Micro-Crack Formation in Hastelloy X”, in press Materials Science & Engineering A.
- Abuzaid W., Sangid M.D., Carroll J.D., Sehitoglu H. and Lambros J., (2012), “Slip Transfer and Plastic Strain Accumulation across Grain Boundaries in Hastelloy X”, in press Journal of the Mechanics and Physics of Solids.
- Carroll J.D., Abuzaid W.Z., Lambros J. and Sehitoglu H., (2012), “On the interactions between strain accumulation, microstructure, and fatigue crack behavior”, in press International Journal of Fracture.
- Carroll J.D., Abuzaid W.Z., Lambros J. and Sehitoglu H., (2012), “High resolution digital image correlation measurements of strain accumulation in fatigue crack growth”, in press International Journal of Fatigue
- Lee Y.-J. and Song J., (2012), “Finite-element-based system reliability analysis of fatigue-induced sequential failures”, Reliability Engineering & System Safety, Vol. 108, pp. 131-141.
- Lee Y.-J. and Song J., (2012), “System reliability updating of fatigue-induced sequential failures”, submitted to ASCE Journal of Structural Engineering.

- O'Hara P., Duarte C.A., Eason T., Garzon J., (2012), "Efficient analysis of transient heat transfer problems exhibiting sharp thermal gradients", *Computational Mechanics*, DOI 10.1007/s00466-012-0750-6
- Ostoich C., Bodony, D. J., Geubelle, P. H., (2012), "Fluid–Thermal Response of Spherical Dome Under a Mach 6.59 Laminar Boundary Layer," *AIAA Journal*, Vol. 50, No. 12, pp. 2791-2808.
- Plews J., Duarte C.A., and Eason T., (2012), "An improved nonintrusive global–local approach for sharp thermal gradients in a standard FEA platform", *International Journal For Numerical Methods In Engineering*, DOI: 10.1002/nme.4279
- Sobotka J.C. and Dodds R.H., (2012), "Extension of generalized plasticity model for thermocyclic loading", submitted to *Journal of Engineering Materials and Technology*.
- Sucheendran M., Bodony, D. J. and Geubelle, P. H. (2012), "Coupled structural-acoustic response of a duct-mounted elastic plate with grazing flow", submitted to *AIAA Journal*.

2011

- Gain A.L., Carroll J., Paulino G.H., Lambros J., (2011), "A hybrid experimental/numerical technique to extract cohesive fracture properties for mode-I fracture of quasi-brittle materials", *International Journal of Fracture*, Vol. 169, pp. 113–131.
- Kang W.-H., Lee Y.-J., Song J. and Gencturk B., (2011), "Further development of matrix-based system reliability method and applications to structural systems", *Structure and Infrastructure Engineering: Maintenance, Management, Life-cycle Design and Performance*, Vol. 8, No. 5, pp. 441-457.
- Lee Y.-J. and J. Song, (2011), "Risk analysis of fatigue-induced sequential failures by branch-and-bound method employing system reliability bounds" *ASCE Journal of Engineering Mechanics*. Vol. 137, No. 12, pp. 807-821, doi:10.1061/(ASCE)EM.1943-7889.0000286.
- O'Hara P., Duarte C.A., Eason T., (2011), "Transient analysis of sharp thermal gradients using coarse finite element meshes", *Comput. Methods Appl. Mech. Engrg.*, Vol. 200, pp. 812–829.
- Shanmugam V., Penmetsa, R.C., and Tuegel, E. (2011), "Calibration of a Probabilistic Cohesive Zone Model for Generating a Fracture Nomograph," *Journal of Fatigue and Fracture of Engineering Materials and Structures*, Vol. 35, pp. 328–346.

2010

- Carroll J., W. Abuzaid, J. Lambros, and H. Sehitoglu, (2010). "An Experimental Methodology to Relate Local Strain to Microstructural Texture," *Rev. Sci. Instrum.* 81, 083703.

Efstathiou C., Sehitoglu H. and Lambros J., (2010). “Multiscale Strain Measurements of Plastically Deforming Polycrystalline Titanium: Role of Deformation Heterogeneities,” *International Journal of Plasticity*, Vol. 26, pp. 93–106, 2010.

2009

Carroll J., Efstathiou C., Lambros J., Sehitoglu H., Hauber B., Spotswood S. and Chona R., (2009) “Investigation of Fatigue Crack Closure Using Multiscale Image Correlation Experiments,” *Engineering Fracture Mechanics*, Vol. 76, No. 15, pp: 2384-2398, DOI: 10.1016/j.engfracmech.2009.08.002.

Kim D.-J., Pereira J.P. and Duarte C.A., (2009). “Analysis of three-dimensional fracture mechanics problems: A two-scale approach using coarse generalized finite element meshes.” *International Journal for Numerical Methods in Engineering*, Vol. 81, pp. 335–365.

O’Hara P., C.A. Duarte, T. Eason, and D.-J. Kim, (2009). “Generalized finite element analysis of three-dimensional heat transfer problems exhibiting sharp thermal gradients.” *Computer Methods in Applied Mechanics and Engineering*, 198(21—26.:1857—1871, <http://dx.doi.org/10.1016/j.cma.2008.12.024>.

Penmetsa R. C., Tuegel, E., and Shanmugam, V., (2009). “Rapid Risk Assessment using Probability of Fracture Nomographs,” *Journal of Fatigue and Fracture of Engineering Materials and Structures*, Vol. 32, 2009, pp.-886-898.

2008

Efstathiou C., Sehitoglu H., Carroll J., Lambros J. and Maier H.J., (2008). “Full-Field Strain Evolution during Intermartensitic Transformations in Single Crystal NiFeGa,” *Acta Materialia*, Vol. 56, pp. 3791-3799.

2007

Stump F.V., E.C.N. Silva and G.H. Paulino, (2007). Optimization of material distribution in functionally graded structures with stress constraints, *Communications in Numerical Methods in Engineering*. Vol.23, No.6, pp. 535-551.

Appendix III – List of MSSC students graduated

MS Degrees (7):

O'Hara P.J., 2007, “Finite element analysis of three-dimensional heat transfer for problems involving sharp thermal gradients”, Civil and Environmental Engineering, UIUC.

Smith L.G., 2008, “Conditional filtering for simplification of aircraft structural system reliability calculation”, Mechanical Engineering, The University of Texas at San Antonio.

Domyancic L.C., 2009, “Structural reliability based method for identifying critical locations”, Mechanical Engineering, The University of Texas at San Antonio.

Gain A.L., 2009, “A hybrid technique to extract cohesive fracture properties of elasto-plastic materials using inverse analysis and digital image correlation”, Civil and Environmental Engineering, UIUC.

Kable B., 2009, “Identifying Structurally Significant Items using Matrix Reanalysis Techniques”, Mechanical and Materials Engineering, Wright State University.

Plews J.A., 2011, “Non-intrusive extension of a generalized finite element method for multiscale problems to the Abaqus analysis platform”, Civil and Environmental Engineering, UIUC.

Casperson M.C., 2012, “Investigation of thermal effects on fatigue crack closure using multiscale digital image correlation experiments”, Aerospace Engineering, UIUC.

Ph.D. Degrees (7):

Efstathiou C., 2008, “Experimental characterization of heterogeneous deformation due to phase transformations, twinning, slip and grain-grain interactions using digital image correlation, Mechanical Science and Engineering, UIUC.

O'Hara P.J., 2010, “A multi-scale generalized finite element method for sharp, transient thermal gradients”, Civil and Environmental Engineering, UIUC.

Carroll J., 2011, “Relating fatigue crack growth to microstructure via multiscale digital image correlation”, Mechanical Science and Engineering, UIUC.

Abuzaid W., 2012, “Quantitative understanding of the role of grain boundaries in polycrystalline deformation via multiscale digital image correlation”, Mechanical Science and Engineering, UIUC.

Lee Y.J., 2012, “Finite-element-based system reliability analysis and updating of fatigue-induced sequential failures”, Civil and Environmental Engineering, UIUC.

Ostoich C., 2013, “Aerothermal and aeroelastic response prediction of aerospace structures in high-speed flows using direct numerical simulation”, Aerospace Engineering, UIUC.

Sucheendran M.M., 2013, “Effect of grazing flow on structural-acoustic response of an elastic plate with sound in a duct”, Aerospace Engineering, UIUC.